UNIVERSITY OF CALIFORNIA SAN DIEGO

Design of Multifunctional Protein Crystals

A dissertation submitted in partial satisfaction of the requirements

for the degree Doctor of Philosophy

in

Chemistry

by

Kenneth Han

Committee in charge:

Professor F. Akif Tezcan, Chair
Professor Michael Burkart
Professor Alexis Komor
Professor Jonathan Pokorski

2023

The Dissertation of Kenneth Han is approved, and it is acceptable in quality and form for publication on microfilm and electronically.

University of California San Diego

2023

DEDICATION

To the many whose shoulders I've stood on,

I could not have done it without you.

EPIGRAPH

“In the beginner's mind there are many possibilities, in the expert's mind there are few.”
Shunryu Suzuki

“Not that the story need be long, but it will take a long while to make it short.”
Henry David Thoreau

“Believe it or not, I can actually draw.”
Jean-Michel Basquiat

TABLE OF CONTENTS

LIST OF FIGURES

LIST OF TABLES

ACKNOWLEDGEMENTS

First, I would like to acknowledge Akif for being my biggest supporter and champion of science. Under his tutelage, I sharpened my skills and grew as a researcher immensely. Witnessing his constant wonder and scientific rigor every day was inspiring. I will always be grateful for the invaluable experiences gained from my time in the Tezcan Lab and hope to carry the wisdom into my next chapters.

I would be remiss if I did not acknowledge Mr. Joel Finbloom (now Professor Finbloom!) for taking a chance and helping me first "explore biology through the lens of chemistry" as an undergraduate researcher. The skills and experience I learned as his mentee have been the foundations I stood on throughout graduate school.

Once joining the Tezcan Lab, I had the opportunity to work alongside many talented people. The group of scientists that were present when I joined the lab was a legendary batch, from whom I learned so much – especially my mentor, Jake. Without his patience and guidance, I would not be the scientist I am today. At times, his breadth of knowledge and insight seemed limitless. Also, special thanks to Ling, my other PIX mentor, for always answering my list of questions with patience. It was an absolute pleasure learning from and working with them both.

I would also like to thank Jie, Yiying, Nicole, Rohit, and Rob. In addition to our many scientific discussions, I am grateful for their friendships and insights beyond the lab. Eating and chatting over lunch with them helped me through the years and will remain a core memory of graduate school. Although Albert and Hannah were a year ahead of me, I am thankful for their help with navigating graduate school, especially since I was the only one in my year. Lastly, as a senior graduate student, I have had the pleasure of welcoming Yui and Deb to the PIX subgroup. I am thankful for their discussions and ability to provide new perspectives.

Beyond the Tezcan Lab. I would like to thank Ivan Rajakovic (SSRL) for his support during our synchrotron experiments, especially during COVID, when I needed urgent SAXS measurements. I would also like to thank the Rappel Lab members (Marco, Richa, Dorsa, and Sanchi) for always kindly responding to my requests to use the confocal microscope. Ricardo from the Sailor lab was instrumental for my GPC-MALS studies, and I am grateful for his help troubleshooting my samples. I have also had the pleasure of working with talented researchers through collaborative projects. I would like to thank Macwin and Pritesh from the laboratory of Prof. Shirley Meng. Although the project ended earlier than we wished, I am grateful to have had the opportunity to explore the impact of incorporating proteins in Li batteries. I would also like to thank Felipe from the laboratory of Prof. Monica Olvera de la Cruz. Understanding and simulating PIX was no trivial task and I'm grateful for his continuous effort and our long discussions.

In my first year, I got to befriend Bryce and Cam. Our on-campus coffee sessions and "sandy" nights have become core memories of graduate school. Lastly, I would like to express my gratitude to my loved ones for being the ultimate support system. Although I can only imagine my mom's confusion on why I am still in school, her blanket understanding and support has been a pillar. Even more, Sophia has seen me at my lowest and helped me climb back up the Sisyphean task of graduate school. Especially when the world was seemingly turned upside down and riddled with uncertainty, the COVID times only fortified our bond. I am immensely grateful for her helping me maintain the sanity of pushing through.

This dissertation was funded in part by UCSD's Teddy Traylor Award and Distinguished Graduate Student Fellowship. Additional funding from the US Army Research Office and Department of Energy (BES, Division of Materials Sciences) are acknowledged and detailed at the end of the individual chapters.

Chapter 2 is reproduced, in part, with permission, from: Han, K., Bailey, J. B., Zhang, L., Tezcan, F. A. “Anisotropic Dynamics and Mechanics of Macromolecular Crystals Containing Lattice-Patterned Polymer Networks” *Journal of the American Chemical Society* **2020** *142* (45), 19402-19410. The dissertation author was the primary author on all reprinted materials.

Chapter 3 is reproduced, in part, with permission, from: Han, K., Na, Y., Zhang, L., Tezcan, F. A. “Dynamic, Polymer-Integrated Crystals for Efficient, Reversible Protein Encapsulation” *Journal of the American Chemical Society* **2022** *144* (23), 10139-10144. The dissertation author was the primary author on all reprinted materials.

Chapter 4 is reproduced, in part, with permission, from: Han, K., Zhang, Z., Tezcan, F. A. “Spatially Patterned, Porous Protein Crystals as Multifunctional Materials” *Journal of the American Chemical Society* **2023** (Accepted). The dissertation author was the primary author on all reprinted materials.

VITA

EDUCATION

2017 B.S., Chemical Biology, University of California, Berkeley

2019 M.S., Chemistry, University of California San Diego

2023 Ph.D., Chemistry, University of California San Diego

HONORS AND AWARDS

2022 UCSD Distinguished Graduate Student Fellowship

2021 Teddy Traylor Award

2017 George C. Pimentel Undergraduate Award

PUBLICATIONS

Han, K.; Zhang, Z.; Tezcan, F.A. Spatially Patterned, Porous Protein Crystals as Multifunctional Materials *J. Am. Chem. Soc.* **2023** (Accepted)

Han, K.* Na, Y.*; Zhang, L.; Tezcan, F.A. Dynamic, Polymer-Integrated Crystals for Efficient, Reversible Protein Encapsulation *J. Am. Chem. Soc.* **2022**, 144 (23), 10139-10144.

Zhu, J.; Avakyan, N.; Kakkis, A.; Hoffnagle, A.M.; **Han, K**.; Li, Y.; Zhang, Z.; Choi, T.; Na, Y.; Yu, C-J.; Tezcan, F.A. Protein Assembly by Design *Chem. Rev.* **2021**, 121, 13701-13796.

Han, K.; Bailey, J.B.; Zhang, L.; Tezcan, F.A. Anisotropic Dynamics and Mechanics of Macromolecular Crystals Containing Lattice-Patterned Polymer Networks. *J. Am. Chem. Soc.* **2020**, 142 (45), 19402-19410.

Finbloom, J.A.; Aanei, I.; Bernard, J.M.; Klass, S.H.; Elledge, S.K.; **Han, K.**; Ozawa, T.; Nicolaides, T.P.; Berger, M.S.; Francis. M.B. Evaluation of Three Morphologically Distinct Virus-Like Particles as Nanocarriers for Convection-Enhanced Drug Delivery to Glioblastoma. *Nanomaterials* **2018**, 8, 1007.

Finbloom, J. A.; **Han, K.**; Slack, C. C.; Furst, A. L.; Francis, M. B. Cucurbit[6]uril-Promoted Click Chemistry for Protein Modification *J. Am. Chem. Soc.* **2017**, 139(29)**,** 9691–9697.

Finbloom, J.A.; **Han, K.**; Aanei, I. L; Hartman, E.C.; Finley, D.T.; Dedeo, M.T.; Fishman, M.; Downing, K. H.; Francis, M.B Stable Disk Assemblies of a Tobacco Mosaic Virus Mutant as Nanoscale Scaffolds for Applications in Drug Delivery. *Bioconjug. Chem.* **2016**, 27, 2480-2485.

FIELDS OF STUDY

Major Field: Chemistry

Studies in Chemical Biology and Bioinorganic Chemistry
Professor F. Akif Tezcan

ABSTRACT OF THE DISSERTATION

Design of Multifunctional Protein Crystals

by

Kenneth Han

Doctor of Philosophy in Chemistry

University of California San Diego, 2023

Professor F. Akif Tezcan, Chair

Proteins are the premier building blocks that Nature uses to create sophisticated systems. From carrying out the biological processes essential for life (e.g., photosynthesis, DNA replication, nitrogen fixation, etc.), to serving as mechanical supports for cells (e.g., cytoskeleton, membrane proteins, etc.), proteins play diverse, functional roles. Due to these capabilities, the synthesis of protein-based materials has become a burgeoning field that aims to introduce new-to-nature functionalities. Notably, researchers have recently begun to view protein crystals as viable

candidates to serve as molecular templates. While historically used for structural analysis, protein crystals have more recently garnered attention as hosts for various extrinsic cargos including small molecules, nanoparticles, and other guest proteins. The Tezcan Lab, in particular, has successfully integrated synthetic polymers into crystals composed of Human Heavy-chain Ferritin (HuHF), resulting in a material termed Polymer-Integrated Protein Crystals (PIX). These hydrogel-crystals exhibit unprecedent characteristics such as reversible expansion/contraction and self-healing, all while maintaining crystallinity. Herein, we have focused on exploring the potential applications and limitations of PIX.

In this dissertation, we elucidate how the different components of PIX can be modified to generate a multifunctional material. Starting with the building block, we created a mutant HuHF variant that exhibits a cysteine residue on the protein surface. By labeling HuHF with a specific small molecule, control over its crystallization behavior was achieved, leading to the formation of two distinct lattice arrangements. The spatial organization of HuHF molecules subsequently influences polymer distribution during PIX formation. Through these experiments, we discovered anisotropic polymer distribution can grant PIX with directional actuation during expansion/ contraction (Chapter 2). In another study, we examined how the dynamicity of PIX can be leveraged to encapsulate macromolecular cargo. By screening different proteins and encapsulation conditions, we revealed PIX can uptake guest proteins with high loading efficiencies (up to 46% w/w). Moreover, we explored the pH-dependency of cargo uptake and release using two model proteins, cytochrome *c* and lysozyme (Chapter 3). Lastly, we developed core-shell protein crystals using two distinct HuHF variants. This unique spatial organization of the HuHF molecules facilitated selective modification of the crystal surface. Due to PIX's ability to encapsulate protein, we further functionalized the interstitial space and created a cell-like system (Chapter 4).

Chapter 1: Design and Application of Porous 3D Networks

1.1 Introduction

Polymerization is the chemical process of linking numerous small monomeric through covalent or non-covalent bond formation to synthesize bulk, macromolecular species. Since its recognition in the 1920s, polymer science has had a widespread impact on fields such as materials science, medicine, and nanotechnology.[1-3] Specifically, the design and synthesis of polymeric three-dimensional (3D) materials have made significant progress through the development of functional porous polymer networks (**Figure 1.1a**).[4-6] Hydrogels represent a large subset of porous materials, given their well-studied physical, chemical, and biological characteristics.[7-9] The soft and amorphous, yet chemically tailorable, nature of hydrogels make them interesting candidates to create bespoke materials with applications for tissue engineering,[10] drug delivery,[11] and stimuli-responsiveness.[12]

In addition to hydrogel polymer networks, porous coordination polymers (PCPs) constitute another significant subset of porous materials (*i.e.*, metal-organic frameworks or MOFs).[5, 13-14] In contrast to soft, amorphous hydrogels, MOFs are rigid, crystalline materials that consist of metal ions or clusters that serve as molecular junctions and are interconnected by organic ligands (**Figure 1.1b**).[13] Generally, the resulting constructs exhibit a 3D lattice with large continuous voids. By screening a wide array of metal ions and organic linkers, chemists have synthesized a multitude of different MOF systems that exhibit unique properties.[15] Like hydrogels, PCPs/MOFs have been thoroughly characterized and studied for their applications in molecular capture/storage,[16] separation,[15] and drug delivery.[17]

Overall, both hydrogels and MOFs are porous materials that exhibit substantial amounts of void volumes, which have been exploited to accommodate guest molecules. Despite the different

methods of preparation and physical characteristics, the design considerations for both are similar in that the building blocks dictate where the chemical functional groups are situated in the resulting network. Depending on the chemical properties, hydrogels and MOFs can be applied in medical or industrial settings and are guided by the spatial positioning of the functional groups within the system. In addition to hydrogels and MOFs, such chemical patterning within a 3D network can be achieved through another class of materials – protein crystals (**Figure 1.1c**). Although they are not polymeric systems, protein crystals can be porous and fulfill the requisite attributes for creating functional 3D materials.[18] X-ray techniques provide molecular-level information about a protein crystal, allowing researchers to determine its porosity and the position of functional groups.[19] Furthermore, in conjunction with advancements in recombinant DNA technology and bioorthoganol chemistry, chemists can site-specifically modify protein crystals with the desired functional groups.[20] Owing to such chemical biology techniques, protein crystals have garnered attention as suitable candidates to process into functional biomaterials. Ultimately, protein crystals represent another highly modular platform, with ongoing research exploring their potential for cargo encapsulation, molecular storage, drug delivery, and catalysis.[18, 20-21]

This chapter aims to provide a comprehensive understanding of porous networks as functional materials, focusing on hydrogels, MOFs, and protein crystals, along with current efforts to further develop their translational applications.

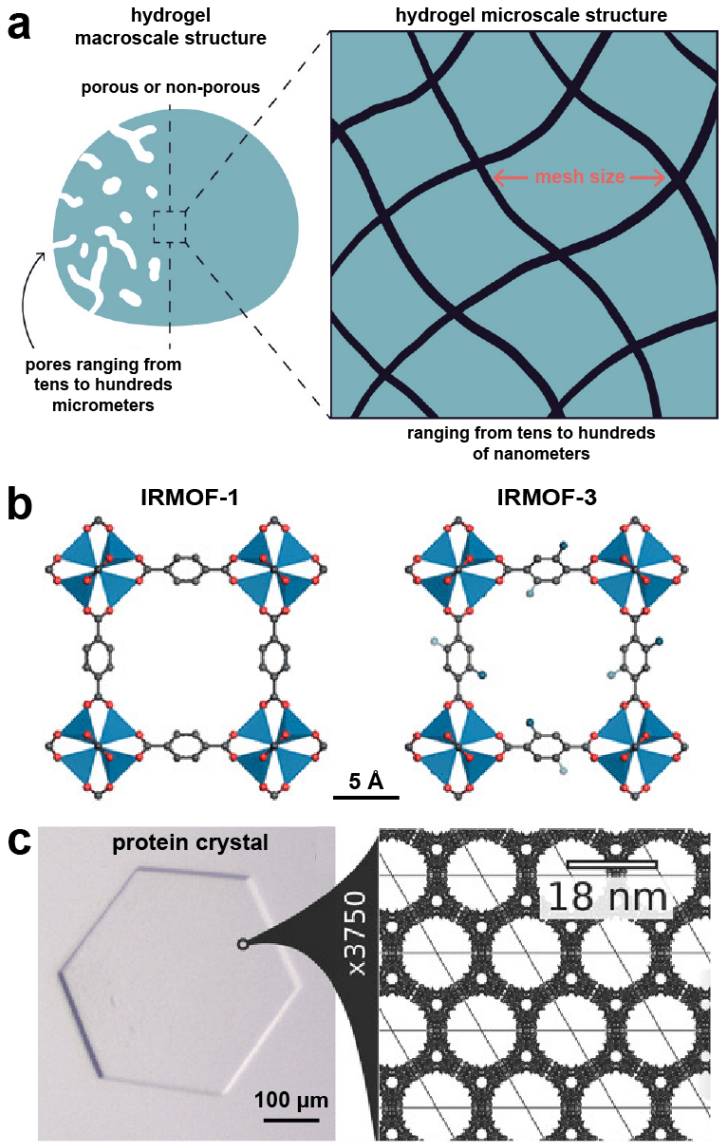

Figure 1.1. Viewing hydrogels, MOFs, and protein crystals as porous materials. **(a)** At the nanoscale, the degree of polymer cross-linking determines the pore size (*i.e.*, mesh size). This can range from 10-100's of nanometers and influences the type/size of cargo the resulting polymer can accommodate. At the macroscale, imperfections in the network can result in macropores that range from 10-100's of micrometers. Such defects can directly influence the polymer's retention capabilities. Adapted from reference 9. **(b)** The structures of IRMOF-1 and IRMOF-3 display the metal junctions (blue) interconnected by the organic linkers (gray). Depending on the linker size, the lattice pore size can be tuned. Furthermore, the linkers can be modified with functional groups to influence the overall reactivity of the MOF. Adapted from reference 15. **(c)** Light micrograph of a protein crystal. Crystallographic analysis reveals the crystal exhibits continuous porosity with 13 nm wide channels. Adapted from reference 21.

1.2 Characteristics of Hydrogels

Hydrogels are 3D, cross-linked networks of hydrophilic polymer chains embedded in a water-rich environment. They possess unique physicochemical properties that make them highly versatile materials and can be synthesized from both naturally-derived and synthetic polymers.[8, 22] Since its conception in 1960,[23] the design and application of hydrogels have remained an active area of research, especially for protein storage and delivery.[24] One of the defining characteristics of hydrogels is their high water content, typically ranging from 70% to 99%, which fosters excellent biocompatibility and enables the encapsulation of hydrophilic cargo, such as therapeutic proteins. Hydrogels can also exhibit unique release behavior due to their porous structure and chemical tunability. By adjusting the interactions between the hydrogel and guest protein through the incorporation of additional functional groups, researchers can achieve controlled encapsulation and release of protein cargo.[9, 25]

Therapeutic biologics, such as proteins and peptides, increasingly represent a large portion of clinically-relevant drugs due to their ability to treat medical conditions ranging from diabetes, cancer, and immune-related diseases.[26] Due to their unique physiochemical properties, proteins offer advantageous qualities (*e.g.*, high specificity and mass production) compared to small molecule drugs. However, proteins suffer from poor stability and are susceptible to proteolytic and chemical degradation, as well as unfolding and aggregation, which lead to loss of function.[24] Furthermore, the bioavailability of protein-based drugs is a common concern, requiring frequent administration.[25] To overcome such limitations, researchers have explored how hydrogels can be applied to stabilize proteins, as well as control their uptake and release behavior.[9, 25]

1.2.1 Hydrogel Polymer Nanoparticles

Among the polymers studied for delivery purposes, both natural and synthetic polymer systems have been investigated. Natural polymers such as alginate, chitosan, and heparin have been explored for applications in vaccine formulation, controlled insulin release, and wound healing.[9] However, due to the advancements in synthetic polymer technology, natural polymers have been overshadowed – especially in the development of polymer nanoparticles.[27-28] Through controlled polymerization conditions, the polydispersity, molecular length, and functional groups of polymers can be chemically tuned to create sophisticated polymer systems.[29-30] For example, poly-lactic acid (PLA)- and poly-(lactic-co-glycolic acid) (PLGA)-based (**Figure 1.2a**) materials are biodegradable, hydrophilic polymers.[27] Over time, PLGA can get hydrolyzed into lactic acid and glycolic acid, which are metabolites the body can process. Interfacing proteins with poly-ethylene glycol (PEG) enhances their overall solubility and bioavailability,[31] which are both desirable qualities when designing therapeutics (**Figure 1.2a**). Owing to such properties, PEG, PLA, and PLGA are the dominant players in this field.

In an early study by Caliceti and co.,[32] the researchers examined the efficacy of PLA and PEG-based hydrogels for insulin storage and release. Specifically, insulin was loaded into hydrogel nanoparticles through physical entrapment (**Figure 1.2b**). Different hydrogel networks were prepared by using different amounts of PEG 6000 or a fixed amount of PEG species but with varying molecular weights. After loading, they tested the release of insulin by placing the resulting hydrogel in a solution that mimics physiological conditions (20 mM phosphate buffer, 0.15 M NaCl, pH 7.2) for 5 minutes. They found that by increasing the PEG 6000 content or the PEG molecular weight led to an increase in the percentage of released insulin. Without any PEG 6000, the PLA hydrogel released ~10% of the entrapped insulin, but at 0.3:1 PEG 6000:PLA (w/w) ratio,

30% of the entrapped insulin was released. When PEG 10,000 and PEG 20,000 were used at the same PEG:PLA ratio, the released insulin increased to 40% and 50%, respectively. Despite high release profiles, a burst release is undesirable due to potential adverse physiological responses, and translational applications require a more controlled, slow release. Therefore, when lower molecular weight PEG species were used and monitored, they observed a slower release profile over a 1,500-h period. This early study suggested that the addition of high amounts of low molecular weight PEGs could provide formulations with appropriate drug release rates. Subsequent studies by Caliceti and co. focused on optimizing the loading by controlling the preparation process and exploring different guest protein cargo within hydrogel systems.[33-36]

In another example of utilizing nanoparticle-based hydrogels, Liu et al. entrapped insulin in PLGA nanoparticles that were later embedded in poly(vinyl alcohol) (PVA) hydrogels.[37] A mixture containing insulin and PLGA species consisting of a 1:1 (w/w) ratio of lactic acid (LA) to glycolic acid (GA) was prepared, emulsified to create insulin-loaded PLGA nanoparticles, and subsequently mixed with PVA hydrogels (**Figure 1.2c**). Overall, the encapsulation efficiency was 72.6%, and the resulting hydrogels exhibited sustained release ranging from 60-100%, over a 240-h period. Furthermore, in-vitro studies revealed that the PLGA nanoparticles helped facilitate a higher release rate and total release amount when compared to free insulin in PVA hydrogels.

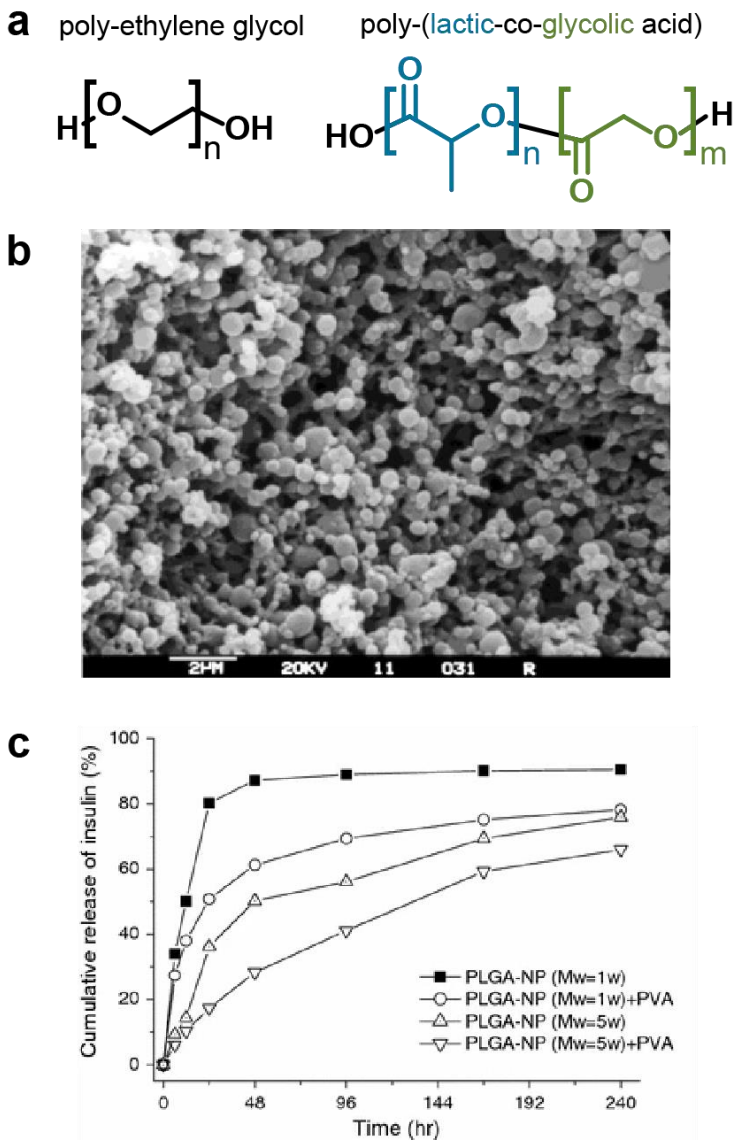

Figure 1.2. Hydrogel characteristics. **(a)** Molecular structures of poly-ethylene glycol (PEG) and poly-(lactic-co-glycolic acid) (PLGA). The hydrophilic functional groups of both PEG and PLGA make them biocompatible materials to interface with proteins. Upon degradation of PLGA networks, lactic acid (blue) and glycolic acid (green) are released and can be metabolized by the body. **(b)** SEM image of insulin-loaded hydrogel nanoparticles containing PEG 6000 reveals spherical particles with smooth surfaces. The protein-loaded materials are then studied for their loading and release capabilities. Adapted from reference 36. **(c)** Release profile displaying the effects of embedding PLGA nanoparticles in poly-vinyl alcohol (PVA). Free nanoparticles display burst release behavior. In contrast, the embedded counterparts display slower release kinetics, which are desirable for translational applications. Using PLGA nanoparticles composed of higher molecular weights (10,000 vs 50,000 Da) further improve the release kinetics. Adapted from reference 37.

The use of PLGA nanoparticles has proven to be an effective approach for slowing the release of cargo from days to months, highlighting their utility as molecular depots. However, in a more recent study by Pakulska et al.,[38] the researchers demonstrated that prolonged controlled release can be achieved without the pre-encapsulation of protein cargo in nanoparticles (**Figure 1.3a,b**). Specifically, they prepared a mixture containing growth factor proteins and PLGA nanoparticles, which were then dispersed within a cross-linked methyl-cellulose (XMC) hydrogel. The resulting hydrogel exhibited long-term controlled release. Screening different nanoparticle concentrations, nanoparticle sizes, or environmental pH suggested that short-range electrostatic interactions between the proteins and the PLGA nanoparticles mainly impact the release profile of the growth factors. PLGA nanoparticles are negatively charged and thus attract the positively charged proteins. However, as PLGA degrades over time, releasing lactic acid, the local pH decreases, causing the PLGA-protein interactions to be unfavorable (**Figure 1.3c**). Through these studies, they demonstrated another approach to creating smart, functional hydrogels that can facilitate the effective delivery of therapeutic proteins.

In addition to using hydrogels as an extended delivery system, nanoparticle hydrogels can be used for the targeted delivery of compounds within the body. In one example of rationally designed nanoparticles, Schmid and co. loaded PLGA nanoparticles with a small-molecule drug, SD-208, and coated the surface with antibody fragments that bind to $CD8^+$ T cells.[39] Specifically, SD-208 inhibits TGFβ (Transforming Growth Factor Beta) signaling, which prolongs T cell activity against cancer cells. The nanoparticle surface was coated with maleimide-exposed PEG groups, to which the antibody fragments were conjugated onto using thiol-maleimide click chemistry (**Figure 1.3d**). Compared to freely administered drugs, the hydrogel nanoparticle platform extended the survival of mice with colorectal cancer, exemplifying the utility of

hydrogels as targeting agents. Similarly designed hydrogel nanoparticles were achieved by Hrkach et al. through combinatorial and high-throughput screening.[40] By varying parameters such as drug concentration, PEG/PLGA molecular weights, and overall charge, they found optimal conditions to form targeting polymeric nanoparticles. Instead of SD-208, they entrapped docetaxel (a chemotherapeutic small molecule) and labeled the surface with *S*,*S*-2-[3-[5-amino-1-carboxypentyl]-ureido]-pentanedioic acid (ACUPA), a prostate-specific membrane antigen (PSMA), to target prostate-specific tumors. Both examples highlight the modularity of polymer platforms and how they can be leveraged to create effective therapeutic systems.

Due to such tailorability, hydrogels have been imbued with various capabilities. For example, PLGA can be used to encapsulate the photothermal agent, indocyanine green (ICG), and heat the surrounding area upon near-infrared (NIR) irradiation. Chen et al. combined ICG with imiquimod (R837), a small molecule useful for activating the immune system, and co-encapsulated both within PLGA nanoparticles to form PLGA-ICG-R837.[41] Upon the uptake of PLGA-ICG-R837 particles by tumor masses, they leveraged ICG's photothermal properties and applied local NIR irradiation to ablate nearby tumor cells (**Figure 1.3e**). Furthermore, the R837 triggered a local immune response, where the apoptotic process released tumor-associated antigens, training the immune system to protect against additional tumor cells.

From serving as molecular depots for sustained cargo release to the targeted delivery of therapeutics, hydrogels are convincingly suitable materials to synthesize multifunctional systems. The studies mentioned in this section represent merely a subset of applications within the field. Efforts to further develop hydrogel technology include incorporating additional functional groups, controlling the release kinetics, and gaining a better understanding of their activity under physiological conditions.

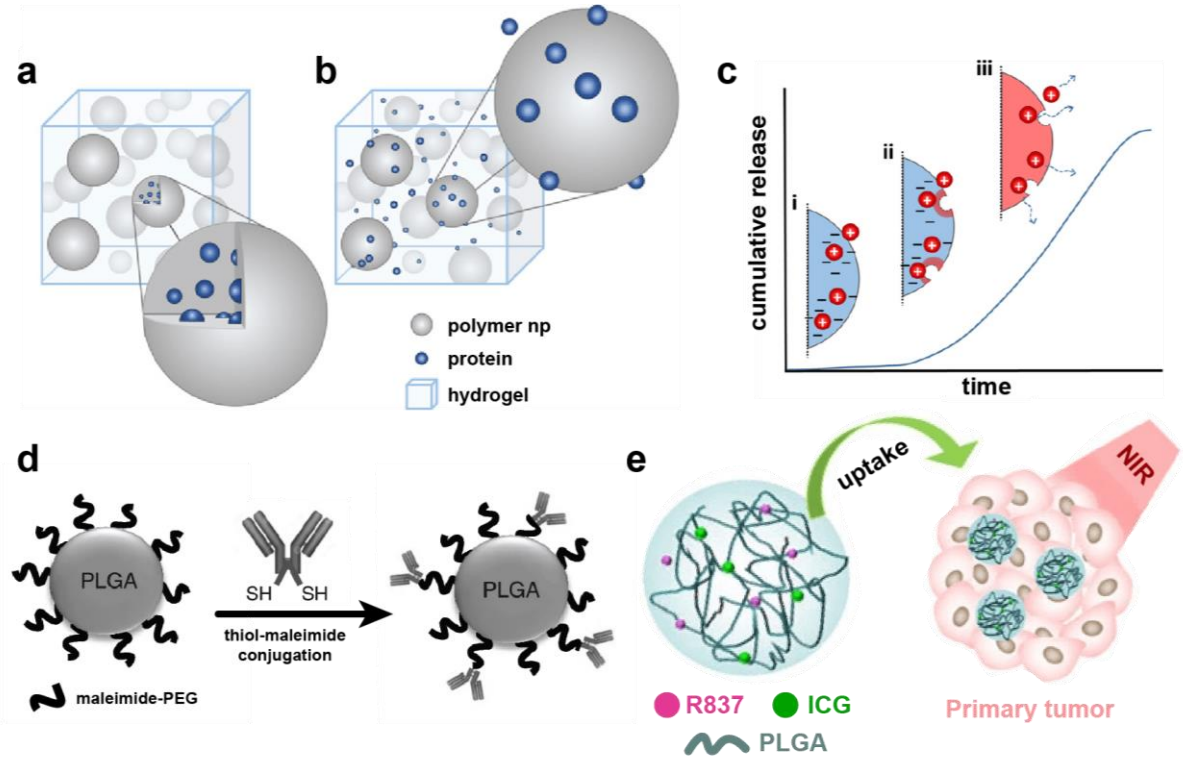

Figure 1.3. Adaptive hydrogel systems. Cartoon structures of hydrogel networks with **(a)** protein-loaded and **(b)** non-protein-loaded PLGA nanoparticles. The two different systems differ in where the protein is situated in the matrix. **(c)** Overtime, the PLGA particles degrade and acidify the local environment. The decrease in pH lead to unfavorable interactions between the protein and nanoparticles, resulting in the slow release of protein cargo. **(a)-(c)** were adapted from reference 38. **(d)** Schematic illustrating the preparation of PLGA nanoparticles coated with targeting moieties. The particles are first coated with maleimide-functionalized PEG to coat the surface with maleimide groups. Upon incubating the nanoparticles in a solution containing antibody fragments with exposed thiols, the particles get modified and specifically target $CD8^+$ T-cells. Adapted from reference 39. **(e)** Illustration presenting the R837- (pink) and ICG-functionalized (green) PLGA nanoparticles. After the tumor uptakes the nanoparticles, the mass is irradiated with near-infrared light to heat the local environment and ablate the surrounding cells. Adapted from reference 41.

1.2.2 Rationally Designed Hydrogels for Nanomedicine

More recently, work has been focused on actively sequestering proteins through the installation of functional groups designed to promote hydrogel-guest interactions. Whether through covalent or non-covalent interactions, a range of sophisticated hydrogels has been developed for translational applications (**Figure 1.4**).[9] Compared to particle-based approaches, where proteins of interest are mechanically entrapped within the matrix, actively sequestering cargo can lead to the synthesis of smart, stimuli-responsive hydrogels.

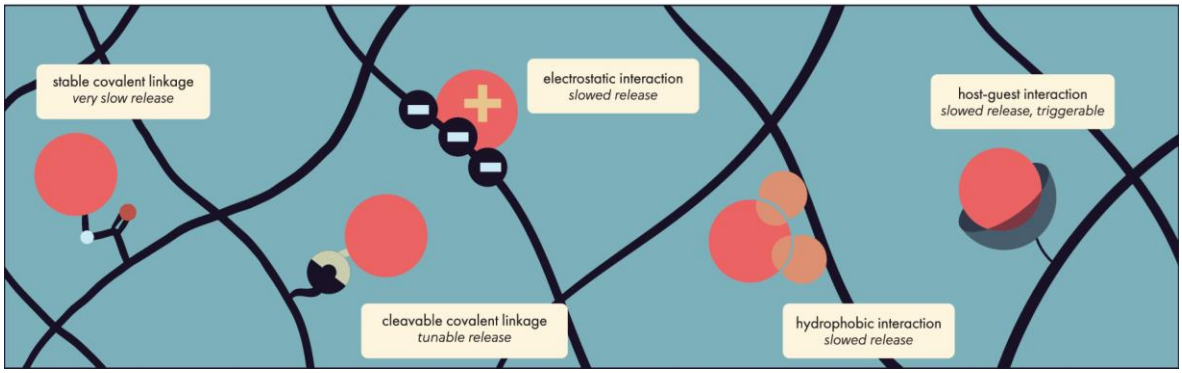

Figure 1.4. The possible interactions between the hydrogel and the guest. The modularity of hydrogels allows the installation of different chemical functional groups. From electrostatic interactions to active host-guest capture and covalent linkages, hydrogel networks can bind to guest proteins via a wide array of contacts, which directly influence the retention and release of guests. Adapted from reference 9.

A common concern surrounding hydrogels is the unintended release of cargo into the surrounding environment over time, leading to unwanted consequences such as degradation and diminished potency of the protein drugs.[25] Tethering proteins to the hydrogel matrix addresses such concerns as the release is better controlled. Many of the examples that involve hydrogel-protein conjugated systems consist of growth factor (GF) proteins as the entrapped cargo.[42-43] Due to their ability to modulate cell differentiation, migration, and adhesion, GFs are important biologics for tissue engineering and are covalently attached by reacting different polymer functional groups with the protein surface.

In an early example, Fan and co. demonstrated that epidermal growth factor (EGF) proteins can be tethered to polymers and exhibit prolonged activity.[44] Specifically, EGF was conjugated onto poly(ethylene oxide) (PEO) via the N-terminus. Upon incubating the functionalized hydrogel with stem cells, the EGF promoted cell differentiation and survival better than freely administered EGF. Alternatively, others have demonstrated that proteins can be immobilized to hydrogels via nucleic acid aptamers, which are short, single-stranded oligonucleotides with high binding capabilities. Using aptamer technology, members of the Wang lab demonstrated aptamers can be co-polymerized with hydrogels to incorporate specific binding within the matrix (**Figure 1.5a**).[45-48] For example, Abune et al. prepared PEG-based hydrogels functionalized with aptamers that bind to vascular endothelial growth factor (VEGF) and basic fibroblast growth factor (bFGF) proteins.[48] The dual GF system displayed synergistic capabilities and promoted cell migration and angiogenesis, which are important processes for tissue repair (**Figure 1.5b**).

Although tethering is an effective approach to increasing the loading and storage of guest cargo, additional methods have been developed to create more sophisticated linkages. Zisch et al. demonstrated that the linker between the hydrogel and GF can include an enzyme-sensitive sequence, such that the protein is released in the presence of matrix metalloproteinases (MMPs).[49] MMPs are sequence-specific peptidases that react on the cell surface. By incorporating the peptide sequence between the polymer and GF, they created a hydrogel capable of delivering GFs on cell demand. Upon subcutaneously injecting the hydrogel in rats, the polymer network was completely remodeled into native, vascularized tissue.

Lastly, work from the Kiick research group demonstrated that the release of GF can be coupled with the degradation of the hydrogel matrix (**Figure 1.5c**).[50] Specifically, a matrix was synthesized by complexing VEGF with a heparin-based, multi-armed star polymer. Due to

VEGF's natural ability to bind to heparin, mixing the two components led to network formation. Upon incubating the functionalized hydrogel with cells expressing a receptor specific to VEGF, ligand exchange occurred, effectively eroding the gel (**Figure 1.5c**). Heparin was chosen due to its ability to interact with the extracellular matrix (ECM). Subsequent work by the Kiick lab screened interfacing VEGF with other polymer systems that interact with the ECM.[51]

In summary, extensive efforts to create multi-modal functional hydrogels have led to innovative strategies to package and deliver therapeutic proteins. The chemical diversity of both polymers and proteins allows for a vast number of combinations or arrangements of protein-polymer hybrid systems and will continue to be an active area of research.

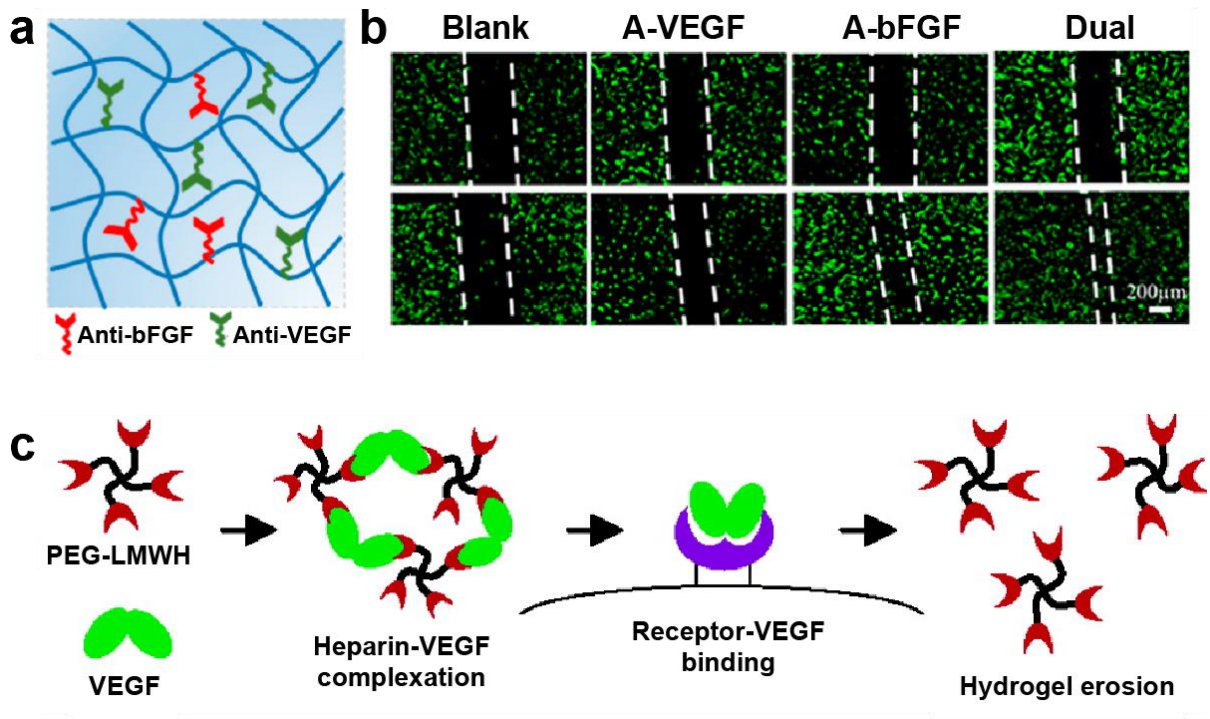

Figure 1.5. Functionalized polymer systems. **(a)** Cartton illustration of an aptamer-functionalized hydrogel network. The aptamers that bind to bFGF and VEGF are shown in red and green, respectively. Such functionalized hydrogel networks allow specific protein sequestration and release. Adapted from reference 48. **(b)** Micrographs of endothelial cells before (top) and after (bottom) incubation with different growth factors (GFs). Without any GFs, there is insignificant cell growth (Blank). There was some cell growth with VEGF or bFGF alone. However, incubating cells with hydrogels functionalized with both GFs (dual) showed significant cell migration. These results demonstrate having both GFs have synergistic affects on tissue repair. Adapted from reference 48. **(c)** Schematic illustrating the preparation and erosion of Heparin-VEGF networks. Heparin is a glycosaminoglycan polymer that naturally sequester and stabilize GFs, such as VEGF. Therefore, in the presence of VEGF, a low molecular weight heparin star polymer (PEG-LMWH) will form a cross-linked protein-polymer network. Upon incubating the polymer with cells, the VEGF-specific receptors will outcompete the heparin, and degrade the network. Through this approach, a targeted and sustained release of GFs can be achieved. Adapted from reference 50.

1.3 MOFs for Protein Uptake

Like hydrogels, MOFs provide unique solutions for the storage and stabilization of proteins. Although hydrogels and MOFs are composed of disparate building blocks, MOFs also offer a wide array of chemical tailorability. Owing to their modular construction, the structural topology, pore functionality, and crystal morphology of MOFs can be precisely tuned.[15] These design features have led to the development of porous materials that demonstrate resistance to a wide range of physical and chemical conditions.

Due to these desirable attributes, researchers have explored the encapsulation of proteins within MOFs. The resulting material of a MOF with entrapped proteins within the lattice is termed protein@MOF, and there are two approaches to synthesizing such constructs. One method is via pore intrusion. After MOF formation, the crystals are then placed in a solution containing protein, and if the protein is small enough, it will passively diffuse into the lattice. The second method is via *in-situ* encapsulation. In addition to the metals and organic linkers, protein is added to the mixture and the solution is subsequently processed to form a MOF. Upon formation, the protein becomes entrapped within the interstitial space, creating protein@MOF systems. Both approaches have been explored and exhibit unique advantages and limitations.

1.3.1 Postsynthetic Encapsulation of Proteins in MOFs via Pore Diffusion

The earliest examples of protein@MOFs involved the pore diffusion approach.[52-53] This approach was first documented by Yaghi and co., who synthesized a series of MOFs with varying apertures (7 - 50 Å) and demonstrated that macromolecules (*i.e.*, proteins) can diffuse into the lattice.[54] In proof-of-principle experiments, they incubated prepared MOFs with myoglobin or green fluorescent protein (GFP) and observed successful perfusion of proteins through the nanopores. When comparing the lattice pore size (>5 nm) (**Figure 1.6a**) with the dimensions of

GFP (<5 nm), it became evident that larger pores could accommodate such macromolecules via passive diffusion. Through confocal fluorescence microscopy measurements, they observed fluorescence from the GFP samples and concluded that the protein cargo retained their tertiary structures. Interestingly, later that year, work by Chen et al. also reported a protein@MOF sample as well. They introduced cytochrome *c* (cyt *c*) into a mesoporous MOF (Tb-mesoMOF).[55] Despite cyt *c* dimensions (2.6 nm × 3.2 nm × 3.3 nm) being larger than the pores of Tb-mesoMOF (1.3 nm and 1.7 nm), successful encapsulation of within the MOF's lattice was observed (**Figure 1.6b**).

Upon analyzing the cyt *c*@Tb-mesoMOF samples via steady-state fluorescence spectroscopy, they discovered that cyt *c* did not exhibit an emission spectrum corresponding to its native conformational state. Moreover, when comparing the spectrum to chemically denatured cyt *c* samples, the cyt *c*@Tb-mesoMOF samples differed. These findings suggested that cyt *c* adopts a new conformational state when within the interstitial space (**Figure 1.6c**) influenced by the MOF, and underscored the complexities of pore diffusion.

More recently, Farha and co. prepared cyt *c*@NU-1000 samples and similarly proposed that cyt *c* underwent conformational changes upon encapsulation in NU-1000.[56] When screening cyt *c*'s peroxidase activity with 2,2′-azino-bis(3-ethylbenzothiazoline-6-sulfonic acid) (ABTS) (**Figure 1.6d**), they observed that the k_{cat}/K_m of cyt *c*@NU-1000 (0.010 mM^{-1} s^{-1}) exceeded that of free cyt *c* (0.008 mM^{-1} s^{-1}). They hypothesized that cyt *c* interacts with the exposed functional groups inside NU-1000, altering its heme coordination environment, resulting in the observed increased catalytic efficiency.

In addition to cyt *c* and NU-1000, Farha et al. has explored a myriad of protein@MOF systems with enhanced capabilities ranging from nerve agent detoxification to stimuli-responsive insulin delivery.[57-62] In efforts to better understand the influence of the exposed functional groups

in MOFs on protein encapsulation, the Farha group examined the diffusion of ubiquitin (p*I* = 6.79) into post-synthetically modified NU-1000.[62] Specifically, they labeled the unsaturated metal nodes with serine or betaine to create MOFs with different degrees of hydrophilicity, with the latter sample being the most cationic (**Figure 1.6e**). Upon comparing the encapsulation efficiency at pH 5.5 and 7.5, betaine-treated NU-1000 was found to sequester more ubiquitin when in pH 7.5 conditions. Given that ubiquitin exhibits a negative charge when pH > p*I*, the protein is attracted to the cationic MOF and perfuses into the lattice more efficiently at pH 7.5 than at pH 5.5. Interestingly, isothermal titration calorimetry experiments revealed that ubiquitin exhibited much higher affinity for NU-1000 at pH 5.5 ($K_a = 0.8 \times 10^4 - 3.4 \times 10^4\ M^{-1}$) compared to its affinity at pH 7.5 ($K_a = 2.3 \times 10^3 - 2.8 \times 10^3\ M^{-1}$). The authors surmised that loading in acidic conditions is impeded by this high affinity. Upon binding to the lattice, instead of diffusing into the center, ubiquitin remains immobilized and obstructs additional protein molecules from binding, thereby limiting the uptake efficiency.

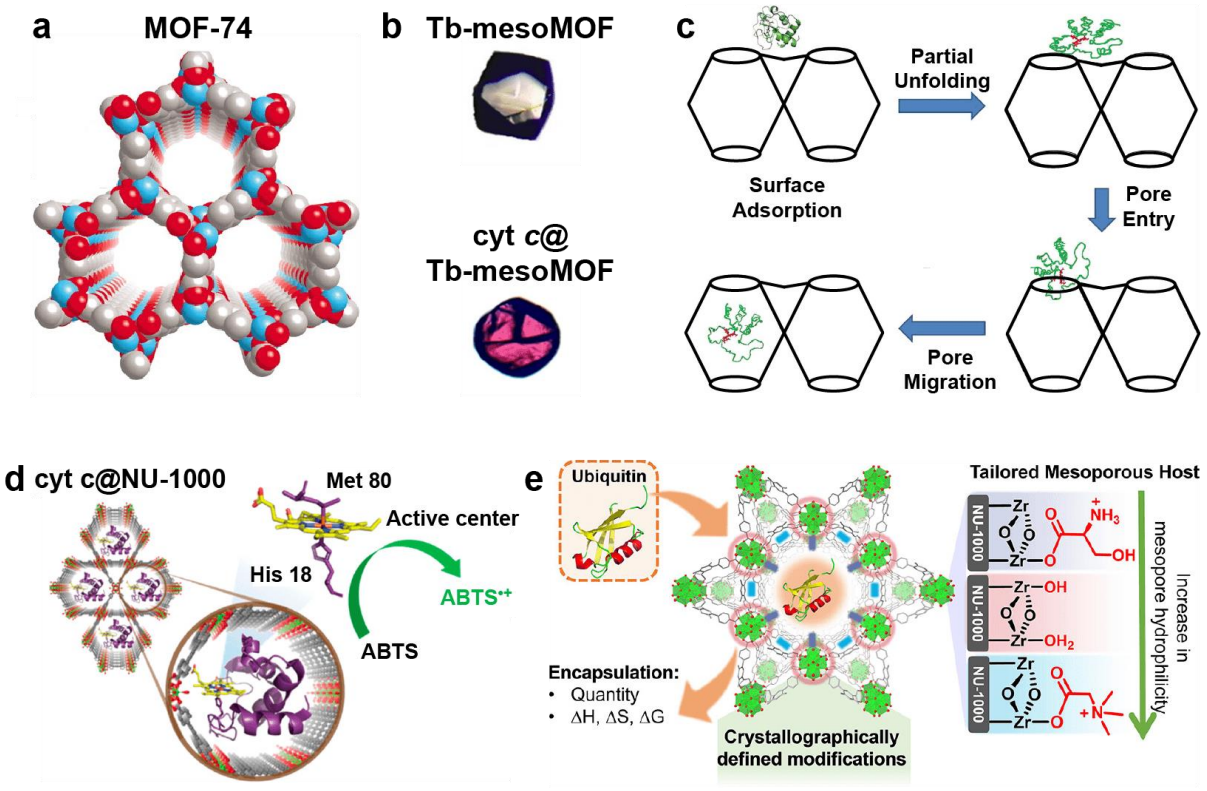

Figure 1.6. Postsynthetic encapsulation of protein cargo in MOFs. **(a)** The crystal structure of MOF-74 reveals its large, continuous voids. The one-dimensional hexagonal pores can be exploited for macromolecular uptake. Adapted from reference 54. **(b)** Images of Tb-mesoMOF before (top) and after cyt *c* encapsulation. There is a noticeable change in the crystal's color after uptake. Adapted from reference 55. **(c)** Cartoon scheme illustrating the process in which cyt *c* enters the crystal lattice, which involves partial unfolding of the protein cargo during the process. Adapted from reference 55. **(d)** Schematic illustration of cyt *c* molecules situated inside the channels of NU-1000. The entrapped cyt *c* molecules exhibit enhanced peroxidase activity due to the altered coordination environment, influenced by the protein-MOF interactions. The activity was screened with ABTS. Adapted from reference 56. **(e)** Crystal NU-1000, which is modified with serine and betaine to alter the electrostatic charges in the interstitial space. Ubiquitin was used as the model protein to screen the uptake by the different NU-1000 constructs. Adapted from reference 62.

1.3.2 In-situ Encapsulation of Proteins in MOFs via Co-precipitation

The conditions necessary for manufacturing MOFs generally require harsh parameters, such as elevated temperatures and organic solvents. Such conditions are not suitable for biomolecules (*i.e.*, proteins), hence requiring postsynthetic encapsulation approaches. However, there exist MOFs that can form under milder conditions that proteins can tolerate, and researchers have leveraged such compatibility to create protein@MOF composites. By including proteins in the precipitation mixture, they can be effectively entrapped within the framework during the MOF synthesis. Due to these facile methods, proteins@MOFs fabricated via *in-situ* encapsulation methods have been well-characterized.[52-53] Among the many examples, the most prevalent are zeolitic imidazolate framework (ZIF)-based MOFs. Although the pore size of ZIFs is approximately 1 nm, the co-precipitation method is not hindered and can efficiently assemble around the protein molecules to form protein@MOF systems.[63]

The first example of co-precipitating MOFs and biomolecules was reported by Falcaro and coworkers.[64] By mixing proteins, enzymes, or DNA in an aqueous solution containing Zn^{2+} ions and 2-methylimidazole (HmIm) at room temperature, the researchers formed protein@ZIF-8 (**Figure 1.7a**). The favorable interactions between the biomolecules and ZIF-8 building blocks led to the nucleation and precipitation of ZIF-8 bio-composites (**Figure 1.7b**). Analyses of the protein@ZIF-8 samples via found by scanning electron microscopy (SEM) and powder X-ray diffraction (PXRD) revealed the samples were crystalline, indicating that the proteins did not hinder MOF formation. Moreover, the ZIF-8 coating provided significant protection against tryptic digestion, thermal denaturation, and organic solvents (**Figure 1.7c**). When comparing the activity of horse radish peroxidase (HRP)@ZIF-8 to free HRP after trypsin exposure, the conversion efficiencies were 88% and 20%, respectively. Remarkably, after boiling in dimethylformamide at

153 °C, the protected HRP@ZIF-8 samples exhibited 90% conversion, while the unprotected HRP completely lost activity.

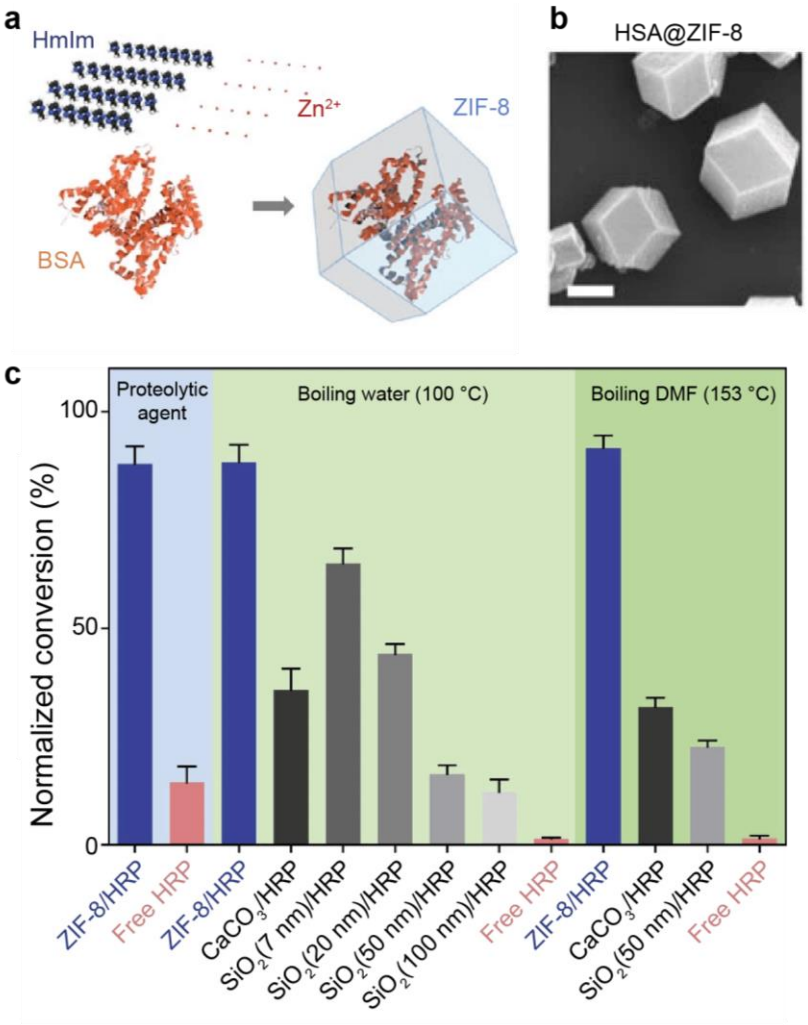

Figure 1.7. Preparation and characterization of *in-situ* encapsulated protein@MOF. **(a)** Schematic illustrating the process of forming BSA@ZIF-8. The protein, metal ions, and ligands co-precipitate upon mixture. **(b)** SEM image of human serum albumin HSA@ZIF-8 samples. The resulting materials are crystalline with sharp edges. **(c)** Comparing the protection performance of ZIF-8 coatings on HRP to other protectants. Encapsulated and free HRP samples are monitored in the presence of trypsin, after treatment in boiling water for 1 h, and after treatment in boiling DMF for 1h. Data were normalized to free HRP activity at room temperature. HRP@ZIF-8 samples performed the best in all three categories and maintained ~90% catalytic efficiencies. All figures were adapted from reference 64.

A follow-up study by Falcaro and co. further investigated how different organic linkers can influence the activity of enzymes.[65] Specifically, when catalase (Cat) is entrapped in ZIF-8, the enzyme loses its activity. However, Cat is entrapped in MAF-7 or ZIF-90, other Zn-based MOFs with more hydrophilic linkers, its activity is maintained (**Figure 1.8a**). They hypothesized that the hydrophobic linkers of ZIF-8 alter Cat's conformational state, impeding its catalytic ability. The results reported by Falcaro and co. demonstrated the utility and tunability of protein@MOFs but also highlight the challenges that need to be overcome for widespread applications.

Similar to postsynthetic immobilization methods, in-situ encapsulation methods can alter the conformational state of the entrapped protein (as demonstrated by Cat@ZIF-8). In a recent study by Walton et al., the tertiary structures of bovine serum albumin (BSA) within ZIFs were investigated using small-angle x-ray scattering (SAXS).[66] Specifically, BSA was entrapped in ZIF-8 and ZIF-67, which are Zn- and Co-based ZIFs respectively, heated to 70 °C, and monitored via SAXS. When comparing the SAXS plots of BSA@ZIF (**Figure 1.8b**) with free BSA (**Figure 1.8c)**, they discovered that the unprotected samples denatured, while the entrapped BSA maintained a SAXS profile characteristic of its native conformation. These experiments first provided direct evidence for the conservation of the tertiary proteins structure within ZIFs and after heat treatment.

The studies discussed in this section highlight the ongoing efforts towards creating functional protein@MOF systems. The results mentioned in these selected studies offer valuable insights into our fundamental understanding of protein encapsulation by porous frameworks and the potential synergistic effects between the protein and the local chemical environment of the host materials. Despite the promising results obtained so far, the full potential of protein@MOFs is yet to be realized.

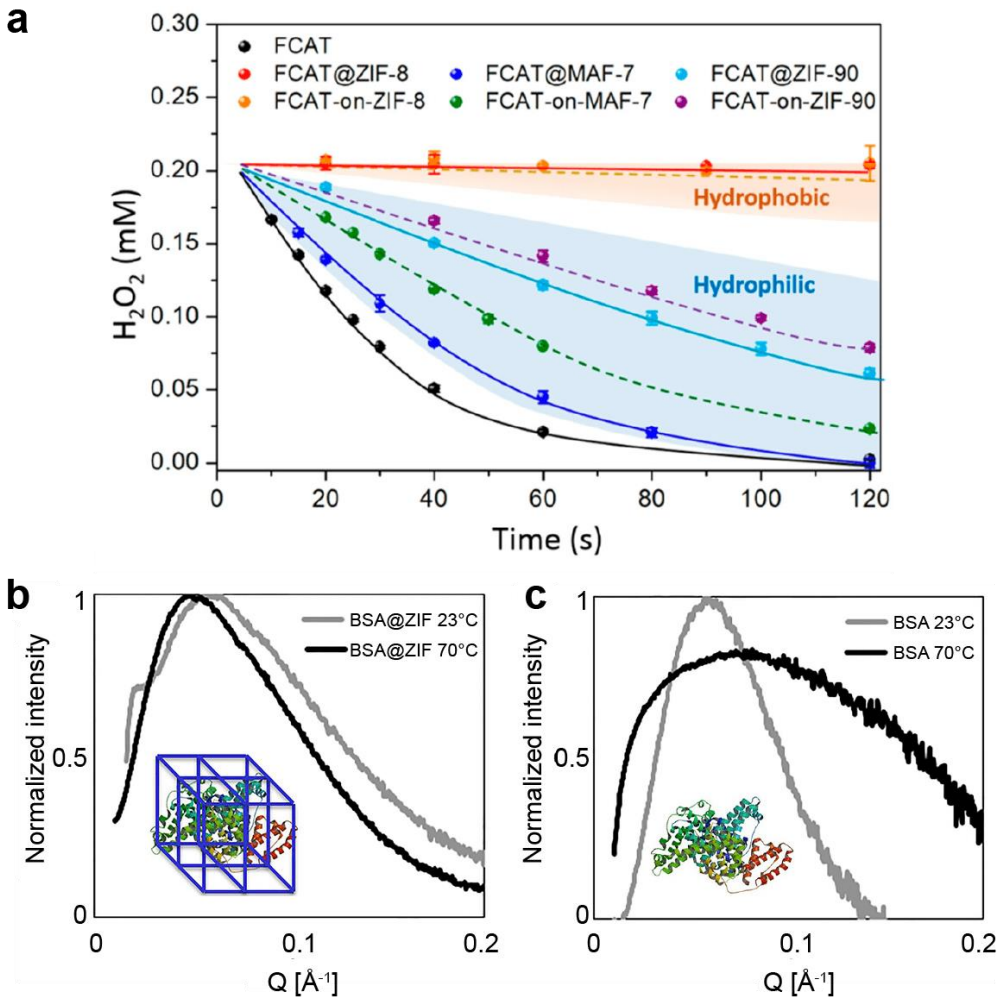

Figure 1.8. Monitoring the activity and conformational state of proteins in ZIFs. **(a)** Catalase (FCAT) activity was monitored after encapsulation in ZIF-8, ZIF-90, and MAF-7. Based on activity measurements, the latter two systems maintain FCAT's activity, which they contribute to the hydrophilic linkers. In contrast, ZIF-8 has hydrophobic linkers, abrogating FCAT's activity. Adapted from reference 65. SAXS measurements of **(b)** BSA@ZIF and **(c)** free BSA reveal that the ZIF lattice helps protect the protein's conformational state at elevated temperatures. Without protection, the BSA molecules lose their characteristic tertiary fold. Adapted from reference 66.

1.3.3. Select Examples of Protein@MOFs

The development of protein@MOFs has been explored through various approaches with different permutations of proteins/enzymes and MOF systems. In an early example of encapsulating two different enzymes within one framework, Zhou et al. synthesized GOx-HRP@PCN-888.[67] Due to PCN-888's formation process, the resulting lattice exhibits three cages with different sizes: 6.2 nm (large cage), 5.0 nm (small cage), and 2.0 nm. Understanding the framework's mesoporosity, the researchers entrapped both glucose oxidase (GOx, dimensions: 6.0 × 5.2 × 7.7 nm^3) and HRP (dimensions: 4.0 × 4.4 × 6.8 nm^3) via stepwise encapsulation methods (**Figure 1.9a**). The two enzyme pairs can perform tandem catalysis where GOx produces H_2O_2 in the presence of glucose, which HRP can then use to oxidize small molecules. To form a dual-enzyme-entrapped MOFs, GOx was first loaded into the lattice, followed by HRP. The largest cavity (6.2. nm) within PCN-888 can accommodate both GOx and HRP, while the 5.0 nm wide pores can only accommodate HRP. When HRP was used first, it occupied both cavities, blocking the uptake of GOx. To prevent single enzyme saturation, it was necessary to use GOx first, since it can only fit within the 6.2 nm wide cages, leaving the 5.0 nm pores available for HRP. Ultimately, the 2.0 nm pores were vacant after dual entrapment, which can be exploited for molecular transport. Upon analyzing the uptake efficiency, the total enzyme encapsulation capacity of GOx-HRP@PCN-888 was 300 weight %. The resulting bienzymatic nanoreactor showed catalytic activity similar to the free enzymes and maintained activity over 4 cycles of reactivity.

In contrast to postsynthetic encapsulation, Willner and coworkers entrapped both GOx and HRP in ZIF-8 nanoparticles via in-situ encapsulation approaches (**Figure 1.9b**).[68] Similar to the previous example, they demonstrated cascade catalysis with glucose and Amplex Red. The loadings of GOx and HRP in the MOFs were 40 and 25.8 μg/mg, respectively. When comparing

the GOX/HRP@ZIF-8 catalytic efficiency to that of free enzymes, they observed a 7.5-fold enhanced reactivity. Furthermore, since the *in-situ* encapsulation method is not limited by the protein size nor the number of proteins, they entrapped β-galactosidase (β-Gal) in addition to GOx and HRP. The loadings of β-Gal, GOx, and HRP encapsulated in the MOFs were 25.6, 30.5, and 18.8 μg/mg, respectively. In the presence of lactose, β-Gal produces glucose, which GOx can consume and produce H_2O_2 for the subsequent HRP-catalyzed oxidation of Amplex Red. Fluorescence measurements of the system revealed the successful operation of the three-enzyme cascade, which was 5.3-fold better than that of free enzymes at equal concentrations. They attribute such enhancements to the high local concentrations of the products produced by the enzymes.

More recently, work by Liu and co. demonstrated the entrapment of GOx and HRP in core-shell ZIF-8 systems.[69] Instead of concomitant entrapment of both enzymes, they performed sequential mineralization for each enzyme. Due to ZIF's ability to mineralize epitaxially, different layers of ZIFs can be synthesized around seed frameworks.[70-71] Leveraging such capabilities, they prepared GOx@ZIF-8 via *in-situ* encapsulation, which was subsequently used for the hierarchical assembly of HRP@ZIF-8 as the shell layer (**Figure 1.9c**). Fluorescence analysis of the resulting bienzyme@ZIF system confirmed successful cascade reactivity and proved to have been performed with higher catalytic efficiency than GOx-co-HRP@ZIF samples. Interestingly, when HRP@ZIF was used as the seed crystal with GOx@ZIF as the outer layer, they observed a 17.1% decrease in the rate of product formation.

Since the first report of simple pore diffusion of protein molecules into MOFs, researchers have explored increasingly more complex approaches to create functionally interesting protein@MOF systems. Like hydrogel systems, MOFs have unequivocally demonstrated their utility as protein carriers, and their prevalence will only grow.

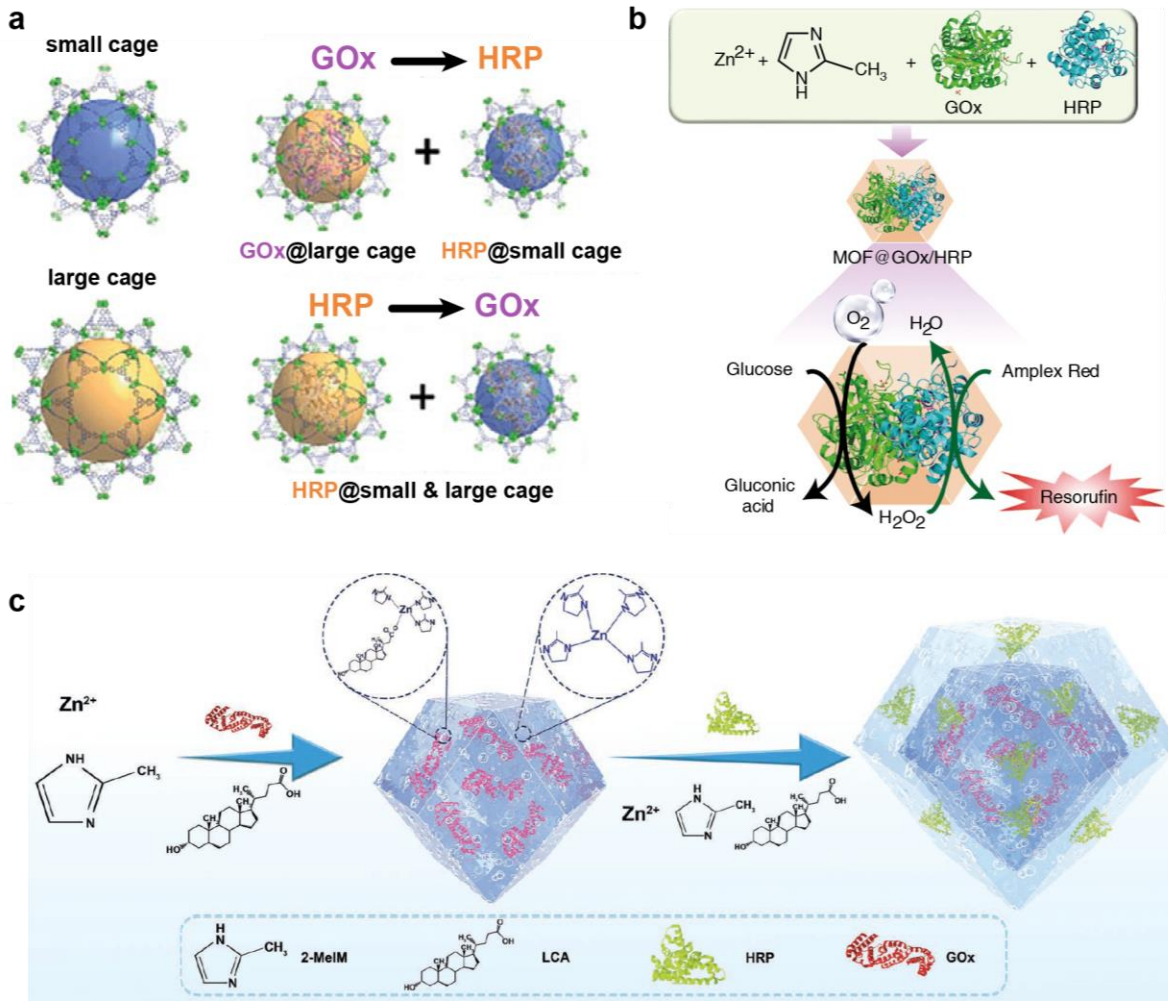

Figure 1.9. Rational preparation of GOx/HRP@MOFs. **(a)** The mesoporosity of PCN-888 includes large and small cavities. The sequential pore diffusion of GOx, then HRP (top), leads to successful incorporation of both enzymes. However, using HRP first leads to the HRP occupying both the large and small cages (bottom). Leveraging the size differences allowed the researchers to create bienzyme@MOF systems. Adapted from reference 67. **(b)** The biomineralization can be extended to more than one type of enzymes. Upon mixing GOx and HRP with Zn^{2+} and HmIm, GOx/HRP@ZIF-8 can be formed. Subsequent activity studies revealed enhanced cascade reactivity due to the higher local concentrations of substrates. Adapted from reference 68. **(c)** Similar to the previous examples, bizenzyme@MOF was synthesized via sequential biomineralization processes. GOx@ZIF-8 was used as a seed crystal and added to a mixture containing HRP, Zn^{2+} and HmIm. This led to the formation of a shell consisting of HRP@ZIF-8. Through this approach, core-shell MOF systems were constructed with different enzymes in each layer. Adapted from reference 69.

1.4 Protein Crystals as Functional Materials

The uptake and encapsulation of guest species by host frameworks have been investigated for various purposes, exemplified by hydrogel and MOF composites. Another interesting class of materials capable of accommodating guest molecules is protein crystals. Although historically utilized for crystallographic structure determination, they are now increasingly being recognized as functional porous materials. Supplemented by decades of research in protein crystallography and recent advancements in chemical biology techniques, protein crystals offer a competitive alternative to hydrogels and MOFs for generating functional materials and systems.

The earliest examples of utilizing protein crystals as solid-state materials were the application of cross-linked enzyme crystals (CLECs).[72-73] Upon crystallizing enzymes, researchers stabilized the crystals by treating them with chemical cross-linkers that react with the residues on the protein surface. Such processes increase the crystal's physical and chemical stability, allowing subsequent use in industrially relevant conditions.[20, 74-77] Despite the early developments in CLECs, more recent studies have focused on leveraging the void space between the protein molecules to template various nanoscale cargo for the development of hybrid protein crystals.

1.4.1 Bioinorganic Protein Crystals

In 2005, Colvin and coworkers reported the first study in which protein crystals were viewed as porous materials to host foreign cargo postsynthetically.[78] Specifically, body-centered cubic crystals of cowpea mosaic virus (CPMV), which exhibit voids that constitute ~50% of the total lattice volume, were cross-linked with glutaraldehyde (to prevent crystal dissolution) and subsequently functionalized with Pt and Pd (**Figure 1.10a**). The resulting Pt particles within the CPMV crystals exhibited crystalline order in the lattice. Through this work, the researchers first

demonstrated that protein crystals can serve as porous frameworks for the development of hybrid functional materials.

Through similar experiments, Ueno et al. demonstrated that hen egg white lysozyme (HEWL) crystals can undergo similar metalation processes using Rh^{3+} ions.[79] Upon crystallization, HEWL forms mesoporous crystals (space group $P4_32_12$) that can facilitate metal deposition within its pores (**Figure 1.10b**). When the crystals were placed in solutions containing Rh^{3+} ions (1-100 mM), the researchers observed metal binding by the HEWL molecules, confirmed by crystallographic analyses. Furthermore, when compared to non-Rh^{3+}-treated crystals, they noticed that the surface amino acid residues underwent conformational changes to capture the metal ions. In the same year, Mann and co. demonstrated that lysozyme crystals can also be functionalized with Ag and Au ions.[80] Through redox studies, Ag/Au nanowires formed within the 1-D pores of lysozyme crystals. The work by laboratories of Ueno and Mann revealed that protein crystals can promote cooperative metal accumulation within the pores to create bioinorganic materials. Interesting follow-up studies by the Ueno and Mann groups delved into imbuing lysozyme crystals with magnetic[81] and plasmonic[82] properties, respectively.

In efforts to further enhance functionality with protein crystals, Ueno and colleagues immobilized organometallic complexes within cross-linked HEWL (CL-HEWL) crystals for subsequent catalytic reactivity.[83] After cross-linking the HEWL crystals with glutaraldehyde (2.5%), CL-HEWL crystals were placed in a solution containing [{Ru(benzene)Cl_2}$_2$] (5 mM) at room temperature for 24 h to immobilize the Ru complexes via pore diffusion (**Figure 1.10c**). Hydrogen-transfer reduction of acetophenone and its derivatives were screened with the resulting Ru-functionalized crystals. Furthermore, when comparing crystals with tetragonal and orthorhombic space groups, the researchers discovered that the different crystals influenced the

enantiomeric excess yields. Through this study they demonstrated that artificial metalloenzyme crystals can be synthesized post-synthetically and the reactions can be manipulated by the protein-substrate interactions.

Another interesting example of combining inorganic chemistry and protein crystallography was reported by Ménage and co., where they immobilized Fe complexes within protein crystals and captured different reaction intermediates during the catalytic process.[84] Specifically, nickel-binding protein, NikA, was crystallized and soaked in a mixture containing Fe complexes. Before data collection, the Fe-functionalized NikA crystals were either treated with reductant or oxidized and flash-cooled at select timepoints to capture the different reaction states. Through these time-dependent crystallographic studies, they elucidated four intermediates and the product of the O_2-mediated aromatic hydroxylation reactions.

Thus far, protein crystals have been thoroughly leveraged as host frameworks for nanoparticle deposition. By leveraging the porosity and passive diffusion of metal ions, researchers have successfully functionalized protein crystals with non-native cofactors. However, the influence of the protein crystal host was determined *a posteriori*, and the binding was not site-selective. To better leverage protein crystals as bio-templates, chemical biology tools, such as genetic and chemical modifications, need to be employed.[18, 20, 85]

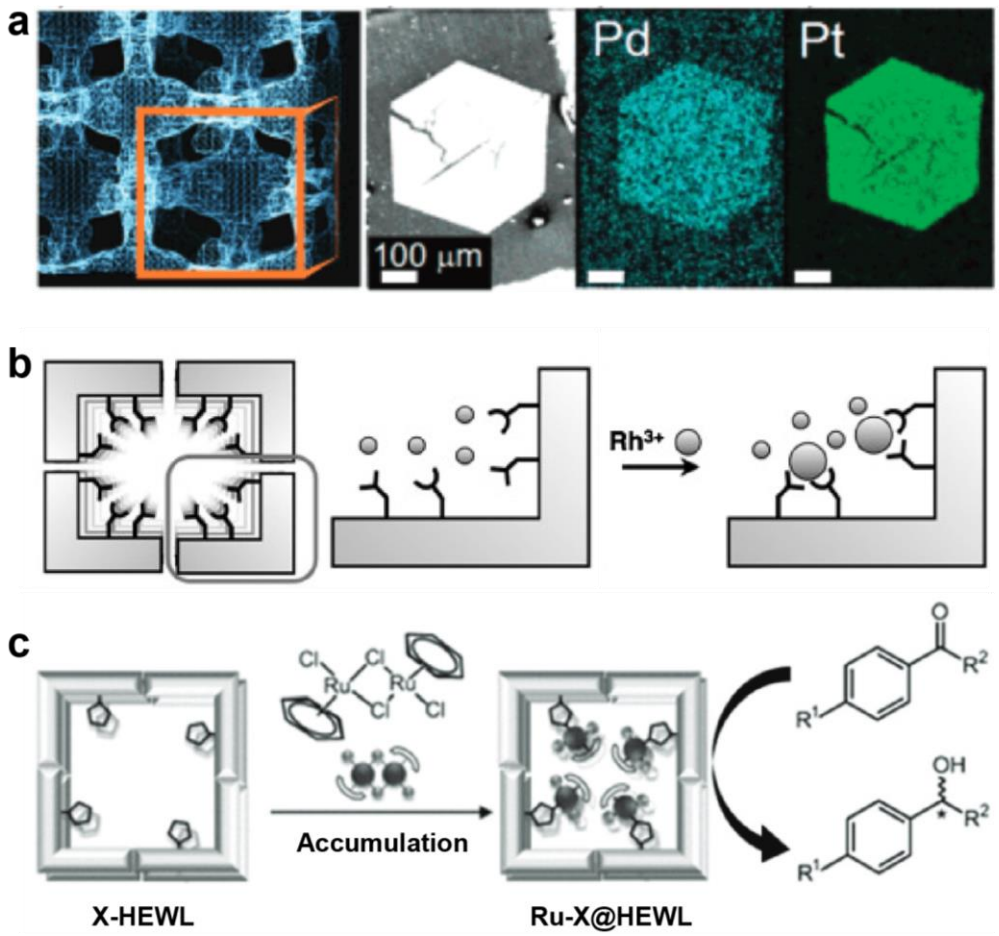

Figure 1.10. Metallization of protein crystals. **(a)** From left to right: The lattice void space is connected throughout the lysozyme crystal (blue mesh), and the orange box represents a single unit cell. SEM image a of cross-linked lysozyme crystal after Pd and Pt functionalization. The presence of different metals is confirmed via EDX analyses. Adapted from reference 78. **(b)** Cartoon scheme illustrating the formation of Rh nanoparticles within the HEWL crystal pores. As the ions diffuse into the pores, they interact with the exposed residues on the protein surface and precipitate into nanoparticles. Adapted from reference 79. **(c)** Schematic representation of functionalizing the HEWL crystals with Rh complexes, which and perform subsequent hydrogenation reactions. Similar to the Rh ions, Rh complexes react with the protein surface and become immobilized through the lattice. The metal complexes remain active within the confine spaces. Adapted from reference 83.

1.4.2 Protein Crystals as Biomolecular Templates

Through X-ray crystallography, the molecular order and positions of amino acids can be precisely revealed, enabling researchers to identify residues that are exposed to the lattice pores. With this information, chemists can pinpoint which residues to target for post-synthetic modifications. In proof-of-principle experiments, Snow et al. demonstrated the capture of nanoparticles via exact metal-mediated interactions within cross-linked protein crystals.[86] Understanding the spatial positioning of the amino acids within the CJ0 crystals, the researchers installed His-tags that point towards the 13 nm-wide pores (**Figure 1.11a**). Upon soaking the genetically modified protein crystal in a solution containing Ni^{2+} ions and Au nanoparticles with an NTA tag, the crystal selectively captured the guest nanoparticles (**Figure 1.11b,c**). Although CJ0 crystals successfully absorbed the Au nanoparticles without the His-tag, the nanoparticles eventually leached out within 4 days. Furthermore, they revealed the binding between the His-tag and NTA is reversible via the addition of EDTA. From these studies, Snow and colleagues demonstrated how to develop protein crystals into rationally designed biotemplates. Subsequent work focused on better understanding the diffusion of nanoparticles into the CJ0 crystals and expanding the immobilization techniques.[87-88]

In another example, Snow and co. revealed the loading process can also be applied to proteins.[21] Through a similar approach, CJ0 crystals were placed in a solution containing fluorescent proteins, mNeonGreen and mCherry. They observed the best sequestration and retention when both the crystal and guest proteins carried His-tags due to the metal-mediated immobilization. Interestingly, in this study, they explored a multistage loading process to achieve different domains of protein capture (**Figure 1.11d**). Specifically, by controlling the cross-linking time, they can limit cross-linking to the perimeter of the crystal, creating a stable shell. The crystal

is then further processed to dissolve the non-cross-linked core. Upon placing the resulting crystal in mCherry, the fluorescent protein selectively binds to the shell, and the non-immobilized particles can be washed away. Subsequent soaking with mNeonGreen leads to the passive diffusion of the secondary protein guest, ultimately creating spatial segregation between the two proteins. In a follow-up study, Snow and coworkers immobilized two different enzymes within the lattice.[89] Similar to the MOF examples,[67-69] HRP and GOx were loaded into the crystal and demonstrated successful cascade reactivity (**Figure 1.11e**). These results contribute to the literature of host frameworks and add protein crystals to the list of available materials that can harbor macromolecular cargo.

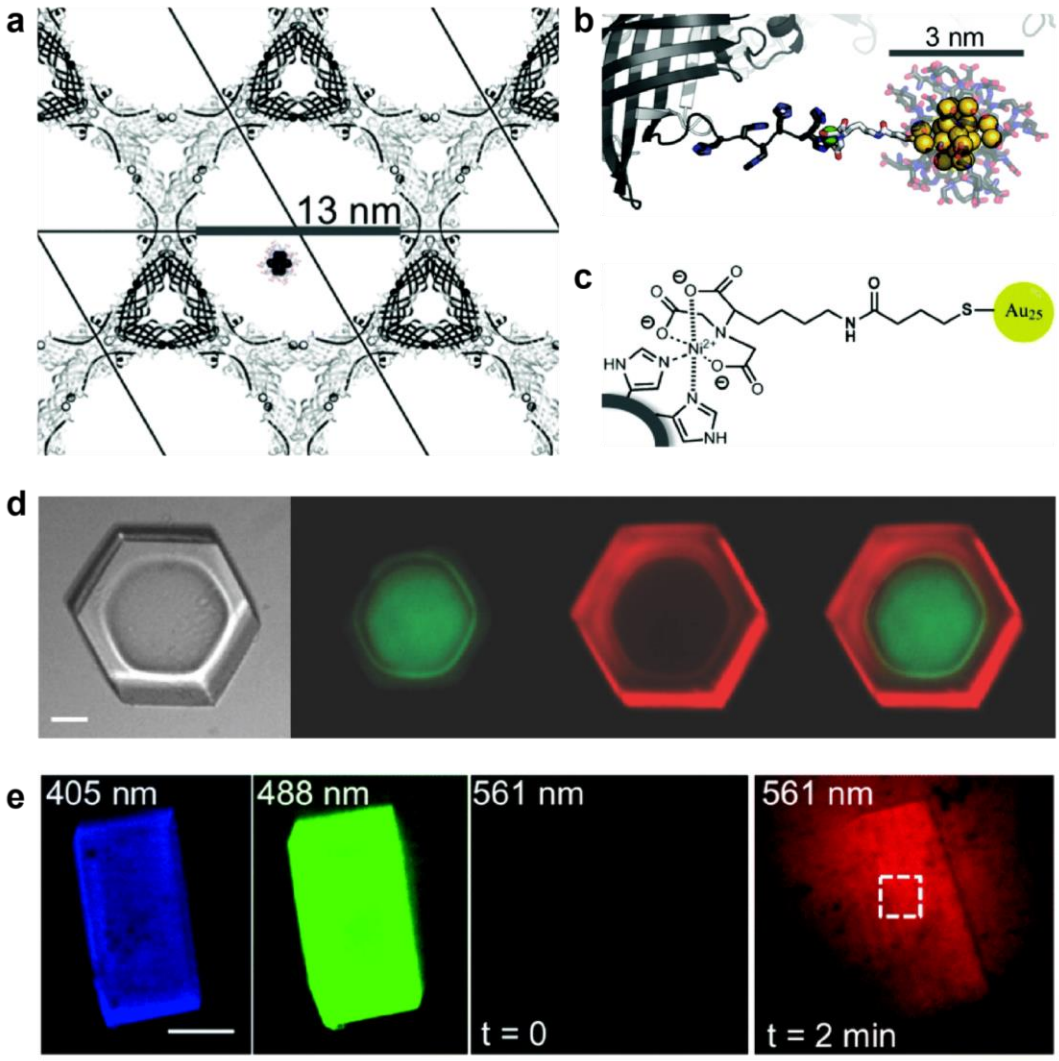

Figure 1.11. Active immobilization of guest molecules within the CJ crystal pores. **(a)** Cartoon depiction of the 13 nm-wide pores in the CJ lattice. Adapted from reference 86. **(b)** and **(c)** The crystal has His-tags pointing into the pores for metal-mediated active capture of NTA-tagged Au nanoparticles. Adapted from reference 86. **(d)** Confocal microscopy images of core-shell CJ protein crystals. The shell is chemically cross-linked and functionalized with mCherry. The core is a liquid solution containing mNeonGreen. The two guest proteins are spatially segregated by employing different uptake mechanisms. Adapted from reference 21**. (e)** Confocal fluorescence microscopy images of GOx and HRP-loaded CJ crystals. The GOx and HRP molecules are labeled with a blue dye (405 nm) and NHS-fluorescein (488 nm), respectively. Analyzing the crystal at different wavelengths reveals both are successfully entrapped in the crystal. The two-step cascade reaction is monitored via the production of resorufin (561 nm). Adapted from reference 89.

The utility of protein crystals as biomolecular templates was also explored by Chmielewski and co. through 3D peptide crystals.[90] Upon the crystallization of coiled-coil peptides (GCN4-p2L), the researchers post-synthetically modified the crystals by attaching His-tagged fluorophores to distinct locations within a single crystal. Specifically, the coiled-coil peptides displayed NTA and His-tags at the N- and C-terminal ends, respectively. In the presence of divalent metals GCN4-p2L assembled into hexagonal rods via a head-to-tail fashion (**Figure 1.12a**). As a result, the crystals presented exposed NTA and His-tags available for targeted capture. Depending on the presence of Ni^{2+} or Zn^{2+} ions, the crystal surface and interstitial space can be selectively modified respectively (**Figure 1.12b,c**).

In a follow-up study, Chmielewski and colleagues co-crystallization GCN4-p2L with His-tagged fluorescent proteins, EGFP or mCherry.[91] Upon analyzing the crystal via confocal fluorescence microscopy, a fluorescent hourglass pattern was observed (**Figure 1.12d**). These observations were attributed to the assembly behavior and protein-protein interactions between the fluorescent proteins and GCN4-p2L peptides. Similar to crystals composed solely of GCN4-p2L, the co-crystallized crystals (EGFP and GCN4-p2L) featured available NTA and His-tags for additional metal binding. Consequently, when EGFP/GCN4-p2L crystals were incubated in a mixture containing mCherry and Ni^{2+}, a multicomponent crystal was formed, with EGFP within the crystal and mCherry immobilized on the surface (**Figure 1.12e**).

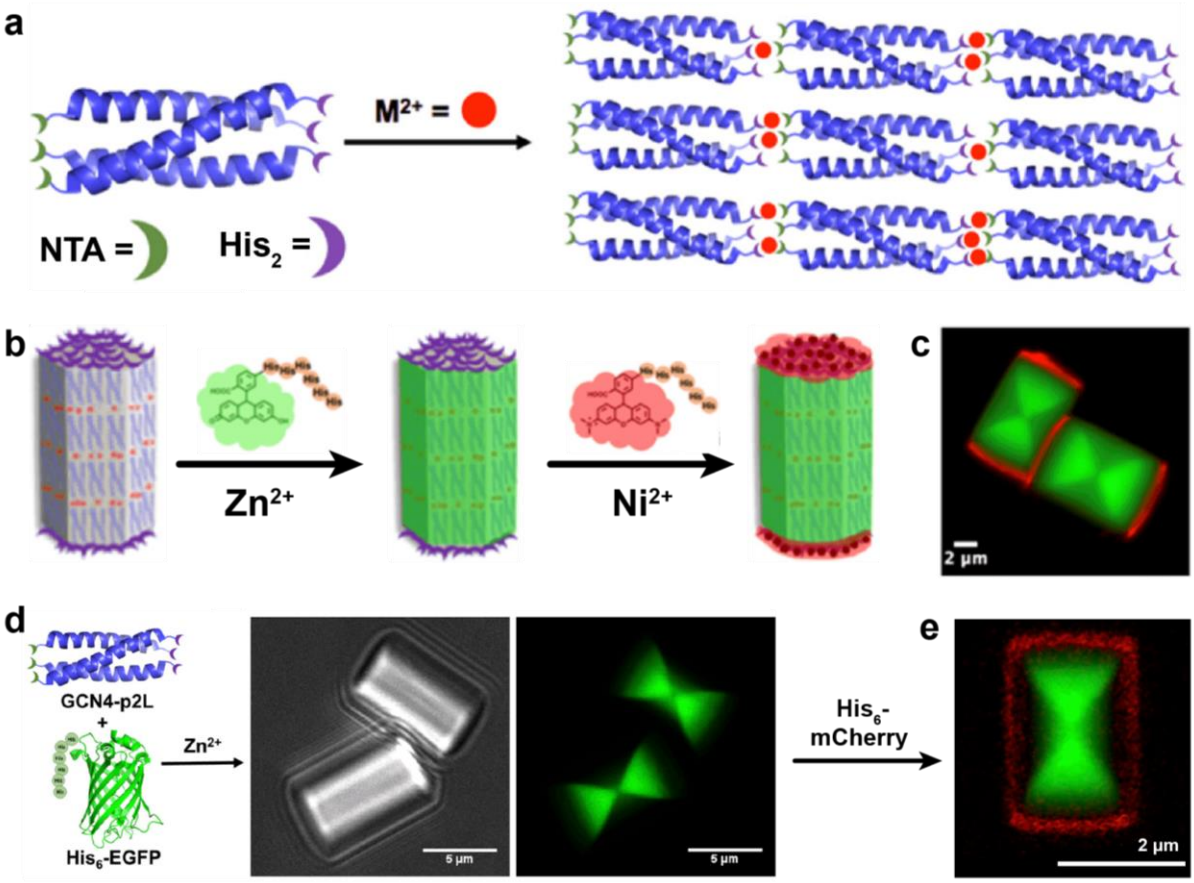

Figure 1.12. Postsynthetic functionalization of GCN4-p2L crystals. **(a)** Cartoon representation illustrating the coiled-coil building block with NTA and His-tags. In the presence of divalent metal ions, the peptides self-assemble into crystals via a head-to-tail fashion. Adapted from reference 90. **(b)** Schematic displaying the sequential functionalization of GCN-p2L crystals with different fluorescent dyes. The use of different metals enable selective labeling of the interstial space and crystal surface. Adapted from reference 90. **(c)** Confocal fluorescence microscopy image of the dual dye-labeled crystal. Adapted from reference 90. **(d)** GCN4-p2L and His-EGFP co-crystallize into hexagonal crystals. The green fluorescence is from the EGFP and exhibit an hourglass shape. Adapted from reference 91. **(e)** The crystal surface can be selective labeled with His-mCherry to achieve a multicomponent protein crystal. The metal binding ligands allow the development of spatially segregated funtional domains. Adapted from reference 91.

1.5 Polymer-Integrated Protein Crystals

Ranging from CLECs to biomolecular templates, researchers have explored a variety of methods to enhance the utility of protein crystals as functional materials, all within the last couple of decades. However, an underexplored avenue is the hybridization of protein crystals with polymeric systems.[92-94] In an early study, Cohen-Hadar et al. soaked lysozyme crystals in a solution containing acrylamide.[93] After the small molecules diffused into the lattice, radical polymerization was initiated *in-crystallo*, resulting in the formation of polymer within the interstitial space (**Figure 1.13a**). The resulting crystal was heavily cracked, with the crystal edges lost (**Figure 1.13b**). Repeating the process with cross-linked crystals prevented deformation and maintained the overall crystal macroscopic morphology (**Figure 1.13c**). Monitoring the polymerization process with fluorescence microscopy confirmed successful polymer formation. However, X-ray crystallographic analyses revealed that the polyacrylamide network decreased the crystal's resolution, as well as the B-factor compared to the non-polymer-integrated samples.

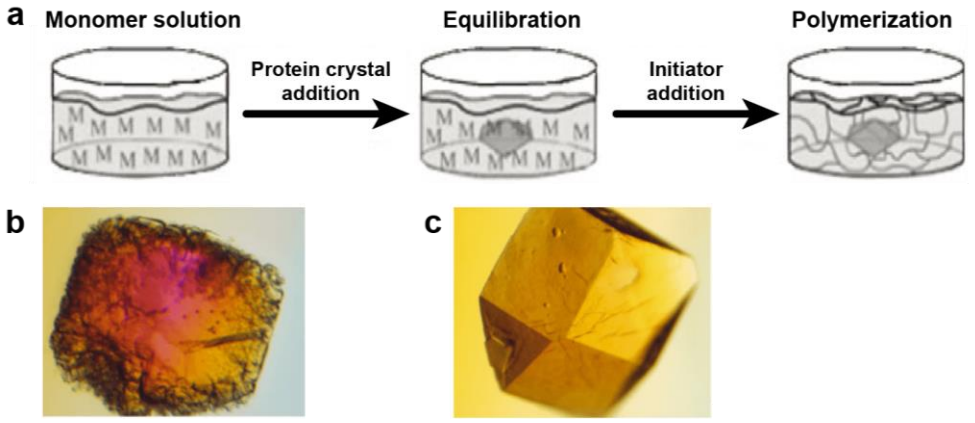

Figure 1.13. Formation of protein-polymer hybrid crystals. **(a)** Schematic illustrating the use of lysozyme crystals as a biomolecular template for polymer. The crystal is soaked in a solution containing acrylamide and subsequently treated with radical initiators to form polyacrylamide within the lattice. Light micrographs of **(b)** non-crosslinked and **(c)** cross-linked lysozyme crystals after polymerization. The cross-linking prevents crystal deformation and maintains the sharp edges characteristic of fresh lysozyme crystals. **(a)-(c)** Adapted from reference 93.

In 2018, Zhang et al. conducted similar studies with ferritin crystals and poly(acrylate-co-acrylamide) (**Figure 1.14a**).[95] Cubic ferritin crystals (space group *F*432) were immersed in a solution containing sodium acrylate, acrylamide, and N,N′-methylenebisacrylamide. After an overnight incubation, radical polymerization was initiated, effectively forming a hydrogel network within the lattice. The resulting crystals remained in pristine condition, eliminating the need for cross-linking. Due to the isotropic presence of the hydrogel, the resulting polymer-integrated protein crystal (PIX) could reversibly expand when placed in water and contract upon the addition of NaCl (**Figure 1.14b**). Furthermore, the hybrid protein crystal exhibited efficient self-healing and yileded the highest-resolution ferritin structure.

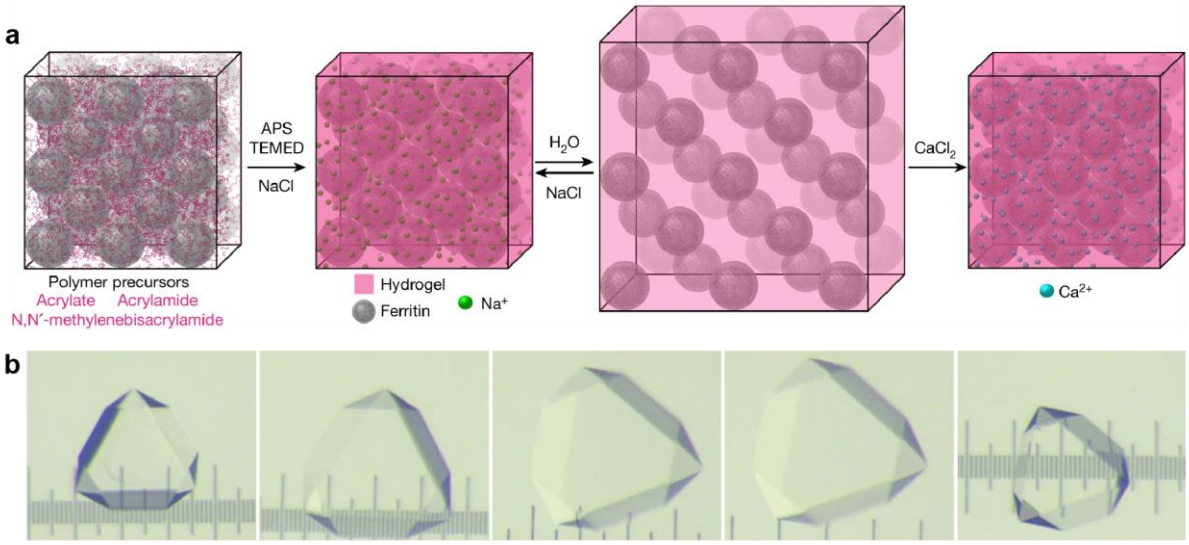

Figure 1.14. Development of hyperexpandable polymer-integrated protein crystals. **(a)** Schematic representation of preparing PIX samples. Polymer precursors are diffused into ferritin crystals for the subsequent formation of a hydrogel network throughout the lattice. Placing the crystal in H_2O initiates crystal expansion, and the addition of NaCl contracts the crystal. $CaCl_2$ can be used to irreversibly contract the crystal. **(b)** Light micrographs of PIX expanding over time when placed in H_2O. The addition of NaCl contracts the crystal back. **(a)-(b)** Adapted from reference 95.

1.6 Dissertation Objectives

Uniquely, PIX possess characteristics that are substantial to polymer systems, MOFs, and protein crystals. Building upon the work by Zhang et al.,[95] this dissertation explores the potential applications and limitations of the ferritin-based PIX platform. Due to ferritin's ability to crystallize into different lattice symmetries, the impact of asymmetrically patterned polymer networks is explored (Chapter 2). Then, considering that PIX are dynamic, porous materials, their capacity to accommodate macromolecular cargo is leveraged to form protein@PIX systems (Chapter 3). Lastly, the assembly of ferritin is meticulously controlled to create core-shell crystals, and subsequently processed into PIX. The resultant core-shell PIX platform permits selective patterning of the interstitial space and crystal surface, thereby emulating a cell-like system (Chapter 4).

1.7 References

1. Mulhaupt, R., Hermann Staudinger and the origin of macromolecular chemistry. *Angew. Chem. Int. Ed.* **2004,** *43*, 1054-63.

2. Zhang, Y. S.; Khademhosseini, A., Advances in engineering hydrogels. *Science* **2017,** *356*.

3. Guo, Y.; Bae, J.; Fang, Z.; Li, P.; Zhao, F.; Yu, G., Hydrogels and Hydrogel-Derived Materials for Energy and Water Sustainability. *Chem. Rev.* **2020,** *120*, 7642-7707.

4. Gu, Y.; Zhao, J.; Johnson, J. A., Polymer Networks: From Plastics and Gels to Porous Frameworks. *Angew. Chem. Int. Ed.* **2020,** *59*, 5022-5049.

5. Slater, A. G.; Cooper, A. I., Porous materials. Function-led design of new porous materials. *Science* **2015,** *348*, aaa8075.

6. De France, K. J.; Xu, F.; Hoare, T., Structured Macroporous Hydrogels: Progress, Challenges, and Opportunities. *Adv. Healthc. Mater.* **2018,** *7*.

7. Liang, Y.; He, J.; Guo, B., Functional Hydrogels as Wound Dressing to Enhance Wound Healing. *ACS Nano* **2021,** *15*, 12687-12722.

8. Sun, J. Y.; Zhao, X.; Illeperuma, W. R.; Chaudhuri, O.; Oh, K. H.; Mooney, D. J.; Vlassak, J. J.; Suo, Z., Highly stretchable and tough hydrogels. *Nature* **2012,** *489*, 133-6.

9. Correa, S.; Grosskopf, A. K.; Lopez Hernandez, H.; Chan, D.; Yu, A. C.; Stapleton, L. M.; Appel, E. A., Translational Applications of Hydrogels. *Chem. Rev.* **2021,** *121*, 11385-11457.

10. Lee, K. Y.; Mooney, D. J., Hydrogels for tissue engineering. *Chem. Rev.* **2001,** *101*, 1869-79.

11. Qiu, Y.; Park, K., Environment-sensitive hydrogels for drug delivery. *Adv. Drug. Deliv. Rev.* **2001,** *53*, 321-39.

12. Dong, L.; Agarwal, A. K.; Beebe, D. J.; Jiang, H., Adaptive liquid microlenses activated by stimuli-responsive hydrogels. *Nature* **2006,** *442*, 551-4.

13. Yaghi, O. M.; O'Keeffe, M.; Ockwig, N. W.; Chae, H. K.; Eddaoudi, M.; Kim, J., Reticular synthesis and the design of new materials. *Nature* **2003,** *423*, 705-14.

14. Lin, Z.; Richardson, J. J.; Zhou, J.; Caruso, F., Direct synthesis of amorphous coordination polymers and metal-organic frameworks. *Nat. Rev. Chem.* **2023,** *7*, 273-286.

15. Qian, Q.; Asinger, P. A.; Lee, M. J.; Han, G.; Mizrahi Rodriguez, K.; Lin, S.; Benedetti, F. M.; Wu, A. X.; Chi, W. S.; Smith, Z. P., MOF-Based Membranes for Gas Separations. *Chem. Rev.* **2020,** *120*, 8161-8266.

16. Sumida, K.; Rogow, D. L.; Mason, J. A.; McDonald, T. M.; Bloch, E. D.; Herm, Z. R.; Bae,

T. H.; Long, J. R., Carbon dioxide capture in metal-organic frameworks. *Chem. Rev.* **2012,** *112*, 724-81.

17. Lawson, H. D.; Walton, S. P.; Chan, C., Metal-Organic Frameworks for Drug Delivery: A Design Perspective. *ACS Appl. Mater. Interfaces.* **2021,** *13*, 7004-7020.

18. Kojima, M.; Abe, S.; Ueno, T., Engineering of protein crystals for use as solid biomaterials. *Biomater. Sci.* **2022,** *10*, 354-367.

19. Ward, A. R.; Snow, C. D., Porous crystals as scaffolds for structural biology. *Curr. Opin. Struct. Biol.* **2020,** *60*, 85-92.

20. Hartje, L. F.; Snow, C. D., Protein crystal based materials for nanoscale applications in medicine and biotechnology. *Wiley Interdiscip. Rev. Nanomed. Nanobiotechnol.* **2019,** *11*, e1547.

21. Huber, T. R.; Hartje, L. F.; McPherson, E. C.; Kowalski, A. E.; Snow, C. D., Programmed Assembly of Host-Guest Protein Crystals. *Small* **2017,** *13*.

22. Hoare, T. R.; Kohane, D. S., Hydrogels in drug delivery: Progress and challenges. *Polymer* **2008,** *49*, 1993-2007.

23. Wichterle, O.; LÍM, D., Hydrophilic Gels for Biological Use. *Nature* **1960,** *185*, 117-118.

24. Vermonden, T.; Censi, R.; Hennink, W. E., Hydrogels for protein delivery. *Chem. Rev.* **2012,** *112*, 2853-88.

25. Li, J.; Mooney, D. J., Designing hydrogels for controlled drug delivery. *Nat. Rev. Mater.* **2016,** *1*.

26. Urquhart, L., Market watch: Top drugs and companies by sales in 2017. *Nat. Rev. Drug. Discov.* **2018,** *17*, 232.

27. Danhier, F.; Ansorena, E.; Silva, J. M.; Coco, R.; Le Breton, A.; Preat, V., PLGA-based nanoparticles: an overview of biomedical applications. *J. Control. Release.* **2012,** *161*, 505-22.

28. Appel, E. A.; Tibbitt, M. W.; Webber, M. J.; Mattix, B. A.; Veiseh, O.; Langer, R., Self-assembled hydrogels utilizing polymer-nanoparticle interactions. *Nat. Commun.* **2015,** *6*, 6295.

29. Perrier, S., 50th Anniversary Perspective: RAFT Polymerization—A User Guide. *Macromolecules* **2017,** *50*, 7433-7447.

30. Chen, M.; Zhong, M.; Johnson, J. A., Light-Controlled Radical Polymerization: Mechanisms, Methods, and Applications. *Chem. Rev.* **2016,** *116*, 10167-211.

31. Hou, Y.; Lu, H., Protein PEPylation: A New Paradigm of Protein-Polymer Conjugation. *Bioconjug. Chem.* **2019,** *30*, 1604-1616.

32. Caliceti, P.; Salmaso, S.; Elvassore, N.; Bertucco, A., Effective protein release from PEG/PLA nano-particles produced by compressed gas anti-solvent precipitation techniques. *J.*

Control. Release. **2004,** *94*, 195-205.

33. Vezzù, K.; Borin, D.; Bertucco, A.; Bersani, S.; Salmaso, S.; Caliceti, P., Production of lipid microparticles containing bioactive molecules functionalized with PEG. *J. Supercrit. Fluids* **2010,** *54*, 328-334.

34. Salmaso, S.; Elvassore, N.; Bertucco, A.; Caliceti, P., Production of solid lipid submicron particles for protein delivery using a novel supercritical gas-assisted melting atomization process. *J. Pharm. Sci.* **2009,** *98*, 640-50.

35. Salmaso, S.; Bersani, S.; Elvassore, N.; Bertucco, A.; Caliceti, P., Biopharmaceutical characterisation of insulin and recombinant human growth hormone loaded lipid submicron particles produced by supercritical gas micro-atomisation. *Int. J. Pharm.* **2009,** *379*, 51-8.

36. Elvassore, N.; Bertucco, A.; Caliceti, P., Production of insulin-loaded poly(ethylene glycol)/poly(l-lactide) (PEG/PLA) nanoparticles by gas antisolvent techniques. *J. Pharm. Sci.* **2001,** *90*, 1628-36.

37. Liu, J.; Zhang, S. M.; Chen, P. P.; Cheng, L.; Zhou, W.; Tang, W. X.; Chen, Z. W.; Ke, C. M., Controlled release of insulin from PLGA nanoparticles embedded within PVA hydrogels. *J. Mater. Sci. Mater. Med.* **2007,** *18*, 2205-10.

38. Pakulska, M. M.; Elliott Donaghue, I.; Obermeyer, J. M.; Tuladhar, A.; McLaughlin, C. K.; Shendruk, T. N.; Shoichet, M. S., Encapsulation-free controlled release: Electrostatic adsorption eliminates the need for protein encapsulation in PLGA nanoparticles. *Sci. Adv.* **2016,** *2*, e1600519.

39. Schmid, D.; Park, C. G.; Hartl, C. A.; Subedi, N.; Cartwright, A. N.; Puerto, R. B.; Zheng, Y.; Maiarana, J.; Freeman, G. J.; Wucherpfennig, K. W.; Irvine, D. J.; Goldberg, M. S., T cell-targeting nanoparticles focus delivery of immunotherapy to improve antitumor immunity. *Nat. Commun.* **2017,** *8*, 1747.

40. Hrkach, J.; Von Hoff, D.; Mukkaram Ali, M.; Andrianova, E.; Auer, J.; Campbell, T.; De Witt, D.; Figa, M.; Figueiredo, M.; Horhota, A.; Low, S.; McDonnell, K.; Peeke, E.; Retnarajan, B.; Sabnis, A.; Schnipper, E.; Song, J. J.; Song, Y. H.; Summa, J.; Tompsett, D.; Troiano, G.; Van Geen Hoven, T.; Wright, J.; LoRusso, P.; Kantoff, P. W.; Bander, N. H.; Sweeney, C.; Farokhzad, O. C.; Langer, R.; Zale, S., Preclinical development and clinical translation of a PSMA-targeted docetaxel nanoparticle with a differentiated pharmacological profile. *Sci. Transl. Med.* **2012,** *4*, 128ra39.

41. Chen, Q.; Xu, L.; Liang, C.; Wang, C.; Peng, R.; Liu, Z., Photothermal therapy with immune-adjuvant nanoparticles together with checkpoint blockade for effective cancer immunotherapy. *Nat. Commun.* **2016,** *7*, 13193.

42. Silva, A. K.; Richard, C.; Bessodes, M.; Scherman, D.; Merten, O. W., Growth factor delivery approaches in hydrogels. *Biomacromolecules* **2009,** *10*, 9-18.

43. Teixeira, S. P. B.; Domingues, R. M. A.; Shevchuk, M.; Gomes, M. E.; Peppas, N. A.; Reis, R. L., Biomaterials for Sequestration of Growth Factors and Modulation of Cell Behavior. *Adv.*

Funct. Mater. **2020,** *30*.

44. Fan, V. H.; Tamama, K.; Au, A.; Littrell, R.; Richardson, L. B.; Wright, J. W.; Wells, A.; Griffith, L. G., Tethered epidermal growth factor provides a survival advantage to mesenchymal stem cells. *Stem Cells* **2007,** *25*, 1241-51.

45. Abune, L.; Davis, B.; Wang, Y., Aptamer-functionalized hydrogels: An emerging class of biomaterials for protein delivery, cell capture, regenerative medicine, and molecular biosensing. *Wiley Interdiscip. Rev. Nanomed. Nanobiotechnol.* **2021,** *13*, e1731.

46. Soontornworajit, B.; Zhou, J.; Zhang, Z.; Wang, Y., Aptamer-functionalized in situ injectable hydrogel for controlled protein release. *Biomacromolecules* **2010,** *11*, 2724-30.

47. Abune, L.; Lee, K.; Wang, Y., Development of a Biomimetic Extracellular Matrix with Functions of Protein Sequestration and Cell Attachment Using Dual Aptamer-Functionalized Hydrogels. *ACS Biomater. Sci. Eng.* **2022,** *8*, 1279-1289.

48. Abune, L.; Zhao, N.; Lai, J.; Peterson, B.; Szczesny, S.; Wang, Y., Macroporous Hydrogels for Stable Sequestration and Sustained Release of Vascular Endothelial Growth Factor and Basic Fibroblast Growth Factor Using Nucleic Acid Aptamers. *ACS Biomater. Sci. Eng.* **2019,** *5*, 2382-2390.

49. Zisch, A. H.; Lutolf, M. P.; Ehrbar, M.; Raeber, G. P.; Rizzi, S. C.; Davies, N.; Schmokel, H.; Bezuidenhout, D.; Djonov, V.; Zilla, P.; Hubbell, J. A., Cell-demanded release of VEGF from synthetic, biointeractive cell ingrowth matrices for vascularized tissue growth. *FASEB J.* **2003,** *17*, 2260-2.

50. Yamaguchi, N.; Zhang, L.; Chae, B. S.; Palla, C. S.; Furst, E. M.; Kiick, K. L., Growth factor mediated assembly of cell receptor-responsive hydrogels. *J. Am. Chem. Soc.* **2007,** *129*, 3040-1.

51. Kim, S. H.; Kiick, K. L., Cell-mediated Delivery and Targeted Erosion of Vascular Endothelial Growth Factor-Crosslinked Hydrogels. *Macromol. Rapid. Commun.* **2010,** *31*, 1231-40.

52. Lian, X.; Fang, Y.; Joseph, E.; Wang, Q.; Li, J.; Banerjee, S.; Lollar, C.; Wang, X.; Zhou, H. C., Enzyme-MOF (metal-organic framework) composites. *Chem. Soc. Rev.* **2017,** *46*, 3386-3401.

53. Liang, W.; Wied, P.; Carraro, F.; Sumby, C. J.; Nidetzky, B.; Tsung, C. K.; Falcaro, P.; Doonan, C. J., Metal-Organic Framework-Based Enzyme Biocomposites. *Chem. Rev.* **2021,** *121*, 1077-1129.

54. Deng, H.; Grunder, S.; Cordova, K. E.; Valente, C.; Furukawa, H.; Hmadeh, M.; Gandara, F.; Whalley, A. C.; Liu, Z.; Asahina, S.; Kazumori, H.; O'Keeffe, M.; Terasaki, O.; Stoddart, J. F.; Yaghi, O. M., Large-pore apertures in a series of metal-organic frameworks. *Science* **2012,** *336*, 1018-23.

55. Chen, Y.; Lykourinou, V.; Vetromile, C.; Hoang, T.; Ming, L. J.; Larsen, R. W.; Ma, S., How can proteins enter the interior of a MOF? Investigation of cytochrome c translocation into a MOF consisting of mesoporous cages with microporous windows. *J. Am. Chem. Soc.* **2012,** *134*, 13188-91.

56. Chen, Y.; Jimenez-Angeles, F.; Qiao, B.; Krzyaniak, M. D.; Sha, F.; Kato, S.; Gong, X.; Buru, C. T.; Chen, Z.; Zhang, X.; Gianneschi, N. C.; Wasielewski, M. R.; Olvera de la Cruz, M.; Farha, O. K., Insights into the Enhanced Catalytic Activity of Cytochrome c When Encapsulated in a Metal-Organic Framework. *J. Am. Chem. Soc.* **2020,** *142*, 18576-18582.

57. Drout, R. J.; Robison, L.; Farha, O. K., Catalytic applications of enzymes encapsulated in metal–organic frameworks. *Coord. Chem. Rev.* **2019,** *381*, 151-160.

58. Chen, Y.; Li, P.; Modica, J. A.; Drout, R. J.; Farha, O. K., Acid-Resistant Mesoporous Metal-Organic Framework toward Oral Insulin Delivery: Protein Encapsulation, Protection, and Release. *J. Am. Chem. Soc.* **2018,** *140*, 5678-5681.

59. Chen, Y.; Li, P.; Zhou, J.; Buru, C. T.; Dordevic, L.; Li, P.; Zhang, X.; Cetin, M. M.; Stoddart, J. F.; Stupp, S. I.; Wasielewski, M. R.; Farha, O. K., Integration of Enzymes and Photosensitizers in a Hierarchical Mesoporous Metal-Organic Framework for Light-Driven CO(2) Reduction. *J. Am. Chem. Soc.* **2020,** *142*, 1768-1773.

60. Wang, S.; Chen, Y.; Wang, S.; Li, P.; Mirkin, C. A.; Farha, O. K., DNA-Functionalized Metal-Organic Framework Nanoparticles for Intracellular Delivery of Proteins. *J. Am. Chem. Soc.* **2019,** *141*, 2215-2219.

61. Li, P.; Moon, S. Y.; Guelta, M. A.; Lin, L.; Gomez-Gualdron, D. A.; Snurr, R. Q.; Harvey, S. P.; Hupp, J. T.; Farha, O. K., Nanosizing a Metal-Organic Framework Enzyme Carrier for Accelerating Nerve Agent Hydrolysis. *ACS Nano* **2016,** *10*, 9174-9182.

62. Sha, F.; Xie, H.; Son, F. A.; Kim, K. S.; Gong, W.; Su, S.; Ma, K.; Wang, X.; Wang, X.; Farha, O. K., Rationally Tailored Mesoporous Hosts for Optimal Protein Encapsulation. *J. Am. Chem. Soc.* **2023**.

63. Moggach, S. A.; Bennett, T. D.; Cheetham, A. K., The effect of pressure on ZIF-8: increasing pore size with pressure and the formation of a high-pressure phase at 1.47 GPa. *Angew. Chem. Int. Ed.* **2009,** *48*, 7087-9.

64. Liang, K.; Ricco, R.; Doherty, C. M.; Styles, M. J.; Bell, S.; Kirby, N.; Mudie, S.; Haylock, D.; Hill, A. J.; Doonan, C. J.; Falcaro, P., Biomimetic mineralization of metal-organic frameworks as protective coatings for biomacromolecules. *Nat. Commun.* **2015,** *6*, 7240.

65. Liang, W.; Xu, H.; Carraro, F.; Maddigan, N. K.; Li, Q.; Bell, S. G.; Huang, D. M.; Tarzia, A.; Solomon, M. B.; Amenitsch, H.; Vaccari, L.; Sumby, C. J.; Falcaro, P.; Doonan, C. J., Enhanced Activity of Enzymes Encapsulated in Hydrophilic Metal-Organic Frameworks. *J. Am. Chem. Soc.* **2019,** *141*, 2348-2355.

66. Murty, R.; Bera, M. K.; Walton, I. M.; Whetzel, C.; Prausnitz, M. R.; Walton, K. S.,

Interrogating Encapsulated Protein Structure within Metal-Organic Frameworks at Elevated Temperature. *J. Am. Chem. Soc.* **2023,** *145*, 7323-7330.

67. Lian, X.; Chen, Y. P.; Liu, T. F.; Zhou, H. C., Coupling two enzymes into a tandem nanoreactor utilizing a hierarchically structured MOF. *Chem Sci.* **2016,** *7*, 6969-6973.

68. Chen, W.-H.; Vázquez-González, M.; Zoabi, A.; Abu-Reziq, R.; Willner, I., Biocatalytic cascades driven by enzymes encapsulated in metal–organic framework nanoparticles. *Nat. Catal.* **2018,** *1*, 689-695.

69. Wu, G.; Li, M.; Luo, Z.; Qi, L.; Yu, L.; Zhang, S.; Liu, H., Designed Synthesis of Compartmented Bienzyme Biocatalysts Based on Core-Shell Zeolitic Imidazole Framework Nanostructures. *Small* **2023,** *19*, e2206606.

70. Yang, J.; Zhang, F.; Lu, H.; Hong, X.; Jiang, H.; Wu, Y.; Li, Y., Hollow Zn/Co ZIF Particles Derived from Core-Shell ZIF-67@ZIF-8 as Selective Catalyst for the Semi-Hydrogenation of Acetylene. *Angew. Chem.* **2015,** *127*, 11039-11043.

71. Tang, J.; Salunkhe, R. R.; Liu, J.; Torad, N. L.; Imura, M.; Furukawa, S.; Yamauchi, Y., Thermal conversion of core-shell metal-organic frameworks: a new method for selectively functionalized nanoporous hybrid carbon. *J. Am. Chem. Soc.* **2015,** *137*, 1572-80.

72. Margolin, A. L.; Navia, M. A., Protein Crystals as Novel Catalytic Materials. *Angew. Chem. Int. Ed.* **2001,** *40*, 2204-2222.

73. Jegan Roy, J.; Emilia Abraham, T., Strategies in making cross-linked enzyme crystals. *Chem. Rev.* **2004,** *104*, 3705-22.

74. Fernandez-Penas, R.; Verdugo-Escamilla, C.; Martinez-Rodriguez, S.; Gavira, J. A., Production of Cross-Linked Lipase Crystals at a Preparative Scale. *Cryst. Growth. Des.* **2021,** *21*, 1698-1707.

75. Lopez, S.; Rondot, L.; Lepretre, C.; Marchi-Delapierre, C.; Menage, S.; Cavazza, C., Cross-Linked Artificial Enzyme Crystals as Heterogeneous Catalysts for Oxidation Reactions. *J. Am. Chem. Soc.* **2017,** *139*, 17994-18002.

76. Khalaf, N.; Govardhan, C. P.; Lalonde, J. J.; Persichetti, R. A.; Wang, Y.-F.; Margolin, A. L., Cross-Linked Enzyme Crystals as Highly Active Catalysts in Organic Solvents. *J. Am. Chem. Soc.* **1996,** *118*, 5494-5495.

77. Zelinski, T.; Waldmann, H., Cross-Linked Enzyme Crystals(CLECs): Efficient and Stable Biocatalysts for Preparative Organic Chemistry. *Angew. Chem. Int. Ed.* **1997,** *36*, 722-724.

78. Falkner, J. C.; Turner, M. E.; Bosworth, J. K.; Trentler, T. J.; Johnson, J. E.; Lin, T.; Colvin, V. L., Virus crystals as nanocomposite scaffolds. *J. Am. Chem. Soc.* **2005,** *127*, 5274-5.

79. Ueno, T.; Abe, S.; Koshiyama, T.; Ohki, T.; Hikage, T.; Watanabe, Y., Elucidation of metal-ion accumulation induced by hydrogen bonds on protein surfaces by using porous lysozyme

crystals containing Rh(III) ions as the model surfaces. *Chem.* **2010,** *16*, 2730-40.

80. Guli, M.; Lambert, E. M.; Li, M.; Mann, S., Template-Directed Synthesis of Nanoplasmonic Arrays by Intracrystalline Metalization of Cross-Linked Lysozyme Crystals. *Angew. Chem.* **2010,** *122*, 530-533.

81. Abe, S.; Tsujimoto, M.; Yoneda, K.; Ohba, M.; Hikage, T.; Takano, M.; Kitagawa, S.; Ueno, T., Porous protein crystals as reaction vessels for controlling magnetic properties of nanoparticles. *Small* **2012,** *8*, 1314-9.

82. Muskens, O. L.; England, M. W.; Danos, L.; Li, M.; Mann, S., Plasmonic Response of Ag- and Au-Infiltrated Cross-Linked Lysozyme Crystals. *Adv. Funct. Mater.* **2013,** *23*, 281-290.

83. Tabe, H.; Abe, S.; Hikage, T.; Kitagawa, S.; Ueno, T., Porous protein crystals as catalytic vessels for organometallic complexes. *Chem. Asian. J.* **2014,** *9*, 1373-8.

84. Cavazza, C.; Bochot, C.; Rousselot-Pailley, P.; Carpentier, P.; Cherrier, M. V.; Martin, L.; Marchi-Delapierre, C.; Fontecilla-Camps, J. C.; Menage, S., Crystallographic snapshots of the reaction of aromatic C-H with O(2) catalysed by a protein-bound iron complex. *Nat. Chem.* **2010,** *2*, 1069-76.

85. Zhu, J.; Avakyan, N.; Kakkis, A.; Hoffnagle, A. M.; Han, K.; Li, Y.; Zhang, Z.; Choi, T. S.; Na, Y.; Yu, C. J.; Tezcan, F. A., Protein Assembly by Design. *Chem. Rev.* **2021,** *121*, 13701-13796.

86. Kowalski, A. E.; Huber, T. R.; Ni, T. W.; Hartje, L. F.; Appel, K. L.; Yost, J. W.; Ackerson, C. J.; Snow, C. D., Gold nanoparticle capture within protein crystal scaffolds. *Nanoscale* **2016,** *8*, 12693-6.

87. Hartje, L. F.; Munsky, B.; Ni, T. W.; Ackerson, C. J.; Snow, C. D., Adsorption-Coupled Diffusion of Gold Nanoclusters within a Large-Pore Protein Crystal Scaffold. *J. Phys. Chem. B.* **2017,** *121*, 7652-7659.

88. Huber, T. R.; McPherson, E. C.; Keating, C. E.; Snow, C. D., Installing Guest Molecules at Specific Sites within Scaffold Protein Crystals. *Bioconjug. Chem.* **2018,** *29*, 17-22.

89. Kowalski, A. E.; Johnson, L. B.; Dierl, H. K.; Park, S.; Huber, T. R.; Snow, C. D., Porous protein crystals as scaffolds for enzyme immobilization. *Biomater. Sci.* **2019,** *7*, 1898-1904.

90. Nepal, M.; Sheedlo, M. J.; Das, C.; Chmielewski, J., Accessing Three-Dimensional Crystals with Incorporated Guests through Metal-Directed Coiled-Coil Peptide Assembly. *J. Am. Chem. Soc.* **2016,** *138*, 11051-7.

91. Curtis, R. W.; Scrudders, K. L.; Ulcickas, J. R. W.; Simpson, G. J.; Low-Nam, S. T.; Chmielewski, J., Supramolecular Assembly of His-Tagged Fluorescent Protein Guests within Coiled-Coil Peptide Crystal Hosts: Three-Dimensional Ordering and Protein Thermal Stability. *ACS Biomater. Sci. Eng.* **2022,** *8*, 1860-1866.

92. Lagziel-Simis, S.; Cohen-Hadar, N.; Moscovich-Dagan, H.; Wine, Y.; Freeman, A.,

Protein-mediated nanoscale biotemplating. *Curr. Opin. Biotechnol.* **2006,** *17*, 569-73.

93. Cohen-Hadar, N.; Wine, Y.; Nachliel, E.; Huppert, D.; Gutman, M.; Frolow, F.; Freeman, A., Monitoring the stability of crosslinked protein crystals biotemplates: a feasibility study. *Biotechnol. Bioeng.* **2006,** *94*, 1005-11.

94. Caruso, F.; Trau, D.; Möhwald, H.; Renneberg, R., Enzyme Encapsulation in Layer-by-Layer Engineered Polymer Multilayer Capsules. *Langmuir* **2000,** *16*, 1485-1488.

95. Zhang, L.; Bailey, J. B.; Subramanian, R. H.; Groisman, A.; Tezcan, F. A., Hyperexpandable, self-healing macromolecular crystals with integrated polymer networks. *Nature* **2018,** *557*, 86-91.

Chapter 2: Anisotropic Dynamics and Mechanics of Macromolecular Crystals Containing Lattice-Patterned Polymer Networks

2.1 Abstract

The mechanical and functional properties of many crystalline materials depend on cooperative changes in lattice arrangements in response to external perturbations. However, the flexibility and adaptiveness of crystalline materials are limited. Additionally, the bottom-up, molecular-level design of crystals with desired dynamic and mechanical properties at the macroscopic level remains a considerable challenge. To address these challenges, we had previously integrated mesoporous, cubic ferritin crystals with hydrogel networks, resulting in hybrid materials (polymer integrated crystals or PIX) which could undergo dramatic structural changes while maintaining crystalline periodicity and display efficient self-healing. The dynamics and mechanics of these ferritin-PIX were devoid of directionality, which is an important attribute of many molecular and macroscopic materials/devices. Here we report that such directionality can be achieved through the use of ferritin crystals with anisotropic symmetries (rhombohedral or trigonal), which enable the templated formation of patterned hydrogel networks *in crystallo*. The resulting PIX expand and contract anisotropically without losing crystallinity, undergo prompt bending motions in response to stimuli, and self-heal efficiently, capturing some of the essential features of sophisticated biological devices like skeletal muscles.

2.2 Introduction

A major goal in materials science is to apply chemical design at the atomic/molecular scale to generate collective structural, dynamic, and mechanical properties at the macroscopic scale[2]. The corresponding transfer and amplification of atomic/molecular-level information requires the molecular building blocks to be organized and appropriately interconnected over multiple length

scales.[3-5] Crystalline materials provide a distinct advantage in this regard in that they are composed of only one or few components arranged periodically, possessing both short and long-range order to allow structural and mechanical coupling in a cooperative manner. Indeed, there is a growing number of dynamic molecular crystals[6-7], flexible protein lattices[8-9], and porous framework materials[10-11], which can promptly undergo dramatic lattice transformations and motions in response to external stimuli, with promising applications in actuation[12-14], gas sorption and separation[15-17], sensing[18-19], and controlled release[20-21], among others[6, 10-11]. However, with relatively few but growing number of exceptions[22-26], these dynamic crystalline materials tend to be brittle, cannot undergo large changes in volume at the macroscale without mechanical failure, or self-heal. These limitations are due to the fact that the lattice components need to be continuously interconnected during structural transformations to maintain crystallinity. While there have been advances in exploiting reticular chemistry approaches to deliberately design flexible porous networks[27-28], the precise dynamic and responsive properties of molecular crystals are typically obtained *a posteriori* (rather than by *de novo* design) and on a case-by-case basis[6-7]. Consequently, the molecular building blocks or the self-assembly conditions cannot be easily altered to obtain different structural and mechanical properties at the macroscopic scale.

Soft polymeric materials like hydrogels provide a complete contrast to crystalline materials in many aspects. They are flexible, responsive, and their mechanical properties can be readily modulated by chemical design or physical manipulation[29-30]. However, these attributes are attained precisely because polymeric materials are devoid of the structural order and coherence of crystalline materials, leading ultimately to a lack of mechanical strength and cooperativity. Previously, we surmised that the complementary but mutually exclusive advantages of crystalline and polymeric materials (crystals: structural order/strength/cooperativity; hydrogels:

flexibility/responsiveness/self-healing) could be combined if molecular crystals and hydrogel networks were chemically and structurally integrated[1]. As a proof-of-principle platform, we used the face-centered-cubic (*fcc*, *F*432 symmetry, $a \approx 180$ Å) crystals of the quasi-spherical, 24meric, iron-storage protein human H-chain ferritin (**Figure 2.1a**)[31-32]. The cubic lattice is formed through the Ca^{2+}-D84/Q86-mediated association of the C_2 symmetric interfaces of each ferritin molecule with twelve neighbors[33]. The ferritin lattice – like many protein crystals – is mesoporous, with continuously linked, nm-sized channels that account for an interstitial solvent content of 39%. This porosity allows the full permeation of ferritin crystals with acrylate polymer precursors and the subsequent formation of a pervasive polyacrylate (pA) hydrogel network within the lattice[1] (**Figure 2.1a**). Owing to the extensive non-covalent interactions between pA sidechains and the surfaces of ferritin molecules, the resulting materials (termed Polymer Integrated Crystals or PIX) behave essentially as singular chemical units that exhibit unprecedented material properties[1]. For example, pA-ferritin PIX can reversibly expand and contract in response to changes in ionic strength by nearly 600% in volume without losing crystalline order (**Figure 2.1a**) and display efficient self-healing. However, as a result of the uniform distribution and isotropic expansion/contraction of the pA network within the protein lattice, the structural dynamics of the first-generation ferritin-PIX was also isotropic, meaning that it lacked directionality[1]. Inspired by the remarkable mechanics of skeletal muscles, there has been extensive interest in designing anisotropic soft-material platforms that display directional motion and anisotropic mechanical properties[34-35]. Accordingly, we asked whether it is possible to control the spatial distribution of hydrogel networks within ferritin-PIX to achieve directional/anisotropic dynamic behavior. Here, we report that the hydrogel networks within PIX can indeed be patterned by the orientation and structural details of the distinct protein-protein interfaces in non-cubic ferritin lattices. The

resulting, anisotropic ferritin-PIX with lattice-patterned hydrogel networks display directional expansion/contraction and rapid bending motions while retaining crystalline order, as well as chemical responsiveness and efficient self-healing behavior. The anisotropic ferritin-PIX thus provide a compelling example for the molecular-scale design of hierarchical materials with bespoke macroscale properties.

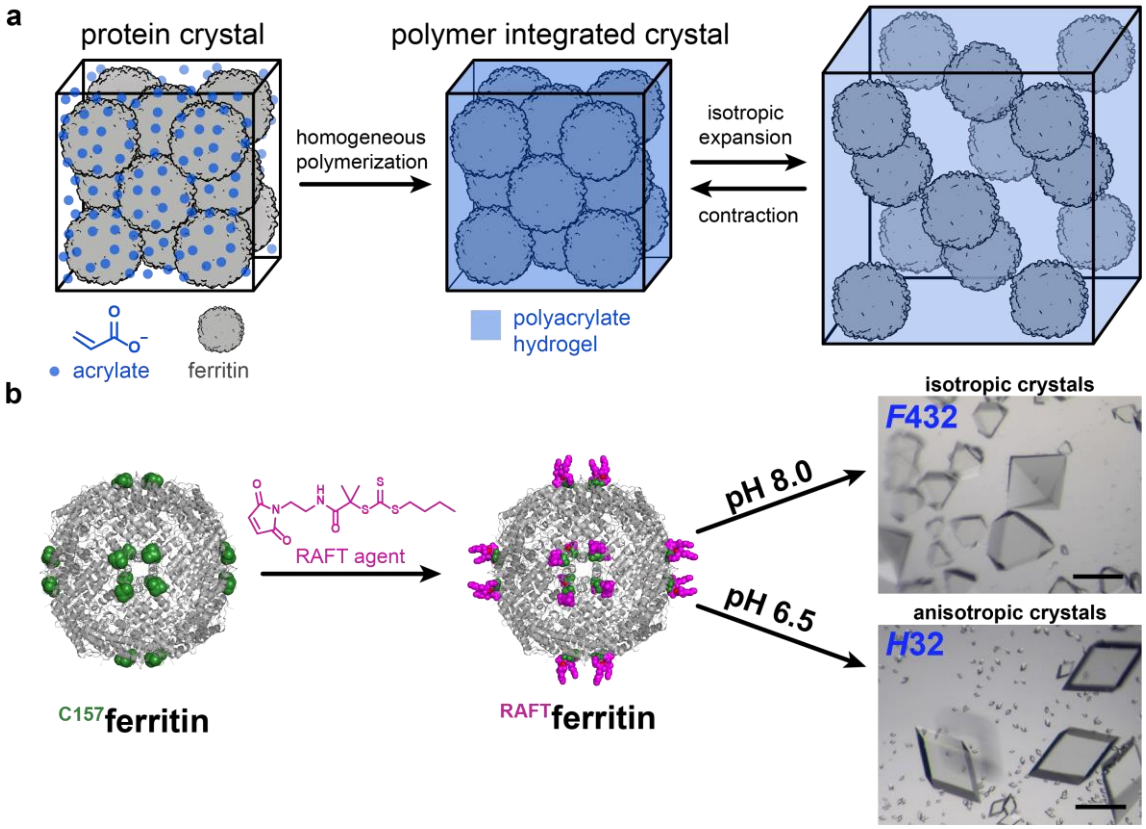

Figure 2.1. Ferritin as a building block for polymer integrated crystals (PIX). (**a)** Schematic representation for the generation and isotropic expansion/contraction properties of cubic ferritin PIX homogeneously infused with a polyacrylate network[1]. **(b)** Schematic for the site-specific conjugation of a maleimide-functionalized RAFT agent to ^{C157}ferritin. The resulting conjugate, ^{RAFT}ferritin, can assemble into isotropic (cubic) or anisotropic (rhombohedral) crystals in a pH-dependent manner (scale bars: 100 μm).

2.3 Results and Discussion

2.3.1 Preparation, Characterization, and Self-Assembly of Ferritin Modified with RAFT Agents

To generate anisotropic ferritin-PIX, we set out to prepare a ferritin variant that was site-selectively modified with RAFT (reversible addition−fragmentation chain-transfer) agents[36-37]. Our rationale was based on our original expectation that the RAFT-modified ferritins could enable the controlled growth of polymer networks in spatially well-defined locations within the protein lattice. RAFT polymerization[36-37] provides excellent compatibility with aqueous solutions and acrylate monomers, does not require transition metal ions (which may interfere with ferritin self-assembly), and has been commonly used to generate covalent protein-polymer hybrids with high efficiency via graft-from strategies.[38-39] Accordingly, we synthesized a Cys-specific maleimide-functionalized trithiocarbonate RAFT agent (**Figure 2.1b and 2.2)**. We used this agent to site-selectively label the ferritin variant, ^{C157}ferritin, which bears a single set of surface-exposed Cys residues (24 total, at positions 157) flanking the ferritin C_4 symmetry axes (**Figure 2.1b and 2.3**). The graft-from growth of the pA polymer from the modified variant (termed ^{RAFT}ferritin) could be induced by the radical initiators VA-044 or APS/TEMED and was confirmed by SDS-PAGE electrophoresis and gel permeation chromatography (GPC) (**Figure 2.4 and 2.5**).

We next examined the self-assembly of ^{RAFT}ferritin into 3D crystals. Under typical conditions used for Ca^{2+}-mediated ferritin crystallization (≥ 5 mM $CaCl_2$, pH 8.0), we obtained octahedron-shaped, *fcc* crystals (*F*432, a = 179.9 Å, PDB ID: 6WYF) of ^{RAFT}ferritin that were isomorphous with those of unmodified ^{C157}ferritin (**Figure 2.1b and 2.6a**). RAFT agents attached to the C157 side chains extend into the 6-nm wide, cube-shaped cavities in the lattice, and can be discerned in the 1.25-Å resolution crystal structure up to the amide group (**Figure 2.6a**). On the

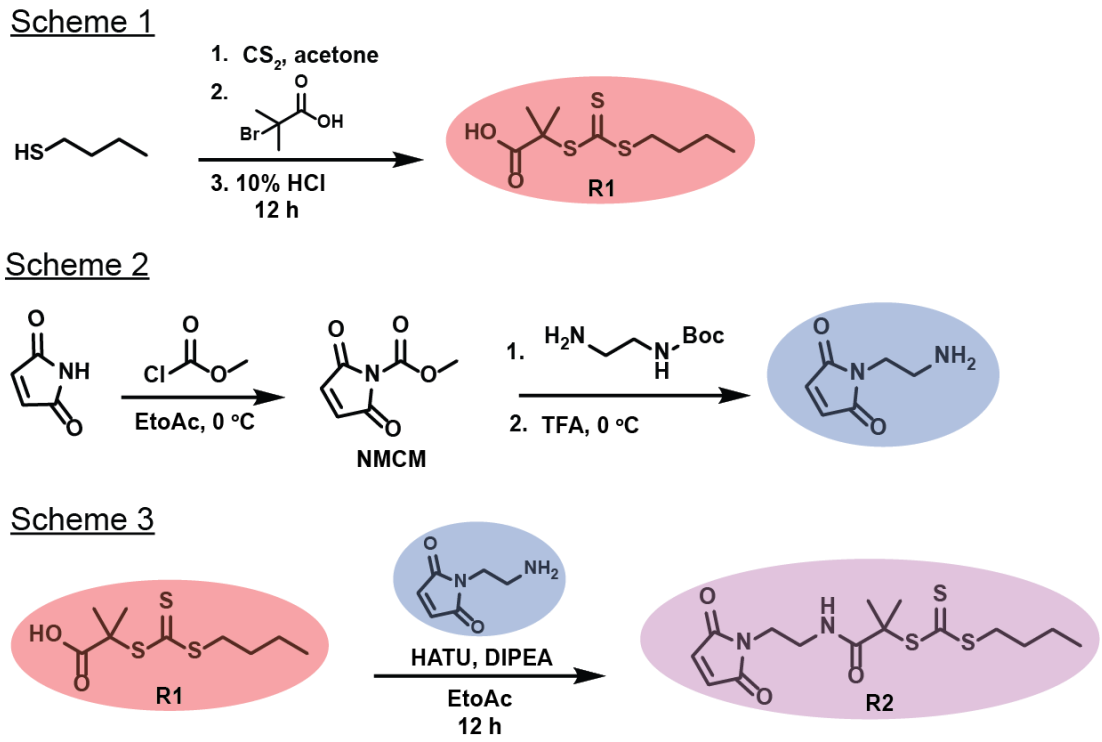

Figure 2.2. Schematic representation of the synthesis of RAFT agent (**R2**). The precursors, **R1** (Scheme 1) and N-(2-aminoethyl)-maleimide (Scheme 2), are first synthesized separately and then combined via HATU-mediated coupling to synthesize **R2** (Scheme 3).

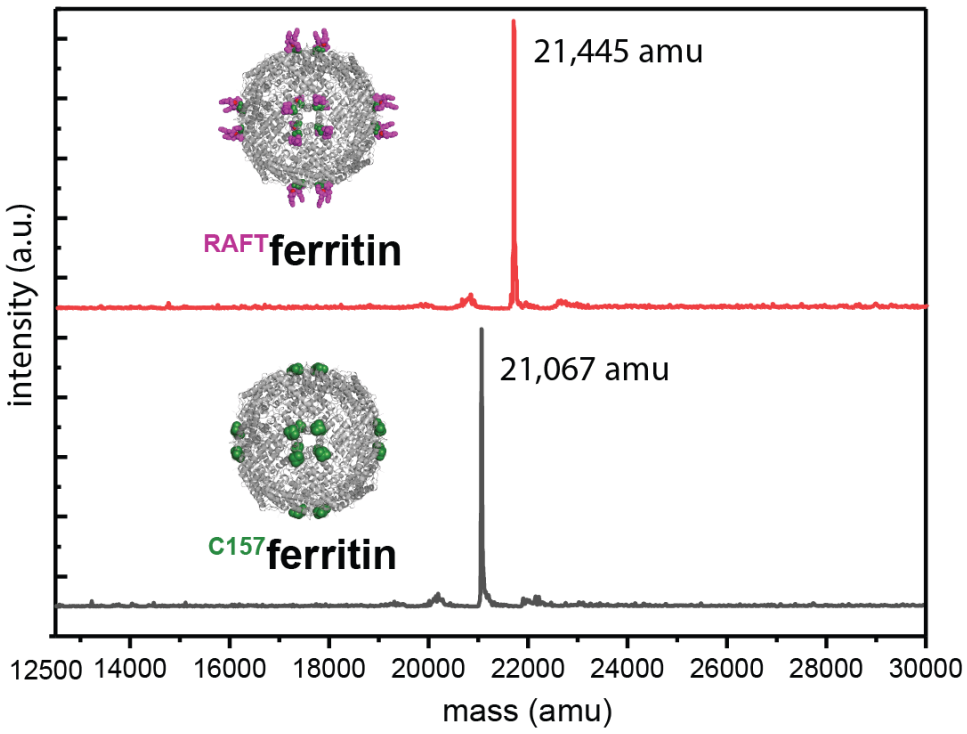

Figure 2.3. ESI-MS analysis of ^{C157}ferritin and ^{RAFT}ferritin. The ^{C157}ferritin spectrum (grey) displays a peak at 21,067 amu. The ^{RAFT}ferritin spectrum (red) displays a peak at 21,445 amu, indicating a mass difference of 378 amu (RAFT agent mass: 374 amu), which is within the instrumental error of the measurement.

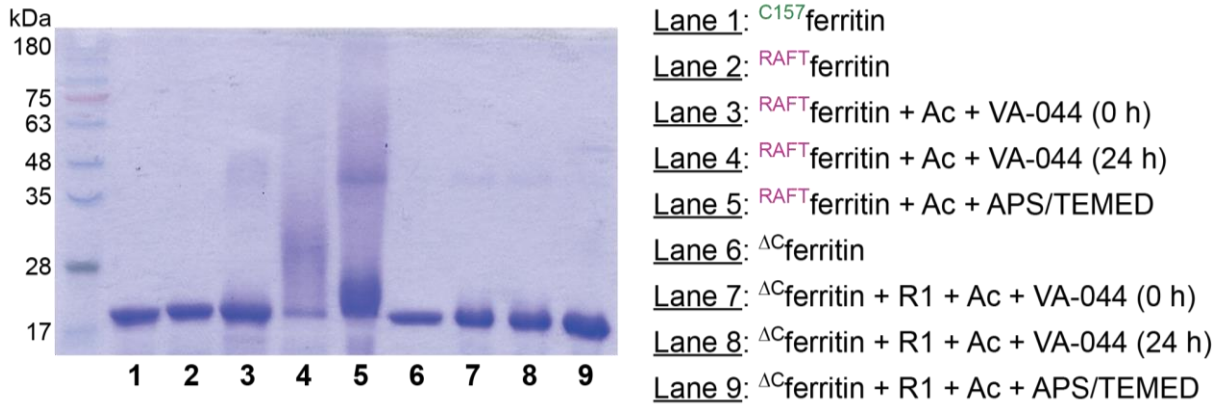

Figure 2.4. Electrophoretic analysis (12% SDS-PAGE) of $^{\Delta C}$ferritin, ^{C157}ferritin, ^{RAFT}ferritin, and protein-polymer samples in solution. Lanes 4 and 5 show streaking, indicating conjugated protein-polymer species are present. Lanes 8 and 9 do not show any streaking, indicating the covalently attached RAFT agent is critical for protein-polymer conjugation.

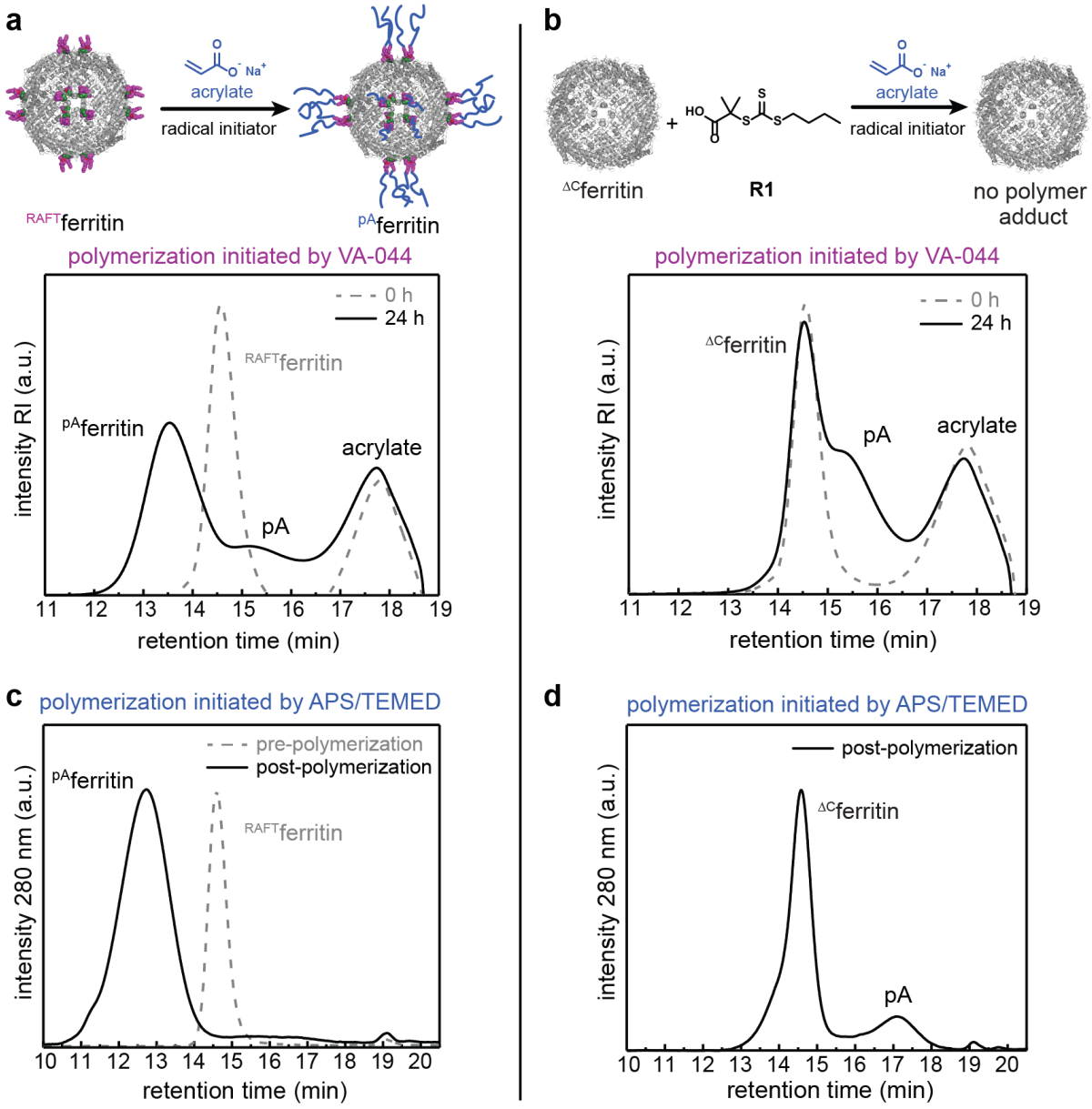

Figure 2.5. Reaction schemes and gel permeation chromatograms for free ^{RAFT}ferritin and $^{\Delta C}$ferritin subjected to polymerization reactions using either VA-044 (25 °C) or APS/TEMED as the radical initiator. (**a)** The graft-from growth of polyacrylate (pA) from ^{RAFT}ferritin is confirmed by the disappearance of the elution peak for free ferritin (at a retention time of 14.6 min) in the chromatograph when initiated by VA-044 or **(c)** APS/TEMED. **(b)** The $^{\Delta C}$ferritin elution time remains unchanged after being treated with polymerization conditions, indicating there is no covalently bound protein-polymer species when initiated by VA-044 or **(d)** APS/TEMED.

other hand, when the solution pH is lowered to ≤6.5, ^{RAFT}ferritin molecules self-assemble into large (≥60 μm) rhombohedron-shaped crystals (*H*32, $a = b = 127.0$ Å, $c = 281.7$ Å, PDB ID: 6WYG) which lack the 3D isotropy of the *fcc* crystals (**Figure 2.1b and 2.6b**).

The rhombohedral ^{RAFT}ferritin crystal lattice can be considered as a layered structure (**Figure 2.6b**). The hexagonal layers in the *ab*-plane are mediated by Ca^{2+}-D84/Q86 interactions between each ferritin molecule and six neighbors (**Figure 2.6c**), as in the cubic crystals. In contrast, the interlayer interactions along the *c*-axis are formed by contacts between the hydrophobic patches consisting of groups of four C157-RAFT moieties surrounding the ferritin C_4 axes (**Figure 2.6d**). These interactions further connect each ferritin molecule with six additional neighbors in the *c*-direction, yielding a quasi-hexagonal close-packed arrangement with a denser packing (interstitial solvent content = 32.5%) than the cubic crystals. Electrostatic calculations show that, at pH = 8, C_4 surfaces of ferritin are highly negatively charged and thus self-repulsive, accounting for the *fcc* arrangement (**Figure 2.7**). Upon lowering the pH to ≤6.5, the negative charge is mostly mitigated, promoting hydrophobic interlayer interactions (**Figure 2.7**). Thus, although each ^{RAFT}ferritin molecule is inherently isotropic, the energetic balance/competition between different interactions (metal-mediated and hydrophobic) governing its self-assembly yield both isotropic and anisotropic lattice arrangements in a condition-dependent manner, similar to what has been observed for spherical nanoparticles[40-41].

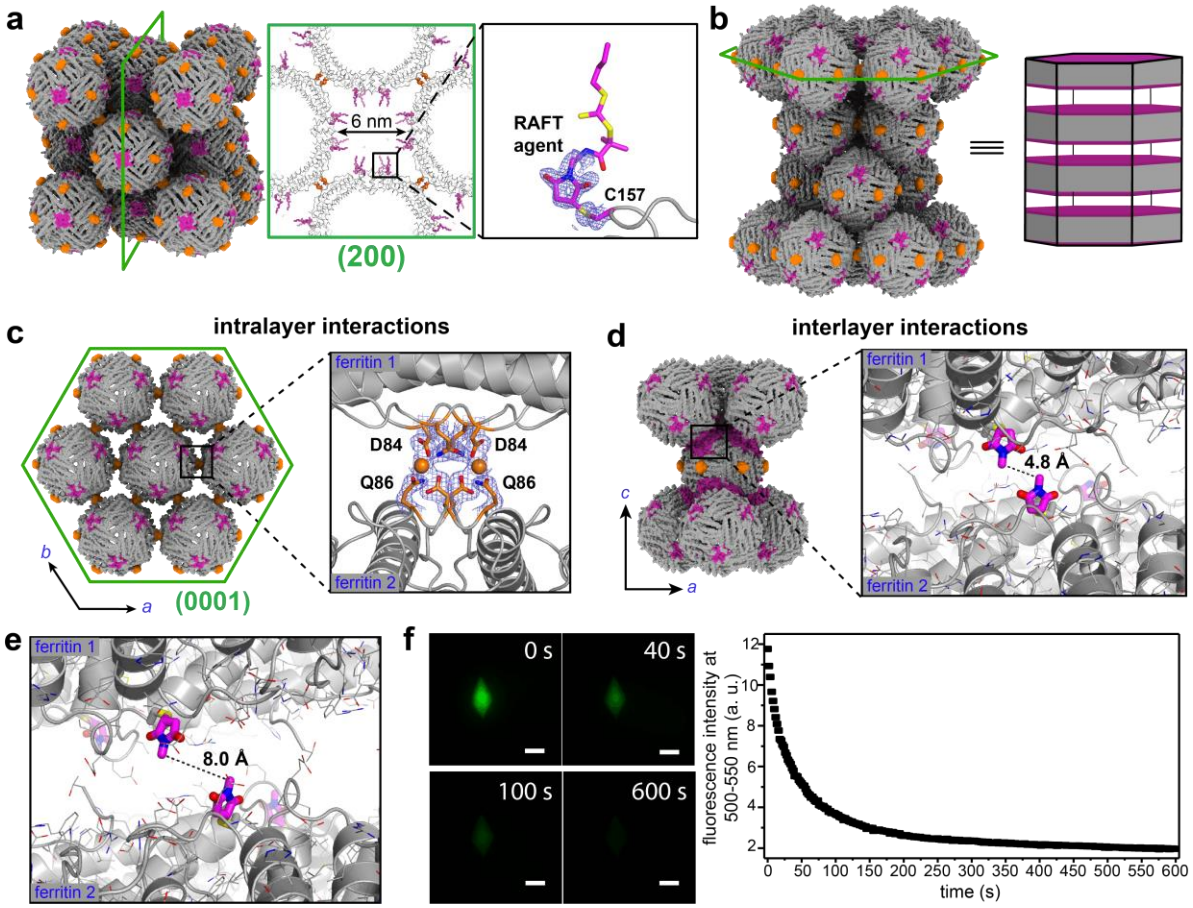

Figure 2.6. Formation and structural properties of ^{RAFT}ferritin crystals/PIX. Surface positions involved in Ca^{2+}-mediated ferritin-ferritin interactions at the ferritin C_2 axes are highlighted in orange and the RAFT-labeled C157 patches at the ferritin C_4 axes are shown in magenta. **(a)** The *fcc* (*F*432) packing arrangement of the isotropic ^{RAFT}ferritin crystals, along with a view of the lattice along the (200) plane and a close-up view of the RAFT agents (magenta) attached to C157 positions. The $2F_o–F_c$ electron density map for a single conformation of the RAFT-labeled C157 site is contoured at 0.7σ. **(b)** The hexagonal-layered (*H*32) packing arrangement of the anisotropic ^{RAFT}ferritin crystals. The (0001) plane is shown as a green hexagon. **(c)** Intralayer interactions between ferritin molecules in the (0001) plane oriented along the *ab* plane are mediated by Ca^{2+} ions (orange spheres) and two pairs of D84 and Q86 side chains. **(d)** Interlayer interactions, oriented along the *c* axis, are mediated by ferritin surfaces that include hydrophobic patches (purple) formed by the RAFT agents. **(e)** Interlayer separation increases by *ca*. 3 Å after acrylate infusion. **(f)** Formation of the pA within rhombohedral ^{RAFT}ferritin crystals is monitored by confocal fluorescence microscopy (left) through the disappearance of pyranine fluorescence, which is complete within 10 min (right, scale bars: 100 μm).

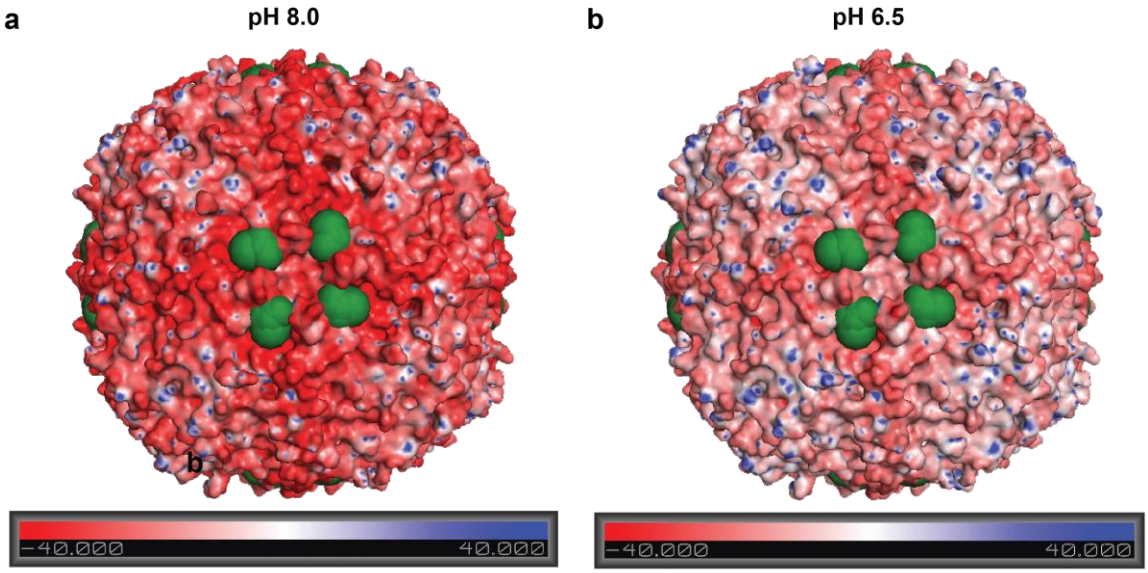

Figure 2.7. Electrostatic potential maps of ^{C157}ferritin at **(a)** pH 8.0 and **(b)** pH 6.5. The potential range is from −40 to +40 k_BT/e.

2.3.2 Anisotropic Dynamics of Rhombohedral ^{RAFT}Ferritin PIX

There have been extensive efforts toward designing hydrogel-based materials that display muscle-like, directional motion, and complex deformations in response to external stimuli[34-35]. However, hydrogels inherently undergo isotropic volumetric changes.[34] Therefore, multi-step physical alignment/patterning strategies and external fields have to be applied to introduce anisotropic arrangements of polymer chains or embedded particles to obtain directional behavior with hydrogels[34-35, 42-47]. In our system, the anisotropic structure of the rhombohedral ^{RAFT}ferritin lattices and the specific positioning of the RAFT agents in these lattices create a unique opportunity to generate an anisotropic hydrogel network solely via (one-step) molecular self-assembly and potentially generate directional actuation.

To investigate this possibility, rhombohedral ^{RAFT}ferritin crystals were first perfused with 1 M of acrylate monomers, which caused no visible loss in the integrity of the crystals. Interestingly, single-crystal X-ray diffraction (sc-XRD) measurements indicated that this treatment caused a 10-Å expansion of the lattice along the *c* axis whereas the *a/b* dimensions increased by only 2 Å (unit cell: $a = b = 128.9$ Å, $c = 291.8$ Å, PDB ID: 6WYH). This behavior is quite similar to that of layered double hydroxide materials, which undergo anisotropic lattice expansion/contraction upon exchange of the intercalating anions in the interlayer spaces[48]. The 2.2-Å resolution structure of the acrylate-soaked ^{RAFT}ferritin revealed a striking picture in which the neighboring hexagonal ferritin layers (*i.e.*, the *ab* planes) were separated from one another by 3-4 Å (**Figure. 2.6e**). This expansion eliminates any observable direct contact between the ferritin molecules along the *c* direction (and increases the interstitial solvent content of the lattice from 32% to 37%), while the Ca^{2+}-mediated intralayer interactions remain intact. These findings

highlight the fluidity of the interlayer interactions and the anisotropy inherent in the rhombohedral crystals.

The formation of the pA hydrogel network within ^{RAFT}ferritin crystals was efficiently mediated by radical initiators VA-044 (0.2% w/v) or APS/TEMED (1% w/v). *In-crystallo* polymerization was monitored by confocal microscopy, whereby we followed the quenching of the fluorescence of pyranine molecules (λ_{max} = 512 nm) infused into the crystals (**Figure 2.6f, and 2.8**). The process was typically complete in <2 min for a typical, 100 μm-sized crystal, but we incubated the acrylate-permeated ^{RAFT}ferritin crystals with radical initiators for at least 5 min to ensure full hydrogel formation within the crystals. These experiments were carried out in the presence of 4 M NaCl to prevent crystal expansion during polymerization. As previously shown[1], the inclusion of chemical crosslinkers like *N*,*N*′-methylenebisacrylamide was unnecessary for the formation of a stable hydrogel owing to the extensive interactions between the ferritin surface and the carboxylate functional groups of pA, which yield a tightly interwoven physical network.

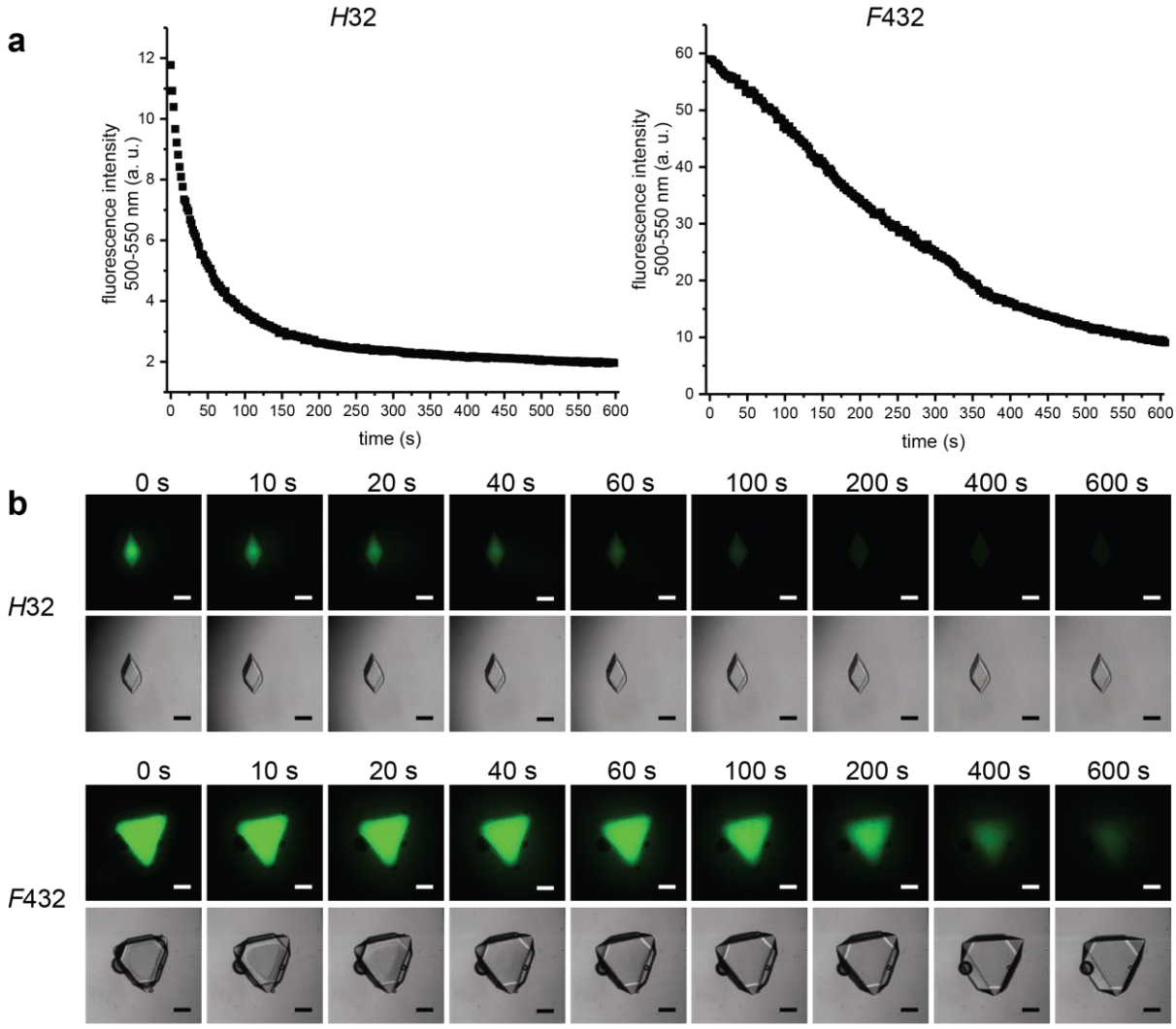

Figure 2.8. *In-crystallo* polymerization of the hydrogel network is monitored by the decrease of integrated pyranine fluorescence (green fluorescence channel). **(a)** The time-dependent decrease of pyranine fluorescence intensity as polymerization occurs is shown. The longer polymerization time for the cubic crystal (right) compared to the rhombohedral crystal (left) is primarily due to differences in size. **(b)** The corresponding bright-field (DIC) images and fluorescence micrographs of rhombohedral (top) and cubic (bottom) ^{RAFT}ferritin PIX. Scale bars correspond to 100 µm.

In a typical expansion experiment, the rhombohedral ^{RAFT}ferritin PIX were transferred into deionized water and monitored by light microscopy for 1-20 min (**Figure 2.9a**). The expansion proceeded rapidly upon transfer and followed biphasic kinetics ($\tau_{fast} \leq 10$ s; $\tau_{slow} > 50$ s), with the PIX growing to nearly 200% of their original dimensions within 1 min (**Figure 2.9b**). When the same experiments were repeated with propionate, a non-polymerizable acrylate analog, no expansion was observed, confirming that the pA polymer matrix was responsible for the reversible expansion of PIX (**Figure 2.10)** Although microcracks were sometimes visible during pA-induced expansion/contraction, the faceted crystal morphology was preserved throughout the process. Upon addition of NaCl and/or $CaCl_2$, the rhombohedral PIX contracted and regained their original dimensions within 5 s (**Figure 2.9a and 2.9b**). The expansion/contraction process was fully reversible over at least eight cycles as long as the expansion was stopped before 2 min (**Figure 2.11**).

Importantly, the structural dynamics of rhombohedral ^{RAFT}ferritin PIX were highly anisotropic, as evidenced by a) the increase in the macroscopic aspect ratio of the crystals (defined as $\frac{long\ axis\ length}{short\ axis\ length}$) by over 50% after 1 min of expansion, and b) concomitant changes in the facet angles from ~56° and ~126° to ~43° and ~137°, respectively (**Figure 2.9a**). In contrast to rhombohedral PIX, the expansion and contraction of cubic ^{RAFT}ferritin PIX were isotropic at all times (**Figure 2.12**), suggesting that directional dynamics do not stem simply from RAFT-polymerization *per se*, but likely from the higher density of the pA network in the interlayer interfaces containing the RAFT agents within the rhombohedral ferritin crystals. Indeed, upon assignment of crystal facet indices, we found that the long crystal axis, which showed disproportionate elongation compared to the short axis, aligned with the *c*-axis of the lattice along which the interlayer interfaces were oriented (**Figure 2.9c**).

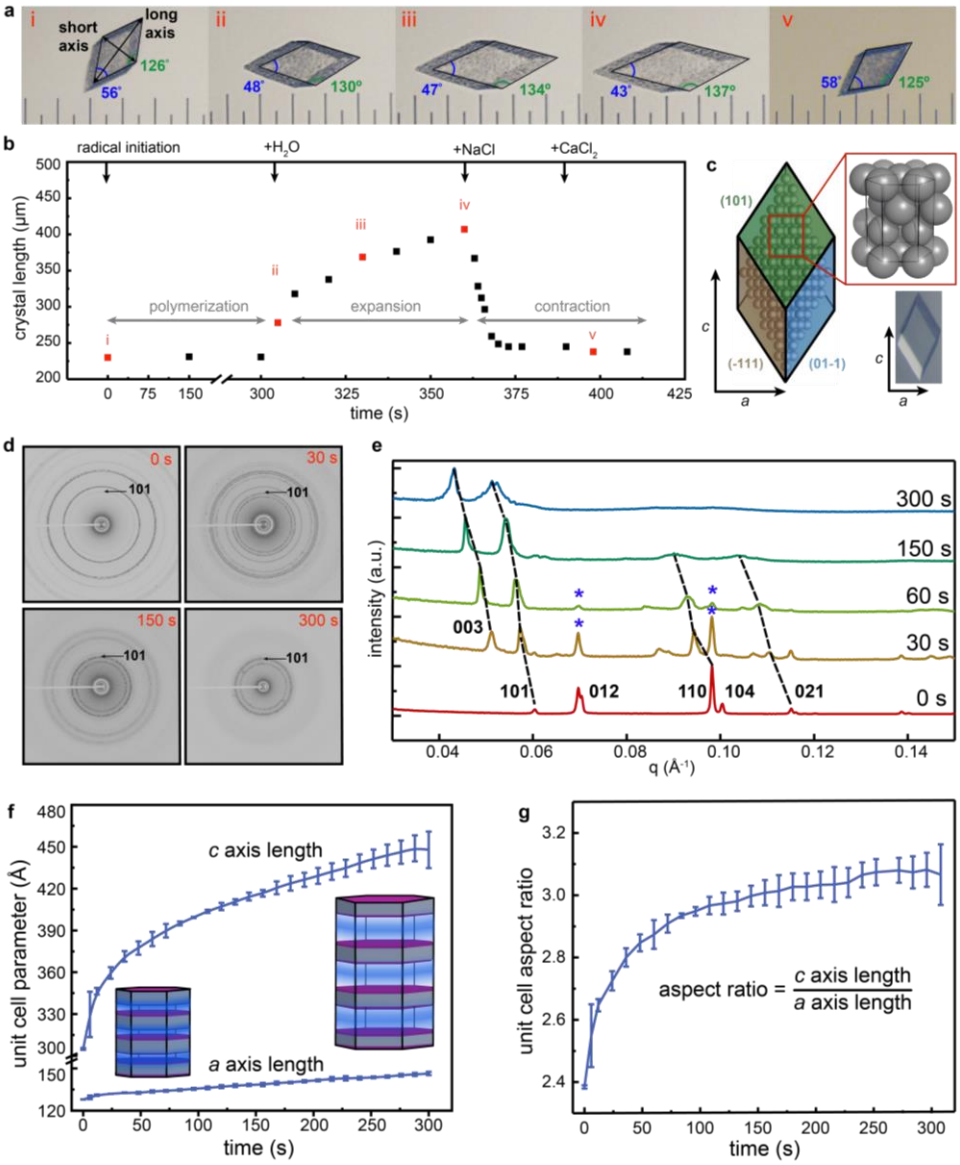

Figure 2.9. Anisotropic expansion and contraction behavior of rhombohedral ^{RAFT}ferritin PIX. **(a)** Monitoring of the anisotropic expansion and contraction of a single rhombohedral ^{RAFT}ferritin PIX by light microscopy. The separation between the major ticks of the ruler is 100 μm. **(b)** The corresponding changes in long-axis length of the same ^{RAFT}ferritin PIX during polymerization, expansion, and contraction. **(c)** Facet indices and lattice orientation in rhombohedral ^{RAFT}ferritin PIX. **(d)** SAXS images collected at different time points during the expansion of rhombohedral ^{RAFT}ferritin PIX and **(e)** the corresponding 1D SAXS profiles. The progression of peaks to lower angles (due to expansion of the unit cell) is indicated with black dashed lines. Peaks corresponding to the original lattice (due to unexpanded crystals) are visible throughout the process and designated with blue asterisks. **(f)** Changes in the unit cell dimensions of rhombohedral PIX during expansion, calculated from the SAXS profiles shown in **(e)**. **(g)** Changes in the aspect ratio (*i.e.*, the anisotropy) of the unit cell of rhombohedral PIX during expansion. Error bars: standard deviation of triplicate measurements.

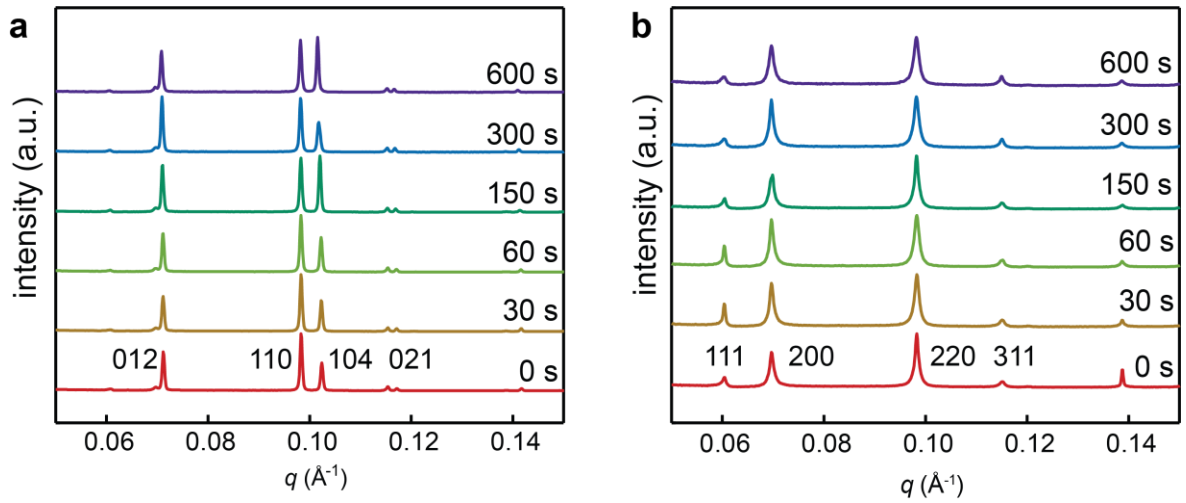

Figure 2.10. 1D SAXS profiles of **(a)** rhombohedral and **(b)** cubic ^{RAFT}ferritin crystals soaked in propionate. The initial peaks corresponding to the unit cell parameters remain unchanged and persist up to 600 s, indicating the expansion observed with acrylate is due to formation of a polyacrylate hydrogel network.

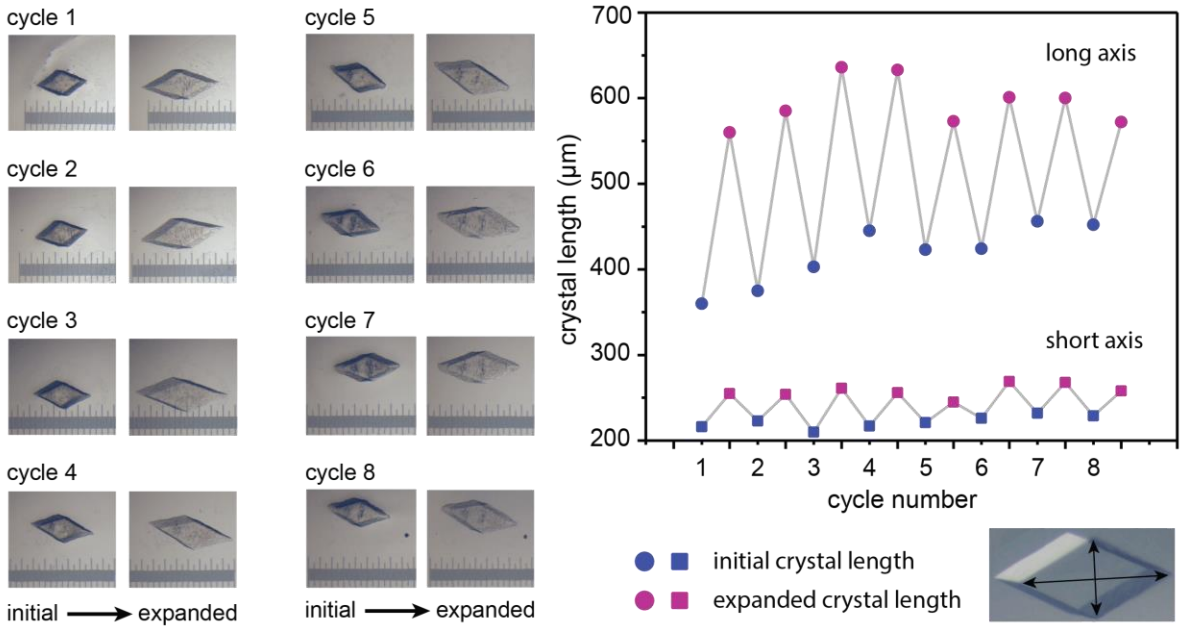

Figure 2.11. Successive expansion–contraction cycles for a single rhombohedral ^{RAFT}ferritin PIX. Light micrographs of the crystal at initial and post-expansion stages in each cycle are shown on the left, and the corresponding changes in edge lengths upon expansion–contraction are shown on the right. The separation between the major ticks of the ruler is 100 µm. The long and short axes measured are indicated on an example crystal at bottom right. Repeated expansion-contraction displays the anisotropic reversibility of the PIX, as the long axis expands significantly more than the short axis during every cycle.

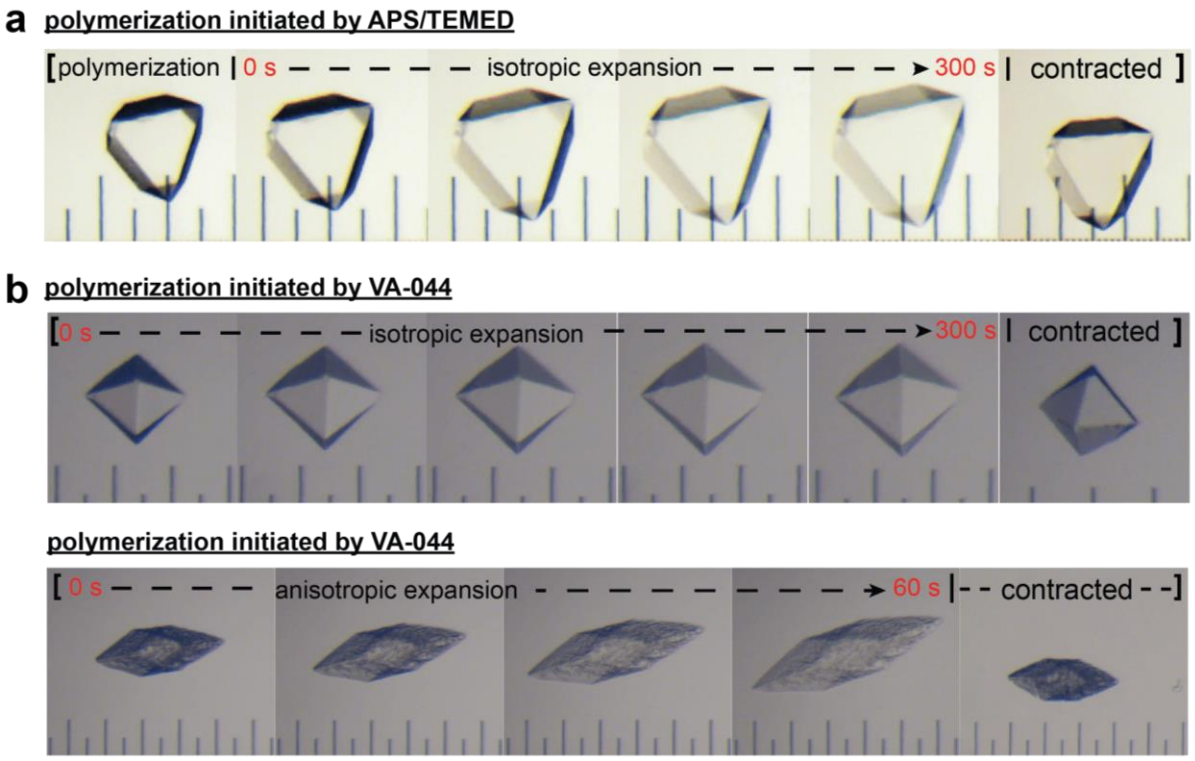

Figure 2.12. Light micrographs of ^{RAFT}ferritin PIX expansion and contraction. **(a)** Isotropic expansion and contraction of a cubic ^{RAFT}ferritin PIX. **(b)** Light micrographs of VA-044 polymerized ^{RAFT}ferritin crystals (top: *F*432, bottom: *H*32) during expansion and contraction. Changing the radical initiator from APS/TEMED to VA-044 does not affect the PIX expansion dynamics of either ^{RAFT}ferritin crystal morphologies. The separation between the major ticks of the ruler is 100 μm.

To elucidate lattice dynamics in molecular detail, we carried out time-dependent, small-angle X-ray scattering (SAXS) measurements on ^{RAFT}ferritin PIX. In these experiments, *in-crystallo* polymerization was initiated by X-ray irradiation, and the diffraction patterns of >100 PIX suspended in sample capillaries were collected. The SAXS profiles of rhombohedral ^{RAFT}ferritin crystals were consistent with a unit cell ($a = b = 127.9$ Å, $c = 293.4$ Å) nearly identical to that measured by sc-XRD (**Figure 2.9d-e**). Time-dependent crystal expansion was indicated by the shift of the Bragg peaks to lower angles, while the rhombohedral symmetry was retained (**Figure 2.9d-e**). As in the case of light microscopy measurements, the continuous increase in anisotropy during crystal expansion was clearly evident in the diffraction patterns. The unit cell became $a = b = 134.5$ Å, $c = 383.5$ Å after 1 min of expansion, corresponding to an increase in the microscopic aspect ratio (defined as $\frac{c\ axis\ length}{a\ axis\ length}$) by 25% and the cell volume by 43% (**Figure 2.9e-f**). After 5 min expansion, the long-range ferritin periodicity was still apparent from the presence of strong (003) and (101) peaks, which yield a unit cell of $a = b = 147.4$ Å, $c = 436.9$ Å (**Figure 2.9d-e**). These values correspond to increases in the cell aspect ratio and volume by 31% and 96%, respectively, compared to unexpanded crystals (**Figure 2.9f-g**). Consistent with light microscopy measurements, the kinetics for the growth of unit cell dimensions and the increase in longitudinal anisotropy was also non-monotonic (**Figure 2.9e-f**). We attribute this behavior to a fast initial expansion of the dense pA network throughout the PIX, which attenuates as the overall polymer density decreases and polymer chain mobility increases. Time-dependent SAXS measurements were repeated for cubic ^{RAFT}ferritin PIX, which confirmed that the cubic symmetry – thus the 3D isotropy – was retained throughout expansion (**Figure 2.13**).

Taken together, our observations are consistent with an anisotropic distribution of the pA polymer matrix within rhombohedral ^{RAFT}ferritin crystals, which we (originally) attributed to a

combination of two factors: 1) the specific interlayer positions of the RAFT agents which promote localized polymer growth, and 2) the wide, weakly bound interlayer interfaces, which are further enlarged upon soaking with acrylate monomers. Both factors would lead to the interlayer zones developing a denser matrix of pA polymer compared to the tighter interfaces along the *ab*-planes, thus generating a lamellar pattern (**Figure 2.14a**). Consequently, the hydration of the PIX produces a larger extent of lattice expansion parallel to the *c*-axis compared to that in the *ab*-plane (**Figure 2.14a**). Although the pA network displays varying densities, it is continuous throughout the mesoporous lattice and forms extensive interactions with the ferritin molecules. The resulting dense mold thus allows the expanded ferritin lattice to fully revert to its original dimensions upon NaCl/$CaCl_2$-induced dehydration. In fact, the sc-XRD measurements show that ^{RAFT}ferritin PIX fully regains near-atomic-level crystallinity upon contraction after 5 min of expansion (**Figure 2.14b**), meaning that ferritin molecules can return to their original lattice positions and orientations after having separated from one another by >20 Å in the *ab*-plane and >40 Å along the *c*-axis.

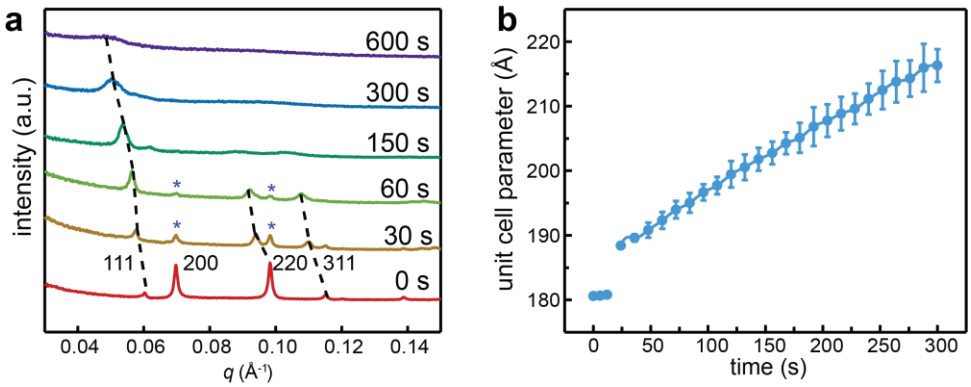

Figure 2.13. SAXS measurements of *F*432 ^{RAFT}ferritin PIX. **(a)** SAXS profiles showing the change in the lattice parameters of the cubic PIX during expansion. Peaks corresponding to the original lattice (due to unexpanded crystals) are designated with blue asterisks. **(b)** Change in the unit cell dimension (*a*) of cubic PIX during expansion, calculated from the SAXS profiles. The cubic symmetry of the lattice is retained during expansion. The error bars are standard deviations determined from measurements done in triplicate.

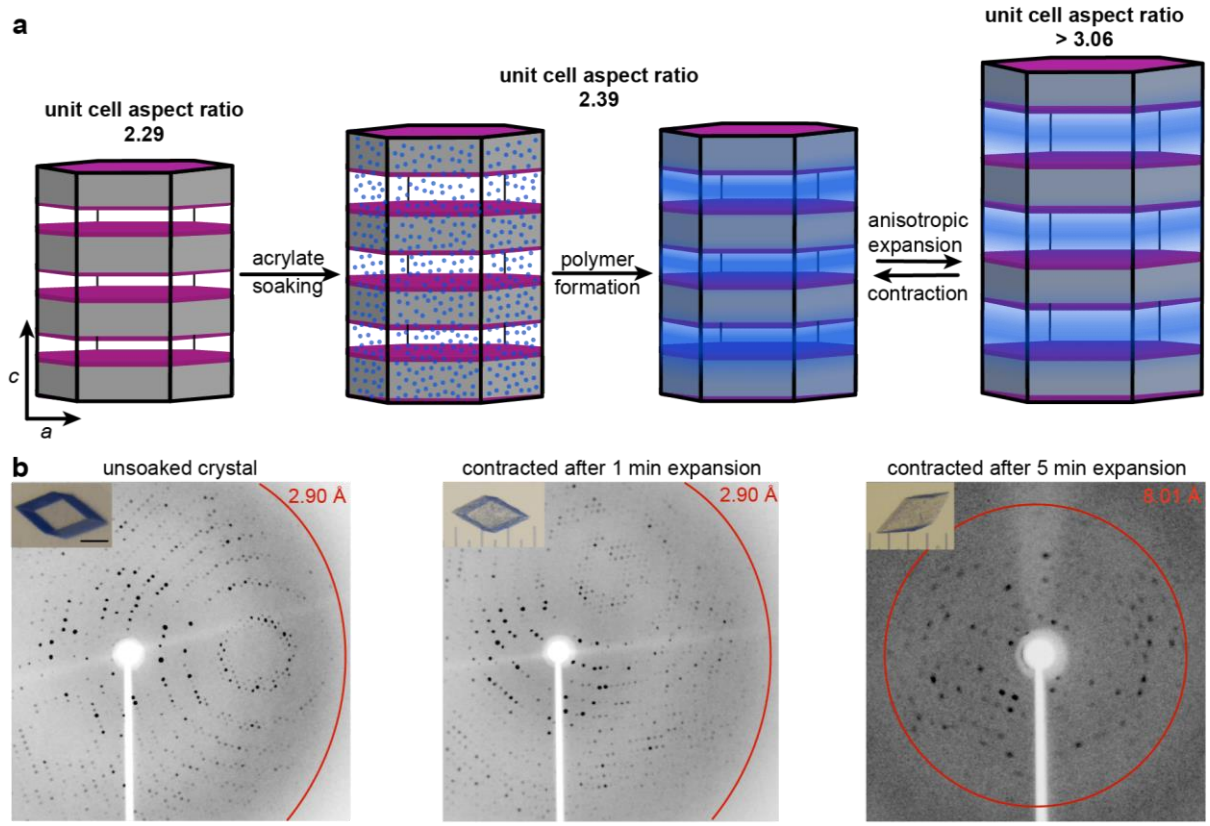

Figure 2.14. Anisotropic expansion/contraction of rhombohedral ^{RAFT}ferritin PIX is enabled by the anisotropic polymer matrix and is fully reversible. **(a)** Schematic summary for the generation of the anisotropic/layered pA network within rhombohedral ^{RAFT}ferritin crystals, which dictates the anisotropic structural dynamics. **(b)** sc-XRD image (at T = 298 K) of native rhomboderal ^{RAFT}ferritin crystal (left), compared to those of a PIX contracted after 1 min of expansion (middle), and after 5 min of expansion (right). The diffraction limits are indicated with red circles. Light micrographs of the crystals are shown in the insets; the scale bar and separation between the major ticks of the ruler are 100 μm.

2.3.3 The Structural Basis of Anisotropic Polymer Distribution in Ferritin PIX

We next examined if the anisotropic pA distribution in ^{RAFT}ferritin PIX indeed could be ascribed to localized polymer growth originating from the RAFT agents on ferritin surfaces. To this end, the ^{RAFT}ferritin PIX were dissolved by treatment with ethylenediaminetetraacetic acid (EDTA) and analyzed by SDS-PAGE and GPC. Interestingly, these ^{RAFT}ferritin PIX samples showed no evidence of covalent attachment between pA chains and ferritin molecules when *in-crystallo* polymerization was induced with APS/TEMED and only minimal yields of graft-from polymerization when VA-044 was used as a radical initiator (**Figure 2.15**). The drastically diminished graft-from polymerization efficiencies are likely due to the steric occlusion of the RAFT agents within the interlayer interfaces and slower molecular diffusion within the crystals. These observations implied that the inherent anisotropy of the rhombohedral crystals was alone responsible for templating an anisotropic hydrogel network in ferritin PIX.

An appropriate control system to test this possibility would be ferritin crystals that are also rhombohedral but lack covalently attached RAFT agents. Since the RAFT agents are directly involved in lattice packing interactions, we were not able to obtain isomorphous rhombohedral crystals using unmodified ^{C157}ferritin. Yet, in the course of exhaustive screening, we found that a ferritin variant lacking Cys157 (termed ΔC) formed lattices with trigonal symmetry ($P3_121$; $a = b$ =131.8 Å, c = 301.8 Å, PDB ID: 7K26) and a rhombohedron-shaped crystal habit that is nearly identical to that of rhombohedral (i.e., $H32$-symmetric) ^{RAFT}ferritin crystals. The 2.7-Å resolution structure of the trigonal crystals indeed revealed a similar hexagonal-layered packing arrangement with an interstitial solvent content of 44.5%, but also indicated that the protein interfaces in these lattices substantially differ from those in their rhombohedral counterpart. Most strikingly, the lattice packing interactions between ferritin molecules are mediated entirely by the interlayer

interfaces directed along the *c* axis, whereas the intralayer interfaces in the *ab* plane are *ca*. 6 Å wide at their narrowest point and devoid of direct ferritin-ferritin contacts (**Figure 2.16a and 2.16b**). Thus, in terms of the orientation of interstitial voids that can be filled with the pA matrix, the trigonal and rhombohedral lattices are orthogonal to one another.

Despite the relative mechanical fragility of the trigonal crystals, we were able to find conditions to form pA matrices within them (**Methods**). The expansion/contraction properties of the resulting PIX were examined by light microscopy, which revealed that they also displayed anisotropic dynamics, but the direction of crystal expansion was orthogonal to that observed with rhombohedral ^{RAFT}ferritin PIX (**Figure 2.16c-e**). Whereas the rhombohedral PIX elongated to assume a lozenge shape (with the acute facet angles decreasing from ~60° to ~45°, **Figure 2.9a**) upon expansion, the trigonal PIX expanded toward a more square-like shape (with the acute facet angles increasing from ~60° to 76°, **Figure 2.16c**), with the overall aspect ratios of the two systems moving in opposite directions (**Figure 2.16d**). These findings establish that 1) the anisotropy of the crystal lattices and the underlying orientation/structure of the protein-protein interfaces alone are sufficient for the formation of anisotropic hydrogel networks within PIX, and 2) they can be used to control the directionality of PIX dynamics.

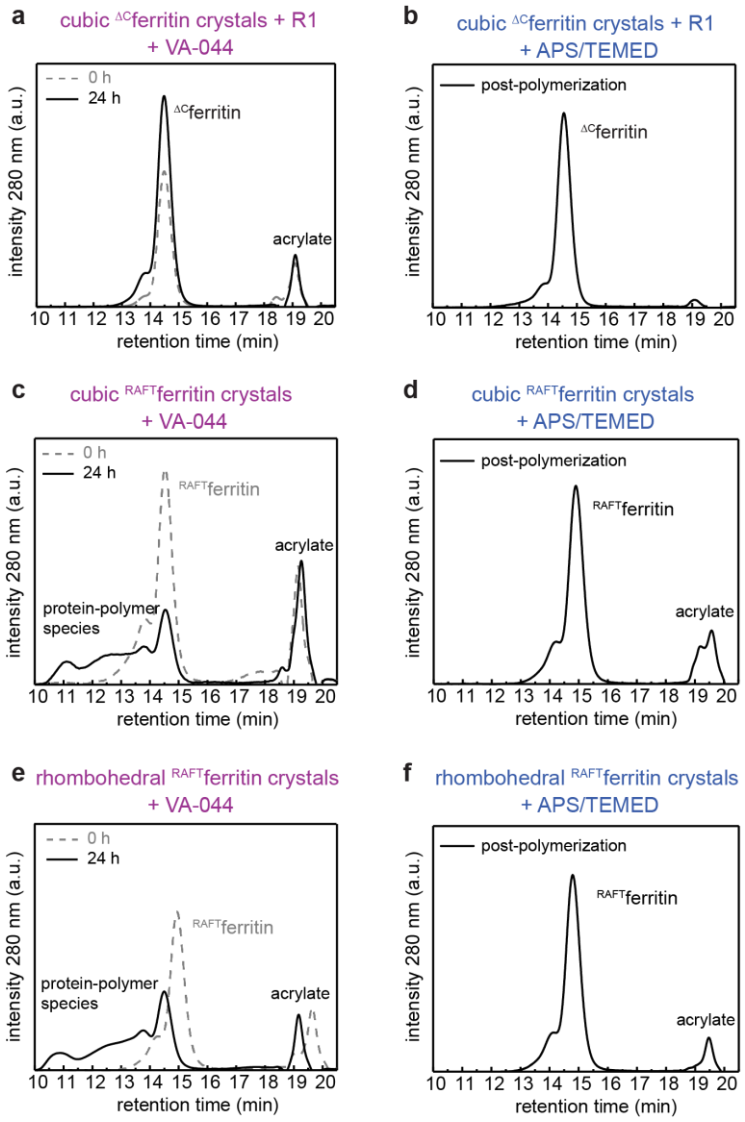

Figure 2.15. Gel permeation chromatograms of various $^{\Delta C}$ferritin and ^{RAFT}ferritin crystal species under different polymerization conditions. The samples were prepared by the dissolution of the crystals/PIX prior to GPC experiments. In **(a)** and **(b)**, the $^{\Delta C}$ferritin crystals (devoid of covalently-attached RAFT agents) were treated with free RAFT agent R1 and the initiator VA-044 (40 °C) or APS/TEMED, respectively. In both cases, $^{\Delta C}$ferritin elution time remains unchanged after being treated under polymerization conditions, indicating there is no covalently-bound protein-polymer species. In **(c)**/**(e)** and **(d)**/**(f)**, the same experiments were conducted with cubic or rhombohedral ^{RAFT}ferritin crystals (which contain covalently attached R2 on ferritin surfaces) that were treated with VA-044 (40 °C) or APS/TEMED, respectively. In the case of APS/TEMED initiation **(d/f)**, the free-ferritin elution time remains unchanged, again indicating a lack of covalently-bound protein-polymer species. In contrast, in the case of VA-044 initiation **(c/e)**, the free-ferritin elution peak is diminished in intensity, with concomitant appearance of a distribution of higher-molecular-weight species, suggesting the potential formation of covalently-bound protein-polymer species.

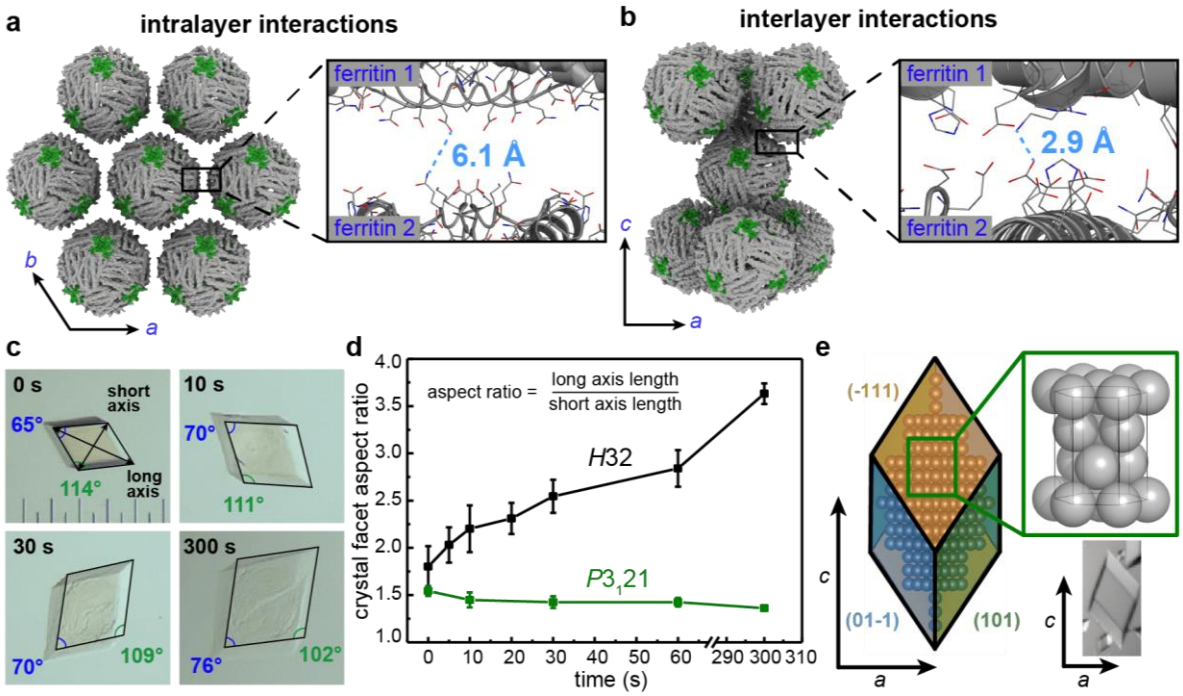

Figure 2.16. Structural properties and anisotropy of $^{\Delta C}$ferritin crystals/PIX with $P3_121$ symmetry. **(a)** $^{\Delta C}$ferritin molecules along the *ab* plane are devoid of any intralayer interactions. The closest side chains, Q86 and D84, are 6.1 Å apart which precludes any salt-bridge interactions. **(b)** Interlayer interactions, oriented along the *c* axis, are mediated by surfaces that include hydrophobic patches. The closest non-covalent interaction is within 3.0 Å and formed by side chains K119 and E116. Where the *H*32 lattice hydrophobic patches would be are highlighted in green. **(c)** Light micrographs of $P3_121$ symmetric PIX during expansion in water. The separation between the major ticks of the ruler is 100 μm. **(d)** Changes in the crystal facet aspect ratios of $P3_121$ and *H*32 symmetric PIX during expansion display their respective anisotropic behavior. Error bars: standard deviation of triplicate measurements. **(e)** Facet indices and lattice orientation in rhombohedral $^{\Delta C}$ferritin PIX.

2.3.4 Anisotropic Mechanical and Self-Healing Properties of Rhombohedral ^{RAFT}Ferritin PIX

Analogous to the mechanical anisotropy of muscles enabled by their underlying anisotropic architecture, the directional alignment of polymer chains or embedded particles within hydrogels have been shown to yield anisotropic mechanical properties with respect to the direction of applied force and generate bending motions[34-35]. This behavior was also borne out in expanded rhombohedral ^{RAFT}ferritin PIX, which possess an alternating pattern of high- and low-molecular density regions aligned along the *c*-axis (**Figure 2.17**). When the expanded PIX were exposed to Ca^{2+} ions to induce contraction, they underwent a drastic bending motion toward the direction of Ca^{2+} influx, with flexion angles of up ~25° in the absence of any apparent cracking. The PIX reverted to the original shape as the Ca^{2+} flux dissipated (**Figure 2.17a**). The bending of the PIX arises from the compression of the hydrogel matrix perpendicular to the hexagonal ferritin *ab*-layers at the Ca^{2+} diffusion front and provides, in essence, a chemosensory/chemotactic motion (**Figure 2.17b**). The actuation is remarkably rapid with a bending rate of >10° s^{-1}, which is one-to-several orders of magnitude higher than those of recently-reported supramolecular and hydrogel systems with some of the fastest reported actuation rates (1.5° s^{-1} and 0.14° min^{-1}, respectively)[49-50]. The rapid actuation by the PIX can be ascribed to the high packing density and the structural cooperativity of the integrated crystal-pA matrix.

Under certain circumstances like excessive bending or fast expansion/contraction, the rhombohedral ^{RAFT}ferritin PIX were observed to develop large fractures, sometimes >75 μm in length and >10 μm in width (**Figure 2.17c**). Consistent with the mechanical anisotropy of these materials, the defects were overwhelmingly oriented along the short crystal axis (*i.e.*, parallel to the hexagonal ferritin layers in the *ab* planes) (**Figure 2.17c**). Owing to the mobility of the

hydrogel matrix and its reversible interactions with the ferritin molecules, these large defects were often scarlessly and autonomously healed. In extreme cases, such as that shown in **Figure 2.17d**, the rhombohedral PIX could even undergo complete lamellation and accordion-like motions to adapt to Ca^{2+} fluxes in solution, followed by full recovery of their original polyhedral morphology within seconds. Such rapid, adaptive motions with attendant self-healing are more typical of soft biological devices like muscles rather than stiff molecular crystals.

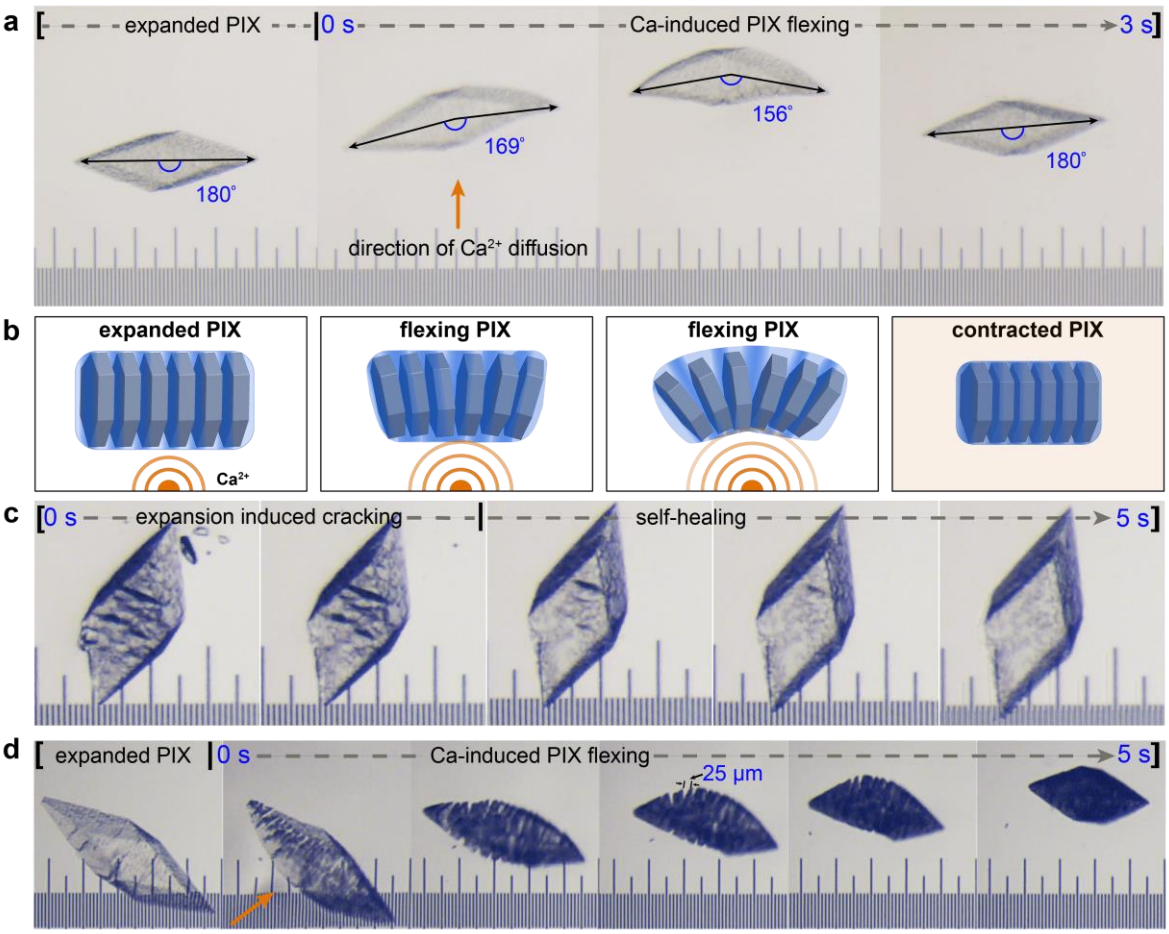

Figure 2.17. Anisotropic mechanical and self-healing behavior of rhombohedral ^{RAFT}ferritin PIX. **(a)** Light micrographs showing the bending motion of an expanded ^{RAFT}ferritin PIX flexing in response to Ca^{2+} flux (oriented along the orange arrow). The separation between the major ticks of the ruler in all images is 100 µm. **(b)** Schematic description for the cation-induced bending motion of the rhombohedral ^{RAFT}ferritin PIX due to the underlying hexagonal-layered lattice arrangement and the anisotropic distribution of the polymer network. **(c)** Defects in rhombohedral ^{RAFT}ferritin PIX are overwhelmingly oriented in the direction of the *ab* planes (orthogonal to the long crystal axis) and often spontaneously healed. **(d)** Highly fractured ^{RAFT}ferritin PIX can undergo lamellation and accordion-like flexing motions in response to Ca^{2+} flux.

2.4 Conclusions

Ranging from abalone nacre and mussel byssus to spider silk and skeletal muscles, nature uses the hierarchical assembly of multi-component materials to simultaneously achieve a combination of vital properties (*e.g.*, strength, toughness, flexibility, damage tolerance) that would be impossible to obtain through the self-assembly of single components alone[51-52]. Accordingly, we have shown here that through the physical integration of two disparate classes of materials, *i.e.*, molecular crystals and hydrogel polymers, we can obtain an unprecedented combination of material attributes and mechanical behaviors: atomic-level order/coherence, directional motion, flexibility, rapid anisotropic actuation, chemical responsiveness, self-healing.

Key to the attainment of anisotropic properties in PIX was the ability of ferritin molecules to form lattices with distinct symmetries and protein-protein interfaces. These differences allowed the templation of alternatively patterned hydrogel networks *in situ*, which ultimately enabled ferritin crystals that essentially possess the same macroscopic morphologies to display orthogonally directed motions. The original intent of this study was to achieve control over the spatial distribution of polymer networks within protein crystals using site-directed RAFT-polymerization strategies. Although our findings revealed that such strategies were not necessary to create patterned hydrogels *in crystallo*, we posit they would still offer important advantages if their efficiencies can be improved, such as the incorporation of polymers with a diverse range of functional groups into protein lattices (regardless of their chemical compatibility with the protein components), construction of multi-polymer networks, and spatio-temporal control over polymer growth within lattices. Combined with the inherent chemical versatility and functions of proteins, such covalently hybridized PIX could offer a unique platform for the study of protein-polymer

interactions and the development of biocatalytic and molecular encapsulation/delivery systems with tunable and responsive mechanical properties.

2.5 Materials and Methods

2.5.1 General Methods.

All reagents were purchased from commercial sources and used without further purification unless noted otherwise. Mass spectrometry (MS) of proteins and small molecules was carried out at the Molecular Mass Spectrometry Facility at UCSD using electrospray ionization (ESI) on a Micromass Quattro Ultima Triple Quadrupole MS. NMR spectra were recorded on Varian Mercury (400 MHz) and Bruker AVA (300 MHz) spectrometers. NMR data are reported as follows: chemical shift, multiplicity (s = singlet, d = doublet, t = triplet, m = multiplet, dd = double doublets), and relative integrated peak area. The spectra were internally referenced to the residual solvent signal (DMSO, δ 2.50 ppm).

2.5.2 Protein expression, purification, and characterization.

The plasmid for the ΔC variant of human heavy-chain ferritin, devoid of all native cysteine residues (C90E, C102A, and C130A), was obtained via site-directed mutagenesis as previously described.[53] ^{C157}ferritin was prepared using QuikChange mutagenesis with primers obtained from Integrated DNA Technologies shown in Table 2.1. Mutant plasmids were transformed into XL-1 blue E. coli cells and purified with QIAprep Spin Miniprep kit (Qiagen). The variant was sequenced (Retrogen) to verify mutagenesis. Expression and purification of $^{\Delta C}$ferritin and ^{C157}ferritin were performed according to the previously published protocol.[54] When handling ^{C157}ferritin, 2 mM DTT was added at each step during purification to prevent disulfide-mediated protein aggregation.

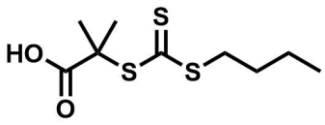

2.5.3 Synthesis of 2-(((butylthio)carbonothioyl)thio)-2-methylpropanoic acid (R1).

2-(((butylthio)carbonothioyl)thio)-2-methylpropanoic acid was synthesized as previously described with minor modifications.[55] Tribasic potassium phosphate (22.88 g, 108 mmol) was dissolved in acetone (180 mL) and stirred for 5 h. 1-butanethiol (11.61 mL, 108 mmol) was added, and the solution was stirred for 1 h. The reaction was cooled to 0 °C, and carbon disulfide (7.82 mL, 129 mmol) was added dropwise over 5 min. The combined solution was stirred for 2 h, followed by the addition of 2-bromo-2 methylpropionic acid (18 g, 108 mol). After stirring for 12 h, the solution was filtered, and the filtrate was concentrated *in vacuo*. A solution containing 10% HCl (200 mL) was added, and the reaction was stirred for 12 h. The product was extracted 2x with hexanes (50 mL), the organic layer was dried over anhydrous sodium sulfate, and the solvent was removed *in vacuo*. The solid was purified by silica gel chromatography with a gradient of 20%-50% ethyl acetate in hexanes. The solvent was removed *in vacuo,* and the precipitate was dissolved in a minimal amount of hexanes. The resulting solution was cooled to −20 °C, and crystals formed overnight. The crystals were filtered and dried *in vacuo,* yielding 20 g of product (74%).^{1}H NMR (400 MHz, DMSO-d_6): δ 3.30 (t, J = 7.3 Hz, 2H), 1.68 – 1.54 (m, 8H), 1.35 (m, J = 15.0, 7.3 Hz, 2H), 0.87 (t, J = 7.3 Hz, 3H) (**Figure 2.18**). Measured molecular weight: (m/z) =253.15 m/z (Calculated: 253.03) ($M + H^+$).

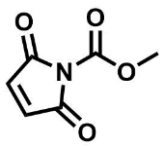

2.5.4 Synthesis of N-(Methoxycarbonyl)maleimide (NMCM).

N-(Methoxycarbonyl)maleimide was synthesized as previously described with minor modifications.[56] Maleimide (388 mg, 4 mmol) and N-methylmorpholine (439 µL, 4 mmol) were dissolved in ethyl acetate (20 mL), cooled to 0 °C, and stirred. Methylchloroformate (310 µL, 4 mmol) was added dropwise to the solution while stirring. After 30 min, the mixture was filtered, and the precipitants were washed with 10 mL ethyl acetate. The filtrate was collected, washed with 5 mL brine, dried over anhydrous sodium sulfate, and the remaining solvent was removed *in vacuo,* yielding 517 mg (83%).^{1}H NMR (300 MHz, DMSO): δ 7.17 (s, 2H), 3.83 (s, 3H) (**Figure 2.19**). Measured molecular weight: (m/z) =156.03 m/z (Calculated: 156.11) ($M + H^{+}$).

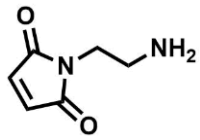

2.5.5 Synthesis of N-(2-aminoethyl)-maleimide.

N-(2-aminoethyl)-maleimide was synthesized as previously described with minor modifications.[57] Methyl 2,5-dioxo-2,5-dihydro-1H-pyrrole-1-carboxylate (6.43 g, 41.5 mmol) was dissolved in saturated $NaHCO_3$ (50 mL) and combined with a solution containing tert-butyl (2-aminoethyl) carbamate (6.56 mL, 41.5 mmol) in saturated $NaHCO_3$ (50 mL). The combined solution was stirred for 40 min at 0 °C and 50 min at room temperature. The reaction was again cooled to 0 °C, and the pH was adjusted to ca. 3 with concentrated H_2SO_4. The solution was extracted 3x with ethyl acetate (20 mL), and the organic layer was dried over anhydrous sodium sulfate concentrated to a brown oil *in vacuo*. This oil was purified by silica gel chromatography (eluted with 50% ethyl acetate in hexanes). The flow-through was concentrated *in vacuo* yielding a white powder. The powder was dissolved in 50 mL dichloromethane and cooled to 0 °C. Trifluoroacetic acid (50 mL) was added to the solution. The solution was stirred for 1 h at 0 °C and concentrated *in vacuo*. Chilled diethyl ether was added to the concentrated solution to

precipitate out N-(2-aminoethyl)-maleimide as a white solid. The precipitate was filtered, washed with diethyl ether, and dried *in vacuo,* yielding 4.92 g of product (75%).^{1}H NMR (400 MHz, DMSO-d_6): δ 8.02 (s, 3H), 7.06 (s, 2H), 3.65 (t, J = 5.8 Hz, 2H), 2.99 (t, J = 5.8 Hz, 2H) (**Figure 2.20**). Measured molecular weight: (m/z) = 141.07 m/z (Calculated: 141.06) ($M + H^+$).

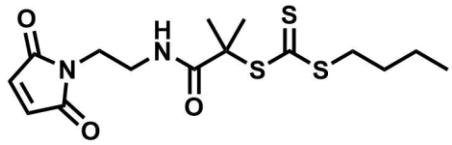

2.5.6 Synthesis of the maleimide-functionalized RAFT agent (R2).

N-(2-aminoethyl)-maleimide (7.14 mmol, 1 g), HATU (7.78 mmol, 2.96 g), and DIPEA (19.46 mmol, 3.39 mL) was dissolved in dimethylformamide (30 mL) and stirred for 10 min. 2-(((butylthio)carbonothioyl)thio)-2-methylpropanoic acid (6.49 mmol, 1.637 g) was added in portions over 5 min, and the reaction was stirred for 12 h. Water (30 mL) was added, and the solution was extracted 3x with 20 mL of ethyl acetate. The organic layer was collected, dried over anhydrous sodium sulfate, and concentrated *in vacuo*. The product was purified by silica gel chromatography with 20%-40% ethyl acetate in hexanes as the eluent. The solvent was removed *in vacuo* and dissolved in a minimal amount of hexanes. The resulting solution was cooled to −20 °C, and crystals formed overnight. The crystals were filtered and dried in vacuo, yielding 2.10 g of product (86%). ^{1}H NMR (300 MHz, DMSO-d_6): δ 8.04 (t, J = 5.8 Hz, 1H), 6.99 (s, 2H), 3.45 (t, J = 5.8 Hz, 2H), 3.31 – 3.25 (m, 2H), 3.19 (dd, J = 11.6, 5.8 Hz, 2H), 1.64 – 1.50 (m, 8H), 1.34 (m, J = 14.3, 7.2 Hz, 2H), 0.87 (t, J = 7.3 Hz, 3H) (**Figure 2.21**).^{13}C NMR (300 MHz, DMSO-d_6): δ 221.79, 171.48, 134.93, 57.76, 38.67, 38.33, 37.18, 36.37, 29.95, 25.77, 21.89, 13.88 (**Figure 2.22**). Measured molecular weight: (m/z) = 397.07 m/z (Calculated: 397.08) ($M + Na^+$).

2.5.7 Conjugation of R2 to ^{C157}ferritin.

A 100 mL solution was prepared with 4 μM ^{C157}ferritin, 25 mM HEPES (pH 7.5), and 1 mM of TCEP-HCl. Then 2 mM (final concentration) of **R2** (dissolved in dimethylformamide) was added dropwise over 5 min to a vigorously stirring solution. The mixture was stirred for 48 h at room temperature and monitored by ESI-MS. Measured molecular weight: (m/z) = 21,445 m/z (Calculated: 21,405).

2.5.8 Graft-from polymerization with free ^{RAFT}ferritin initiated with VA-044.

A 1.5-mL buffered solution containing 50 mM MES (pH 6.5), 1 M sodium acrylate, and 41 μM ^{RAFT}ferritin was prepared in a 6 mL glass vial with a stir bar and sealed with a septum. The solution was degassed under a N_2 atmosphere. 50 μL of a degassed 50 mM stock solution of VA-044 was added, and the polymerization reaction stirred for 24 h at either room temperature or 40 °C. After 24 h, a 100-μL aliquot was removed, exposed to air to quench the polymerization, and diluted to 2 mL with water. A control sample was prepared identically, except that the 41 μM ^{RAFT}ferritin was replaced with 41 μM $^{\Delta C}$ferritin and 1 mM R1.

2.5.9 Graft-from polymerization with free ^{RAFT}ferritin initiated with APS/TEMED.

A 300 μL solution containing ^{RAFT}ferritin (41 μM), APS (1% (w/v)), TEMED (1% (v/v)), and sodium acrylate (1 M) was prepared and stirred for 5 min. Unreacted sodium acrylate, APS, TEMED, and short polymer chains were removed and replaced with water using a 30 kDa MWCO spin concentrator. A control sample was prepared identically, except that the 41 μM ^{RAFT}ferritin was replaced with 41 μM $^{\Delta C}$ferritin and 1 mM R1.

2.5.10 Gel permeation chromatography.

Samples for GPC prepared in solution (described above) were all filtered through a 22 μm syringe filter (Pall Corporation) and loaded into an Agilent 1260 Infinity HPLC or Hitachi

Chromaster system equipped with an RI detector. Both systems were connected to 2 sequential 8-μm, mixed bed, 300 x 7.5 mm PL aquagel-OH mixed medium columns (Agilent Technologies) run in the aqueous phase, 0.2 M $NaNO_3$ and 0.01 M NaH_2PO_4 (pH 7.0), at 1 mL/min. The resulting chromatograms are shown in Figures S4 and S11.

2.5.11 Preparation of sodium acrylate-infused ferritin crystals.

Protein crystals were formed through sitting drop vapor diffusion. The conditions that gave octahedron- or rhombohedron-shaped crystals are detailed in Table 2.2. Smaller crystals could also be formed in larger quantities without a reservoir solution. After ferritin crystal formation (which takes 1-2 days), both the well and reservoir solutions were replaced with a solution containing 60 mM $CaCl_2$, 1 M sodium acrylate, and either 25 mM MES (pH 6.5) or 12.5 mM HEPES (pH 8.0). The trigonal ferritin crystals were soaked in a solution consisting of a 1:1 mixture of 2 M sodium acrylate and the reservoir solution. All crystals were soaked for >12 h to ensure complete monomer infusion.

2.5.12 Monitoring of the expansion and contraction of PIX with light microscopy.

Single crystals were transferred with a mounted CryoLoop onto a glass slide with a microscopic ruler (OMAX). All images and videos were obtained on an SZX7 (Olympus) microscope equipped with an Infinity 1 CCD (Lumenera). A 10-μL solution containing 4 M NaCl, 1% (w/v) APS, and 1% (v/v) TEMED was added to the crystal. After 5 min of polymerization, the crystal was removed with a Cryoloop and placed on a clean glass slide. Water (10 μL) was added to the crystal to initiate the expansion of the PIX. The expansion was monitored for 5 to 20 min, depending on the sample. To initiate contraction, 10 μL of either 4 M NaCl or 1 M $CaCl_2$ was carefully injected into the solution containing the crystal. Reversible expansion-contraction could be repeated if NaCl was used to induce crystal contraction. Crystal size was determined by

measuring the edge length of a facet relative to the microscopic ruler using the Fiji image processing package.

2.5.13 Polymerization of sodium acrylate-infused ferritin crystals initiated with VA-044.

After soaking the ferritin crystals in the sodium acrylate solution (as described above), the well and reservoir were replaced with a solution containing 4 M NaCl, 0.2% (w/v) VA-044, and 25 mM MES (pH 6.5). The tray was transferred into an anaerobic tent. After 48 h the crystal trays were removed and exposed to an aerobic environment to quench polymerization and expansion/contraction was monitored as described above.

2.5.14 Monitoring of pyranine fluorescence during *in-crystallo* polymerization.

Both cubic and rhombohedral ^{RAFT}ferritin crystals were soaked in the 1 M sodium acrylate solution supplemented with 10 mM (0.5%) pyranine (Sigma-Aldrich). After 24 h, one single crystal was transferred onto a glass slide, and polymerization was initiated by adding 30 µL of 1% (w/v) APS, and 1% (v/v) TEMED in 4 M NaCl. Hydrogel polymerization throughout the crystal and the corresponding decrease of pyranine fluorescence was monitored with a 10x air objective on the confocal microscope as described above, using a filter to collect light at 500–550 nm (green channel). DIC and fluorescence (488 nm excitation) images were captured at 2-s intervals with 100-ms (DIC) and 100-ms (fluorescence) exposures.

2.5.15 Assessment of *in-crystallo* graft-from polymerization initiated with VA-044.

Cubic and rhombohedral ferritin crystals were prepared in 24-well culture plates without a reservoir solution. After two days, the crystals were harvested and collected into 1.5 mL Eppendorf tubes. The resulting supernatant was discarded, and 200 µL of the sodium acrylate solution (described above) was added. After soaking for > 12 h, small portions of the crystal pellet (~7 µL each) were aliquoted into 0.65 mL Eppendorf tubes and transferred into an anaerobic tent. 75 µL

of a solution containing 60 mM $CaCl_2$, 0.2% (w/v) VA-044, and 25 mM MES (pH 6.5) was added to each tube to initiate polymerization. The tubes were placed on a heat block at 40 °C. Each sample was taken out of the tent and exposed to air at predetermined timepoints. The contents of each tube were transferred into a well of a 24-well culture plate. A 200 µL solution containing 25 mM EDTA (pH 7.0) was added into each well to dissolve the crystals. The plate was placed on a gel rocker >12 h and then analyzed by GPC as described above.

2.5.16 Assessment of *in-crystallo* graft-from polymerization initiated with APS/TEMED.

Ferritin crystals were prepared and transferred into a sodium acrylate solution, as described above. These crystals were then incubated with a 200 µL solution containing 4 M NaCl, 1% (w/v) APS, and 1% (v/v) TEMED. After 5 min, the crystals were pelleted, and the supernatant was discarded. Crystals were dissolved as described above and analyzed with GPC.

2.5.17 Expansion of PIX monitored using SAXS.

Both cubic and rhombohedral ^{RAFT}ferritin crystals were prepared and transferred into the sodium acrylate solution as described above. After soaking for 24 h, multiple crystals (n>100) were transferred to an Eppendorf tube. The crystals settled to the bottom overnight and were transferred, along with 50 µL of sodium acrylate solution, into 1.5-mm quartz capillaries (Hampton). The capillaries were sealed with molding clay. The ^{RAFT}ferritin crystals in capillaries were analyzed at beamline 4-2 of the Stanford Synchrotron Radiation Lightsource (SLAC National Accelerator Laboratory). Data were collected using collimated X-ray radiation (1.127 Å, 11 keV) calibrated with a silver behenate standard. Polymerization was initiated in-situ by the X-ray irradiation (1.5 s exposure), and images were collected every 6 s for up to 20 min. It is important to note that in this procedure, “polymerized” crystals immediately began expanding upon the commencement of data collection. SAXS measurements and polymerization occurred

concomitantly. Scattered radiation was detected using a Rayonix225HE detector, and one-dimensional scattering data were obtained through azimuthal averaging of the two-dimensional data to produce plots of the scattering intensity as a function of the scattering vector length, $q=4\pi\sin(\theta/\lambda)$, where θ is one-half of the scattering angle and λ is the wavelength of the X-rays used. Analysis of the one-dimensional data was performed using the powder diffraction processing software JADE (MDI).

2.5.18 Single-crystal X-ray diffraction of ferritin crystals at 100K.

Crystals were prepared and imaged using light microscopy, as described above. Single-crystal XRD data for the cubic, rhombohedral, and trigonal ferritin crystals were collected at 100 K at beamline 12-2 of SSRL, beamline 502 of ALS, and beamline 9-2 of SSRL. The data were integrated using iMosflm[58] and scaled with Aimless.[59] The structures for cubic, rhombohedral, acrylate-infused rhombohedral, and acrylate-infused trigonal ferritin crystals were determined at resolutions 1.25 Å, 2.27 Å, 2.22 Å, and 2.70 Å, respectively. Molecular replacement was performed with Phaser[60] using the ferritin structure (PDB ID, 6B8F) as a search model. Rigid-body, positional, thermal, TLS, and atom-occupancy refinements were carried out using Phenix.[61] Coot[62] was used for iterative manual model building. All figures were produced with Pymol[63] or ChimeraX.[64]

2.5.19 Single-crystal X-ray diffraction of ^{RAFT}ferritin crystals at 298K.

^{RAFT}ferritin crystals were prepared as described above. A single crystal (>100 μm) was harvested using a mounted CryoLoop and transferred into a 0.1 mm special glass capillary (Hampton) loaded with 20 μL of the reservoir solution. The diameter of the capillary was smaller than the width of the selected crystal. The bottom 1/3 of the crystal loaded capillary was removed, and mild centrifugal force was applied to trap the crystal between the walls of the capillary. The

ends of the capillary were sealed with clay, and the capillary was mounted onto an APEX II CCD diffractometer (Bruker) with Cu Kα radiation (1.5418 Å). Images were analyzed with the Apex III software (Bruker).

2.5.20 Indexing of the crystal facets for rhombohedral and trigonal ferritin crystals.

Rhombohedral and trigonal ferritin crystals were harvested with a mounted CryoLoop, cryoprotected with perfluoropolyether, and mounted onto an APEX II CCD diffractometer (Bruker) with Cu Kα radiation (1.5418 Å). Three sets of three images (30 s exposures, 1° ϕ rotation per image) were collected at starting at three different ϕ positions (0°, 60°, and 120°). Additionally, a 360° video was captured. The orientation matrix was determined through the XRD images and mapped onto the crystal facets using the Apex III software (Bruker).

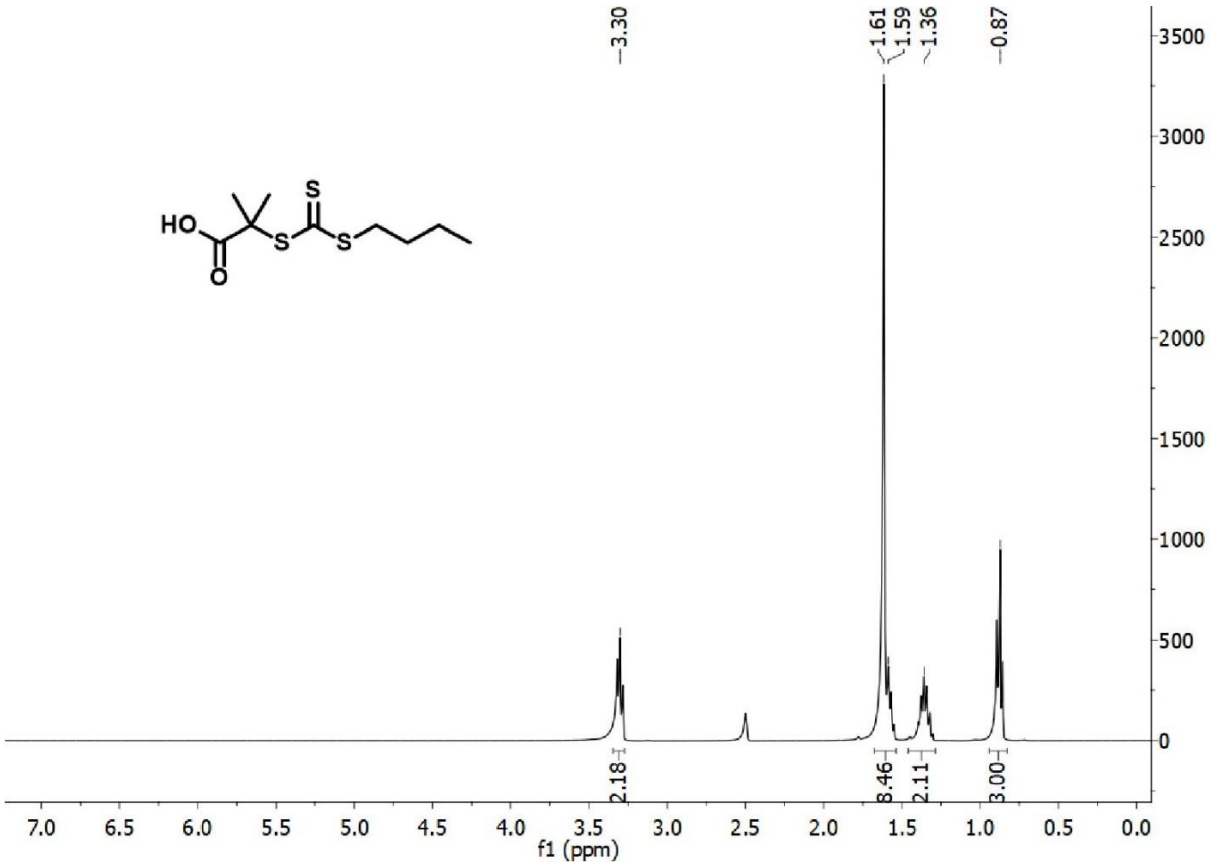

Figure 2.18. ^{1}H NMR spectrum of 2-(((butylthio)carbonothioyl)thio)-2-methylpropanoic acid (**R1**) in DMSO-d_6.

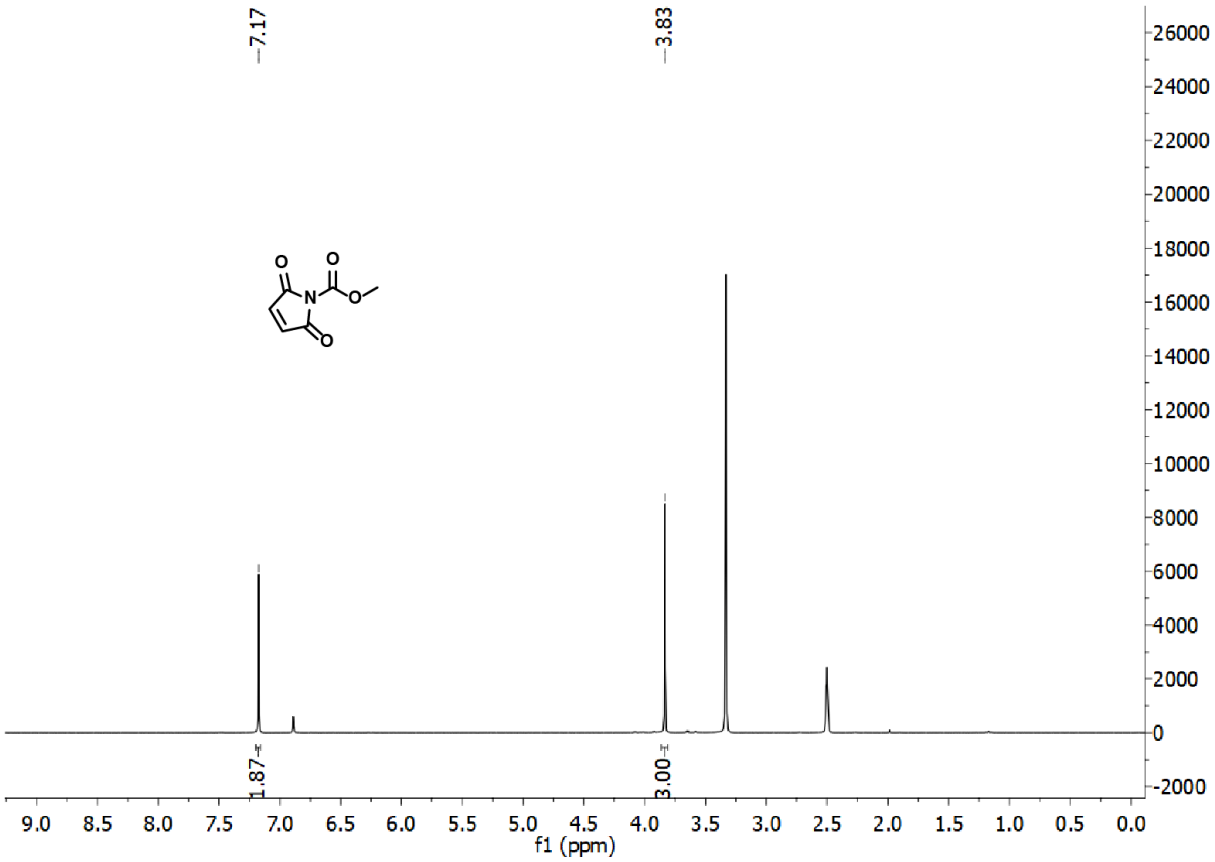

Figure 2.19. ^{1}H NMR spectrum of N-(Methoxycarbonyl)maleimide (NMCM) in DMSO-d_6.

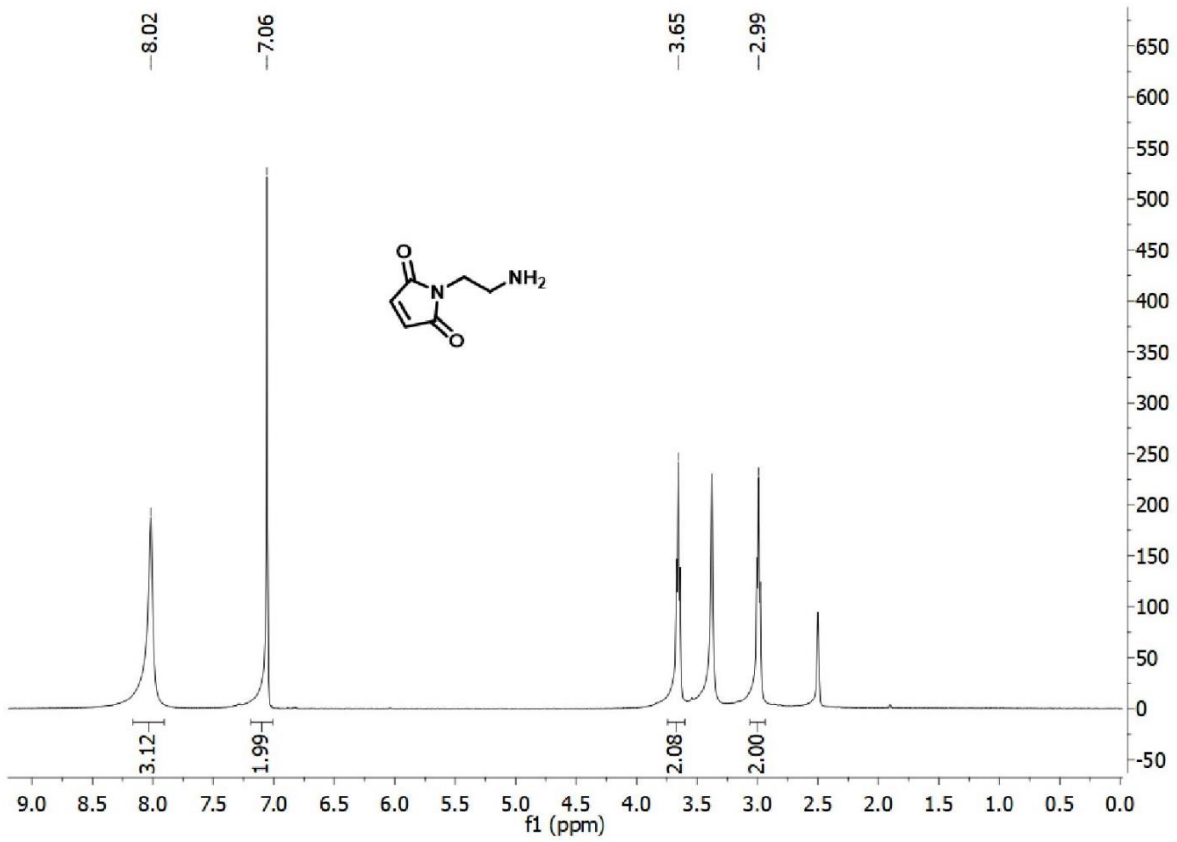

Figure 2.20. ^{1}H NMR spectrum of N-(2-aminoethyl)-maleimide in DMSO-d_6.

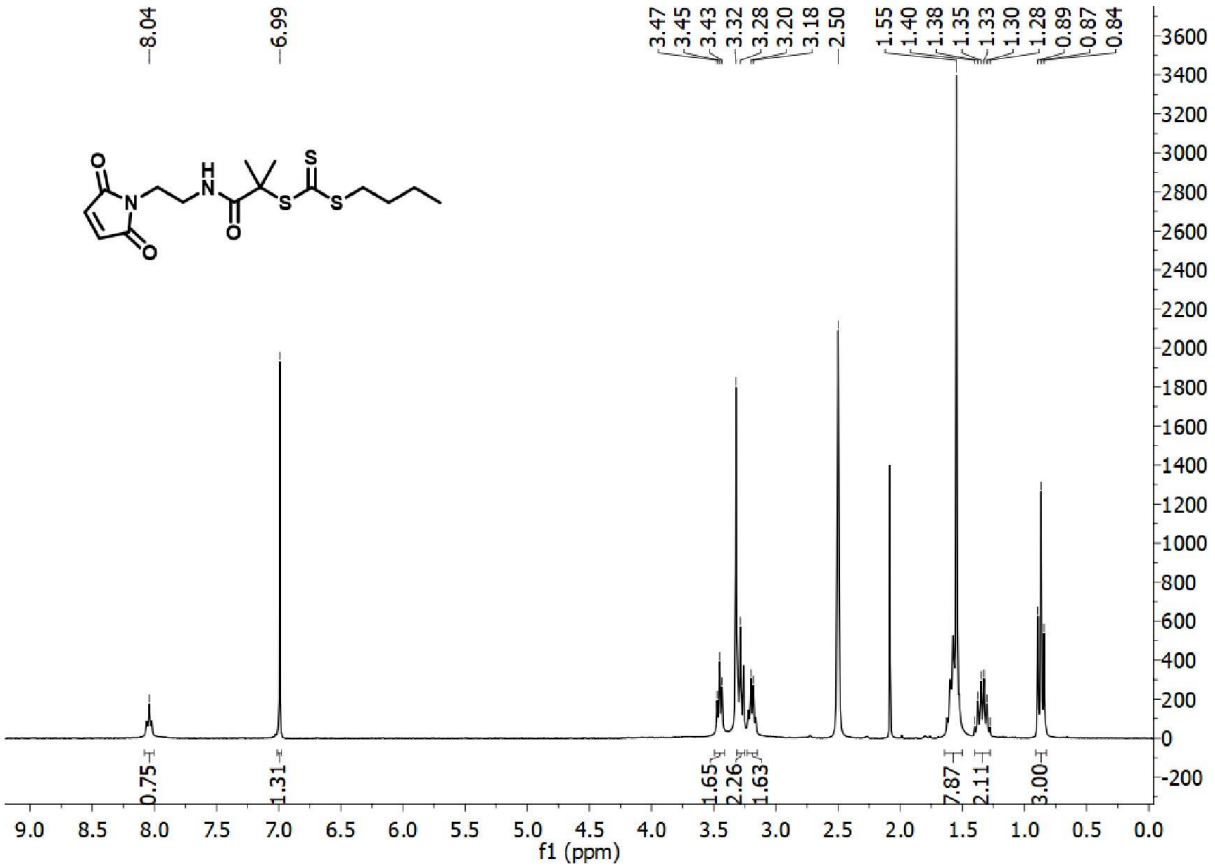

Figure 2.21. ^{1}H NMR spectrum of **R2** in DMSO-d_6.

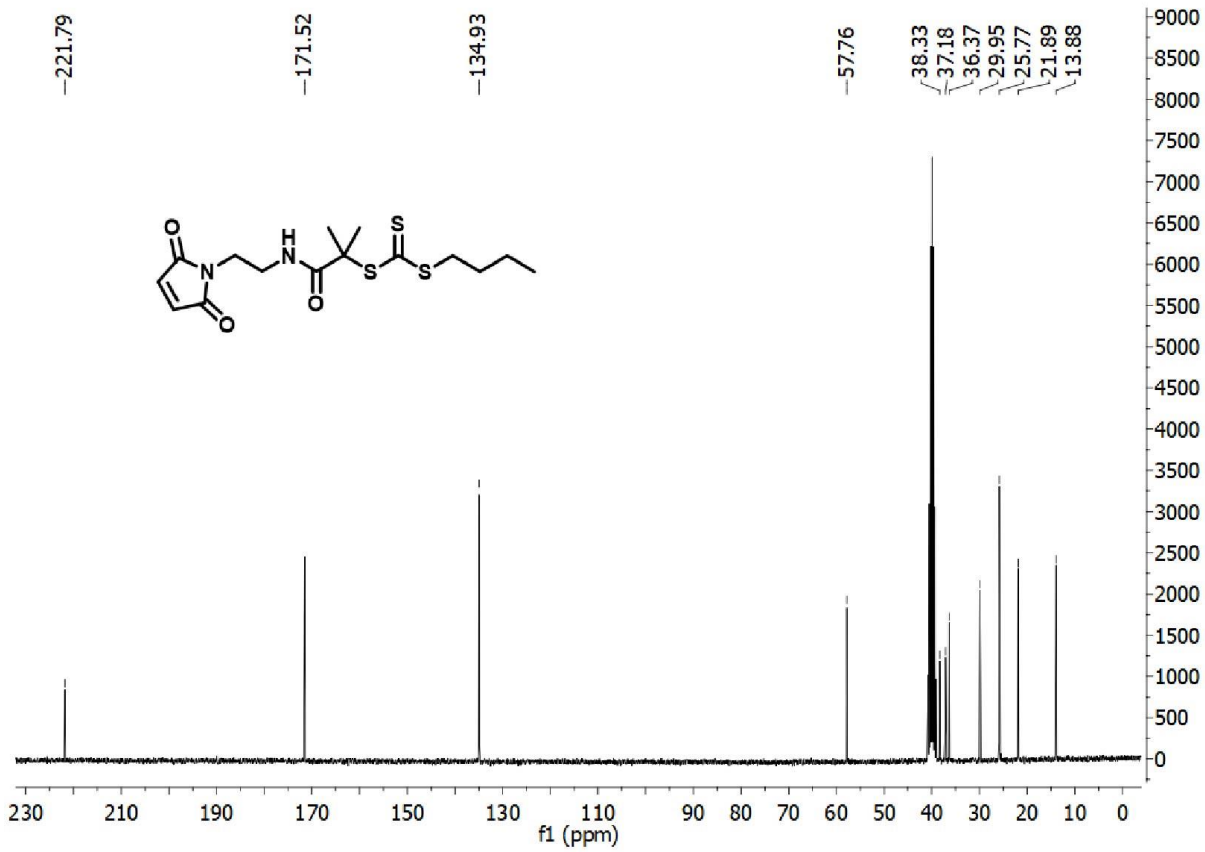

Figure 2.22. ^{13}C NMR spectrum of **R2** in DMSO-d_6.

Table 2.1 Primers for site-directed mutagenesis.

Variant	Mutation	Primer Sequence
157C ΔC*	K157C	5'-CCAACCTGCGTTGCATGGGTGCACC-3' 5'-GGTGCACCCATGCAACGCAGGTTGG-3'

Table 2.2 Self-assembly conditions for: (1) cubic (*F*432) and rhombohedral (*H*32) ^{RAFT}ferritin crystals and (2) trigonal ($P3_121$) and cubic (*F*432) $^{\Delta C}$ferritin crystals.

*F*432 ^{RAFT}ferritin	Stock protein solution	25 µM in 15 mM HEPES (pH 7.0)
	Reservoir	500 µL total volume: 25 mM HEPES (pH 8.0), 10 mM $CaCl_2$, 140 mM NaCl
	Sitting drop	5 µL reservoir, 5 µL of 25 µM ^{RAFT}ferritin
*H*32 ^{RAFT}ferritin	Stock protein solution	25 µM in 15 mM HEPES (pH 7.0)
	Reservoir	500 µL total volume: 50 mM MES (pH 6.5), 6 mM $CaCl_2$
	Sitting drop	5 µL reservoir, 5 µL of 25 µM ^{RAFT}ferritin
$P3_121$ $^{\Delta C}$ferritin	Stock protein solution	25 µM in 50 mM Tris (pH 7.5), 1 M NaCl
	Reservoir	525 µL total volume: 100 µL of 500 mM HEPES (pH 7.0), 125 µL of 1 M NH_4OAc, 300 µL 2-Methyl-2,4-pentanediol
	Sitting drop	5 µL reservoir, 5 µL of 25 µM $^{\Delta C}$ferritin
*F*432 $^{\Delta C}$ferritin	Stock protein solution	25 µM in 150 mM Tris (pH 7.4), 150 mM NaCl
	Reservoir	500 µL total volume: 50 mM HEPES (pH 7.0), 12 mM $CaCl_2$
	Sitting drop	5 µL reservoir, 5 µL of 25 µM $^{\Delta C}$ferritin

Table 2.3 X-ray data collection and refinement statistics. Numbers in parentheses correspond to the highest resolution shell.

	Cubic ^{RAFT}ferritin (PDB: 6WYF)	**Rhombohedral ^{RAFT}ferritin (PDB: 6WYG)**	**Ac-infused rhombohedral ^{RAFT}ferritin (PBD: 6WYH)**	**Ac-infused trigonal $^{\Delta C*}$ferritin (PDB: 7K26)**
Data collection				
Space group	*F*432	*H*32	*H*32	$P3_121$
Cell dimensions				
a, *b* (Å)	179.94	126.810	128.880	131.57
c (Å)	179.94	281.285	291.810	306.65
α, β (°)	90	90	90	90
γ (°)	90	120	120	120
Resolution (Å)	54.25-1.25	93.76-2.27	97.27-2.22	91.44-2.70
No. unique reflections	64164	38783	46081	85108
Multiplicity	59.1 (20.7)	6.4 (6.2)	3.5 (3.1)	18.0 (19.1)
CC1/2	1.000 (0.791)	0.998 (0.843)	0.972 (0.571)	0.996 (0.744)
Rmerge	0.099 (1.322)	0.080 (1.488)	0.115 (0.662)	0.266 (2.012)
$\langle I / \sigma I \rangle$	29.5 (2.7)	12.6 (1.8)	4.4 (1.5)	8.5 (1.7)
Completeness (%)	93.0 (99.9)	95.7 (99.4)	99.4 (99.1)	99.8 (100)
Refinement				
R_{work} / R_{free}	0.113/0.131	0.209/0.260	0.193/0.245	0.198/0.254
No. atoms				
Protein	1480	5484	5652	16859
Ligand/ion	38	49	53	75
Water	329	269	695	366
B-factors (Å^2)				
Protein	12.84	55.74	30.12	59.65
Ligand/ion	42.95	73.40	57.57	66.26
Water	30.04	48.51	37.12	48.75
R.m.s. deviations				
Bond lengths (Å)	0.009	0.008	0.004	0.005
Bond angles (°)	1.065	0.902	0.613	0.733
MolProbity[65] score	1.27	1.35	1.03	1.44
Clashscore	5.08	5.11	2.18	5.23
Ramachandran plot (%)				
Favored	98.82	97.65	97.80	97.09
Outliers	0.00	0.15	0.29	0.15
Rotamers (%)				
Favored	96.25	89.03	92.98	87.99
Poor	0.62	0.18	0.17	0.06

2.6 Acknowledgements

We thank the following colleagues for assistance: R. Alberstein and R. Subramanian for data processing and helpful discussions; A. Rheingold, H. Nguyen, and M. Gembicky for XRD; I. Rajkovic for SAXS; W.J. Rappel for confocal microscopy. This work was primarily funded by the US Army Research Office (W911NF-19-1-0228). Additional funding was provided by US Department of Energy (BES, Division of Materials Sciences, Biomolecular Materials Program, DE-SC0003844) for SAXS studies and the initial development of the PIX concept. Crystallographic data were collected at Stanford Synchrotron Radiation Lightsource (SSRL), Advanced Light Source (ALS) and the Crystallography Facility of the University of California, San Diego. SAXS data were collected at SSRL. SSRL and ALS are supported by the DOE Office of Science, Office of Basic Energy Sciences under contracts DE-AC02-76SF00515 and DE-AC02-05CH11231, respectively.

Chapter 2 is reproduced, in part, with permission, from: Han, K., Bailey, J. B., Zhang, L., Tezcan, F. A. "Anisotropic Dynamics and Mechanics of Macromolecular Crystals Containing Lattice-Patterned Polymer Networks" *Journal of the American Chemical Society* **2020** *142* (45), 19402-19410. The dissertation author was the primary author on all reprinted materials.

2.7 References

1. Zhang, L.; Bailey, J. B.; Subramanian, R. H.; Groisman, A.; Tezcan, F. A., Hyperexpandable, self-healing macromolecular crystals with integrated polymer networks. *Nature* **2018,** *557*, 86-91.

2. Seeman, N. C.; Belcher, A. M., Emulating biology: Building nanostructures from the bottom up. *Proc. Natl. Acad. Sci. USA* **2002,** *99*, 6451-6455.

3. Kushner, A. M.; Guan, Z., Modular Design in Natural and Biomimetic Soft Materials. *Angew. Chem. Int. Ed.* **2011,** *50*, 9026-9057.

4. Barthelat, F.; Yin, Z.; Buehler, M. J., Structure and mechanics of interfaces in biological materials. *Nat. Rev. Mater.* **2016,** *1*, 16007.

5. Buehler, M. J.; Yung, Y. C., Deformation and failure of protein materials in physiologically extreme conditions and disease. *Nat. Mater.* **2009,** *8*, 175-188.

6. Naumov, P.; Chizhik, S.; Panda, M. K.; Nath, N. K.; Boldyreva, E., Mechanically Responsive Molecular Crystals. *Chem. Rev.* **2015,** *115*, 12440-12490.

7. Sato, O., Dynamic molecular crystals with switchable physical properties. *Nat. Chem.* **2016,** *8*, 644-656.

8. Suzuki, Y.; Cardone, G.; Restrepo, D.; Zavattieri, P. D.; Baker, T. S.; Tezcan, F. A., Self-assembly of coherently dynamic, auxetic, two-dimensional protein crystals. *Nature* **2016,** *533*, 369-373.

9. Alberstein, R.; Suzuki, Y.; Paesani, F.; Tezcan, F. A., Engineering the entropy-driven free-energy landscape of a dynamic nanoporous protein assembly. *Nat. Chem.* **2018,** *10*, 732-739.

10. Horike, S.; Shimomura, S.; Kitagawa, S., Soft porous crystals. *Nat. Chem.* **2009,** *1*, 695-704.

11. Schneemann, A.; Bon, V.; Schwedler, I.; Senkovska, I.; Kaskel, S.; Fischer, R. A., Flexible metal–organic frameworks. *Chem. Soc. Rev.* **2014,** *43*, 6062-6096.

12. Ghosh, S.; Reddy, C. M., Elastic and Bendable Caffeine Cocrystals: Implications for the Design of Flexible Organic Materials. *Angew. Chem. Int. Ed.* **2012,** *51*, 10319-10323.

13. Karothu, D. P.; Mahmoud Halabi, J.; Li, L.; Colin-Molina, A.; Rodríguez-Molina, B.; Naumov, P., Global Performance Indices for Dynamic Crystals as Organic Thermal Actuators. *Adv. Mater.*, 1906216.

14. Kobatake, S.; Takami, S.; Muto, H.; Ishikawa, T.; Irie, M., Rapid and reversible shape changes of molecular crystals on photoirradiation. *Nature* **2007,** *446*, 778-781.

15. Mason, J. A.; Oktawiec, J.; Taylor, M. K.; Hudson, M. R.; Rodriguez, J.; Bachman, J. E.;

Gonzalez, M. I.; Cervellino, A.; Guagliardi, A.; Brown, C. M., Methane storage in flexible metal–organic frameworks with intrinsic thermal management. *Nature* **2015,** *527*, 357-361.

16. Sato, H.; Kosaka, W.; Matsuda, R.; Hori, A.; Hijikata, Y.; Belosludov, R. V.; Sakaki, S.; Takata, M.; Kitagawa, S., Self-Accelerating CO Sorption in a Soft Nanoporous Crystal. *Science* **2014,** *343*, 167-170.

17. Couck, S.; Denayer, J. F. M.; Baron, G. V.; Rémy, T.; Gascon, J.; Kapteijn, F., An Amine-Functionalized MIL-53 Metal−Organic Framework with Large Separation Power for CO_2 and CH_4. *J. Am. Chem. Soc.* **2009,** *131*, 6326-6327.

18. Chen, Q.; Chang, Z.; Song, W. C.; Song, H.; Song, H. B.; Hu, T. L.; Bu, X. H., A controllable gate effect in cobalt (II) organic frameworks by reversible structure transformations. *Angew. Chem. Int. Ed.* **2013,** *52*, 11550-11553.

19. Takashima, Y.; Martínez, V. M.; Furukawa, S.; Kondo, M.; Shimomura, S.; Uehara, H.; Nakahama, M.; Sugimoto, K.; Kitagawa, S., Molecular decoding using luminescence from an entangled porous framework. *Nat. Commun.* **2011,** *2*, 168.

20. McKinlay, A. C.; Eubank, J. F.; Wuttke, S.; Xiao, B.; Wheatley, P. S.; Bazin, P.; Lavalley, J. C.; Daturi, M.; Vimont, A.; De Weireld, G.; Horcajada, P.; Serre, C.; Morris, R. E., Nitric Oxide Adsorption and Delivery in Flexible MIL-88(Fe) Metal–Organic Frameworks. *Chem. Mater.* **2013,** *25*, 1592-1599.

21. Chen, Q.; Chang, Z.; Song, W.-C.; Song, H.; Song, H.-B.; Hu, T.-L.; Bu, X.-H., A Controllable Gate Effect in Cobalt(II) Organic Frameworks by Reversible Structure Transformations. *Angew. Chem. Int. Ed.* **2013,** *52*, 11550-11553.

22. Panda, M. K.; Ghosh, S.; Yasuda, N.; Moriwaki, T.; Mukherjee, G. D.; Reddy, C. M.; Naumov, P., Spatially resolved analysis of short-range structure perturbations in a plastically bent molecular crystal. *Nat Chem* **2015,** *7*, 65-72.

23. Serre, C.; Mellot-Draznieks, C.; Surblé, S.; Audebrand, N.; Filinchuk, Y.; Férey, G., Role of Solvent-Host Interactions That Lead to Very Large Swelling of Hybrid Frameworks. *Science* **2007,** *315*, 1828-1831.

24. Worthy, A.; Grosjean, A.; Pfrunder, M. C.; Xu, Y.; Yan, C.; Edwards, G.; Clegg, J. K.; McMurtrie, J. C., Atomic resolution of structural changes in elastic crystals of copper(II) acetylacetonate. *Nat Chem* **2018,** *10*, 65-69.

25. Commins, P.; Al-Handawi, M. B.; Karothu, D. P.; Raj, G.; Naumov, P., Efficiently self-healing boronic ester crystals. *Chem. Sci.* **2020,** *11*, 2606-2613.

26. Commins, P.; Hara, H.; Naumov, P., Self-Healing Molecular Crystals. *Angew. Chem. Int. Ed.* **2016,** *55*, 13028-13032.

27. Wei, Y.-S.; Chen, K.-J.; Liao, P.-Q.; Zhu, B.-Y.; Lin, R.-B.; Zhou, H.-L.; Wang, B.-Y.; Xue, W.; Zhang, J.-P.; Chen, X.-M., Turning on the flexibility of isoreticular porous coordination

frameworks for drastically tunable framework breathing and thermal expansion. *Chem. Sci.* **2013,** *4*, 1539-1546.

28. Pang, J.; Wu, M.; Qin, J.-S.; Liu, C.; Lollar, C. T.; Yuan, D.; Hong, M.; Zhou, H.-C., Solvent-Assisted, Thermally Triggered Structural Transformation in Flexible Mesoporous Metal–Organic Frameworks. *Chem. Mater.* **2019,** *31*, 8787-8793.

29. Zhang, Y. S.; Khademhosseini, A., Advances in engineering hydrogels. *Science* **2017,** *356*, eaaf3627.

30. Jeon, S.-J.; Hauser, A. W.; Hayward, R. C., Shape-Morphing Materials from Stimuli-Responsive Hydrogel Hybrids. *Acc. Chem. Res.* **2017,** *50*, 161-169.

31. Theil, E. C., Ferritin: structure, gene regulation, and cellular function in animals, plants, and microorganisms. *Ann. Rev. Biochem.* **1987,** *56*, 289-315.

32. Huard, D. J.; Kane, K. M.; Tezcan, F. A., Re-engineering protein interfaces yields copper-inducible ferritin cage assembly. *Nat. Chem. Biol* **2013,** *9*, 169-76.

33. Lawson, D. M.; Artymiuk, P. J.; Yewdall, S. J.; Smith, J. M.; Livingstone, J. C.; Treffry, A.; Luzzago, A.; Levi, S.; Arosio, P.; Cesareni, G.; Thomas, C. D.; Shaw, W. V.; Harrison, P. M., Solving the structure of human H ferritin by genetically engineering intermolecular crystal contacts. *Nature* **1991,** *349*, 541-4.

34. Sano, K.; Ishida, Y.; Aida, T., Synthesis of Anisotropic Hydrogels and Their Applications. *Angew. Chem. Int. Ed.* **2018,** *57*, 2532-2543.

35. Park, N.; Kim, J., Hydrogel-Based Artificial Muscles: Overview and Recent Progress. *Adv. Intell. Sys.* **2020,** *2*, 1900135.

36. Chiefari, J.; Chong, Y. K.; Ercole, F.; Krstina, J.; Jeffery, J.; Le, T. P. T.; Mayadunne, R. T. A.; Meijs, G. F.; Moad, C. L.; Moad, G.; Rizzardo, E.; Thang, S. H., Living Free-Radical Polymerization by Reversible Addition−Fragmentation Chain Transfer: The RAFT Process. *Macromolecules* **1998,** *31*, 5559-5562.

37. Boyer, C.; Bulmus, V.; Davis, T. P.; Ladmiral, V.; Liu, J.; Perrier, S., Bioapplications of RAFT Polymerization. *Chem. Rev.* **2009,** *109*, 5402-5436.

38. De, P.; Li, M.; Gondi, S. R.; Sumerlin, B. S., Temperature-Regulated Activity of Responsive Polymer−Protein Conjugates Prepared by Grafting-from via RAFT Polymerization. *J. Am. Chem. Soc.* **2008,** *130*, 11288-11289.

39. Cobo, I.; Li, M.; Sumerlin, B. S.; Perrier, S., Smart hybrid materials by conjugation of responsive polymers to biomacromolecules. *Nat. Mater.* **2015,** *14*, 143-159.

40. Akcora, P.; Liu, H.; Kumar, S. K.; Moll, J.; Li, Y.; Benicewicz, B. C.; Schadler, L. S.; Acehan, D.; Panagiotopoulos, A. Z.; Pryamitsyn, V.; Ganesan, V.; Ilavsky, J.; Thiyagarajan, P.; Colby, R. H.; Douglas, J. F., Anisotropic self-assembly of spherical polymer-grafted nanoparticles.

Nat. Mater. **2009,** *8*, 354-359.

41. Lu, C.; Urban, M. W., Stimuli-responsive polymer nano-science: Shape anisotropy, responsiveness, applications. *Prog. Polymer Sci.* **2018,** *78*, 24-46.

42. Yu, Y.; Nakano, M.; Ikeda, T., Directed bending of a polymer film by light. *Nature* **2003,** *425*, 145-145.

43. Jiang, S.; Liu, F.; Lerch, A.; Ionov, L.; Agarwal, S., Unusual and Superfast Temperature-Triggered Actuators. *Adv. Mater.* **2015,** *27*, 4865-4870.

44. Erb, R. M.; Sander, J. S.; Grisch, R.; Studart, A. R., Self-shaping composites with programmable bioinspired microstructures. *Nat. Commun.* **2013,** *4*, 1712.

45. Liu, M.; Ishida, Y.; Ebina, Y.; Sasaki, T.; Hikima, T.; Takata, M.; Aida, T., An anisotropic hydrogel with electrostatic repulsion between cofacially aligned nanosheets. *Nature* **2015,** *517*, 68-72.

46. Chin, S. M.; Synatschke, C. V.; Liu, S.; Nap, R. J.; Sather, N. A.; Wang, Q.; Álvarez, Z.; Edelbrock, A. N.; Fyrner, T.; Palmer, L. C.; Szleifer, I.; Olvera de la Cruz, M.; Stupp, S. I., Covalent-supramolecular hybrid polymers as muscle-inspired anisotropic actuators. *Nat. Commun.* **2018,** *9*, 2395.

47. Qin, H.; Zhang, T.; Li, N.; Cong, H.-P.; Yu, S.-H., Anisotropic and self-healing hydrogels with multi-responsive actuating capability. *Nat. Commun.* **2019,** *10*, 2202.

48. Yu, J.; Wang, Q.; O'Hare, D.; Sun, L., Preparation of two dimensional layered double hydroxide nanosheets and their applications. *Chem. Soc. Rev.* **2017,** *46*, 5950-5974.

49. Chen, J.; Leung, F. K.-C.; Stuart, M. C. A.; Kajitani, T.; Fukushima, T.; van der Giessen, E.; Feringa, B. L., Artificial muscle-like function from hierarchical supramolecular assembly of photoresponsive molecular motors. *Nat. Chem.* **2018,** *10*, 132-138.

50. Iwaso, K.; Takashima, Y.; Harada, A., Fast response dry-type artificial molecular muscles with [c2]daisy chains. *Nat. Chem.* **2016,** *8*, 625-632.

51. Fratzl, P.; Weinkamer, R., Nature's hierarchical materials. *Prog. Mater. Sci.* **2007,** *52*, 1263-1334.

52. Espinosa, H. D.; Rim, J. E.; Barthelat, F.; Buehler, M. J., Merger of structure and material in nacre and bone – Perspectives on de novo biomimetic materials. *Prog. Mater. Sci.* **2009,** *54*, 1059-1100.

53. Huard, D. J. E.; Kane, K. M.; Tezcan, F. A., Re-engineering protein interfaces yields copper-inducible ferritin cage assembly. *Nat. Chem. Biol*. **2013**, 9 (3), 169-176.

54. Sontz, P. A.; Bailey, J. B.; Aln, S.; Tezcan, F. A., A Metal Organic Framework with Spherical Protein Nodes: Rational Chemical Design of 3D Protein Crystals. *J. Am. Chem. Soc.*

2015, 137 (36), 11598-11601.

55. Jia, Z. F.; Bobrin, V. A.; Truong, N. P.; Gillard, M.; Monteiro, M. J., Multifunctional Nanoworms and Nanorods through a One-Step Aqueous Dispersion Polymerization. *J. Am. Chem. Soc.* **2014**, 136 (16), 5824-5827.

56. Keller, O.; Rudinger, J., Preparation and Some Properties of Maleimido Acids and Maleoyl Derivatives of Peptides. *Helv. Chim. Acta* **1975**, 58 (2), 531-541.

57. Uehara, T.; Rokugawa, T.; Kinoshita, M.; Nemoto, S.; Lazaro, G. G. F.; Hanaoka, H.; Arano, Y., Ga-67/68-Labeling Agent That Liberates Ga-67/68-NOTA-Methionine by Lysosomal Proteolysis of Parental Low Molecular Weight Polypeptides to Reduce Renal Radioactivity Levels. *Bioconj. Chem.* **2014**, 25 (11), 2038-2045.

58. Battye, T. G. G.; Kontogiannis, L.; Johnson, O.; Powell, H. R.; Leslie, A. G. W., iMOSFLM: a new graphical interface for diffraction-image processing with MOSFLM. *Acta Crystallogr. D* **2011**, 67, 271-281.

59. Evans, P. R.; Murshudov, G. N., How good are my data and what is the resolution? *Acta Crystallogr. D* **2013**, 69, 1204-1214.

60. Mccoy, A. J.; Grosse-Kunstleve, R. W.; Adams, P. D.; Winn, M. D.; Storoni, L. C.; Read, R. J., Phaser crystallographic software. *J. Appl. Crystallogr*. **2007**, 40, 658-674.

61. Adams, P. D.; Afonine, P. V.; Bunkoczi, G.; Chen, V. B.; Davis, I. W.; Echols, N.; Headd, J. J.; Hung, L. W.; Kapral, G. J.; Grosse-Kunstleve, R. W.; McCoy, A. J.; Moriarty, N. W.; Oeffner, R.; Read, R. J.; Richardson, D. C.; Richardson, J. S.; Terwilliger, T. C.; Zwart, P. H., PHENIX: a comprehensive Python-based system for macromolecular structure solution. *Acta Crystallogr. D* **2010**, 66, 213-221.

62. Emsley, P.; Cowtan, K., Coot: model-building tools for molecular graphics. *Acta Crystallogr. Sect. D-Struct. Biol.* **2004**, 60, 2126-2132.

63. The PyMOL Molecular Graphics System Version 1.3, https://pymol.org/2/support.html (Schrödinger LLC).

64. Goddard, T. D.; Huang, C. C.; Meng, E. C.; Pettersen, E. F.; Couch, G. S.; Morris, J. H.; Ferrin, T. E., UCSF ChimeraX: Meeting modern challenges in visualization and analysis. *Prot. Sci.* **2018**, 27 (1), 14-25.

65. Chen, V. B.; Arendall, W. B. I.; Headd, J. J.; Keedy, D. A.; Immormino, R. M.; Kapral, G. J.; Murray, L. W.; Richardson, J. S.; Richardson, D. C., MolProbity: all-atom structure validation for macromolecular crystallography. *Acta Crystallogr. D* **2010**, 66, 12-21.

Chapter 3: Dynamic, Polymer-Integrated Crystals for Efficient, Reversible Protein Encapsulation

3.1 Abstract

Crystalline materials are increasingly being used as platforms for encapsulating proteins to create stable, functional materials. However, the uptake efficiencies and stimuli-responsiveness of crystalline frameworks are limited by their rigidities. We have recently reported a new form of materials, Polymer-Integrated Crystals (PIX), which combine the structural order of protein crystals with the dynamic, stimuli-responsive properties of synthetic polymers. Here we show that the crystallinity, flexibility and chemical tunability of PIX can be exploited to encapsulate guest proteins with high loading efficiencies (up to 46% w/w). The electrostatic host-guest interactions enable reversible, pH-controlled uptake/release of guest proteins as well as the mutual stabilization of the host and the guest, thus creating a uniquely synergistic platform toward the development of functional biomaterials and the controlled delivery of biological macromolecules.

3.2 Introduction

Proteins perform diverse biochemical functions (e.g., catalysis, binding, signal/energy transduction) with high efficiencies and specificities.[1-3] These functions, along with their inherent biocompatibility, have motivated the use of proteins in industrial, biotechnological and medical applications.[4-8] Yet, most of such applications involve conditions that can be quite different than the cellular environment and therefore require proteins to be modified, packaged in alternative forms or combined with carrier platforms to increase their stabilities while maintaining/augmenting their functions.[9-16] In these regards, encapsulation of proteins in synthetic, solid-state platforms, such as metal-organic frameworks (MOFs), hydrogen bonded-organic frameworks (HOFs), and porous protein crystals has emerged as a particularly promising

approach.[17-33] However, a limitation of crystalline materials–synthetic or biological–is that they are generally rigid and do not allow the penetration of guest proteins larger than the lattice pores.[34-35] As a result, most MOFs or protein crystals are not amenable to high-yield entrapment or stimuli-controlled release of guest proteins. It is possible to increase protein encapsulation yields through co-crystallization or protein-templated crystallization strategies.[22, 36-44] However, such strategies lead to the permanent immobilization of guest proteins within the lattice, as the release requires the irreversible dissolution of the material, thus limiting the recyclability of such systems and their applications in controlled delivery/uptake.[13, 45-49]

Alternatively, proteins have also been encapsulated in cross-linked gels, such as natural polymers and synthetic hydrogel systems.[50] The dynamic properties and tunable chemical functionalities of polymers are particularly advantageous for tailoring the responsive uptake/release of cargo.[51-52] However, such polymer-based systems often necessitate the modification of guest proteins into a non-native state, suffer from low yields of uptake and release (partly due to heterogeneous pore sizes), and exhibit weak mechanical strength.[53-56] A strong, porous material that exhibits the responsiveness and tailorability of polymers as well as the ability to reversibly uptake/release proteins in their native state with high efficiency would address the current limitations of both purely crystalline or purely polymeric systems.

To this end, we have sought here to employ dynamic crystalline materials as host systems for protein encapsulation. We recently introduced Polymer-Integrated Crystals (PIX) that consist of human heavy-chain ferritin (HuHF) crystals infused with polymer networks that endow the lattice with adaptive properties.[57] The HuHF crystals are formed through Ca^{2+}-mediated interactions between the 12-nm-diameter HuHF cages (**Figure 3.1**). This arrangement yields a mesoporous, face-centered-cubic lattice (*F*432, a = 18.1 nm), with discrete 6-nm-wide interstitial

chambers that are interconnected by 2-nm-wide channels. This continuous porosity allows permeation of small solutes (i.e., polymer precursors) and the subsequent formation of a uniform polyacrylate-co-acrylamide (pAAm) matrix throughout the lattice. Owing to the extensive non-covalent interactions between the resulting polymer matrix and the crystalline framework of HuHF-PIX, the crystals are not only highly thermo- and chemo-stable, but also highly flexible, capable of reversible, uniform expansion/contraction (up to 600% in volume) and efficient self-healing.[57-58] Remarkably, the polymer component accounts for only ~7% of the mass of HuHF-PIX (**Calculations 3.1**), which possess a modulus of ~1.2 GPa typical of protein/organic crystalline materials.[57] Yet, despite this high mechanical strength, HuHF-PIX exhibit the adaptive behavior typical of soft hydrogels, whereby their expansion can be induced by placing them in low-ionic strength solutions and reversed by the addition of cations (e.g., Na^+, Ca^{2+}) while preserving the crystalline structural integrity.

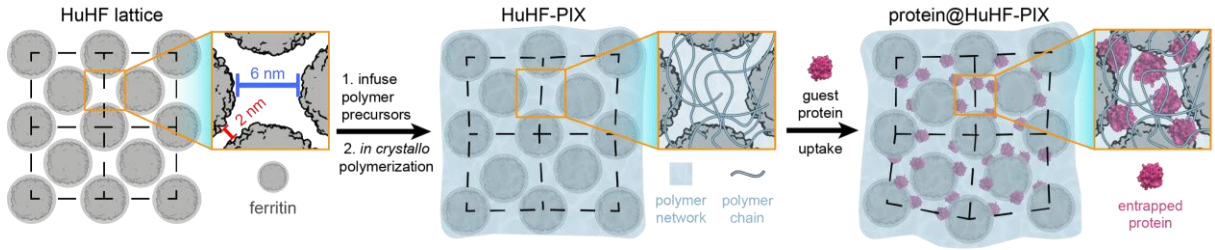

Figure 3.1. Schematic representation for the uptake of guest proteins in HuHF-PIX.

3.3 Results and Discussion

3.3.1 Preparation and Characterization of protein@HuHF-PIX

Given that both HuHF (*p*I = 5.1) and the pAAm matrix (*p*Ka ≤5) are negatively charged near neutral pH, we envisioned HuHF-PIX could sequester positively charged proteins such as equine cytochrome *c* (cyt-*c*, 12.4 kDa, *p*I = 10.3, dimensions = 2.5 x 2.5 x 3.5 nm) and hen egg-white lysozyme (14.3 kDa, *p*I = 11.4, dimensions = 3.0 x 3.0 x 5.0 nm). Importantly, both proteins

are larger than the 2-nm-wide interstitial channels, suggesting they should normally not be able to permeate the lattice. To examine protein uptake by HuHF-PIX, we used a standard set of conditions whereby HuHF-PIX crystals were placed in salt-free solutions of 200 mM cyt-*c* or rhodamine-labeled lysozyme, initially at pH 6.0 (**Figure 3.2**). Both proteins were sequestered by HuHF-PIX within minutes, with the total uptake saturating at 175 mM and 110 mM for cyt-*c* and lysozyme (limited by the amount of PIX used), respectively (**Figure 3.3a-b**). Through HPLC analysis, the loading capacity of HuHF-PIX was determined to be 26% w/w for both proteins, corresponding to estimated concentrations of 28.0 mM for cyt-*c* and 17.1 mM for lysozyme in the lattice interstices (**Figure 3.4 and Calculations 3.2 and 3.3**).

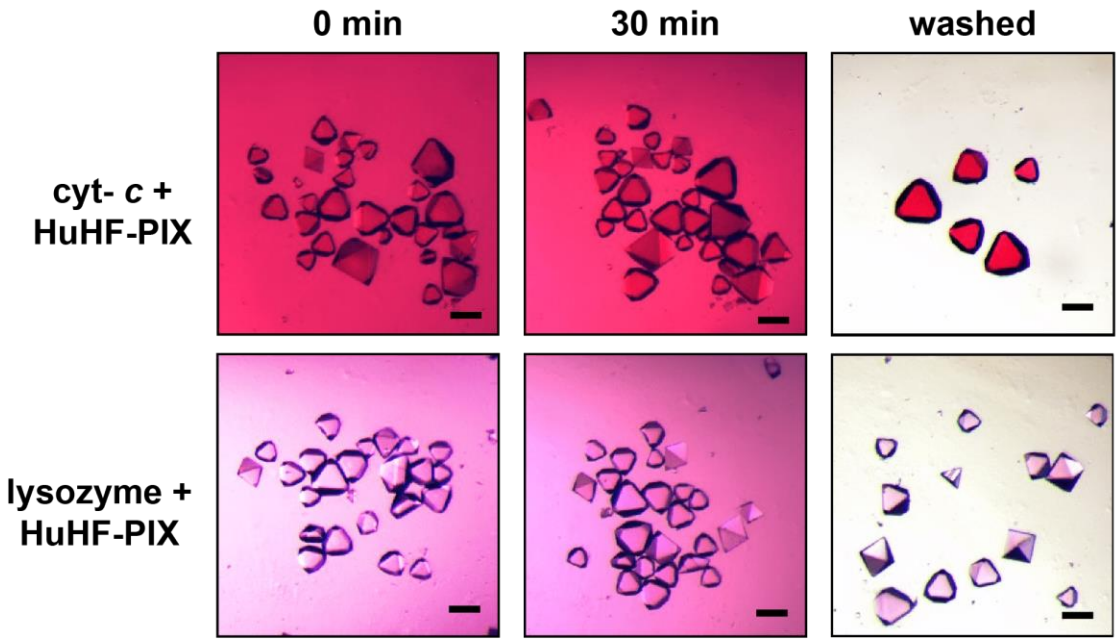

Figure 3.2. Light micrographs of HuHF-PIX samples incubated in a solution of rhodamine-labeled cyt-*c* (top) or lysozyme (bottom). The crystals were monitored over a 30-min period and subsequently washed. The resulting PIX become colored, indicating the guest protein absorption by PIX (see Figure 3.11 for confocal fluorescence images). Scale bars correspond to 100 μm.

Interestingly, despite the fact that the guest protein solutions did not contain Na^+ or Ca^{2+}, we did not observe substantial crystal expansion during incubation. This observation indicates that the positively charged cyt-*c* and lysozyme molecules act as polycations and prevent HuHF-PIX from expanding/dissolving. Small-angle X-ray scattering (SAXS) experiments showed that cyt-*c* loaded HuHF-PIX retained their crystallinity, whereby the unit cell dimensions increased by ~10% to a = 20.6 nm, corresponding to a volumetric increase of 45% (**Figure 3.3c**). As judged by the disappearance of Bragg peaks (**Figure 3.3c**) as well as the loss of single-crystal X-ray diffraction (**Figure 3.5**), lysozyme uptake disrupted the crystalline periodicity, likely owing to the larger size of lysozyme compared to cyt-*c*. Yet, the faceted morphology and structural integrity of HuHF-PIX were maintained (**Figures 3.3d, 3.8c and 3.6**). The overall negative charge of HuHF molecules was found to be critical for guest uptake: HuHF-PIX prepared with a more positively charged HuHF variant (^{POS}HuHF, *p*I = 6.7) did not sequester cyt-*c* or lysozyme at pH 6 **(Figure 3.7**).

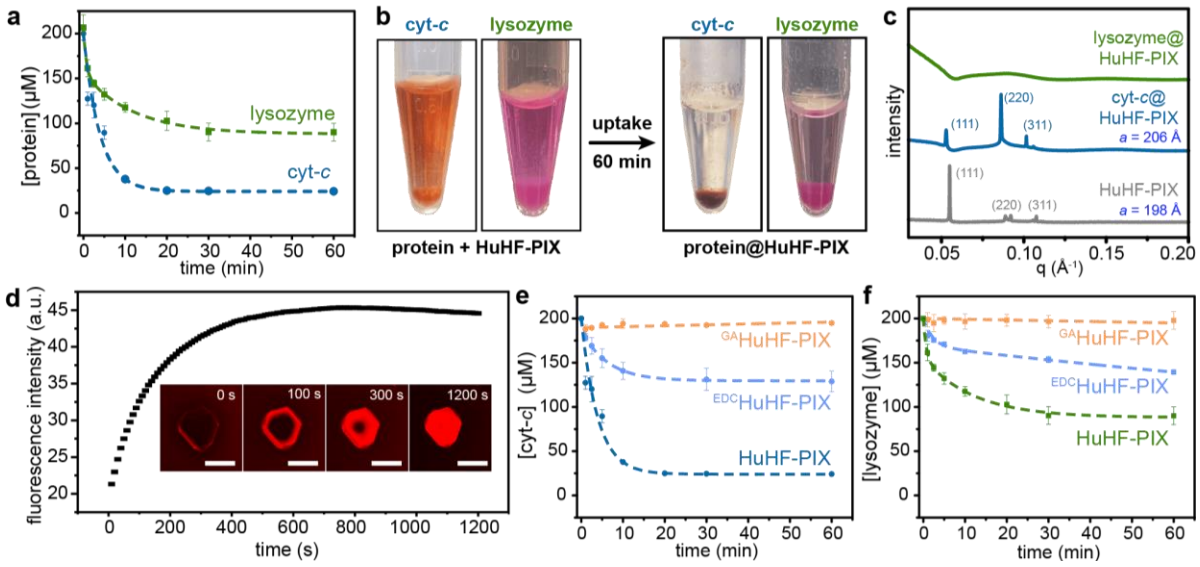

Figure 3.3. (a) Time-dependent uptake of cyt-*c* and rhodamine-labeled lysozyme by HuHF-PIX at pH 6, and **(b)** corresponding photographs for the samples at t = 0 and t = 1 h. **(c)** 1D SAXS profiles for HuHF-PIX, cyt-*c*@HuHF-PIX and lysozyme@HuHF-PIX. **(d)** Uptake of rhodamine-lysozyme by HuHF-PIX as monitored by confocal fluorescence microscopy of a single crystal (inset). The fluorescence intensity corresponds to the integrated value over the entire crystal volume (scale bars, 50 μm). **(e)** ^{EDC}HuHF-PIX and ^{GA}HuHF-PIX uptake of cyt-*c* and **(f)** lysozyme, compared to non-crosslinked HuHF-PIX.

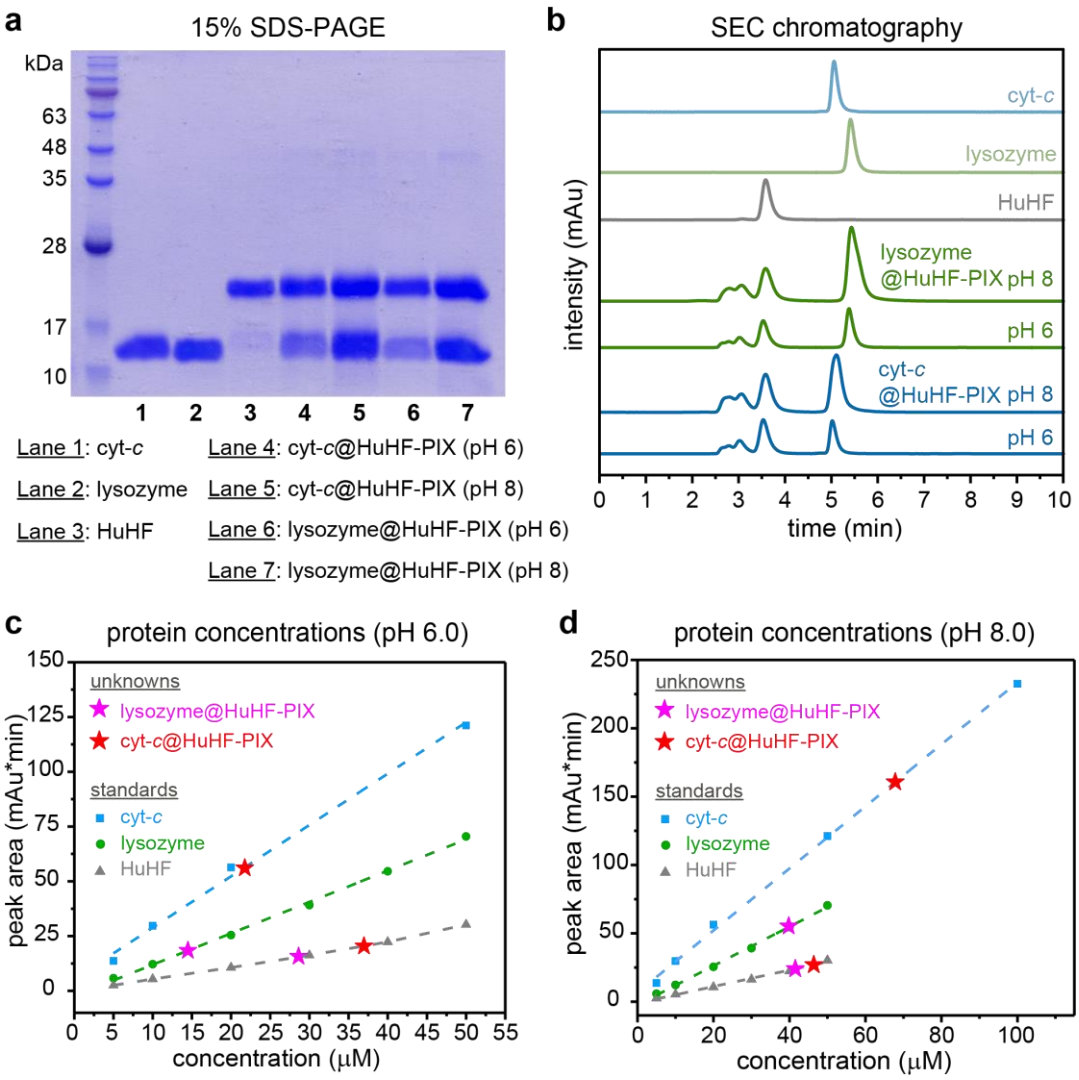

Figure 3.4. (a) Electrophoretic analysis and **(b)** SEC chromatograms of cyt-*c*, lysozyme, HuHF, cyt-*c*@HuHF-PIX, and lysozyme@HuHF-PIX. Densitometric analysis of the SDS-PAGE gel in **(a)** allowed the determination of the loading capacities (weight of guest protein / weight of total protein in crystals) to be 27%, 36%, 21% and 36% for lanes 4 – 7, respectively. The SEC peaks around 2.5 - 3 min in panel **(b)** are polymer species. (**c, d**) Standard curves for cyt-*c*, lysozyme, and HuHF concentrations at pH 6.0 and pH 8.0 were constructed using SEC-HPLC measurements of known concentrations of these proteins. The calculated protein concentrations in the cyt-*c*@HuHF-PIX, and lysozyme@HuHF-PIX samples are indicated by ★ symbols on their respective standard curves. Further analysis of the SDS-PAGE and chromatograms are detailed in Calculations 3.2 and 3.3.

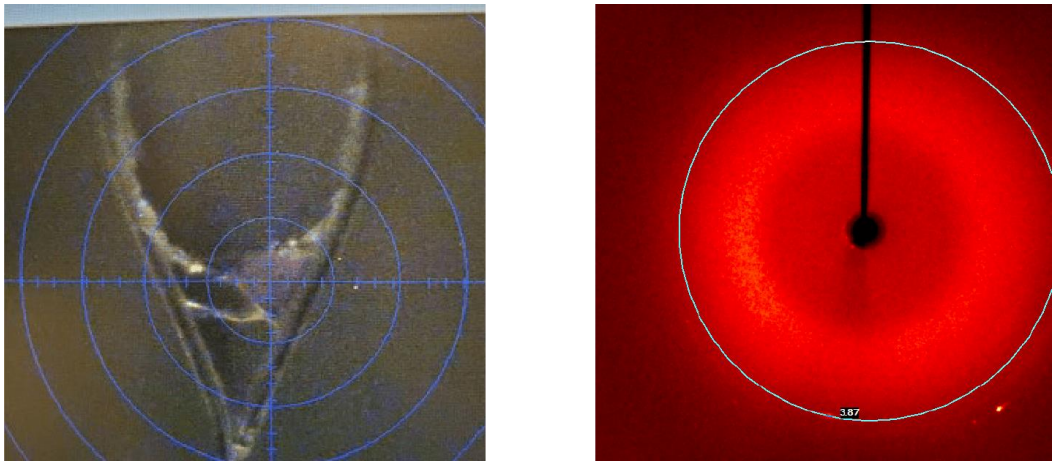

Figure 3.5. Images of lysozyme@HuHF-PIX on a CryoLoop (left) and its X-ray diffraction image, showing the lack of high-angle diffraction peaks (*i.e.*, the loss of atomic order) (right).

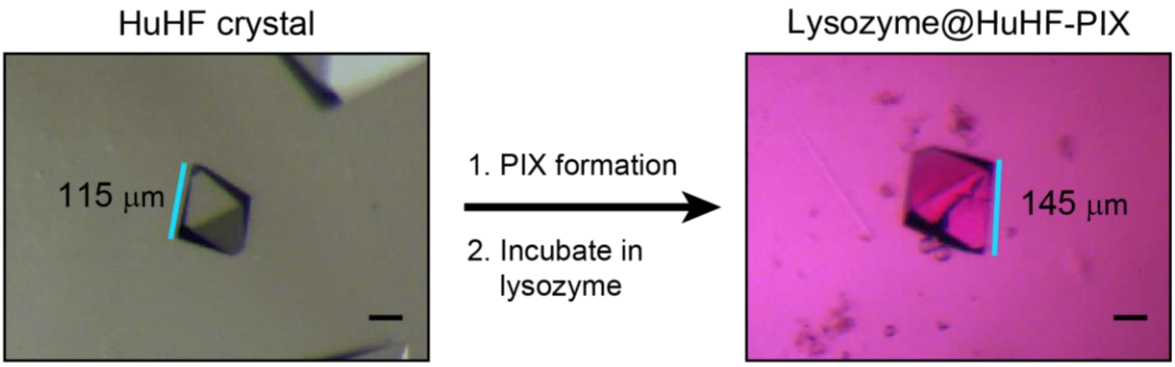

Figure 3.6. Light micrographs of an HuHF crystal before PIX formation (left) and after PIX formation/lysozyme uptake (right). The edge of the crystal (cyan) increases from 115 µm to 145 µm in this process, corresponding to a unit cell edge length increase by 26%. Scale bars correspond to 50 µm.

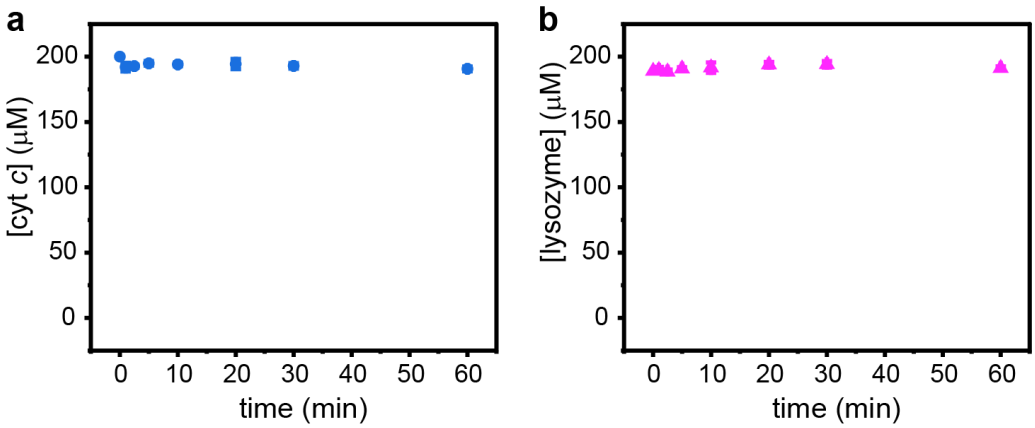

Figure 3.7. Monitoring the uptake of **(a)** cyt-*c* and **(b)** lysozyme by ^{POS}HuHF-PIX. The protein concentration in the supernatant remained constant at 200 mM, indicating the lack of any uptake.

3.3.2 pH-dependent Uptake/Release and Catalytic Activity of Protein Cargo

To exploit the electrostatic interactions between PIX and the guest proteins, we next conducted the uptake experiments at pH 8, where both the HuHF and pAAm components of PIX should be fully deprotonated, but cyt-c and lysozyme (*p*I's >10) should retain their positive charges. Indeed, the uptake capacities for both proteins increased (**Figures 3.8a-b**) and reached loadings of 46% w/w (~49 mM) for cyt-c and 39% w/w (~26 mM) for lysozyme at saturation (**Figure 3.4 and Calculations 3.2**), illustrating the synergy between the pAAm matrix and negatively charged HuHF lattice to enable guest proteins to pack tightly within the lattice.

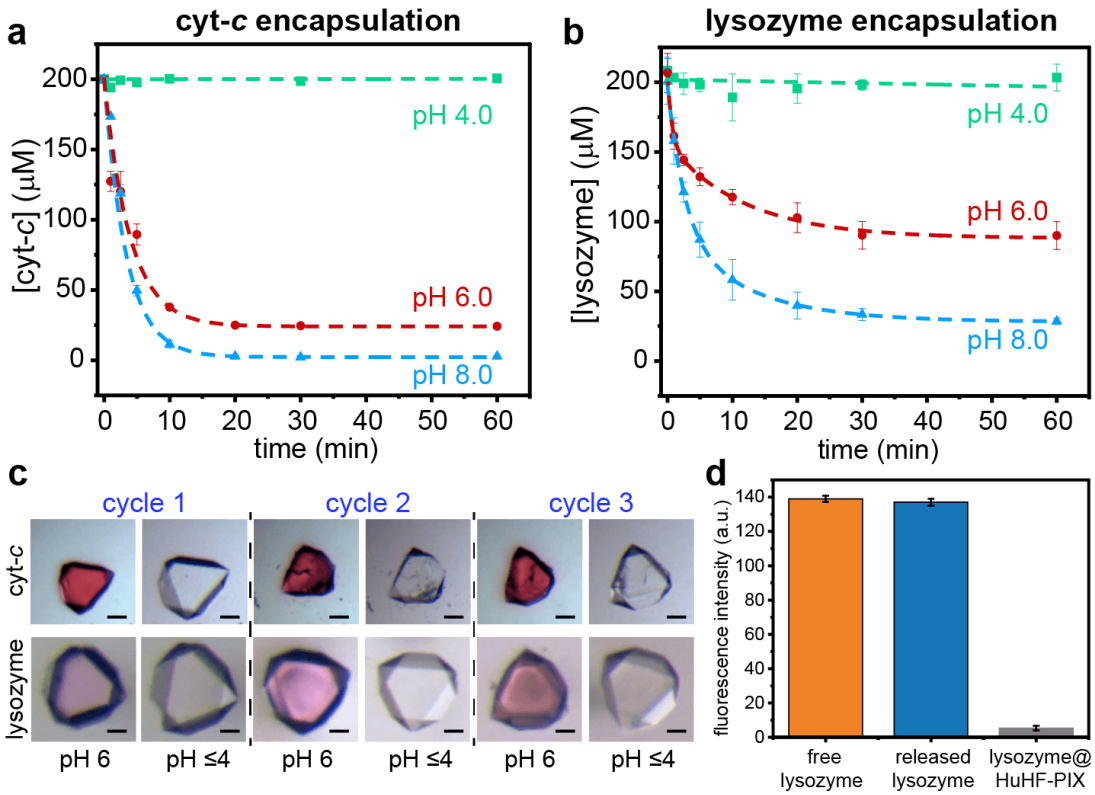

Figure 3.8. (a) pH-dependence of cyt-*c* and **(b)** lysozyme uptake by HuHF-PIX. **(c)** Reversible, pH-dependent uptake and release of cyt-*c* by a single HuHF-PIX, monitored by light microscopy (scale bars, 50 μm). **(d)** Catalytic activity of free, released and PIX-encapsulated lysozyme for bacterial wall degradation.

To further examine the role of the polymer component on guest uptake, we repeated the uptake experiments with HuHF crystals lacking the pAAm matrix. We observed minimal uptake for cyt-*c* and none for lysozyme, consistent with its larger size (**Figure 3.9**). The fact that cyt-*c* can perfuse into the HuHF crystals at all is indicative of "adaptive inclusion",[59] meaning the HuHF lattice possesses some flexibility, allowing penetration by oppositely charged cyt-*c* molecules. Yet, unlike the cyt-*c*@HuHF-PIX samples, HuHF crystals incubated in cyt-*c* solutions were not stable and dissolved over several hours. Similarly, the exposure of HuHF crystals to lysozyme led to visible protein aggregation on the crystal surfaces and rapid dissolution thereafter (**Figure 3.10**). Thus, the presence of a pAAm matrix in the lattice was crucial for maintaining the integrity of protein@HuHF-PIX.

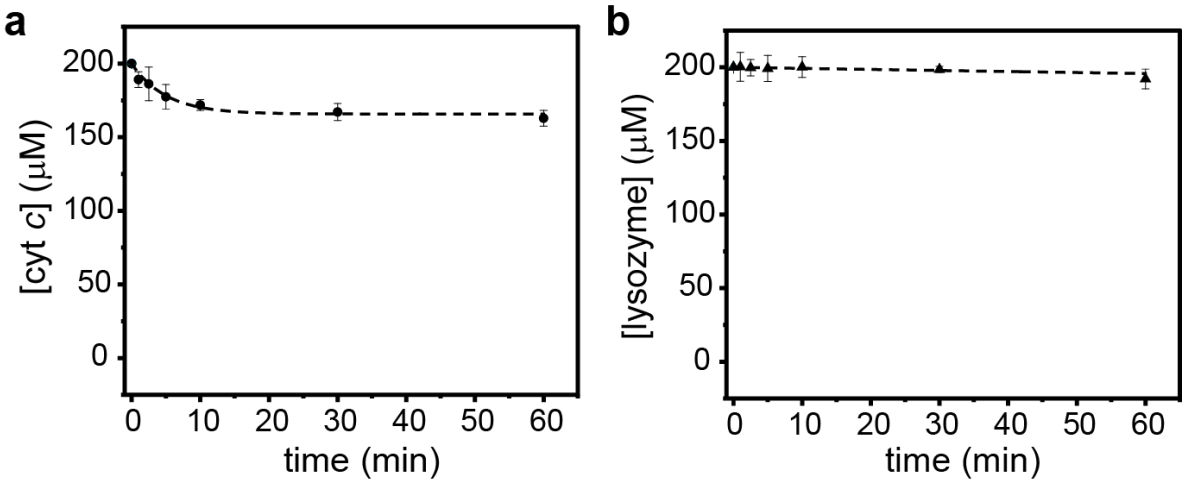

Figure 3.9. Monitoring the uptake of **(a)** cyt-*c* and **(b)** lysozyme by HuHF crystals (not containing polymers). The small amount of cyt-*c* uptake (37 mM) is attributed to the small size of this protein combined with some limited flexibility of the HuHF crystals. No uptake of lysozyme was observed.

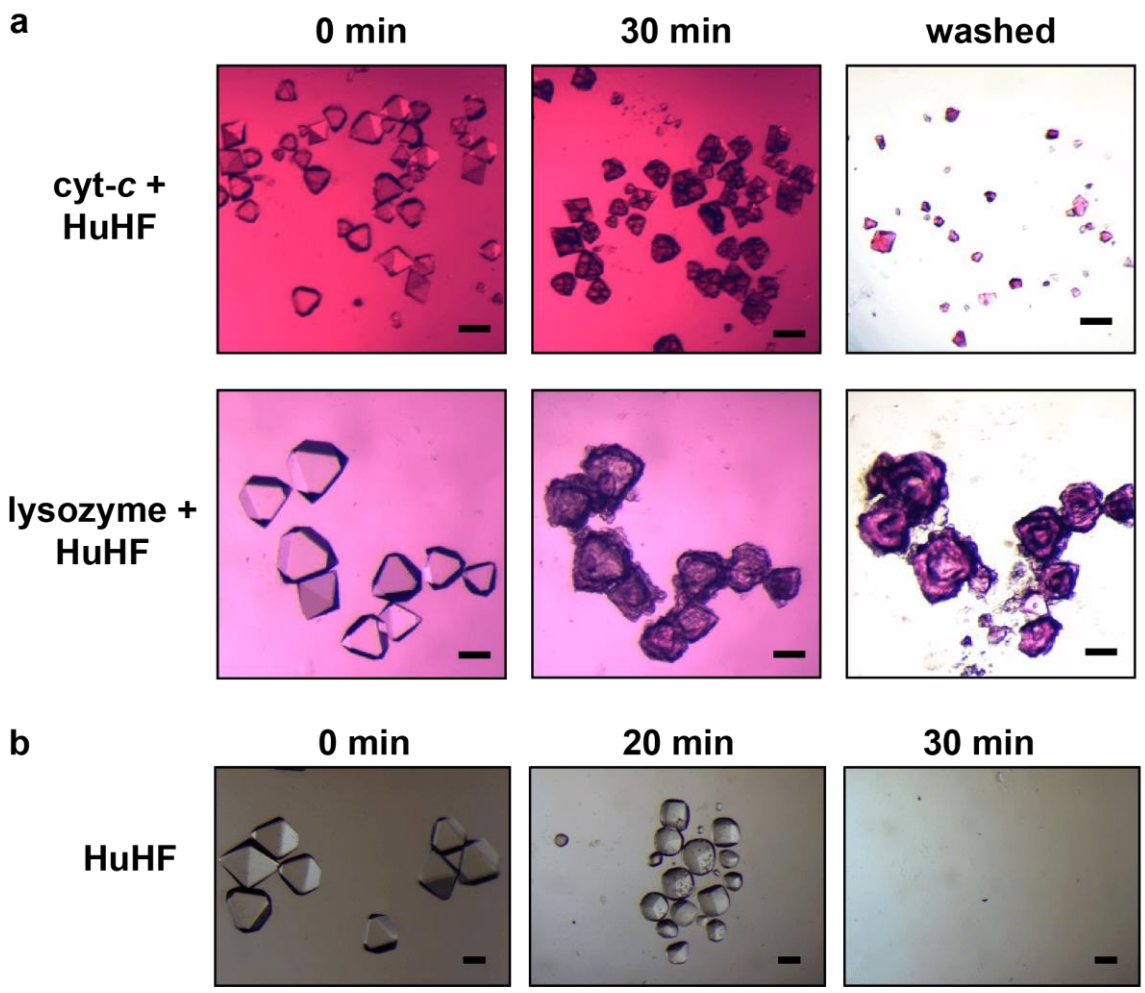

Figure 3.10. (a) Light micrographs of HuHF crystals (not containing polymers) incubated in a solution containing rhodamine-labeled cyt-*c* (top) or lysozyme (bottom) in 20 mM MES (pH 6.0). The crystals became heavily deformed after 30 min of incubation and some dissolved during the wash process. **(b)** In the absence of guest proteins, HuHF crystals fully dissolve in the same buffer solution. Scale bars correspond to 100 μm.

To investigate the role of lattice flexibility in guest uptake, we prepared two crosslinked HuHF-PIX systems: 1) PIX prepared with glutaraldehyde-treated HuHF crystals (^{GA}HuHF-PIX), which should be incapable of any expansion due to direct crosslinks between HuHF molecules and 2) HuHF-PIX treated with EDC (^{EDC}HuHF-PIX) to covalently link the pAAm matrix with Lys sidechains on HuHF surfaces, which are expected to display limited flexibility. ^{GA}HuHF-PIX were indeed incapable of any protein uptake, whereas ^{EDC}HuHF-PIX displayed ~40% of the loading capacity of non-crosslinked HuHF-PIX (**Figures 3.3e-f and 3.11-13**). These results establish that the flexibility of HuHF-PIX is an absolute requirement for protein encapsulation.

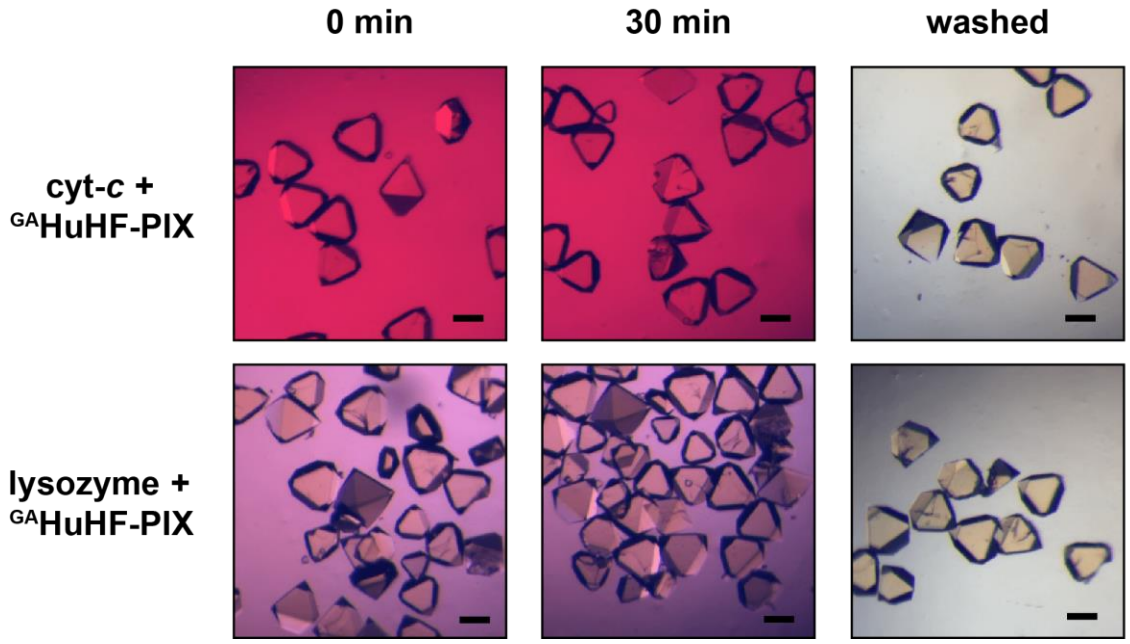

Figure 3.11. Light micrographs of ^{GA}HuHF-PIX samples incubated in a solution of rhodamine-labeled cyt-*c* (top) or lysozyme (bottom). The crystals remain pristine throughout the process and do not change color (indicating lack of cargo uptake). Scale bars correspond to 100 μm.

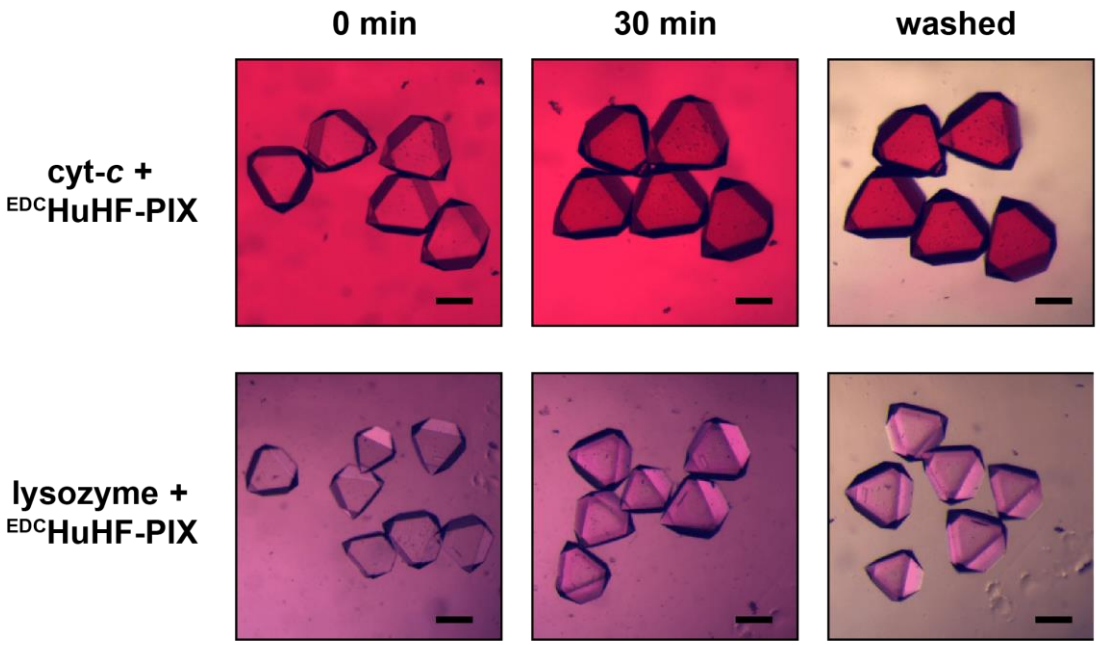

Figure 3.12. Light micrographs of ^{EDC}HuHF-PIX samples incubated in a solution of rhodamine-labeled cyt-*c* (top) or lysozyme (bottom). The crystals remain pristine throughout the incubation and during the wash. See Figure 3.13 for confocal fluorescence images. Scale bars correspond to 100 μm.

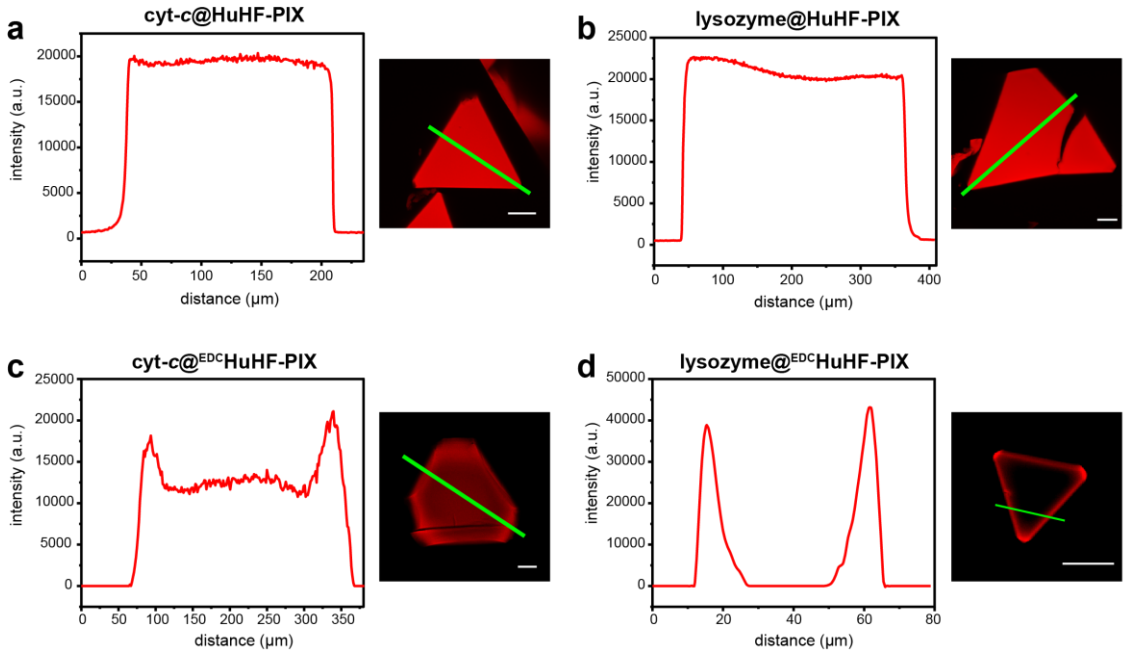

Figure 3.13. Confocal fluorescence micrographs (right) of guest-protein-loaded HuHF-PIX and ^{EDC}HuHF-PIX, with corresponding spatial emission intensity profiles (left). **(a)** Cyt-*c*@HuHF-PIX and **(b)** lysozyme@HuHF-PIX samples show homogenous distribution of guest proteins throughout the crystal center, while **(c)** cyt-*c*@^{EDC}HuHF-PIX and **(d)** lysozyme@^{EDC}HuHF-PIX show less penetration by guest proteins. The measured axes are indicated in green, and the scale bars represent 50 μm.

In acidic solutions (pH ≤4), the protein and polymer components of HuHF-PIX become positively charged. Consequently, their ability to uptake cyt-*c* and lysozyme is eliminated (**Figures 3.8a-b**). Given this pH dependence, we envisioned HuHF-PIX could act as a pH-responsive, reversible uptake/release system. Monitored at the bulk and individual crystal scales (**Figures 3c and 3.14-18**), both protein@HuHF-PIX samples indeed released >90% of protein cargo within <2.5 min upon transfer into a solution of pH ≤4 and were reloaded at pH ≥6. The reversible uptake/release could be repeated over multiple cycles (**Figure 3.19**). Protein reloading was frequently accompanied by the formation of large cracks on HuHF-PIX, yet, the crystals maintained their structural integrity, and the cracks often self-healed owing to the dynamic polymer-lattice interactions. In addition to pH, increased ionic strength (e.g., ≥0.1 M NaCl and $CaCl_2$) also enabled efficient release of encapsulated cyt-*c* and lysozyme from HuHF-PIX within minutes (**Figure 3.20**).

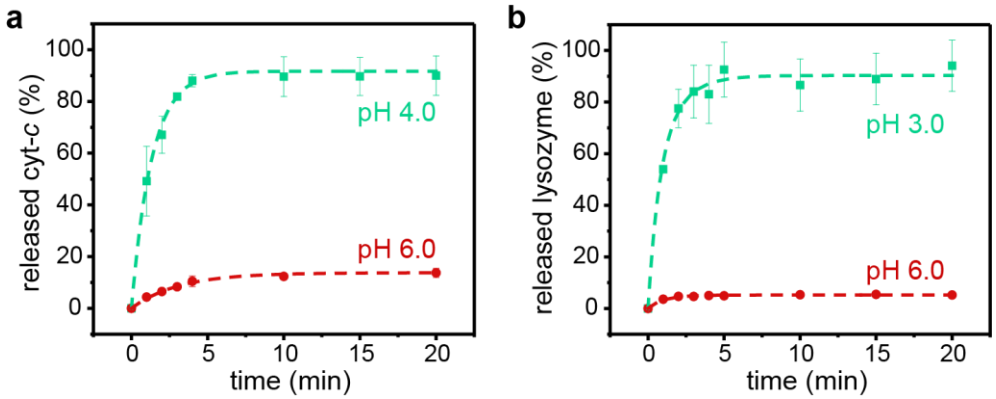

Figure 3.14. pH-dependent release of guest proteins from **(a)** cyt-*c*@HuHF-PIX and **(b)** lysozyme@HuHF-PIX samples, monitored by UV-vis spectroscopy.

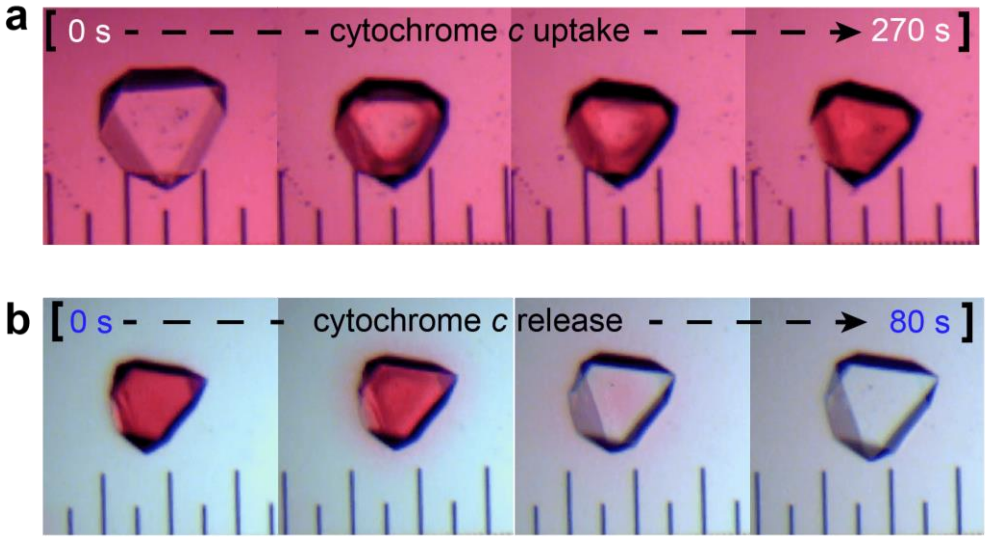

Figure 3.15. Light micrographs monitoring a single HuHF-PIX sample during **(a)** uptake and **(b)** release of cyt-*c*. The uptake occurs upon placing the crystal in a solution containing 200 mM cyt-*c* (20 mM MES, pH 6.0) and the release is initiated by exchanging the crystals into a solution 20 mM acetate (pH 4.0). The separation between the major ticks of the ruler is 100 µm.

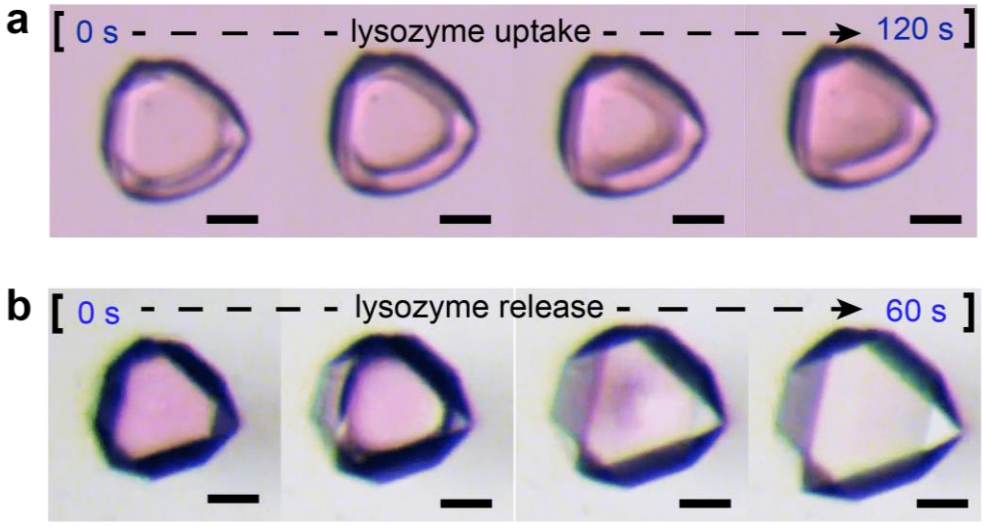

Figure 3.16. Light micrographs monitoring a single HuHF-PIX sample during **(a)** uptake and **(b)** release of lysozyme. The uptake occurs upon placing the crystal in a solution containing 200 mM lysozyme (20 mM MES, pH 6.0) and the release is initiated by exchanging the crystals into a solution 20 mM acetate (pH 4.0). Scale bars correspond to 100 µm.

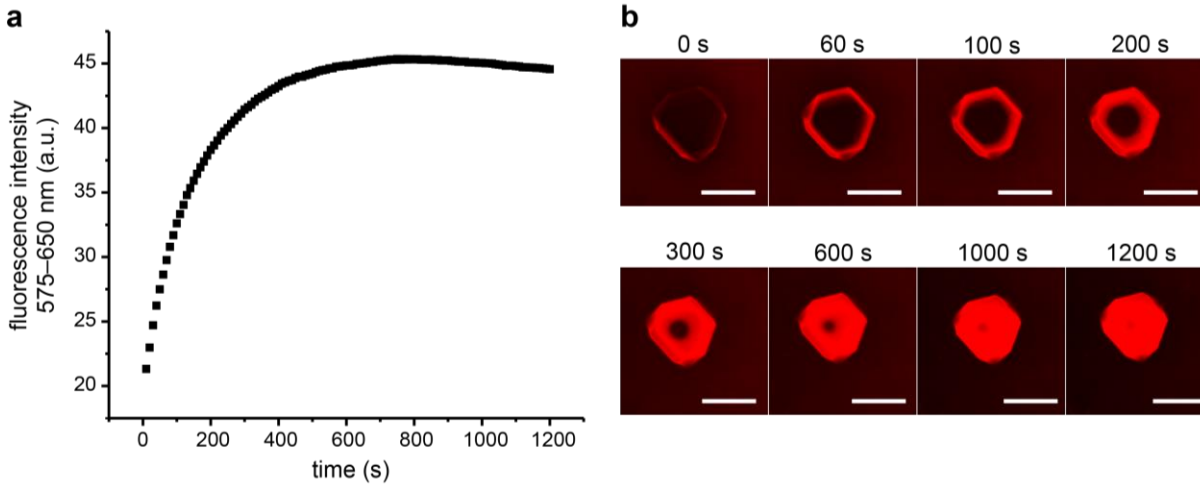

Figure 3.17. Uptake of rhodamine-labeled lysozyme by HuHF-PIX monitored by confocal fluorescence microscopy. **(a)** Uptake occurs upon placing the crystal in a solution containing 200 mM lysozyme (20 mM MES, pH 6.0) and can be followed by the increase in fluorescence of the crystal. **(b)** As the cargo diffuses into the lattice, a ring forms along the outer edges, and ultimately closes to saturate the entire crystal. Scale bars correspond to 50 µm.

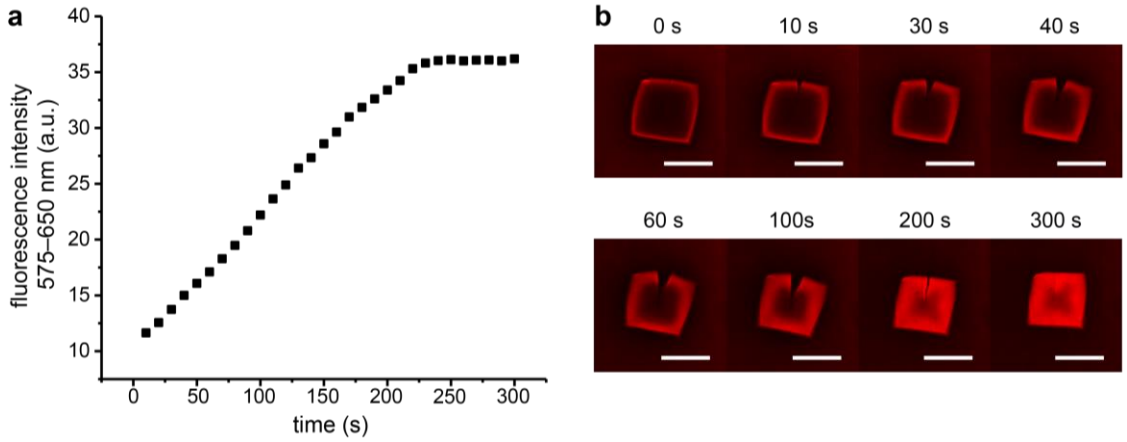

Figure 3.18. Uptake of rhodamine-labeled cyt-*c* by HuHF-PIX monitored by confocal fluorescence microscopy. **(a)** The uptake occurs upon placing the crystal in a solution containing 200 mM cyt-*c* (20 mM MES, pH 6.0) and can be followed by the increase in fluorescence of the crystal. **(b)** As the cargo diffuses into the lattice, a ring forms along the outer edges, and ultimately closes to saturate the entire crystal. Furthermore, a crystal fracture forms and self-heals during uptake. Scale bars correspond to 50 µm.

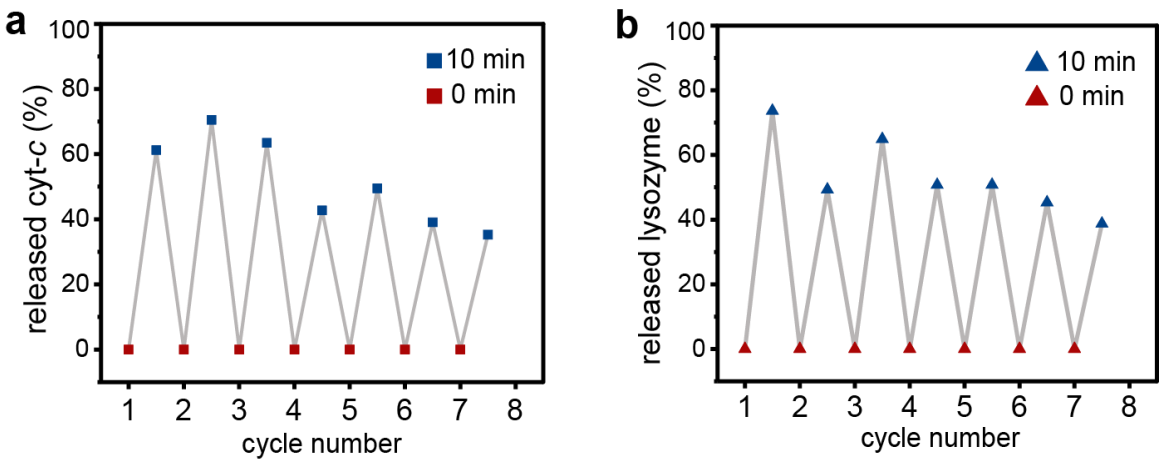

Figure 3.19. Successive uptake-release of **(a)** cyt-*c* and **(b)** lysozyme using bulk samples of HuHF-PIX. After loading HuHF-PIX with guest protein in a 20 mM MES solution (pH 6.0), the samples were placed in acidic conditions (pH ≤4) to initiate release. The concentration of released protein in the supernatant was measured after 10 min. This process was repeated for a total of 7 cycles. The decline in cycling efficiency is attributed to the loss of guest protein during the wash process that occurs between each uptake and release step.

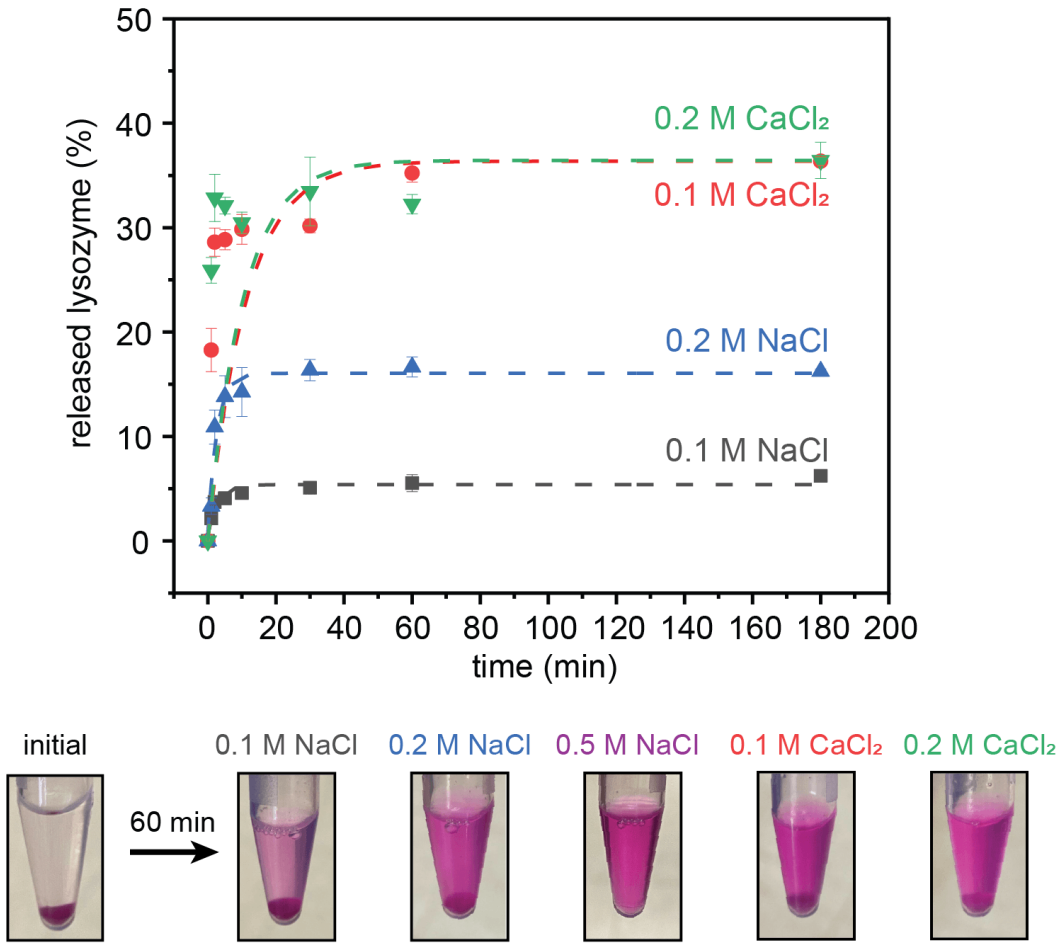

Figure 3.20. Ionic-strength-dependent release of rhodamine-labeled lysozyme from HuHF-PIX in the presence of Na^+ or Ca^{2+}. When lysozyme@HuHF-PIX were placed in a solution containing 0.1 M NaCl, approximately 6% of the entrapped lysozyme were released. At 0.2 M NaCl, the extent of protein release increased to 16%, indicating the release of lysozyme is tunable and dependent on the NaCl concentration. At 0.5 M NaCl, lysozyme was completely outcompeted by Na^+ from the HuHF-PIX matrix, leading to its complete dissolution. Protein release from lysozyme@HuHF-PIX samples was considerably more rapid and more efficient (~36%) with both 0.1 M or 0.2 M $CaCl_2$ due to the combined ability of Ca^{2+} to exert an electrostatic effect and crosslink the HuHF-PIX matrix to sterically occlude guest proteins.

We next probed the stability and activity of encapsulated cyt-*c* and lysozyme, with the expectation that the active lattice-polymer matrix could control the accessibility of the external environment. In solution, both proteins were prone to tryptic digestion at pH 8 (**Figure 3.21**).[60-61] Yet, once encapsulated in HuHF-PIX, both were protected from hydrolysis by trypsin (23.4 kDa, *p*I =10.5, dimensions = 3.0 x 3.5 x 5.0 nm), which is too large to enter the PIX framework. Cyt-*c* encapsulated in HuHF-PIX possessed UV-visible signatures characteristic of its folded form (Soret maximum at 410 nm in oxidized state)[62] and could be reversibly reduced and oxidized upon ascorbate and H_2O_2 treatment, respectively (**Figure 3.22**), indicating the retention of its native structure/function within PIX. Cyt-*c*@HuHF-PIX was also catalytically active in the H_2O_2-mediated oxidation of ABTS (2,2'-azino-bis(3-ethylbenzothiazoline-6-sulfonic acid)),[63] yet, the catalytic rate was low (k_{obs} = 0.09 min^{-1} at pH 8) compared to free cyt-*c* (**Figure 3.23**), likely owing to the repulsive interactions between HuHF-PIX and negatively-charged ABTS. In contrast to H_2O_2 and ABTS, the natural substrates of lysozyme, i.e., bacterial cell walls, could not penetrate lysozyme@HuHF-PIX. Consequently, lysozyme@HuHF-PIX displayed <5% of cell wall degradation activity compared to free lysozyme. Yet, the catalytic activity was fully recovered upon pH-induced release of the entrapped lysozyme (**Figure 3.8d**).

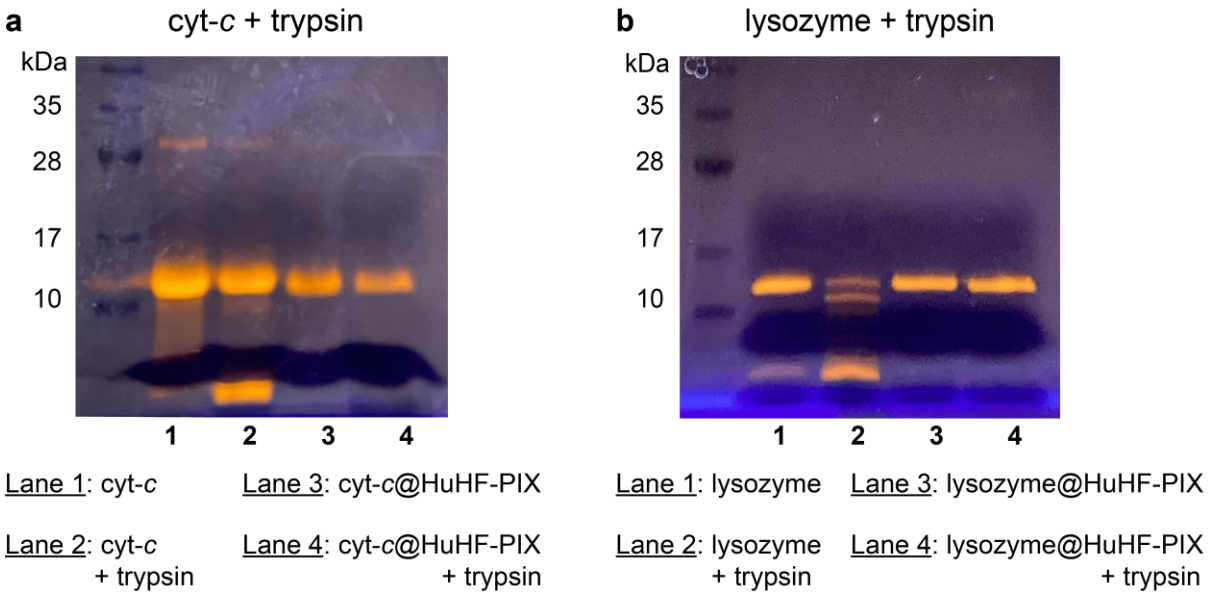

Figure 3.21. Electrophoretic analysis (15% SDS-PAGE) of rhodamine-labeled free protein and protein@HuHF-PIX after trypsin digestion. Free **(a)** cyt-*c* and **(b)** lysozyme are susceptible to degradation (lane 2) but are protected when entrapped in HuHF-PIX (lane 4). The gels were imaged under UV-irradiation.

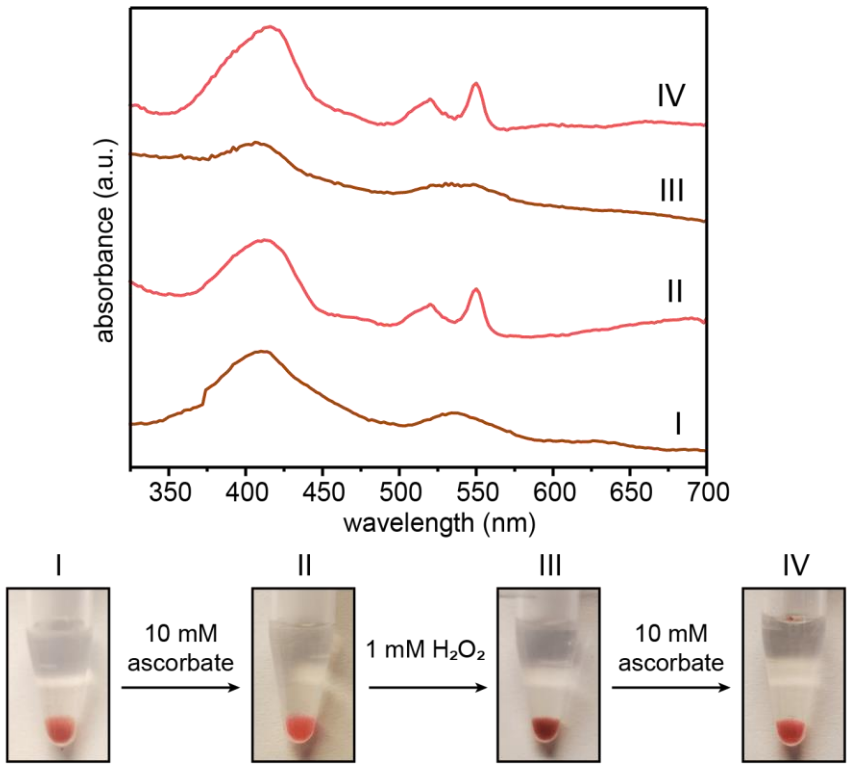

Figure 3.22. Reversible redox activity of cyt-*c*@HuHF-PIX monitored by UV-vis spectroscopy (top) and photographs of the corresponding samples (bottom). Note that background scattering by cyt-*c*@HuHF-PIX particles perturbs the UV-vis spectra and the relative intensities/shapes of different absorption bands are not representative of the spectra of dilute solution samples. The initial sample (**I**), untreated cyt-*c*@HuHF-PIX, displayed a UV-vis spectrum with a Soret maximum at 410 nm, indicative of folded, oxidized cyt-c. Transferring the crystals into a solution containing ascorbate (**II**) led to the expected red-shift of the Soret band maximum and the emergence of Q-bands at 520 nm and 550 nm, indicative of folded, reduced cyt-c. Exchanging the solution into 1 mM H_2O_2 (**III**) caused a blue-shift of the Soret band to 406 nm, consistent with peroxide-mediated oxidation concomitant with the displacement of the Met axial ligand from the heme. Subsequent incubation in ascorbate (**IV**) led to the recovery of the Soret- and Q-bands at 410 nm, 520 nm and 550 nm, indicating that the cyt-*c* molecules entrapped in HuHF-PIX retain their native redox activity.

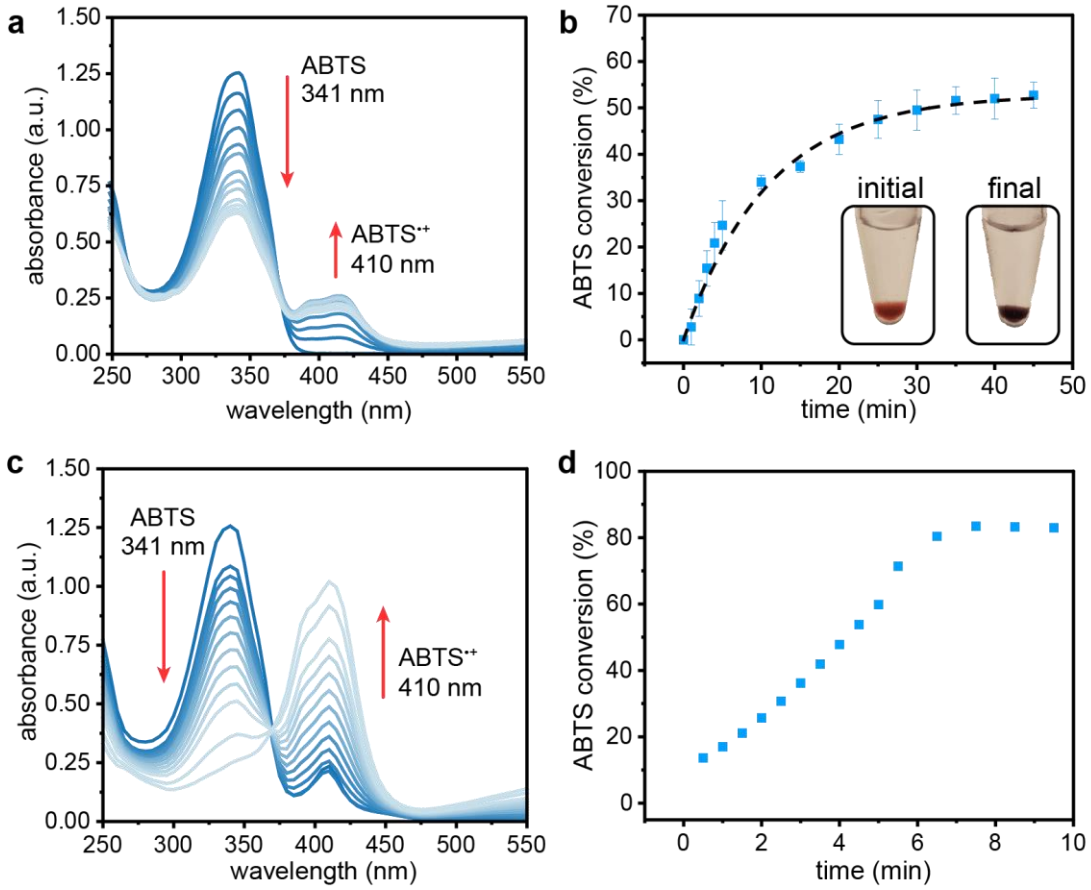

Figure 3.23. Catalytic H_2O_2-mediated ABTS-oxidation activity of cyt-c@HuHF-PIX. **(a)** UV-vis spectra showing the change in ABTS concentration in the presence of cyt-*c*@HuHF-PIX. The expected amount of increase in the absorbance of the product ($ABTS^+$) at 410 nm is not observed due to the partial sequestration of $ABTS^+$ in HuHF-PIX. **(b)** Kinetics of cyt-c@HuHF-PIX-mediated oxidation of ABTS, monitored by changes in absorbance at 341 nm. The darkening of the cyt-*c*@HuHF-PIX is consistent with $ABTS^+$ sequestration in the lattice (inset). **(c)** UV-vis spectra showing the change in ABTS concentration in the presence of free cyt-*c*. The concomitant increase in the absorbance of $ABTS^+$ was observed. **(d)** Amount of ABTS converted, determined by monitoring absorbance at 341 nm.

3.3.3 Encapsulation of Protein Cargo via Expansion/Contraction

Finally, we sought to exploit the expansion/contraction ability of HuHF-PIX to encapsulate larger, negatively charged proteins, using green fluorescent protein (GFP, 26 kDa, dimensions = 3.0 x 3.2 x 5.2 nm, *p*I = 5.5) as a model (**Figure 3.24a**). Upon immersion into a solution of GFP under standard conditions, HuHF-PIX promptly began to expand as expected from the inability of GFP to counter the solvation of the pAAm matrix. After 30 min, at which point HuHF-PIX reach ~130% of their original dimensions (**Figure 3.25**), excess NaCl was added to contract the crystals and entrap GFP. Confocal fluorescence microscopy of the resulting crystals revealed GFP was present throughout the entire crystal volume (**Figure 3.24b**) and SAXS measurements indicated that GFP@HuHF-PIX retained their crystallinity (**Figure 3.26**). In contrast, HuHF-PIX samples that were incubated in a GFP solution with NaCl (and thus unable to expand) did not sequester any GFP (**Figure 3.27**). Although the amount of GFP sequestered in this fashion is low (<1 wt %), compared to cyt-*c* and lysozyme, our results show HuHF-PIX can encapsulate macromolecules that are more than twice as large as the smallest lattice pores.

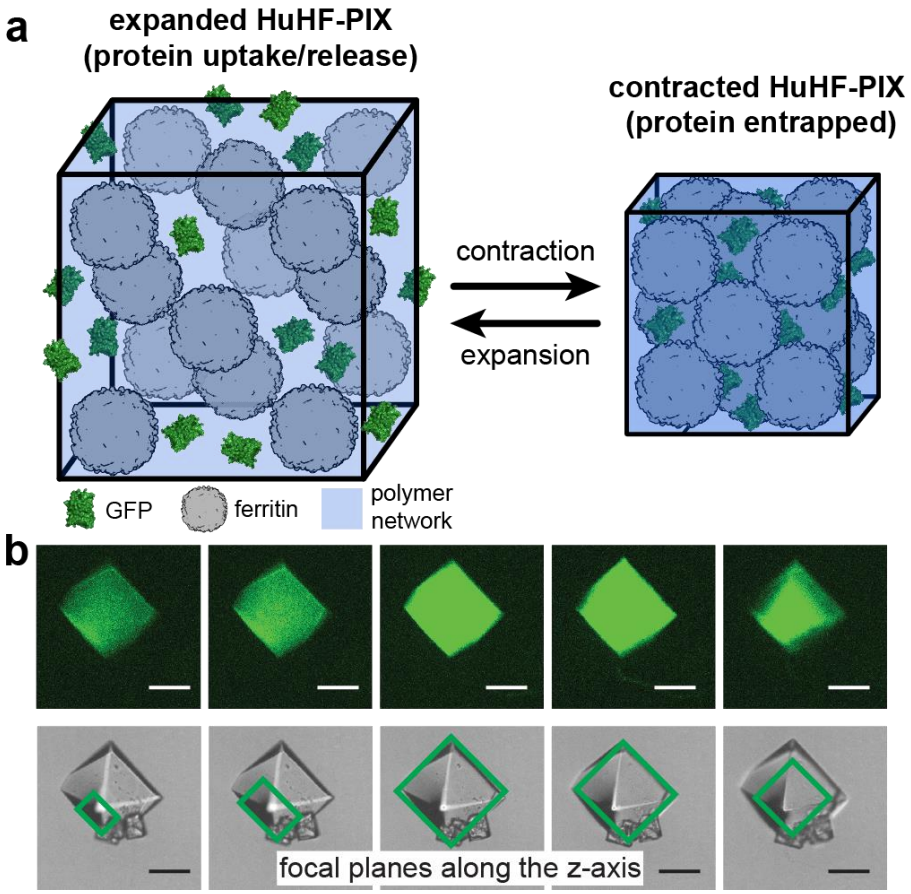

Figure 3.24. (a) Schematic representation for the encapsulation of large proteins (e.g., GFP) in PIX through expansion and contraction. **(b)** Confocal fluorescence microscopy images of GFP@HuHF-PIX (above) and corresponding bright-field images with the focal planes (green boxes) (scale bars, 50 μm).

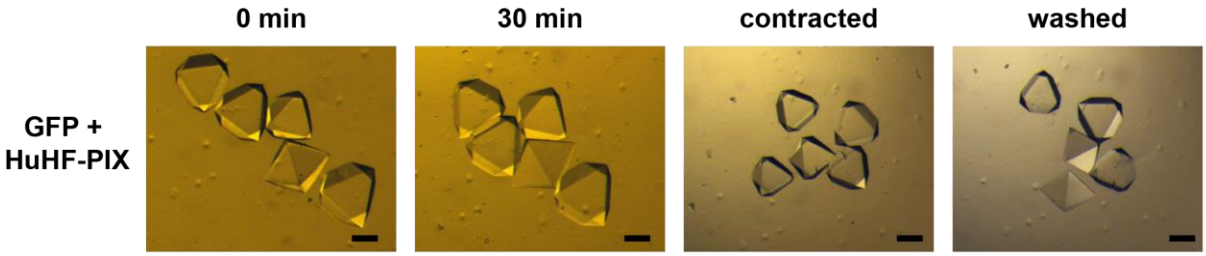

Figure 3.25. Light micrographs of HuHF-PIX crystals placed in a solution of GFP (200 mM in a 20 mM MES solution, pH 6.0). After 30 min, whereby the HuHF-PIX crystals expanded by ~30% in dimensions, NaCl and $CaCl_2$ were introduced to the solution to induce HuHF-PIX contraction. The resulting GFP@HuHF-PIX samples were washed with 20 mM MES (pH 6.0) and remained contracted. See Figure 3.27 for confocal fluorescence microscopy images. Scale bars correspond to 100 µm.

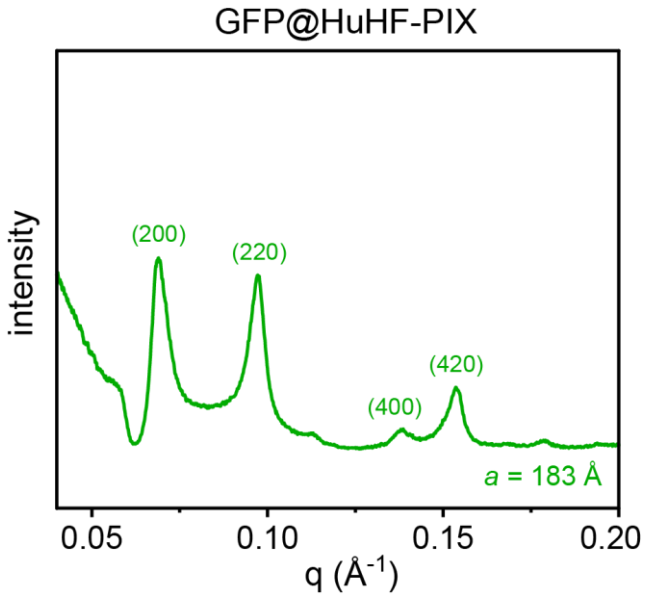

Figure 3.26. 1D SAXS profile for GFP@HuHF-PIX. The presence of Bragg peaks indicates the material is crystalline (*F*432, a = 183 Å) after the expansion and contraction of PIX in the presence of GFP.

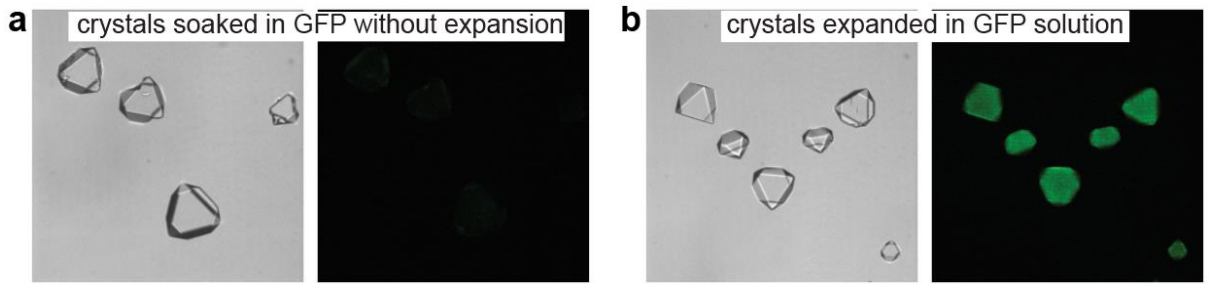

Figure 3.27. Encapsulation of GFP by HuHF-PIX monitored by confocal microscopy (bright field-left; fluorescence-right). **(a)** Non-expanded HuHF-PIX soaked in GFP solution supplemented with NaCl display no GFP encapsulation whereas **(b)** HuHF-PIX crystals show thorough GFP encapsulation upon incubation in a GFP solution containing no salt (enabling expansion) and subsequent contraction.

3.4 Conclusions

PIX are unique materials that seamlessly combine structural coherence and strength of porous crystalline materials and their discrete, particulate nature with the flexibility and stimuli-responsiveness of polymers. We have shown here that these complementary but mutually exclusive properties can be exploited for the highly efficient uptake/release of guest proteins in an externally tunable fashion. In turn, the guest proteins can themselves influence the stability and mechanical properties of PIX, creating a synergistic, dynamic host-guest system. Given that both the host protein (i.e., lattice) and polymer components are readily modified genetically and/or chemically, we envision that PIX can be used for encapsulating a breadth of macromolecules in controlled release/delivery applications and for the construction of multi-functional materials.

3.5 Methods

3.5.1 General Methods.

All reagents were purchased from commercial sources and used without further purification unless noted otherwise. Equine cytochrome *c* (cyt-c, Prod. No. C2506) and glutaraldehyde (Prod. No. G6257) were purchased from Sigma Aldrich. Hen egg white lysozyme

(Prod. No. C0022) was purchased from BioPioneer Inc. EnzChek™ Lysozyme Assay Kit (Cat. No. E22013), NHS-Rhodamine (Cat. No. 46406), trypsin (Cat. No 90058), and EDC (Cat. No. 22980) were purchased from Thermo Scientific. ABTS (Prod. No. 10102946001) was purchased from Roche.

3.5.2 Protein expression, purification, and characterization of HuHF.

The plasmid for the ΔC variant of human heavy-chain ferritin (HuHF), devoid of all native cysteine residues (C90E, C102A, and C130A), was obtained via site-directed mutagenesis as previously described.[64] Ferritin was prepared using QuikChange mutagenesis with primers obtained from Integrated DNA Technologies. Mutant plasmids were transformed into XL1-Blue *E. coli* cells and purified with QIAprep Spin Miniprep kit (Qiagen). The variant was sequenced (Retrogen) to verify mutagenesis. Expression and purification of HuHF were performed according to a previously published protocol.[65]

3.5.3 Protein expression, isolation, and purification of ^{POS}HuHF.

The gene for the ^{POS}HuHF variant (containing mutations A18K, E90K, N98R, A102K, H105K, N109K, D123K, C130A, and E162R on the ΔC variant), was obtained from Integrated DNA Technologies and inserted into the plasmid vector pJexpress through restriction enzyme ligation. Restriction enzyme sites *NdeI* (5') and *XhoI* (3') were first added to the gene through PCR amplification. Then, the restriction enzymes *NdeI* and *XhoI* were used to digest the gene following the protocol of New England Biolabs (NEB, https://nebcloner.neb.com). The resulting gene fragments were separated using a spin column with a 30 kDa molecular weight (MW) cutoff. T4 ligase was used for the ligation of the ^{POS}ferritin gene into the plasmid following the protocol of NEB. The final vector was transformed into XL1-Blue cells via heat-shock and subjected to sequencing, which confirmed successful insertion of the gene.

The expression and purification protocols for ^{POS}HuHF were adapted from those reported by Künzle and coworkers.[66] Plasmids (pJexpress vector) containing the ^{POS}HuHF gene were amplified in and isolated from XL1-Blue cells (via MiniPrep), transformed into BL21 (DE3) *E. coli* cells via heat shock, and plated onto lysogeny broth (LB) agar containing 100 μg/mL ampicillin. Colonies or freezer stocks of BL21 cells containing ^{POS}HuHF plasmids were used to inoculate starter cell cultures (200 mL LB medium, 100 μg/mL ampicillin) that were incubated for 16 hours at 37 °C with shaking at 200 rpm and used to inoculate 1-L LB cultures (10 mL starter culture per flask) supplemented with 100 μg/mL ampicillin. Cells were grown at 37 °C to an OD_{600} of ~0.2. Overexpression of the protein was induced by addition of isopropyl β-D-1-thiogalactopyranoside (IPTG) to a total concentration of 0.25 mM and the cells were incubated at 37 °C for 5 h prior to collection by centrifugation (6000×g for 10 min). Pellets were stored at −80 °C. Frozen cell pellets were thawed and resuspended in buffer (15 mM Tris (pH 7.4), 150 mM NaCl) with 1 mM phenylmethylsulfonyl fluoride (PMSF), 5 mM DTT, and ~25 μM lysozyme. Cells were sonicated for 12 min on ice (59 s pulse on, 30 s pulse off), and the lysate was clarified by centrifugation (12,000×g, 20 min, 4 °C). After collection of the supernatant by decanting, the cell pellet was resuspended in buffered 1% (v/v) Triton X-100 solution and sonicated again (on ice, same parameters).

After sonication, RNase (~20 μM final concentration) was added to the protein solution and incubated at 37 °C for 3 h to degrade all the RNA in solution, a step we found to be necessary to ensure binding of ^{POS}HuHF to cation-exchange resins. This solution was then heat-treated in a water bath at 65 °C for 15 min to induce denaturation and precipitation of most other contaminants. The soluble fraction containing ^{POS}HuHF was separated by centrifugation (12,000×g, 10 min). Ammonium sulfate was then added to this clarified solution until reaching a concentration of 70%

(w/v), at which point ^{POS}HuHF precipitates out to separate it from most remaining impurities. Following centrifugation (12,000×g, 10 min), the isolated protein pellet was fully dissolved into a solution of 50 mM MES (pH 6.0) and 0.5 M NaCl, filtered, loaded onto an Uno-S cation exchange column (Bio-Rad) on a DuoFlow chromatography workstation (Bio-Rad), and eluted using a linear 0.5-2 M NaCl gradient at the same pH. Following assessment of the eluted fractions by SDS-PAGE, only highly pure (>95% purity) fractions were collected and combined without further purification. The resulting solution was transferred into dialysis tubing (6,000-8,000 Da MW cutoff, Thermo Fisher) and dialyzed against a buffered solution containing 50 mM Tris (pH 7.5) and 1 M NaCl.

3.5.4 Protein expression, isolation, and purification of GFP.

The gene for monomeric superfolder GFP (sfGFP) was provided by Dr. Suckjoon Jun's group (UC San Diego) and incorporated into the plasmid vector pJexpress through the same NEB protocol as described above.[67] The expression and purification of sfGFP were carried out according to previously published protocols.[68] Protein plasmids isolated from XL1-Blue cells were transformed into BL21 (DE3) *E. coli* cells and plated onto LB agar containing 100 µg/mL ampicillin. Colonies or freezer stocks of BL21 containing GFP-pJexpress vectors were used to inoculate starter cell cultures (200 mL LB medium, 100 µg/mL ampicillin). Cultures were incubated for 16 h at 37 °C with shaking at 200 rpm prior to inoculating 1 L LB cultures (10 mL per flask) supplemented with 100 µg/mL ampicillin. Cells were grown to OD_{600} = 0.6-0.8 at 37 °C and protein expression was then induced by addition of IPTG to a final concentration of 1 mM. Cells were incubated at 37 °C for 4 h and yielded bright green solutions, confirming the expression of sfGFP. The cells were harvested by centrifugation (6,000×g, 10 min). Pellets were stored at −80 °C. Frozen cells were thawed and resuspended in a buffer solution containing 50 mM Tris

(pH 8.0), 20 mM EDTA, and 50 mM NaCl. The cells were then lysed by sonication (in an ice-bath) for 12 min total, with 30 s pulse on and 59 s off. Resulting cell debris was removed by centrifugation at 4 °C at 12,000×g for 20 min. Next, ammonium sulfate was directly added to the solution to purify the sfGFP by precipitation. At 40% saturated ammonium sulfate, the sfGFP remains soluble, and precipitated impurities were removed by centrifugation at 12,000× g. Upon reaching 65% ammonium sulfate, bright green precipitates formed and were separated by centrifugation at 12,000×g. The resulting pellet was then dissolved into a minimal volume of 50 mM Tris (pH 8.0), subjected to size exclusion chromatography (SEC) using Sephacryl-300 resin, and followed by anion exchange chromatography (Q column, Bio-Rad) to further purify the protein, collecting only peak fractions (as determined by UV-vis absorbance 488 nm) at the end of each purification step. The protein eluted from the Q column at approximately 110 mM NaCl in 50 mM Tris (pH 8.0). The purity of the final GFP solution was confirmed by SDS-PAGE.

3.5.5 Preparation of HuHF crystals and HuHF-PIX.

Polymer precursor solution: 25 mM HEPES (pH 7.0), 30 mM $CaCl_2$, 917 mM (8.625% w/v) sodium acrylate, 352 mM (2.5% w/v) acrylamide and 13 mM (0.2% w/v) *N,N′*-methylenebis(acrylamide). *Polymerization solution*: 4 M NaCl, 1% (w/v) APS and 1% (v/v) TEMED. HuHF crystals were formed using sitting drop crystallization trays (Hampton) or in 24-well culture plates (Costar) without a reservoir for bulk preparation, as previously described (Table 3.1).[65] After crystal formation (which takes 1-2 days), the well solution was replaced with the polymer precursor solution (20 mL for sitting drop wells or 200 mL for culture plates) and left to incubate for >12 h to ensure full infusion of the monomers. The crystals were then placed in the polymerization solution (20 mL for sitting drop wells or 200 mL for culture plates) for >10 min to

effectively form a gel within the crystal lattice. The polymerization solution was used to dislodge and harvest the HuHF-PIX from the wells into Eppendorf tubes for subsequent use.

3.5.6 Formation of ^{GA}HuHF-PIX.

After HuHF crystal formation, the crystallization solution was exchanged for a mixture containing 25 mM HEPES (pH 7.0), 30 mM $CaCl_2$, and 2.5% glutaraldehyde (v/v). After >12 h, the crosslinked crystals, ^{GA}HuHF, were washed 5 times with 25 mM HEPES (pH 7.0) and processed into ^{GA}HuHF-PIX following procedures described above.

3.5.7 Formation of ^{EDC}HuHF-PIX.

Newly formed HuHF-PIX were washed with 20 mM MES (pH 6.0) and placed in a freshly prepared solution of 5 mM 1-ethyl-3-(3-dimethylaminopropyl)- carbodiimide hydrochloride, EDC, (20 mM MES pH 6.0) for 10 min. The newly crosslinked crystals were washed and stored in 20 mM MES (pH 6.0) for later use.

3.5.8 Small-scale preparation of guest-loaded PIX.

HuHF-PIX samples, formed in sitting drop wells as described above, were washed with 20 mM MES (pH 6.0) and placed in a crystal tray well with 20 mL of cytochrome *c* or lysozyme (200 mM, 20 mM MES pH 6.0). These steps can be repeated using HuHF crystals, ^{GA}HuHF-PIX, and ^{EDC}HuHF-PIX.

3.5.9 Bulk preparation of guest-loaded PIX.

Wells of freshly harvested HuHF-PIX were washed and suspended with 200 mL of 20 mM MES (pH 6.0) and transferred to a clean tube. After carefully decanting the solution with a micropipette, 500 mL of either cyt-*c* or lysozyme (200 mM in 20 mM MES (pH 6.0), 20 mM HEPES (pH 8.0) or 20 mM acetate (pH 4.0) were added into the tube and placed on a gel rocker for 60 min. Samples of HuHF crystals, ^{GA}HuHF-PIX, and ^{EDC}HuHF-PIX were prepared in a similar

fashion. Guest protein@HuHF-PIX samples were mainly prepared in pH 6.0 solutions, unless noted otherwise.

3.5.10 Analysis of HuHF crystals grown in cell culture wells.

Given that all protein uptake and release experiments with HuHF-PIX involve the use of suspensions of crystalline materials, it is crucial to ensure that every sample in a set of experiments (including replicates) contain the same amount of HuHF protein. To ensure that this is indeed the case, we have first used standardized conditions for the bulk-scale formation of HuHF crystals (see above). We then analyzed the protein content in aliquots of HuHF crystal suspensions taken from different crystal growth wells. The well solutions were exchanged for a 500-μL mixture containing 100 μM ethylenediaminetetraacetic acid (EDTA), and the tray was placed on a gel rocker at room temperature. After >12 h, the crystals fully dissolved and the well solutions were analyzed by gel electrophoresis (12% SDS-PAGE) and Bradford protein assay. Aliquots of 5 mL and 10 mL from each well were taken for gel analysis and Bradford assay, respectively. As shown in the figure below, results from both analyses show excellent consistency among the individual wells.

Gel electrophoretic analysis

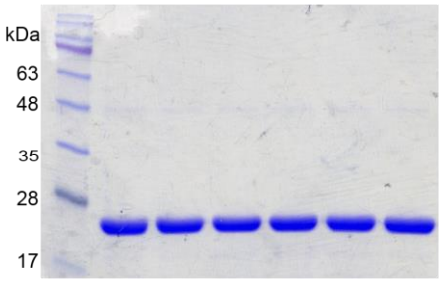

Lanes 1-6: wells 1-6

Bradford protein assay

sample	concentration
well 1	195 μM
well 2	198 μM
well 3	186 μM
well 4	195 μM
well 5	194 μM
well 6	196 μM
average	194 ± 4 μM

3.5.11 Size exclusion chromatography/HPLC analysis of guest proteins in PIX.

Cyt-*c*@HuHF-PIX and lysozyme@HuHF-PIX crystals were transferred into wells containing 500-mL solutions composed of 50 mM HEPES (pH 7.0) and 500 mM NaCl, and placed on a rocker. After >6 h, the PIX crystals dissolved and the samples were prepared for size exclusion

chromatrography (SEC) by passing the solutions through 0.22 μm Spin-X centrifuge tube filters (Costar, 0.5 mL capacity). SEC experiments were conducted by injecting 10 mL of dissolved PIX sample into a Thermo Scientific Vanquish UHPLC connected to a single MAbPac SEC-1, 5 μm, 300 Å, analytical column PEEK 4.0 × 150 mm (Thermo Scientific) run in the aqueous phase (50 mM HEPES (pH 7.0) and 500 mM NaCl) at 0.3 mL/min. The same protocol was followed for cyt-*c*, lysozyme, and HuHF solutions to generate the standard curves in **Figure 3.4**.

3.5.12 SAXS measurements of guest-loaded PIX.

Cyt-*c*@HuHF-PIX and lysozyme@HuHF-PIX samples were prepared as described above. The crystals were suspended and transferred with 25 mL of the MES (pH 6.0) solution into 1.5-mm quartz capillaries (Hampton). The capillaries were sealed with molding clay and analyzed at Beamline 4-2 of the Stanford Synchrotron Radiation Lightsource (SLAC National Accelerator Laboratory). Data were collected using collimated X-ray radiation (1.127 Å, 11 keV) after being calibrated with a silver behenate standard. Scattered radiation was detected using a Rayonix225HE detector, and one-dimensional scattering data were obtained through azimuthal averaging of the two-dimensional data to produce plots of the scattering intensity as a function of the scattering vector length, $q = 4\pi\sin(\theta/\lambda)$, where θ is one-half of the scattering angle and λ is the wavelength of the X-rays used. Analysis of the one-dimensional data was performed using the powder diffraction processing software JADE (MDI).

3.5.13 Singe-crystal X-ray diffraction measurement of lysozyme@HuHF-PIX.

Lysozyme@HuHF-PIX samples were freshly prepared in sitting drop trays, as described above. A single crystal was cryoprotected in perfluoropolyether, transferred to a Bruker Microstar APEX II CCD diffractometer equipped with Cu Kα radiation (λ = 1.54178 Å), and measured at 100 K.

3.5.14 Monitoring protein encapsulation efficiency in ^{POS}HuHF-PIX.

Freshly prepared ^{POS}HuHF-PIX were prepared (as described above) and transferred into an Eppendorf tube containing 500 mL of cyt-*c* or lysozyme (200 mM in 20 mM MES pH 6.0). The tube was placed on a gel rocker to keep the crystals suspended. Aliquots of the supernatant were taken and analyzed via UV-vis spectrometry (Cary 60) to measure the encapsulation over time.

3.5.15 Assessment of protein encapsulation in PIX.

Freshly prepared HuHF-PIX were transferred into Eppendorf tubes containing 500 mL of cyt-*c* or lysozyme (200 mM) and placed on a gel rocker to keep the crystals suspended. Aliquots (10–60 mL) of the supernatant were taken out at predetermined time points, diluted, and analyzed via UV-vis spectrometry to calculate the protein concentration in the supernatant using the following extinction coefficients: cyt-*c* (ε_{410} = 106,000 $M^{-1}cm^{-1}$) and lysozyme (ε_{280} = 38,940 $M^{-1}cm^{-1}$). The buffer solutions used for dilutions contained 20 mM acetate (pH 4.0), 20 mM MES (pH 6.0), or 20 mM HEPES (pH 8.0).

3.5.16 Synthesis of rhodamine-labeled proteins.

1-mL solutions containing 20 mg of lysozyme or cyt-*c* were buffered in 50 mM HEPES (pH 8.0). 1 mM (final concentration) of NHS-rhodamine (dissolved in DMF) was added directly into these solutions. The reactions were carried out at 4°C overnight, protected from light. The rhodamine-labeled products were then washed thoroughly with the same 50 mM HEPES buffer solution and concentrated using Amicon Ultra-0.5 centrifugal filter units (3 kDa MWCO).

3.5.17 Monitoring the uptake and release of guest proteins from HuHF-PIX with light microscopy.

Individual crystals of HuHF-PIX were transferred with a mounted CryoLoop onto a glass slide with a microscopic ruler (OMAX). All images and videos were obtained on an SZX7

(Olympus) microscope equipped with an Infinity1 CCD (Lumenera). A 10-μL solution containing 200 μM of rhodamine-labeled cyt-*c* or lysozyme (20 mM MES, pH 6.0) was added to the drops containing HuHF-PIX crystals. After 5 min, the suspensions were exchanged into solutions of 20 mM acetate (pH ≤4) to initiate the release of cargo from the crystal. The uptake-release process was repeated for multiple cycles.

3.5.18 Confocal microscopy measurements of guest-loaded HuHF-PIX.

Guest-loaded HuHF-PIX samples were transferred onto a glass slide and the fluorescence was monitored with a 10x air objective on the confocal microscope (Zeiss), using a filter to collect 500–550 nm (green channel for GFP) or 575–600 nm (red channel for rhodamine) light. Differential interference contrast (DIC) and fluorescence (488 nm excitation for green channel, 564 nm for red channel) images were captured using 100-ms exposure.

3.5.19 Monitoring the guest-protein uptake with confocal microscopy.

Single crystals of HuHF-PIX were placed onto a glass slide, and 10-mL solutions of rhodamine-labeled cyt-*c* or lysozyme (20 mM MES pH 6.0) were added on top to initiate cargo uptake. The uptake was monitored with a 10x air objective on the confocal microscope using the red channel, as described above.

3.5.20 pH-dependent release of guest proteins from HuHF-PIX.

Freshly prepared cyt-*c*@HuHF-PIX or lysozyme@HuHF-PIX samples were washed with a 20 mM MES solution (pH 6.0) and then placed in a 500-mL solution of 20 mM acetate (pH ≤4) to initiate release of guest proteins 10-mL aliquots of the supernatant were taken at selected time points and analyzed by UV-vis spectrometry upon dilution.

3.5.21 Uptake-release cycling of cargo using HuHF-PIX.

Freshly prepared HuHF-PIX samples were placed in a 500 mL solution (20 mM MES, pH 6.0) containing cyt-*c* or lysozyme. After 30 min, the crystals were washed with a 20 mM MES solution (pH 6.0) at least three times and were placed into a 500 µL solution of 20 mM acetate (pH ≤4) to trigger protein release. After 10 min, the supernatant was carefully extracted and the crystals were washed again with a 20 mM MES solution (pH 6.0) three times. Guest protein reloading was initiated by the addition of 500 µL solutions of cyt-*c* or lysozyme (20 mM MES pH 6.0) into the tubes. This loading and release process was repeated for a total of 7 cycles. The protein concentration in the supernatant was measured by UV-vis spectrometry after each loading (30 min) and release (10 min) step.

3.5.22 Ionic-strength dependent release of protein@HuHF-PIX.

Bulk amounts of rhodamine-labeled lysozyme@HuHF-PIX samples were freshly prepared in 20 mM MES (pH 6.0). The samples were then placed in a 500-µL solution containing 0.1 M NaCl, 0.2 M NaCl, 0.1 M $CaCl_2$, or 0.2 M $CaCl_2$ in 20 mM MES (pH 6.0) to initiate the release of guest proteins. At select time points, 10-µL aliquots of the supernatant were taken and used to measure the concentration of released lysozyme by UV-vis spectrometry. The release of rhodamine-labeled lysozyme was monitored at 550 nm.

3.5.23 Monitoring activity of lysozyme@HuHF-PIX via EnzChek.

Lysozyme activity was determined by monitoring the fluorescence intensity increase upon degradation of the fluorescently labeled *Micrococcus lysodeikticus* bacterial cell walls (EnzCheck Lysozyme Assay, Thermo Fisher Scientific). The cell wall substrate was diluted to 50 µg/mL using 20 mM MES solution (pH 6.0). 50 µL of the substrate suspension was mixed with 50 µL of three different lysozyme samples. (1) Free lysozyme (30 mM) in 20 mM MES (pH 6.0). (2) Free lysozyme (30 mM) after being released from HuHF-PIX entrapment. Lysozyme@HuHF-PIX

samples were dissolved (as described above) and filtered with a 30 kDa MWCO spin concentrator to isolate lysozyme from the mixture. The filtrate was collected and buffer exchanged into 20 mM MES (pH 6.0) using a 3 kDa MWCO spin concentrator. (3) EDC-crosslinked lysozyme@HuHF-PIX. Freshly prepared lysozyme@HuHF-PIX samples were incubated in a 5 mM EDC solution (20 mM MES, pH 6.0) at room temperature. After 10 min, the crystals were washed and used for activity assays. Each sample was placed in the substrate suspension at 37 °C for 30 min, and the supernatant fluorescence (ex/em: 485/530 nm) was measuring by a 96-well plate reader (Tecan).

3.5.24 Assessment of the reversible redox activity of cyt-c in cyt-*c*@HuHF-PIX via UV-vis.

Cyt-*c*@HuHF-PIX crystals were transferred to a clean Eppendorf tube (1.5 mL) containing 500 µL of a 5 mM EDC solution (20 mM MES, pH 6.0) and placed on a gel rocker to keep the crystals suspended. After 10 min, the freshly cross-linked crystals were washed with a 500 mL solution of 1 M NaCl twice, followed by a wash with a 20 mM Tris solution (pH 8.0) until the UV-vis spectrum of the supernatant showed no cyt-*c* in the solution. The crystals were then suspended with 500 µL of the buffer solution and transferred into a quartz cuvette. Before measuring the UV-vis spectrum, the solution was agitated with a pipette to suspend the crystals. The crystal suspension was measured at least 5 times. Then, the crystals were placed back into the Eppendorf tube, and the solution was exchanged into 10 mM sodium ascorbate in a 20 mM Tris solution (pH 8.0). After 60 min, the crystals were measured via UV-vis and placed back into the tube. The solution was exchanged into 10 mM H_2O_2 in 20 mM Tris (pH 8.0) and measured again. Lastly, the H_2O_2 was decanted, exchanged for 10 mM sodium ascorbate in 20 mM Tris (pH 8.0) and measured via UV-vis. The crystals were incubated in the newly exchanged solution for 60 min before UV-vis measurements.

3.5.25 Monitoring cyt-*c* activity for ABTS oxidation *in crystallo* and in solution.

Cross-linked samples of cyt-*c*@HuHF-PIX were prepared as described above. The solution was then replaced with a 500 mL mixture containing ABTS (30 mM), H_2O_2 (1 mM), and 20 mM Tris (pH 8.0). The UV-vis spectra of aliquots from the supernatant were collected at select timepoints; the aliquots were promptly added back into the reaction tube. Conditions with free cyt-*c* (2 mM) in 20 mM MES (pH 6.0) was also tested as a control.

3.5.26 Trypsin digestion studies.

Rhodamine-labeled cyt-*c* and lysozyme were used to prepare protein@HuHF-PIX samples in large scale. The protein@HuHF-PIX crystals were then placed in an Eppendorf tube with 100 µL solution of 10 mM Tris (pH 8.0). A 10-µL solution containing trypsin (0.1 mg/mL) (MS Grade Pierce trypsin protease, Thermo Fisher Scientific) and 5 mM dithiothreitol (DTT) was added into the tubes, and left to incubate at 37 °C. After 1 h, the crystals were washed with a 10 mM Tris solution (pH 8.0) to remove excess trypsin. Aliquots (2 mL) of the treated protein@HuHF-PIX samples, suspended in minimal solution, were placed into a tube containing 0.5 M EDTA (8 µL). The crystals immediately dissolved, and the resulting solutions were prepared for gel electrophoretic analysis (15% SDS-PAGE).

3.5.27 Preparation and characterization of GFP@HuHF-PIX samples.

Freshly prepared HuHF-PIX were washed multiple times with 500 µL solutions of 20 mM MES (pH 6.0). After a third wash, a 500 µL solution of GFP (200 µM in 20 mM MES, pH 6.0) was added to the crystals and placed on a gel rocker. After 30 min, 100 µL of a 4 M NaCl solution was added portion-wise (4 x 25 µL) to induce PIX contraction and the concomitant entrapment of GFP. Excess protein solution was decanted, and the crystals were washed with a solution

containing 5 M NaCl and 1 M $CaCl_2$. Confocal imaging (500-550 nm) and SAXS measurements were performed as described above.

Table 3.1. Crystallization conditions for HuHF and ^{POS}HuHF crystals.

HuHF	Stock protein solution	25 µM in 15 mM Tris (pH 7.4), 150 mM NaCl
	Reservoir	500 µL total volume: 50 mM HEPES (pH 7.0), 12 mM $CaCl_2$
	Sitting drop	5 µL reservoir, 5 µL of 25 µM HuHF
	Cell culture well	100 µL reservoir, 100 µL of 25 µM HuHF
^{POS}HuHF	Stock protein solution	30 µM in 15 mM Tris (pH 7.5), 1 M NaCl
	Reservoir	500 µL total volume: 25 mM HEPES (pH 7.0), 90 mM $CaCl_2$, 1,550 mM NaCl
	Sitting drop	5 µL reservoir, 5 µL of 25 µM ^{POS}HuHF
	Cell culture well	100 µL reservoir, 100 µL of 25 µM ^{POS}HuHF

Calculations 3.1 – Determination of polymer content in PIX

Compound	Molecular weight (g/mol)	Concentration
HuHF	21,056	-
Sodium acrylate	94.04	917 mM
Acrylamide	71.08	352 mM
N,N′-methylenebis(acrylamide)	154.17	13 mM

Volume of unit cell and interstitial space

Note: There are 4 complete HuHF cages in one *F*432 unit cell and the interstitial volume occupies 40% of the lattice.[57]

$$\text{Volume of unit cell} = a^3 = (18.1\text{ nm})^3 = 5929.7\ nm^3$$
$$\text{Volume of interstitial space} = 5929.7\ nm^3 \times 40\ \% = 2371.9\ nm^3$$

Mass of HuHF in one unit cell

$$24\text{ HuHF monomers} \times 4\ cages \times 21{,}056\ Da \times \frac{1}{6.022 * 10^{23}} = 3.356 \times 10^{-18}\ g$$

Mass of sodium acrylate in one unit cell

$$917\text{ mM} \times 2371.9\ nm^3 \times 94.04\ Da = 2.045 \times 10^{-19}\ g$$

Mass of acrylamide in one unit cell

$$352\text{ mM} \times 2371.9\ nm^3 \times 71.08\ Da = 5.934 \times 10^{-20}\ g$$

Mass of *N,N′*-methylenebis(acrylamide) in one unit cell

$$13\text{ mM} \times 2371.9\ nm^3 \times 154.17\ Da = 4.749 \times 10^{-21}\ g$$

Mass percentage of polymer precursors in one unit cell

$$\frac{2.045 \times 10^{-19}\ g + 5.934 \times 10^{-20}\ g + 4.749 \times 10^{-21}\ g}{3.356 \times 10^{-18}\ g + 2.045 \times 10^{-19}\ g + 5.934 \times 10^{-20}\ g + 4.749 \times 10^{-21}\ g} \times 100$$
$$= \mathbf{7.41}\ \%$$

Calculations 3.2 - Determination of protein compositions in PIX by HPLC

Standard curve of proteins from HPLC analysis

Protein	Point-slope formula for standard curves
Cytochrome *c*	$y = 2.269x + 6.727$
Lysozyme	$y = 1.431x - 2.352$
HuHF	$y = 0.602x - 0.967$

y = peak area
x = concentration

Quantification of proteins unknowns from HPLC analysis

Cyt-*c*@HuHF-PIX			
pH	**Metric**	**HuHF**	**Cytochrome *c***
pH 6.0	Peak area (mAu*min)	20.4	56.1
	Calculated concentration (μM)	35.5	21.8
	[HuHF]:[cyt-c] ratio	1.63	
	Mass percentage	26 %	
pH 8.0	Peak area (mAu*min)	27.0	160.7
	Calculated concentration (μM)	46.4	67.8
	[HuHF]:[cyt-*c*] ratio	0.68	
	Mass percentage	46 %	

Lysozyme@HuHF-PIX			
pH	**Metric**	**HuHF**	**Lysozyme**
pH 6.0	Peak area (mAu*min)	15.7	18.4
	Calculated concentration (μM)	27.7	14.0
	[HuHF]:[lysozyme] ratio	1.97	
	Mass percentage	26 %	
pH 8.0	Peak area (mAu*min)	24.0	55.3
	Calculated concentration (μM)	41.5	39.8
	[HuHF]:[lysozyme] ratio	1.04	
	Mass percentage	39 %	

Calculations 3.3 - Determination of guest protein concentrations in PIX

Unit cell and interstitial volume of cyt-*c*@HuHF-PIX

$$\text{Unit cell edge length of cytochrome } c\text{@PIX from SAXS (}\mathbf{Figure\ 3.2c}\text{)} = 20.6\ nm$$

$$\text{Volume of cytochrome } c\text{@PIX unit cell} = a^3 = (20.6\ \text{nm})^3 = 8741.8\ nm^3$$

$$\text{Volume of interstitial space} = 8741.8\ nm^3 \times 40\ \% = 3496.7\ nm^3$$

Note: There are 4 HuHF cages in one *F*432 unit cell and the interstitial volume composes 40% of the lattice.[57]

Concentration of HuHF in unit cell

$$[\text{HuHF}] = \frac{4\ cages}{8741.8\ nm^3} \times \frac{1\ nm^3}{10^{-21}\ cm^3} \times \frac{1\ cm^3}{1\ mL} \times \frac{1000\ mL}{L} \times \frac{1\ mol}{6.022 \times 10^{23}} \times \frac{24\ monomers}{1\ cage} = 18.2\ mM$$

Mass of HuHF in one unit cell

$$24\ \text{HuHF monomers} \times 4\ cages \times 21{,}056\ Da = 2{,}021{,}376\ Da$$

Molecules of cytochrome *c*

$$[\text{cytochrome } c]_{unit\ cell} = 18.2\ mM \times \frac{1}{1.63^{\blacklozenge}} = 11.2\ mM$$

◆ The [HuHF]:[cyt-*c*] ratio is calculated using SEC-HPLC analysis (**Figure 3.4**).

$$[\text{cytochrome } c]_{interstitial\ space} = \frac{11.2\ mM \times 8741.8\ nm^3}{3496.7\ nm^3} = 28.0\ mM$$

$$\text{Molecules of cytochrome } c = \frac{28.0\ mmol}{L} \times \frac{1\ L}{1000\ cm^3} \times \frac{10^{-21}\ cm^3}{1\ nm^3} \times 3496.7\ nm^3 \times \frac{1\ mol}{10^3\ mmol} \times \frac{6.022 \times 10^{23}}{1\ mol} = 58\ \text{cytochrome } c\ \text{molecules}$$

Mass of cytochrome *c* in one unit cell

$$58\ \text{cytochrome } c\ \text{molecules} \times 12{,}270\ \text{Da} = 711{,}660\ \text{Da}$$

Mass percentage of cytochrome *c*

$$\frac{711{,}660\ \text{Da}}{2{,}021{,}376\ Da + 711{,}660\ \text{Da}} \times 100 = 26\ \%$$

Theoretical number of cytochrome *c* allowed in cyt-*c*@HuHF-PIX interstitial volume

Cytochrome *c* volume: $2.5\ nm \times 2.5\ nm \times 3.5\ nm = 22\ nm^3$

$$\frac{3496.7\ nm^3}{22\ nm^3} = 158 \text{ cytochrome } c \text{ molecules}$$

Unit cell and interstitial volume of lysozyme@HuHF-PIX

Unit cell edge length of lysozyme@PIX from **Figure 3.5** $= 18.1\ nm * 1.26 = 22.8\ nm$

Volume of lysozyme@PIX unit cell $= a^3 = (22.8\ \text{nm})^3 = 11{,}852.3\ nm^3$

Volume of interstitial space $= 11{,}852.3\ nm^3 \times 40\ \% = 4740.9\ nm^3$

Concentration of HuHF in unit cell

$$[\text{HuHF}] = \frac{4\ cages}{11{,}852.3\ nm^3} \times \frac{1\ nm^3}{10^{-21}\ cm^3} \times \frac{1\ cm^3}{1\ mL} \times \frac{1000\ mL}{L} \times \frac{1\ mol}{6.022 \times 10^{23}} \times \frac{24\ monomers}{1\ cage}$$
$$= 13.4\ mM$$

Mass of HuHF in one unit cell

$$24 \text{ HuHF monomers} \times 4\ cages \times 21{,}056\ Da = 2{,}021{,}376\ Da$$

Molecules of lysozyme

$$[\text{lysozyme}]_{unit\ cell} = 13.4\ mM \times \frac{1}{1.97^{\blacklozenge}} = 6.83\ mM$$

◆ The [HuHF]:[lysozyme] ratio is calculated using -SEC-HPLC analysis (**Figure 3.4**).

$$[\text{lysozyme}]_{interstitial\ space} = \frac{6.83\ mM \times 11{,}852.3\ nm^3}{4740.9\ nm^3} = 17.1\ mM$$

Molecules of lysozyme

$$= \frac{17.1\ mmol}{L} \times \frac{1\ L}{1000\ cm^3} \times \frac{10^{-21}\ cm^3}{1\ nm^3} \times 4740.9\ nm^3 \times \frac{1\ mol}{10^3\ mmol}$$
$$\times \frac{6.022 \times 10^{23}}{1\ mol} = 48 \text{ lysozyme molecules}$$

Mass of lysozyme in one unit cell

$$48 \text{ lysozyme molecules} \times 14{,}307\ \text{Da} = 686{,}736\ \text{Da}$$

Mass percentage of lysozyme

$$\frac{686{,}736\ \text{Da}}{2{,}021{,}376\ Da + 686{,}736\ \text{Da}} \times 100 = 26\ \%$$

Theoretical number of lysozyme allowed in lysozyme@HuHF-PIX interstitial volume

Lysozyme volume: $3.0\ nm\ \times\ 3.0\ nm \times\ 5.0\ nm = 45\ nm^3$

$$\frac{4740.9\ nm^3}{45\ nm^3} = 105 \text{ lysozyme molecules}$$

3.6 Acknowledgements

We thank the members of the Tezcan group for helpful discussions and the following colleagues for assistance: Prof. Suckjoon Jun for the GFP gene, Dr. Ivan Rajkovic for his help with the SAXS measurements, and Prof. W. J. Rappel for confocal microscopy. This work was supported by US Department of Energy (BES, Division of Materials Sciences, Biomolecular Materials Program, DE-SC0003844; for the development of the PIX concept and protein encapsulation), US Army Research Office (W911NF-19-1-0228, for PIX characterization, structural measurements), UC San Diego Materials Research Science and Engineering Center (UCSD MRSEC, for additional PIX characterization and structural measurements), supported by the National Science Foundation (Grant DMR-2011924). Some confocal microscopy experiments were conducted at the UCSD School of Medicine Microscopy Core, supported by the NIH, NINDS P30 NS047101. SAXS data were collected at SSRL, which is supported by the DOE Office of Science, Office of Basic Energy Sciences, under Contract DE-AC02-76SF00515. Single-crystal X-ray diffraction data were collected at the UCSD Crystallography Facility. F.A.T. also acknowledges the John Simon Guggenheim Memorial Foundation for a fellowship.

Chapter 3 is reproduced, in part, with permission, from: Han, K., Na, Y., Zhang, L., Tezcan, F. A. "Dynamic, Polymer-Integrated Crystals for Efficient, Reversible Protein Encapsulation" *Journal of the American Chemical Society* **2022** *144* (23), 10139-10144. The dissertation author was the primary author on all reprinted materials.

3.7 References

1. Brändén, C.; J., T., *Introduction to protein structure*. Garland Pub.: New York, NY, 2009.

2. Cooper, G. M. H. R. E., *The cell : a molecular approach*. ASM Press ; Sinauer Associates: Washington, D.C.; Sunderland, Mass., 2009.

3. Zhu, J.; Avakyan, N.; Kakkis, A.; Hoffnagle, A. M.; Han, K.; Li, Y.; Zhang, Z.; Choi, T. S.; Na, Y.; Yu, C. J.; Tezcan, F. A., Protein Assembly by Design. *Chem. Rev.* **2021,** *121*, 13701-13796.

4. Chen, X.; Gao, C.; Guo, L.; Hu, G.; Luo, Q.; Liu, J.; Nielsen, J.; Chen, J.; Liu, L., DCEO Biotechnology: Tools To Design, Construct, Evaluate, and Optimize the Metabolic Pathway for Biosynthesis of Chemicals. *Chem. Rev.* **2018,** *118*, 4-72.

5. Schrittwieser, J. H.; Velikogne, S.; Hall, M.; Kroutil, W., Artificial Biocatalytic Linear Cascades for Preparation of Organic Molecules. *Chem. Rev.* **2018,** *118*, 270-348.

6. Bornscheuer, U. T.; Huisman, G. W.; Kazlauskas, R. J.; Lutz, S.; Moore, J. C.; Robins, K., Engineering the third wave of biocatalysis. *Nature* **2012,** *485*, 185-94.

7. Qin, X.; Yu, C.; Wei, J.; Li, L.; Zhang, C.; Wu, Q.; Liu, J.; Yao, S. Q.; Huang, W., Rational Design of Nanocarriers for Intracellular Protein Delivery. *Adv. Mater.* **2019,** *31*, 1902791-1902791.

8. Devine, P. N.; Howard, R. M.; Kumar, R.; Thompson, M. P.; Truppo, M. D.; Turner, N. J., Extending the application of biocatalysis to meet the challenges of drug development. *Nat. Rev. Chem.* **2018,** *2*, 409-421.

9. Iyer, P. V.; Ananthanarayan, L., Enzyme stability and stabilization—Aqueous and non-aqueous environment. *Process Biochem.* **2008,** *43*, 1019-1032.

10. Chakraborti, S.; Lin, T.-Y.; Glatt, S.; Heddle, J. G., Enzyme encapsulation by protein cages. *RSC Adv.* **2020,** *10*, 13293-13301.

11. Panganiban, B.; Qiao, B.; Jiang, T.; DelRe, C.; Obadia, M. M.; Nguyen, T. D.; Smith, A. A. A.; Hall, A.; Sit, I.; Crosby, M. G.; Dennis, P. B.; Drockenmuller, E.; Olvera de la Cruz, M.; Xu, T., Random heteropolymers preserve protein function in foreign environments. *Science* **2018,** *359*, 1239-1243.

12. Doonan, C.; Ricco, R.; Liang, K.; Bradshaw, D.; Falcaro, P., Metal-Organic Frameworks at the Biointerface: Synthetic Strategies and Applications. *Acc. Chem. Res.* **2017,** *50*, 1423-1432.

13. Luzuriaga, M. A.; Welch, R. P.; Dharmarwardana, M.; Benjamin, C. E.; Li, S.; Shahrivarkevishahi, A.; Popal, S.; Tuong, L. H.; Creswell, C. T.; Gassensmith, J. J., Enhanced Stability and Controlled Delivery of MOF-Encapsulated Vaccines and Their Immunogenic Response In Vivo. *ACS Appl. Mater. Interfaces.* **2019,** *11*, 9740-9746.

14. Liang, W.; Xu, H.; Carraro, F.; Maddigan, N. K.; Li, Q.; Bell, S. G.; Huang, D. M.; Tarzia, A.; Solomon, M. B.; Amenitsch, H.; Vaccari, L.; Sumby, C. J.; Falcaro, P.; Doonan, C. J., Enhanced

Activity of Enzymes Encapsulated in Hydrophilic Metal-Organic Frameworks. *J. Am. Chem. Soc.* **2019,** *141*, 2348-2355.

15. Chen, T. T.; Yi, J. T.; Zhao, Y. Y.; Chu, X., Biomineralized Metal-Organic Framework Nanoparticles Enable Intracellular Delivery and Endo-Lysosomal Release of Native Active Proteins. *J. Am. Chem. Soc.* **2018,** *140*, 9912-9920.

16. Margolin, A. L.; Navia, M. A., Protein Crystals as Novel Catalytic Materials. *Angew. Chem., Int. Ed.* **2001,** *40*, 2204-2222.

17. Lian, X.; Fang, Y.; Joseph, E.; Wang, Q.; Li, J.; Banerjee, S.; Lollar, C.; Wang, X.; Zhou, H. C., Enzyme-MOF (metal-organic framework) composites. *Chem. Soc. Rev.* **2017,** *46*, 3386-3401.

18. Chen, Y.; Lykourinou, V.; Vetromile, C.; Hoang, T.; Ming, L. J.; Larsen, R. W.; Ma, S., How can proteins enter the interior of a MOF? Investigation of cytochrome c translocation into a MOF consisting of mesoporous cages with microporous windows. *J. Am. Chem. Soc.* **2012,** *134*, 13188-91.

19. Liang, W.; Wied, P.; Carraro, F.; Sumby, C. J.; Nidetzky, B.; Tsung, C. K.; Falcaro, P.; Doonan, C. J., Metal-Organic Framework-Based Enzyme Biocomposites. *Chem. Rev.* **2021,** *121*, 1077-1129.

20. Chen, Y.; Li, P.; Zhou, J.; Buru, C. T.; Dordevic, L.; Li, P.; Zhang, X.; Cetin, M. M.; Stoddart, J. F.; Stupp, S. I.; Wasielewski, M. R.; Farha, O. K., Integration of Enzymes and Photosensitizers in a Hierarchical Mesoporous Metal-Organic Framework for Light-Driven CO2 Reduction. *J. Am. Chem. Soc.* **2020,** *142*, 1768-1773.

21. Liang, W.; Carraro, F.; Solomon, M. B.; Bell, S. G.; Amenitsch, H.; Sumby, C. J.; White, N. G.; Falcaro, P.; Doonan, C. J., Enzyme Encapsulation in a Porous Hydrogen-Bonded Organic Framework. *J. Am. Chem. Soc.* **2019,** *141*, 14298-14305.

22. Chen, G.; Huang, S.; Shen, Y.; Kou, X.; Ma, X.; Huang, S.; Tong, Q.; Ma, K.; Chen, W.; Wang, P.; Shen, J.; Zhu, F.; Ouyang, G., Protein-directed, hydrogen-bonded biohybrid framework. *Chem* **2021,** *7*, 2722-2742.

23. Li, P.; Moon, S. Y.; Guelta, M. A.; Harvey, S. P.; Hupp, J. T.; Farha, O. K., Encapsulation of a Nerve Agent Detoxifying Enzyme by a Mesoporous Zirconium Metal-Organic Framework Engenders Thermal and Long-Term Stability. *J. Am. Chem. Soc.* **2016,** *138*, 8052-5.

24. Tang, J.; Liu, J.; Zheng, Q.; Li, W.; Sheng, J.; Mao, L.; Wang, M., In-Situ Encapsulation of Protein into Nanoscale Hydrogen-Bonded Organic Frameworks for Intracellular Biocatalysis. *Angew. Chem., Int. Ed.* **2021,** *60*, 22315-22321.

25. Wang, C.; Liao, K., Recent Advances in Emerging Metal- and Covalent-Organic Frameworks for Enzyme Encapsulation. *ACS Appl. Mater. Interfaces.* **2021,** *13*, 56752-56776.

26. Majewski, M. B.; Howarth, A. J.; Li, P.; Wasielewski, M. R.; Hupp, J. T.; Farha, O. K., Enzyme encapsulation in metal–organic frameworks for applications in catalysis. *CrystEngComm* **2017,** *19*, 4082-4091.

27. Lyu, F.; Zhang, Y.; Zare, R. N.; Ge, J.; Liu, Z., One-pot synthesis of protein-embedded metal-organic frameworks with enhanced biological activities. *Nano Lett.* **2014,** *14*, 5761-5.

28. Khanh Nguyen, T.; Toan Pham, T.; Ueno, T., Engineering of protein crystals for development of bionanomaterials. *Jpn. J. Appl. Phys.* **2019,** *58*, SI0802.

29. Kowalski, A. E.; Johnson, L. B.; Dierl, H. K.; Park, S.; Huber, T. R.; Snow, C. D., Porous protein crystals as scaffolds for enzyme immobilization. *Biomater Sci* **2019,** *7*, 1898-1904.

30. Heater, B. S.; Yang, Z.; Lee, M. M.; Chan, M. K., In Vivo Enzyme Entrapment in a Protein Crystal. *J. Am. Chem. Soc.* **2020,** *142*, 9879-9883.

31. Heater, B. S.; Lee, M. M.; Chan, M. K., Direct production of a genetically-encoded immobilized biodiesel catalyst. *Sci. Rep.* **2018,** *8*, 12783.

32. Abe, S.; Ijiri, H.; Negishi, H.; Yamanaka, H.; Sasaki, K.; Hirata, K.; Mori, H.; Ueno, T., Design of Enzyme-Encapsulated Protein Containers by In Vivo Crystal Engineering. *Adv. Mater.* **2015,** *27*, 7951-6.

33. Nguyen, T. K.; Abe, S.; Kasamatsu, M.; Maity, B.; Yamashita, K.; Hirata, K.; Kojima, M.; Ueno, T., In-Cell Engineering of Protein Crystals with Nanoporous Structures for Promoting Cascade Reactions. *ACS Appl. Nano Mater.* **2021,** *4*, 1672-1681.

34. Deng, H.; Grunder, S.; Cordova, K. E.; Valente, C.; Furukawa, H.; Hmadeh, M.; Gandara, F.; Whalley, A. C.; Liu, Z.; Asahina, S.; Kazumori, H.; O'Keeffe, M.; Terasaki, O.; Stoddart, J. F.; Yaghi, O. M., Large-pore apertures in a series of metal-organic frameworks. *Science* **2012,** *336*, 1018-23.

35. Lian, X.; Chen, Y. P.; Liu, T. F.; Zhou, H. C., Coupling two enzymes into a tandem nanoreactor utilizing a hierarchically structured MOF. *Chem Sci.* **2016,** *7*, 6969-6973.

36. Chen, G.; Kou, X.; Huang, S.; Tong, L.; Shen, Y.; Zhu, W.; Zhu, F.; Ouyang, G., Modulating the Biofunctionality of Metal-Organic-Framework-Encapsulated Enzymes through Controllable Embedding Patterns. *Angew. Chem., Int. Ed.* **2020,** *59*, 2867-2874.

37. Liang, K.; Ricco, R.; Doherty, C. M.; Styles, M. J.; Bell, S.; Kirby, N.; Mudie, S.; Haylock, D.; Hill, A. J.; Doonan, C. J.; Falcaro, P., Biomimetic mineralization of metal-organic frameworks as protective coatings for biomacromolecules. *Nat. Commun.* **2015,** *6*, 7240.

38. Maddigan, N. K.; Tarzia, A.; Huang, D. M.; Sumby, C. J.; Bell, S. G.; Falcaro, P.; Doonan, C. J., Protein surface functionalisation as a general strategy for facilitating biomimetic mineralisation of ZIF-8. *Chem Sci.* **2018,** *9*, 4217-4223.

39. Nair, M. S.; Lee, M. M.; Bonnegarde-Bernard, A.; Wallace, J. A.; Dean, D. H.; Ostrowski, M. C.; Burry, R. W.; Boyaka, P. N.; Chan, M. K., Cry protein crystals: a novel platform for protein delivery. *PLoS One* **2015,** *10*, e0127669.

40. Hashimoto, T.; Ye, Y.; Ui, M.; Ogawa, T.; Matsui, T.; Tanaka, Y., Protein encapsulation in the hollow space of hemocyanin crystals containing a covalently conjugated ligand. *Biochem. Biophys. Res. Commun.* **2019,** *514*, 31-36.

41. Huber, T. R.; Hartje, L. F.; McPherson, E. C.; Kowalski, A. E.; Snow, C. D., Programmed Assembly of Host-Guest Protein Crystals. *Small* **2017,** *13*, 1602703-9.

42. Hashimoto, T.; Ye, Y.; Matsuno, A.; Ohnishi, Y.; Kitamura, A.; Kinjo, M.; Abe, S.; Ueno, T.; Yao, M.; Ogawa, T.; Matsui, T.; Tanaka, Y., Encapsulation of biomacromolecules by soaking and co-crystallization into porous protein crystals of hemocyanin. *Biochem. Biophys. Res. Commun.* **2019,** *509*, 577-584.

43. Korpi, A.; Ma, C.; Liu, K.; Nonappa; Herrmann, A.; Ikkala, O.; Kostiainen, M. A., Self-Assembly of Electrostatic Cocrystals from Supercharged Fusion Peptides and Protein Cages. *ACS Macro. Lett.* **2018,** *7*, 318-323.

44. Selivanovitch, E.; Uchida, M.; Lee, B.; Douglas, T., Substrate Partitioning into Protein Macromolecular Frameworks for Enhanced Catalytic Turnover. *ACS Nano* **2021,** *15*, 15687-15699.

45. Chen, Y.; Li, P.; Modica, J. A.; Drout, R. J.; Farha, O. K., Acid-Resistant Mesoporous Metal-Organic Framework toward Oral Insulin Delivery: Protein Encapsulation, Protection, and Release. *J. Am. Chem. Soc.* **2018,** *140*, 5678-5681.

46. Huo, J.; Aguilera-Sigalat, J.; El-Hankari, S.; Bradshaw, D., Magnetic MOF microreactors for recyclable size-selective biocatalysis. *Chem Sci.* **2015,** *6*, 1938-1943.

47. Yang, Z.; Zheng, J.; Chan, C. F.; Wong, I. L. K.; Heater, B. S.; Chow, L. M. C.; Lee, M. M. M.; Chan, M. K., Targeted delivery of antimicrobial peptide by Cry protein crystal to treat intramacrophage infection. *Biomaterials* **2019,** *217*, 119286.

48. Hartje, L. F.; Bui, H. T.; Andales, D. A.; James, S. P.; Huber, T. R.; Snow, C. D., Characterizing the Cytocompatibility of Various Cross-Linking Chemistries for the Production of Biostable Large-Pore Protein Crystal Materials. *ACS Biomater. Sci. Eng.* **2018,** *4*, 826-831.

49. Nguyen, T. K.; Negishi, H.; Abe, S.; Ueno, T., Construction of supramolecular nanotubes from protein crystals. *Chem Sci.* **2019,** *10*, 1046-1051.

50. Vermonden, T.; Censi, R.; Hennink, W. E., Hydrogels for protein delivery. *Chem. Rev.* **2012,** *112*, 2853-88.

51. Chou, C.; Syu, S.; Chang, J. H.; Aimar, P.; Chang, Y., Bioinspired Pseudozwitterionic Hydrogels with Bioactive Enzyme Immobilization via pH-Responsive Regulation. *Langmuir* **2019,** *35*, 1909-1918.

52. Liu, C.; Wan, T.; Wang, H.; Zhang, S.; Ping, Y.; Cheng, Y., A boronic acid-rich dendrimer with robust and unprecedented efficiency for cytosolic protein delivery and CRISPR-Cas9 gene editing. *Sci. Adv.* **2019,** *5*, eaaw8922.

53. Fisher, S. A.; Baker, A. E. G.; Shoichet, M. S., Designing Peptide and Protein Modified Hydrogels: Selecting the Optimal Conjugation Strategy. *J. Am. Chem. Soc.* **2017,** *139*, 7416-7427.

54. Lim, S.; Jung, G. A.; Muckom, R. J.; Glover, D. J.; Clark, D. S., Engineering bioorthogonal protein-polymer hybrid hydrogel as a functional protein immobilization platform. *Chem. Commun.* **2019,** *55*, 806-809.

55. Rehmann, M. S.; Skeens, K. M.; Kharkar, P. M.; Ford, E. M.; Maverakis, E.; Lee, K. H.; Kloxin, A. M., Tuning and Predicting Mesh Size and Protein Release from Step Growth Hydrogels. *Biomacromolecules* **2017,** *18*, 3131-3142.

56. Kirchhof, S.; Abrami, M.; Messmann, V.; Hammer, N.; Goepferich, A. M.; Grassi, M.; Brandl, F. P., Diels-Alder Hydrogels for Controlled Antibody Release: Correlation between Mesh Size and Release Rate. *Mol. Pharm.* **2015,** *12*, 3358-68.

57. Zhang, L.; Bailey, J. B.; Subramanian, R. H.; Groisman, A.; Tezcan, F. A., Hyperexpandable, self-healing macromolecular crystals with integrated polymer networks. *Nature* **2018,** *557*, 86-91.

58. Han, K.; Bailey, J. B.; Zhang, L.; Tezcan, F. A., Anisotropic Dynamics and Mechanics of Macromolecular Crystals Containing Lattice-Patterned Polymer Networks. *J. Am. Chem. Soc.* **2020,** *142*, 19402-19410.

59. Liu, Y.; Ma, Y.; Yang, J.; Diercks, C. S.; Tamura, N.; Jin, F.; Yaghi, O. M., Molecular Weaving of Covalent Organic Frameworks for Adaptive Guest Inclusion. *J. Am. Chem. Soc.* **2018,** *140*, 16015-16019.

60. Zhang, L.; Du, J., A sensitive and label-free trypsin colorimetric sensor with cytochrome c as a substrate. *Biosens. Bioelectron.* **2016,** *79*, 347-52.

61. Canfield, R. E., The Amino Acid Secpence of Egg White Lysozyme *J. Biol. Chem.* **1963,** *238*, 2698-2707.

62. Telford, J. R.; Tezcan, F. A.; Gray, H. B.; Winkler, J. R., Role of ligand substitution in ferrocytochrome c folding. *Biochemistry* **1999,** *38*, 1944-9.

63. Chen, Y.; Jimenez-Angeles, F.; Qiao, B.; Krzyaniak, M. D.; Sha, F.; Kato, S.; Gong, X.; Buru, C. T.; Chen, Z.; Zhang, X.; Gianneschi, N. C.; Wasielewski, M. R.; Olvera de la Cruz, M.; Farha, O. K., Insights into the Enhanced Catalytic Activity of Cytochrome c When Encapsulated in a Metal-Organic Framework. *J. Am. Chem. Soc.* **2020,** *142*, 18576-18582.

64. Huard, D. J. E.; Kane, K. M.; Tezcan, F. A., Re-engineering protein interfaces yields copper-inducible ferritin cage assembly. *Nat. Chem. Biol.* **2013,** *9*, 169-176.

65. Sontz, P. A.; Bailey, J. B.; Ahn, S.; Tezcan, F. A., A Metal Organic Framework with Spherical Protein Nodes: Rational Chemical Design of 3D Protein Crystals. *J. Am. Chem. Soc.* **2015,** *137*, 11598-11601.

66. Künzle, M.; Eckert, T.; Beck, T., Binary protein crystals for the assembly of inorganic nanoparticle superlattices. *J. Am. Chem. Soc.* **2016,** *138*, 12731-12734.

67. Ke, N.; Landgraf, D.; Paulsson, J.; Berkmen, M., Visualization of periplasmic and cytoplasmic proteins with a self-labeling protein tag. *J. Bacteriol.* **2016,** *198*, 1035-1043.

68. Zhou, X. P.; Shi, Q. H.; Xing, X. H.; Sun, Y., Rapid purification of enhanced green fluorescent protein from Escherichia coli. *Chin. J. Chem. Eng.* **2006,** *14*, 229-234.

Chapter 4: Spatially Patterned, Porous Protein Crystals as Multifunctional Materials

4.1 Abstract

While the primary use of protein crystals has historically been in crystallographic structure determination, they have recently emerged as promising materials with many advantageous properties such as high porosity, biocompatibility, stability, structural and functional versatility, and genetic/chemical tailorability. Here we report that the utility of protein crystals as functional materials can be further augmented through their spatial patterning and control of their morphologies. To this end, we took advantage of the chemically and kinetically controllable nature of ferritin self-assembly and constructed core-shell crystals with chemically distinct domains, tunable structural patterns and morphologies. The spatial organization within ferritin crystals enabled the generation of patterned, multi-enzyme frameworks with cooperative catalytic behavior. We further exploited the differential growth kinetics of ferritin crystal facets to assemble Janus-type architectures with an anisotropic arrangement of chemically distinct domains. These examples represent a step toward using protein crystals as reaction vessels for complex multi-step reactions and broadening their utility as functional, solid-state materials. Our results demonstrate that morphology control and spatial patterning, which are key concepts in materials science and nanotechnology, can also be applied for engineering protein crystals.

4.2 Introduction

The design of crystalline substances with new structural, chemical, and physical attributes is a major goal in materials science and engineering.[1-4.] Although the primary utility of protein crystals has historically been in crystallographic structure determination, they are now also being recognized as functional solid-state materials.[5-18.] Protein crystals typically have high porosities with a typical water contents of 30-80%, sometimes even exceeding 90%,[15, 19-20.] Crystallization

generally increases the stability of the proteins,[16, 21.] and with proper modifications (*e.g.*, chemical crosslinking[22-23.]), protein crystals can even be rendered resistant to denaturation in organic solvents.[8, 24-25.] Importantly, protein (or peptide) crystals can be readily modified with organic, inorganic or biological functionalities to augment their inherent functions, enabling diverse applications in biocatalysis, separation, and therapeutics.[5, 19, 25-34.]

While obtaining protein crystals has traditionally been a trial-and-error process involving the extensive screening of crystallization conditions, there has been considerable recent progress in the rational design of protein assemblies and crystalline protein arrays.[35-45.] The resulting ability to program the structure, connectivity and porosity of protein crystals raises exciting possibilities in terms of expanding the functional scope of these biomaterials, particularly when complemented by their post-synthetic processability to create chemically patterned systems.[46.] Furthermore, it has been demonstrated that self-assembly of proteins into crystalline arrays can be chemically induced through metal or ligand binding.[47-61.] This provides a means to kinetically control the protein crystallization process and possibly tune the morphologies and spatial patterning of protein crystals to create multi-functional materials similar to core-shell and Janus-type metal-organic frameworks (MOFs) and colloidal crystals.[62-70.]

To probe this possibility in the current work, we used mesoporous crystals of human heavy-chain ferritin (HuHF). HuHF is a cage-like, 24meric iron-storage protein with octahedral (432) symmetry, an outer diameter of 12 nm and an inner diameter of 8 nm. Due to its high stability, ease of genetic and chemical modification, and ability to encapsulate various inorganic nanocrystals and biological/chemical cargo in its hollow interior, HuHF and other ferritins have found diverse practical applications.[29, 71-79.] From the standpoint of crystallization, HuHF can be considered as a patchy, colloidal nanoparticle[80.] whose high symmetry promotes its self-assembly

into distinct and predictable 3D lattices through the proper modification of its surface patches. For example, the C_2 symmetric surfaces of HuHF can be modified with Asp84 and Gln86 mutations to enable the metal-mediated (*e.g.*, Ca^{2+}, Zn^{2+} or Cd^{2+}) formation of face-centered cubic (fcc) lattices.[50, 81.] On the other hand, the installment of stable 3His-Zn^{2+} coordination sites onto the C_3 symmetric surfaces allows HuHF to assemble into body-centered cubic (bcc) lattices through coordination of ditopic organic linkers with metal chelating headgroups, yielding *bona fide* protein-MOFs in the process.[50, 82.] We further demonstrated that Ca^{2+}-directed $^{D84/Q86}$HuHF crystals, which feature large interstitial solvent channels, could be fully permeated with polyacrylate-based polymers that form an extensive hydrogel framework surrounding the HuHF proteins.[83-84.] The resulting hybrid materials, termed Polymer-Integrated Protein Crystals (PIX), were capable of reversibly expanding (by up to 600% by volume) and contracting without losing crystallinity and taking up guest proteins (≤45% w/w) that were considerably larger than the solvent channels in the unexpanded HuHF crystals.[85.] Thus, HuHF crystals furnish a versatile platform that combines several desirable properties: (1) chemically inducible and kinetically controllable self-assembly into prescribed lattice structures, (2) hollow, spherical components that can be functionalized in their interior and exterior, (3) polymer-enabled dynamic/adaptive behavior that further allows the uptake of large biological cargo in lattice interstitial spaces.

In this study, we set out to exploit these properties toward fabricating spatially patterned, multi-functional HuHF crystals (**Figure 4.1**). First, we describe how the kinetic control of HuHF crystal formation enables the construction of various core-shell architectures composed of different HuHF variants, which can be site-specifically functionalized to form distinct functional domains. We then convert the core-shell HuHF crystals into adaptive PIX, allowing the construction of patterned, multi-enzyme frameworks with cooperative catalytic behavior. Finally, we show that

the differential growth kinetics of HuHF crystal facets can be exploited to create Janus-type architectures with an anisotropic arrangement of chemically distinct domains. These examples represent an important step toward using protein crystals as reaction vessels for complex multi-step reactions, and in general, broadening their utility as functional, solid-state materials.

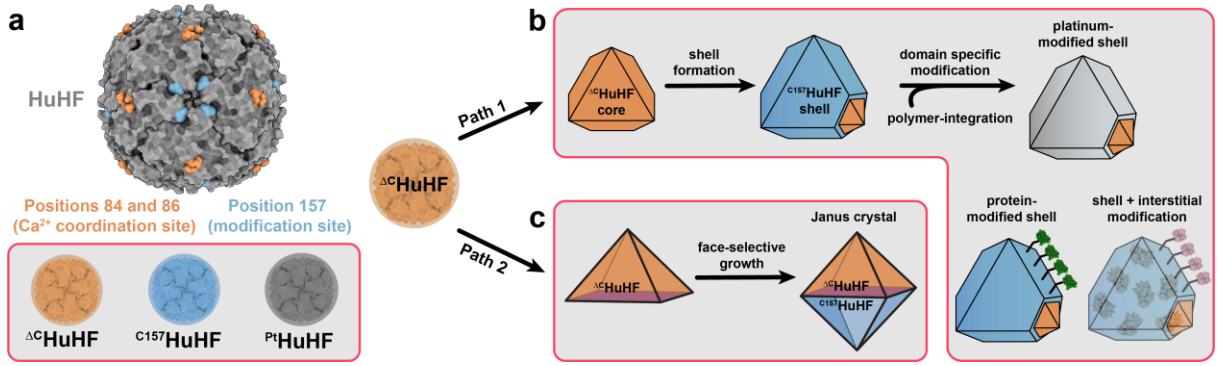

Figure 4.1. Schematic illustration for the development of spatially patterned HuHF crystals. **(a)** Cartoon representation of a single HuHF cage highlighting the residues 84 and 86 which serve as Ca^{2+} coordination sites as well as residue 157 that serves as the primary site of covalent modification. Three different HuHF building blocks were used to create distinct domains of functionality. **(b)** Different HuHF variants can be used to form core-shell HuHF crystals, which can be further modified to achieve multivariate, functional protein crystals. **(c)** Janus-type protein crystals can be formed by leveraging facet-selective assembly.

4.3 Results and Discussion

4.3.1 Synthesis and Characterization of Core-Shell HuHF Crystals

For engineering spatially patterned protein crystals, we used three distinct HuHF variants as building blocks: (1) $^{\Delta C}$HuHF, the parent species, has the Asp84/Gln86 pair of mutations on the C_2 symmetric surface patches for Ca^{2+}-mediated crystallization and is devoid of any Cys residues; (2) ^{C157}HuHF, which is the same as $^{\Delta C}$HuHF with an added Cys157 mutation near the C_4 symmetric surface patches for chemical modification with thiol-reactive agents (**Table 4.1**); (3) ^{Pt}HuHF, which is the same as $^{\Delta C}$HuHF, but it contains Pt nanocrystals in its interior cavity. The Ca^{2+}-mediated formation of $^{\Delta C}$HuHF crystals occurs within 1-2 days from dilute (25 μM) protein solutions equilibrated against ~400-fold excess (~5 mM) Ca^{2+} solution at neutral pH and room temperature (**Table 4.2**). The resulting crystals typically grow to 50-200 μm in size and predominantly possess quasi-truncated octahedral morphologies consistent with an *fcc* (*F*432 space group, $a \approx 180$ Å) lattice arrangement. We discuss the morphologies of HuHF crystals in more detail under the section "Janus-like Patterning of HuHF Crystals".

In initial experiments to generate core-shell crystals, mature $^{\Delta C}$HuHF crystals were thoroughly washed and placed in a fresh solution of ^{C157}HuHF and Ca^{2+} for seeded growth (**Figure 4.2a**). The solution also contained tris(2-carboxyethyl)phosphine (TCEP) a reducing agent to prevent disulfide-mediated aggregation of ^{C157}HuHF. After 12 h, the crystals were visibly larger, consistent with the epitaxial growth of ^{C157}HuHF layers on the $^{\Delta C}$HuHF seed crystals (**Figure 4.2b**). Upon screening different Ca^{2+} concentrations, the growth of secondary ^{C157}HuHF crystallites was determined to be insignificant at concentrations ≤4.5 mM (**Figure 4.3**). Through confocal light microscopy, the isotropic growth rate was determined to be approx. 0.5 nm/s (**Figure 4.4**), which corresponds to the addition of 2-3 layers of ferritin molecules per min to each

of the equivalent {111} faces. Scanning electron microscopy (SEM) images showed that the crystalline surfaces were smooth; in fact, any defects in the seed $^{\Delta C}$HuHF crystals were filled/repaired upon incubation in ^{C157}HuHF solutions (**Figure 4.2c, 4.5, and 4.6**). Single-crystal X-ray diffraction (sc-XRD) analysis of the epitaxially grown $^{\Delta C}$HuHF@^{C157}HuHF crystals revealed native-like diffraction (*F*432 space group, *a* = 180.4 Å) with no evidence of twinning/deformation or growth of a non-*fcc* lattice (**Figure 4.2d**).

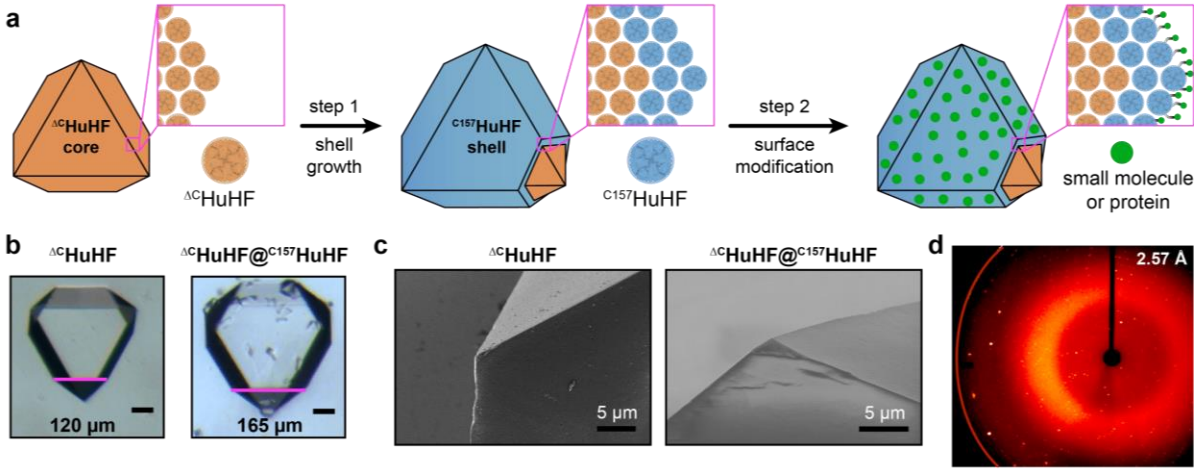

Figure 4.2. Preparation and characterization of $^{\Delta C}$HuHF@^{C157}HuHF crystals. **(a)** Cartoon illustration for the synthesis and functionalization of $^{\Delta C}$HuHF@^{C157}HuHF crystals. **(b)** Light micrographs of $^{\Delta C}$HuHF and $^{\Delta C}$HuHF@^{C157}HuHF crystals. The magenta lines illustrate the increase in crystal edge length upon shell growth. Scale bar: 50 µm. **(c)** SEM images detailing the surfaces of $^{\Delta C}$HuHF and $^{\Delta C}$HuHF@^{C157}HuHF crystals. **(d)** X-ray diffraction pattern of a $^{\Delta C}$HuHF@^{C157}HuHF crystal reveals the shell forming process does not perturb the crystallinity or lead to the formation of an alternative (*i.e.*, non-fcc) lattice.

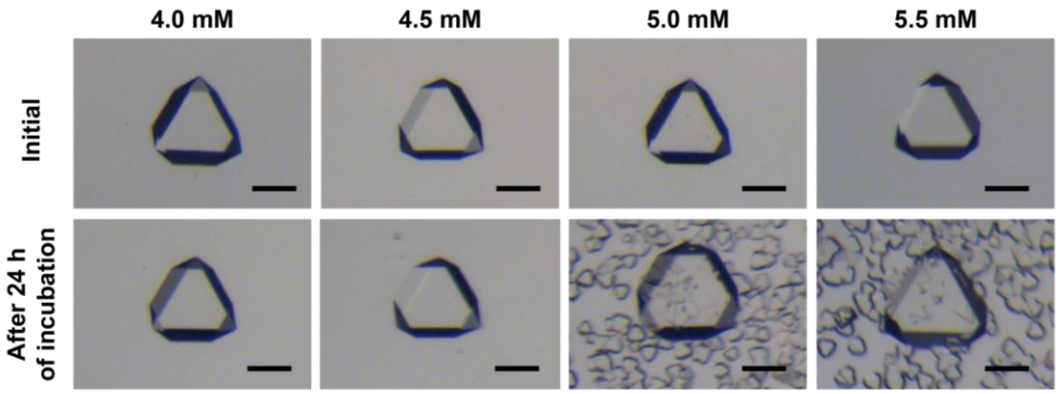

Figure 4.3. Light micrographs of HuHF crystals before and after shell formation. The secondary heterogeneous nucleation of crystallites on HuHF crystals, as well as their growth in solution, are dependent on and can be controlled by the Ca^{2+} concentration. Scale bar: 100 µm.

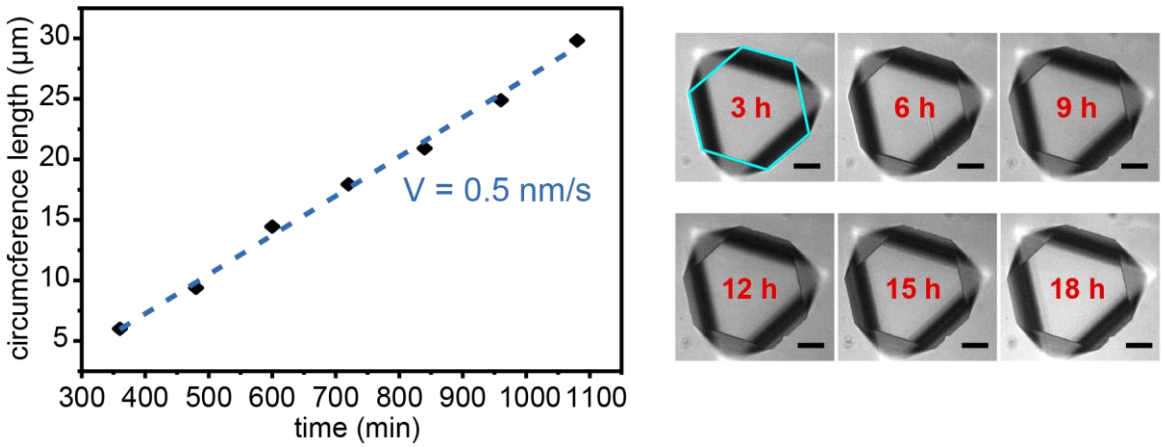

Figure 4.4. Plot (left) displaying the perimeter edge length of a crystal over time. The epitaxial growth rate of ^{C157}HuHF was determined to be 0.5 nm/s. Confocal microscopy images (right) displaying a single $^{\Delta C}$HuHF crystal transforming into a $^{\Delta C}$HuHF@^{C157}HuHF core-shell crystal. The measured length is indicated in cyan. Scale bars: 50 µm

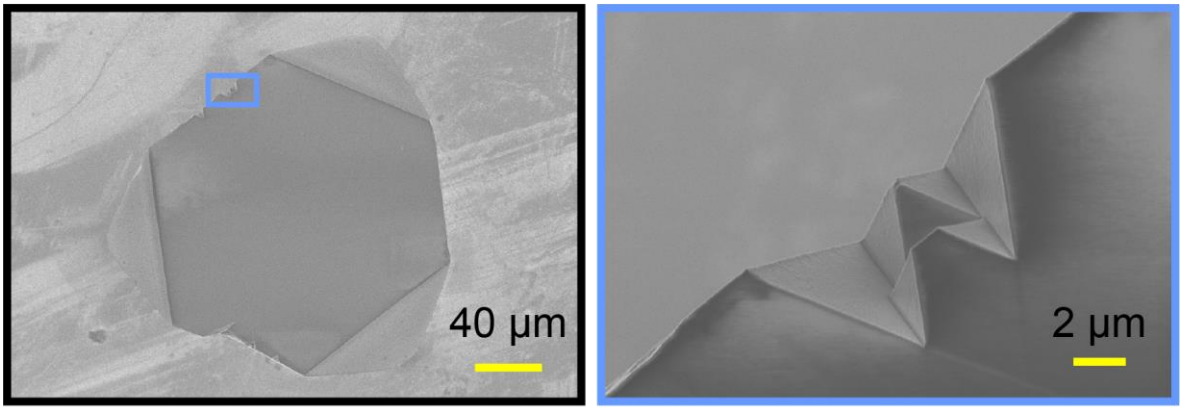

Figure 4.5. SEM images of a $^{\Delta C}$HuHF@^{C157}HuHF crystal. A higher magnification image (blue box) displays parts of the crystal edges that were in the shell completion process.

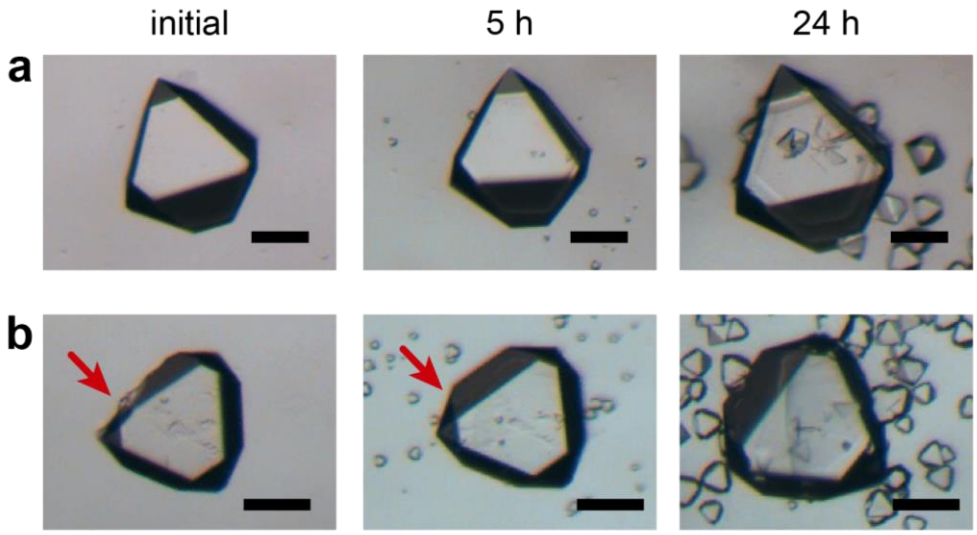

Figure 4.6. Light micrographs of $^{\Delta C}$HuHF crystals in ^{C157}HuHF crystallization conditions. **(a)** As the ^{C157}HuHF layer grows over time, the crystal's macromolecular shape is maintained. **(b)** This process can be utilized to restore chipped crystals (red arrow). The smaller crystals around the large crystal are pure ^{C157}HuHF crystals that simultaneously form. Scale bars: 100 µm

To confirm the formation of distinct protein layers, $^{\Delta C}$HuHF@^{C157}HuHF crystals were treated with fluorescein-5-maleimide, a Cys-specific fluorophore. Confocal fluorescence imaging of the resulting crystals showed fluorescence only in a peripheral shell formed by the ^{C157}HuHF molecules (**Figure 4.7a**). When the duration of the epitaxial growth in ^{C157}HuHF solution was varied from 1 to 24 h, we observed a corresponding increase in the width of the fluorescent shell (from 4.7 μm to 11 μm for a ~150-μm wide crystal) (**Figure 4.8**). Repetition of the same experiments with $^{\Delta C}$HuHF crystals that were reincubated in a fresh solution of $^{\Delta C}$HuHF molecules yielded non-fluorescent crystals, confirming that labeling by fluorescein-5-maleimide is specific to ^{C157}HuHF (**Figure 4.9**). To reverse the order of core-shell assembly, we used ^{C157}HuHF crystals as seeds and placed them in a solution of $^{\Delta C}$HuHF molecules, followed by fluorescein-5-maleimide labeling (**Figure 4.7b**). These crystals possessed a fluorescent core and a non-fluorescent shell (**Figure 4.7c**). Finally, when epitaxial growth was carried out over multiple steps alternating between $^{\Delta C}$HuHF and ^{C157}HuHF solutions, we obtained in lamellar core-shell crystals with alternating fluorescent/non-fluorescent layers (**Figure 4.7d and 4.10**).

Taken together, these observations indicate that the Ca^{2+}-mediated self-assembly of HuHF crystals occurs with high fidelity and in a kinetically controllable fashion, allowing the facile formation of layered architectures. To the best of our knowledge, the $^{\Delta C}$HuHF/^{C157}HuHF crystals represent the first core-shell protein crystals assembled from chemically distinct building blocks.

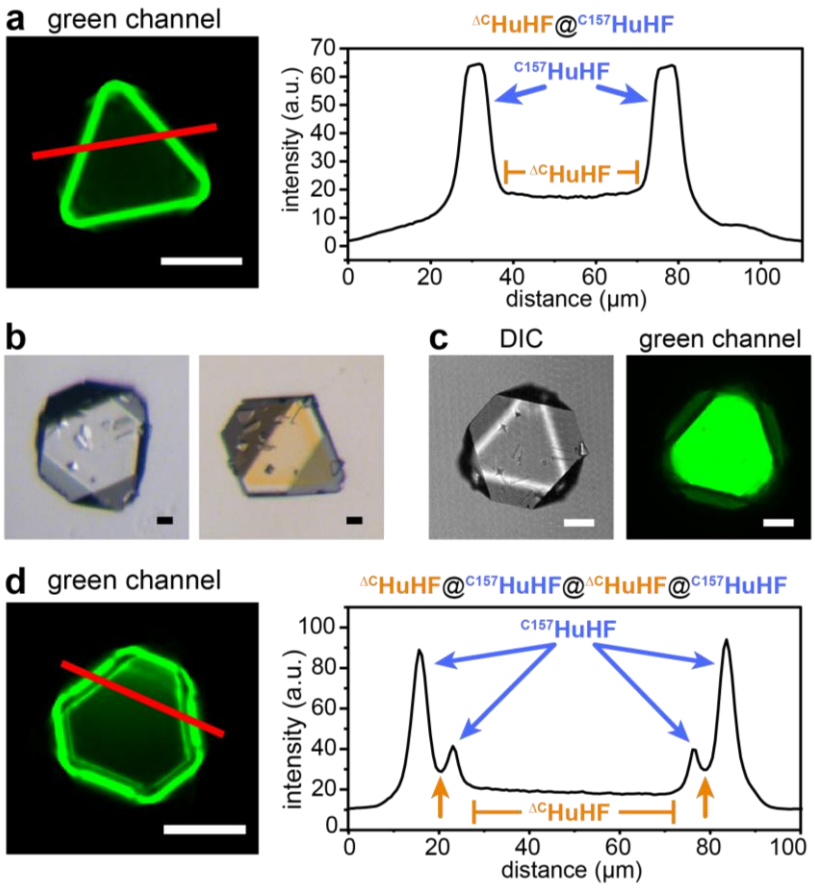

Figure 4.7. Visualization of layered HuHF crystals. **(a)** Confocal fluorescence image of a fluorescein-labeled $^{\Delta C}$HuHF@^{C157}HuHF crystal, with corresponding spatial emission intensity profile plotted along the red line. **(b)** Light micrograph of a ^{C157}HuHF@ $^{\Delta C}$HuHF crystal before (left) and after (right) fluorescein labeling. **(c)** Confocal microscopy images of the crystal in **(b)**. **(d)** Confocal fluorescence image of a fluorescein-labeled $^{\Delta C}$HuHF@^{C157}HuHF@ $^{\Delta C}$HuHF@^{C157}HuHF crystal, with corresponding spatial emission intensity profile along the red line. The peaks represent the ^{C157}HuHF layers (blue arrows) and are spatially separated by $^{\Delta C}$HuHF layers (tan arrows). Green channel: 500-550 nm. All scale bars: 50 μm.

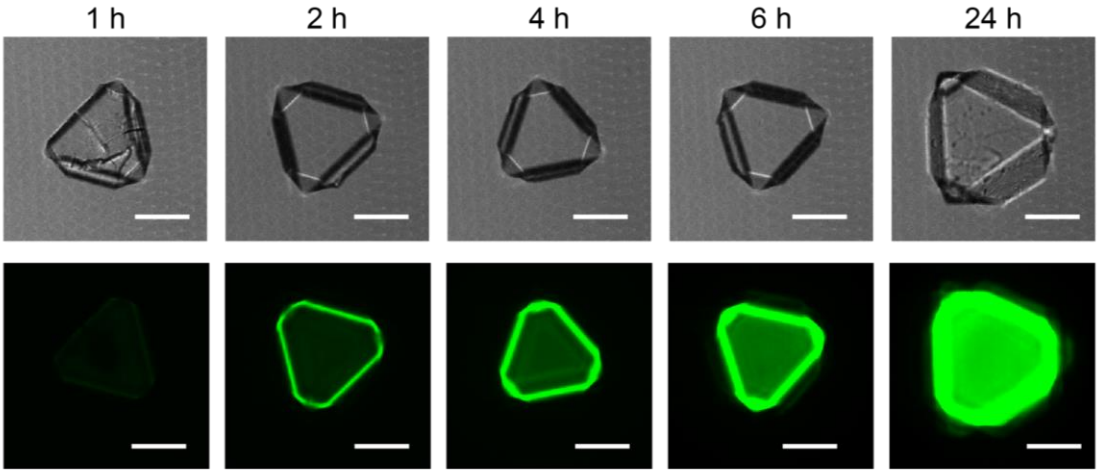

Figure 4.8. DIC (top) and fluorescence (bottom) confocal microscopy of fluorescein-labeled $^{\Delta C}$HuHF@^{C157}HuHF core-shell crystals. The center cross-section displays how the shell grows with longer incubation periods. Subsequent analysis of the shells reveals they are 4.7, 5.4, 7.0, and 11.0 μm thick for 2, 4, 6, and 24 h incubated crystals, respectively. Scale bars: 50 μm

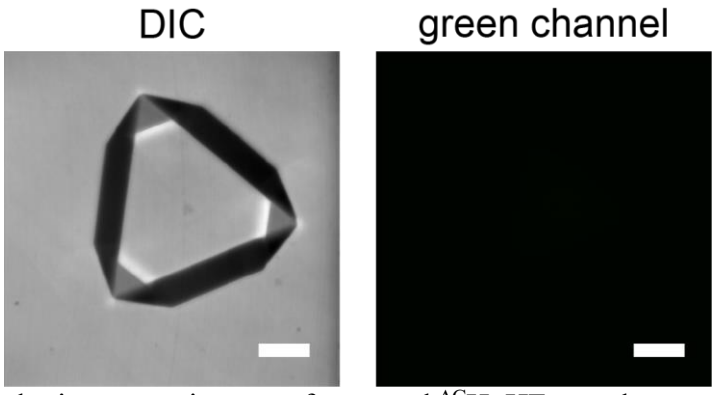

Figure 4.9. Confocal microscopy images of a control $^{\Delta C}$HuHF sample treated with fluorescein-5-maleimide. The crystal displays no fluorescence due to lack of reactive thiol functional groups. Green channel: 500-550 nm. Scale bar: 50 μm.

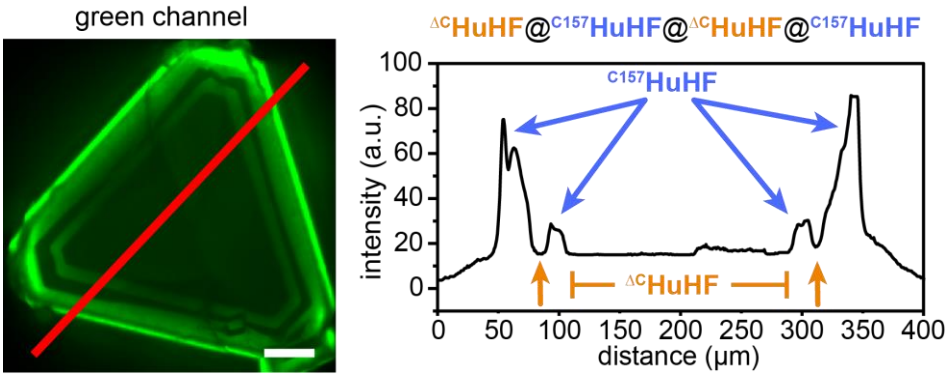

Figure 4.10. Fluorescence image of a $^{\Delta C}$HuHF@^{C157}HuHF@$^{\Delta C}$HuHF@^{C157}HuHF crystal (left). The corresponding spatial emission intensity profile (right) along the red line displays peaks representing the spatially resolved ^{C157}HuHF layers. The peaks are separated by valleys that represent the unlabeled/non-fluorescent $^{\Delta C}$HuHF layers. Green channel: 500-550 nm. Scale bar: 50 μm.

4.3.2 Functionalization of Core-Shell HuHF Crystals with Inorganic Nanoparticles and Proteins

We next sought to exploit spatial patterning within HuHF crystals to generate separate functional domains, further leveraging the fact that both the interior and the exterior of the individual HuHF molecules can be readily modified.

Given the natural role of HuHF in iron mineralization and storage, it has been frequently used a vessel for templating the growth of various inorganic nanoparticles in its interior cavity.[71.] As a model system, we chose Pt nanocrystals given their efficient catalase- and peroxidase-like activities whether they are isolated or entrapped within HuHF cages. Following previously reported procedures, we first synthesized ^{Pt}HuHF through the treatment of HuHF with excess Pt^{2+} in the presence of $NaBH_4$ as a reductant.[74.] The presence of Pt nanocrystals within ^{Pt}HuHF cages was confirmed with transmission electron microscopy (TEM) and energy-dispersive X-ray (EDX) spectroscopy (**Figure 4.11a and 4.12**). Under similar, Ca^{2+}-mediated crystallization conditions as $^{\Delta C}$HuHF, ^{Pt}HuHF formed large, dark gray crystals that were morphologically similar to $^{\Delta C}$HuHF crystals (**Figure 4.11b and 4.13**). This observation indicates that ^{Pt}HuHF can be used as a crystallographically equivalent building block as $^{\Delta C}$HuHF and ^{C157}HuHF, and any potential attachment of Pt^{2+} or Pt^0 species on the protein surface does not affect Ca^{2+}-directed self-assembly. The presence of encapsulated Pt within ^{Pt}HuHF was further confirmed by X-ray fluorescence measurements (**Figure 4.11c**).

To form $^{\Delta C}$HuHF@^{Pt}HuHF core-shell structures (**Figure 4.11d**), $^{\Delta C}$HuHF crystals were placed in ^{Pt}HuHF solutions in the presence of 5 mM Ca^{2+} and observed to grow by ~40% overnight (as measured by edge lengths) (**Figure 4.14**). To probe the formation of the ^{Pt}HuHF shell and the catalytic activity of the ^{Pt}HuHF molecules within, we placed individual $^{\Delta C}$HuHF, ^{Pt}HuHF, and

$^{\Delta C}$HuHF@^{Pt}HuHF crystals in separate solutions containing 400 mM H_2O_2. As clearly visible by eye or light microscopy, only the latter two samples led to the formation of gas bubbles, consistent with the formation of O_2 through the catalase-like activity of ^{Pt}HuHF (**Figure 4.11e and 4.15**). $^{\Delta C}$HuHF@^{Pt}HuHF crystals also displayed peroxidase activity, as determined by their ability to catalyze the H_2O_2-mediated oxidation of Amplex Red into the fluorescent molecule resorufin (**Figure 4.11f**). The product fluorescence was uniformly distributed over the entire core of the $^{\Delta C}$HuHF@^{Pt}HuHF crystals due to the facile diffusion of resorufin throughout the mesoporous lattice, whereas the ^{Pt}HuHF-containing shell of the crystals remained distinctly dark due to the quenching of resorufin fluorescence by the HuHF-encapsulated Pt nanoparticles (**Figure 4.11f**).

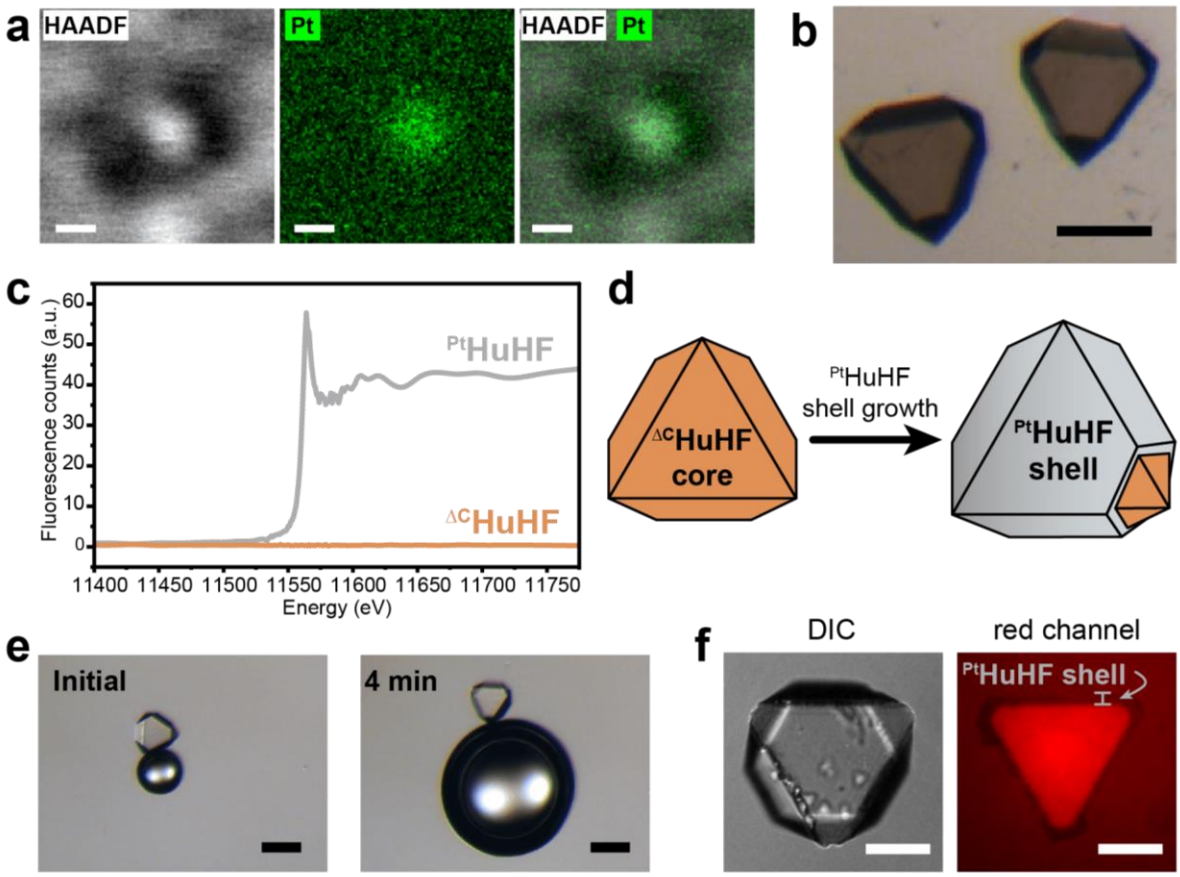

Figure 4.11. Preparation, crystallization and characterization of ^{Pt}HuHF. **(a)** TEM and EDX analysis of ^{Pt}HuHF molecules. Overlaying the dark-field and Pt maps reveal the HuHF cavity is functionalized with Pt nanoparticles. Scale bar: 5 nm. **(b)** Light micrograph of ^{Pt}HuHF crystals. Scale bar: 100 µm. **(c)** X-ray fluorescence plot confirming the ^{Pt}HuHF crystals contain Pt, while the $^{\Delta C}$HuHF crystal does not. **(d)** Schematic illustrating the formation of $^{\Delta C}$HuHF@^{Pt}HuHF. **(e)** Light micrographs of a $^{\Delta C}$HuHF@^{Pt}HuHF crystal displaying continuous O_2 formation over time, confirming that the HuHF-encapsulated Pt nanoparticles are active. Scale bar: 100 µm. **(f)** Confocal micrographs of a $^{\Delta C}$HuHF@^{Pt}HuHF crystal displaying peroxidase activity. The HuHF-encapsulated Pt nanoparticles in the shell quench the fluorescence, leading to the appearance of the shell as a dark outline. Red channel: 575-650 nm. Scale bar: 50 µm.

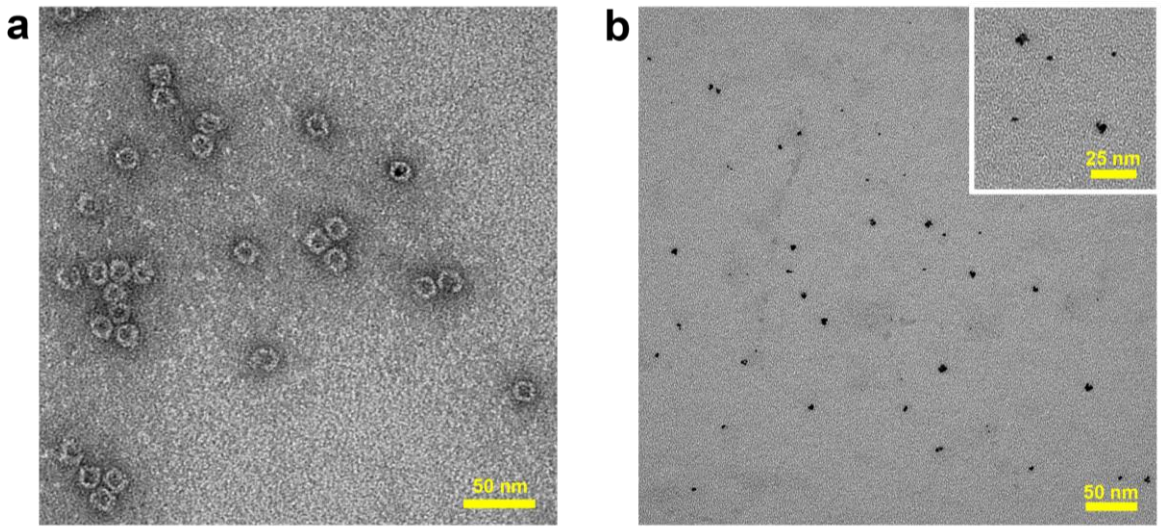

Figure 4.12. TEM images of **(a)** stained (with uranyl acetate) and **(b)** non-stained ^{Pt}HuHF. The staining process helps visualize the HuHF molecules but hinders observing the Pt nanoparticles. The non-stained sample reveals the Pt nanoparticles encapsulated within ^{Pt}HuHF cages.

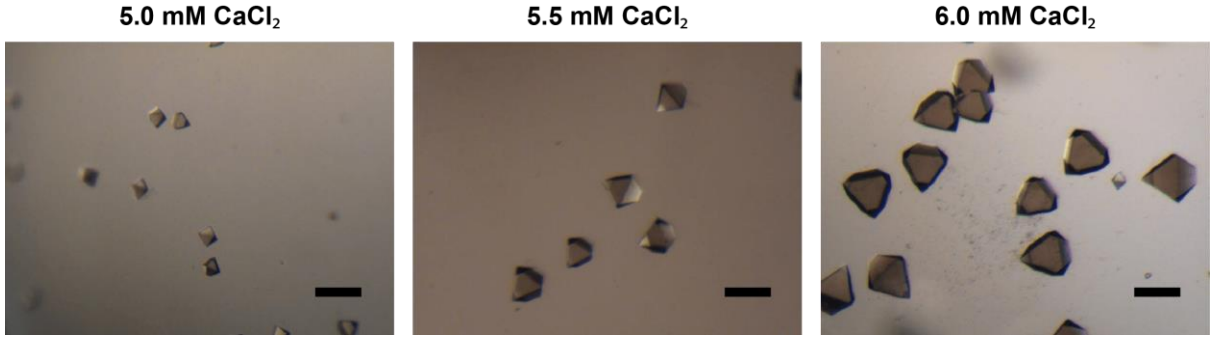

Figure 4.13. Light micrographs of ^{Pt}HuHF crystals formed in different concentrations of $CaCl_2$. The largest single crystals were formed in the presence of 6.0 mM $CaCl_2$. Furthermore, the ^{Pt}HuHF crystals are noticeably colored dark gray due to the Pt nanoparticles. Scale bars: 100 μm.

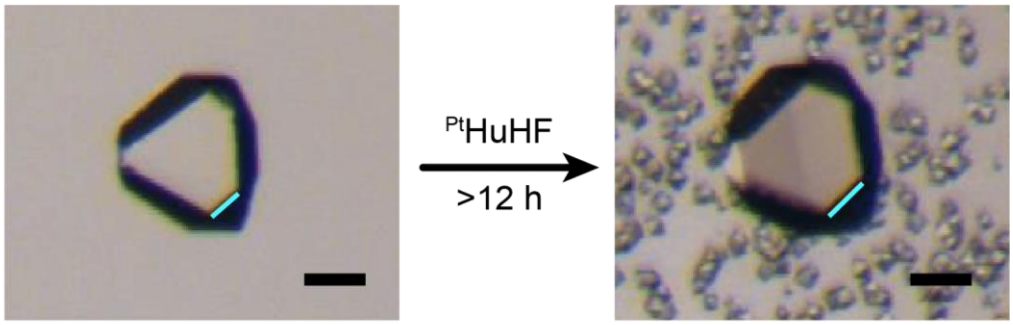

Figure 4.14. Light micrographs of a single $^{\Delta C}$HuHF crystal in ^{Pt}HuHF crystal forming conditions (5.0 mM $CaCl_2$). After >12 h incubation, the crystal size increased and is surrounded by ^{Pt}HuHF crystallites, suggesting $^{\Delta C}$HuHF@^{Pt}HuHF formation. The measured edge length (cyan) increased ~40% after incubation. Scale bar: 50 μm.

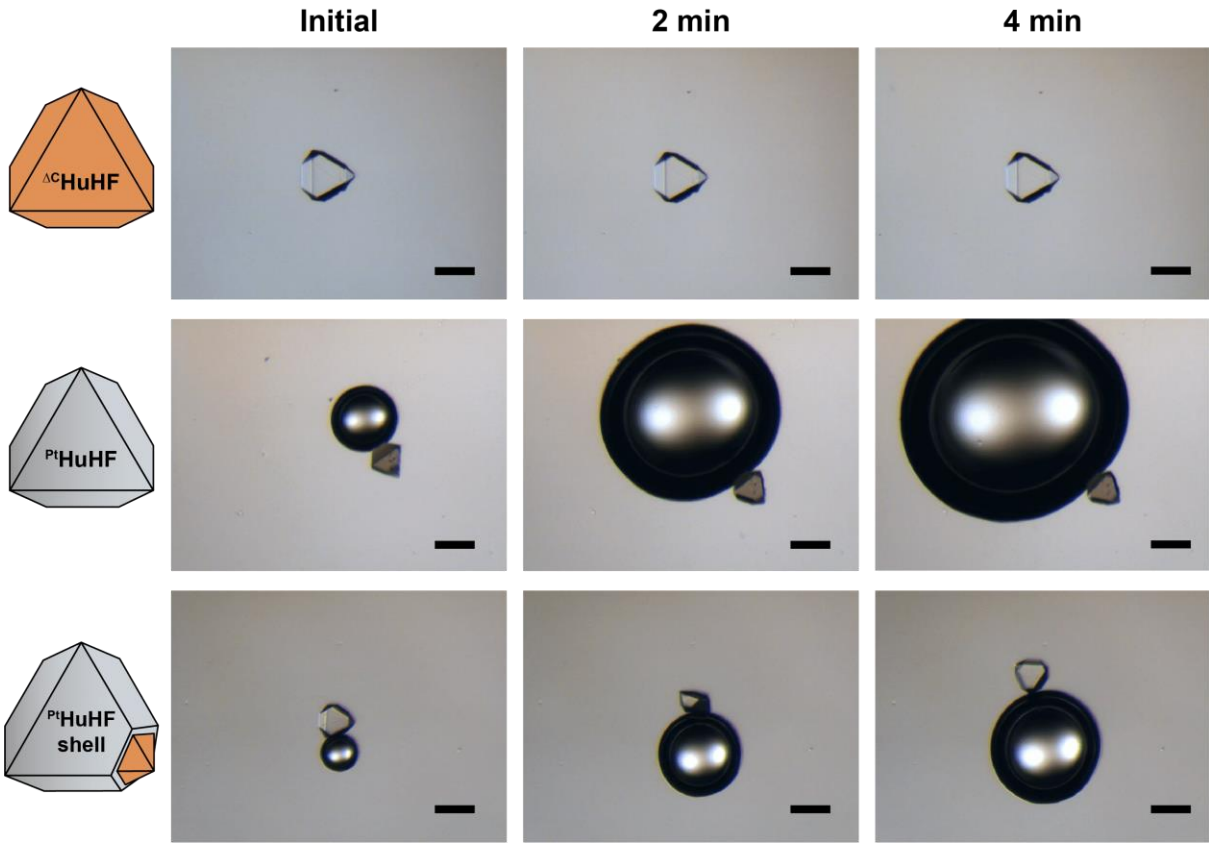

Figure 4.15. Light micrographs of $^{\Delta C}$HuHF (top), ^{Pt}HuHF (middle) and $^{\Delta C}$HuHF@^{Pt}HuHF (bottom) crystals in a solution containing H_2O_2 (400 mM). Expectedly, the $^{\Delta C}$HuHF sample does not form any bubbles due to the lack of Pt nanoparticles. In contrast, the other two crystal samples produced bubbles due to the Pt decomposing H_2O_2 and producing O_2. Scale bar: 100 μm

To further expand the functionality of patterned HuHF crystals, we again took advantage of the site-specific chemical reactivity of the $^{\Delta C}$HuHF@^{C157}HuHF core-shell crystals for covalent labeling with extrinsic proteins (**Figure 4.16a**), using green fluorescent protein (GFP; dimensions: 3.0 × 3.2 × 5.2 nm^3) as a test case. We first prepared a Cys-reactive, maleimide-functionalized derivative of GFP (mal-GFP) by treating its surface lysine residues with sulfo-SMCC (sulfosuccinimidyl-4-(N-maleimidomethyl)cyclohexane-1-carboxylate) (**Figure 4.17**). $^{\Delta C}$HuHF@^{C157}HuHF crystals were then reacted with mal-GFP overnight and imaged by confocal microscopy, which revealed a thin fluorescent outline (**Figure 4.16b**) consistent with GFP labeling. The fluorescent GFP corona was considerably less thick than that observed when similarly prepared $^{\Delta C}$HuHF@^{C157}HuHF crystals were treated with fluorescein-5-maleimide, indicating that mal-GFP only reacts with surface-exposed ^{C157}HuHF molecules as it is too large to penetrate into the crystal lattice (the narrowest interstitial channels in HuHF crystals are ~2 nm wide).

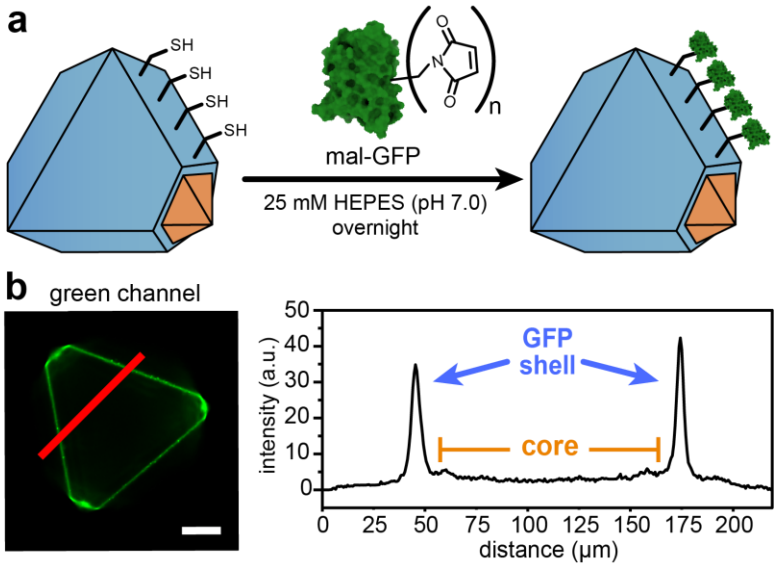

Figure 4.16. Site-selective modification of the Cys thiol groups on the crystal surfaces with maleimide-functionalized proteins. **(a)** Cartoon illustration for the attachment of mal-GFP onto the $^{\Delta C}$HuHF@^{C157}HuHF crystal surface. **(b)** Confocal fluorescence image of a GFP-labeled crystal, with corresponding spatial emission intensity profile along the red line. Green channel: 500-550 nm. Scale bar: 50 μm.

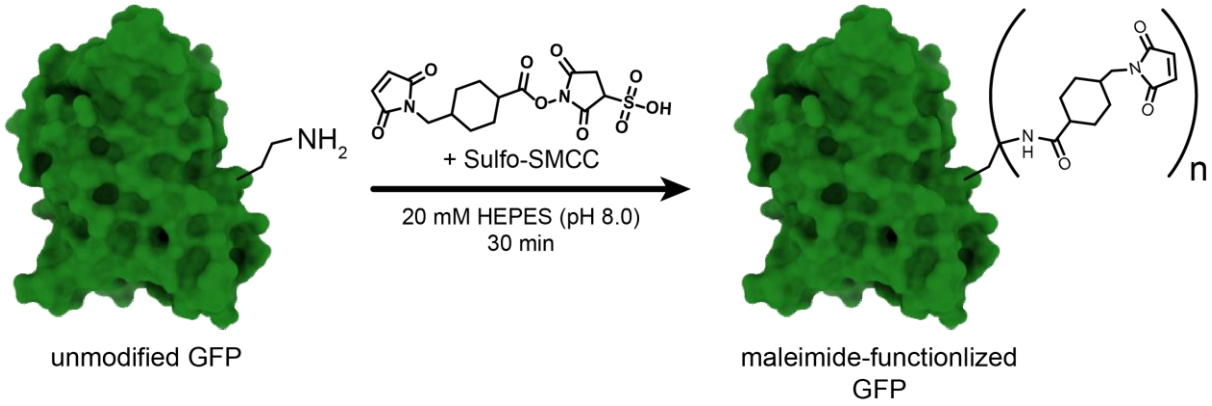

Figure 4.17. Schematic representation for the modification of Lys residues on GFP with sulfo-SMCC to create a maleimide-functionalized GFP.

4.3.3 Adaptive Core-Shell HuHF Crystals for Multi-Enzyme Patterning

To overcome the impenetrability of $^{\Delta C}$HuHF@^{C157}HuHF crystals to large macromolecules, we decided to process them into adaptive PIX, which were previously shown to take up guest proteins considerably larger than the lattice interstitial channels.[85.] To this end, $^{\Delta C}$HuHF@^{C157}HuHF crystals were infused with acrylate, acrylamide and bis-acrylamide, which were then polymerized *in crystallo* to form a hydrogel network within the lattice.[83.] Upon confirming that $^{\Delta C}$HuHF@^{C157}HuHF PIX showed the same reversible expansion/contraction behavior as was observed with pure HuHF PIX (**Figure 4.18**), we set out to generate a spatially patterned, dual-enzyme system consisting of glucose oxidase (GOx; dimensions: 5.2 × 5.0 × 7.7 nm^3) and horseradish peroxidase (HRP; dimensions: 3.5 × 3.8 × 5.4 nm^3) (**Figure 4.19a**). GOx and HRP are model enzymes that have been utilized to demonstrate cooperative, cascade reactions.[5, 86-87.] Specifically, GOx catalyzes the O_2-mediated oxidation of glucose into D-glucono-δ-lactone and produces H_2O_2, which HRP can utilize to oxidize small molecules such as Amplex Red to produce resorufin (**Figure 4.19b**).

First, the shell of the $^{\Delta C}$HuHF@^{C157}HuHF was labeled with maleimide-functionalized GOx (mal-GOx) using the aforementioned procedure for preparing mal-GFP. The GOx-labeled crystal was then processed into PIX, which were then expanded in a low-ionic-strength solution containing HRP, followed by its salt-induced contraction to entrap HRP molecules within the lattice. Upon incubating the resulting PIX in a buffered solution (pH 6.0) containing glucose (1 mM) and Amplex Red (100 μM), we observed that the crystals became fluorescent (**Figure 4.19c**). By contrast, the crystals remained non-fluorescent in control experiments, in which (a) no glucose was added to the complete system, (b) PIX were not labeled with GOx, or (c) non-functionalized PIX were used (**Figure 4.20**). These observations confirmed the core-shell crystals were

successfully functionalized with GOx and HRP and that the resulting system was capable of supporting cooperative catalytic reactions in a contained environment.

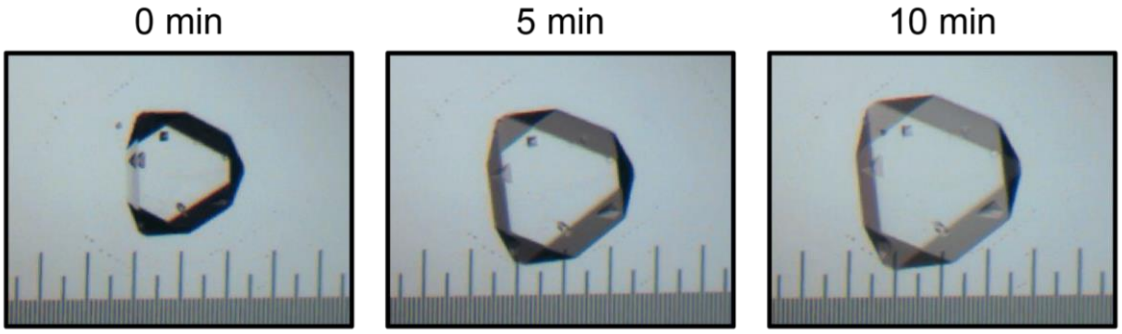

Figure 4.18. Light micrographs of a $^{\Delta C}$HuHF@^{C157}HuHF crystal that has been processed into a PIX and placed in water. Due to the hydrogel network in the lattice, the crystal isotropically expands over time. Furthermore, we observed that the crystallites on the crystal surface expand as well. The major ticks on the ruler are separated by 100 μm.

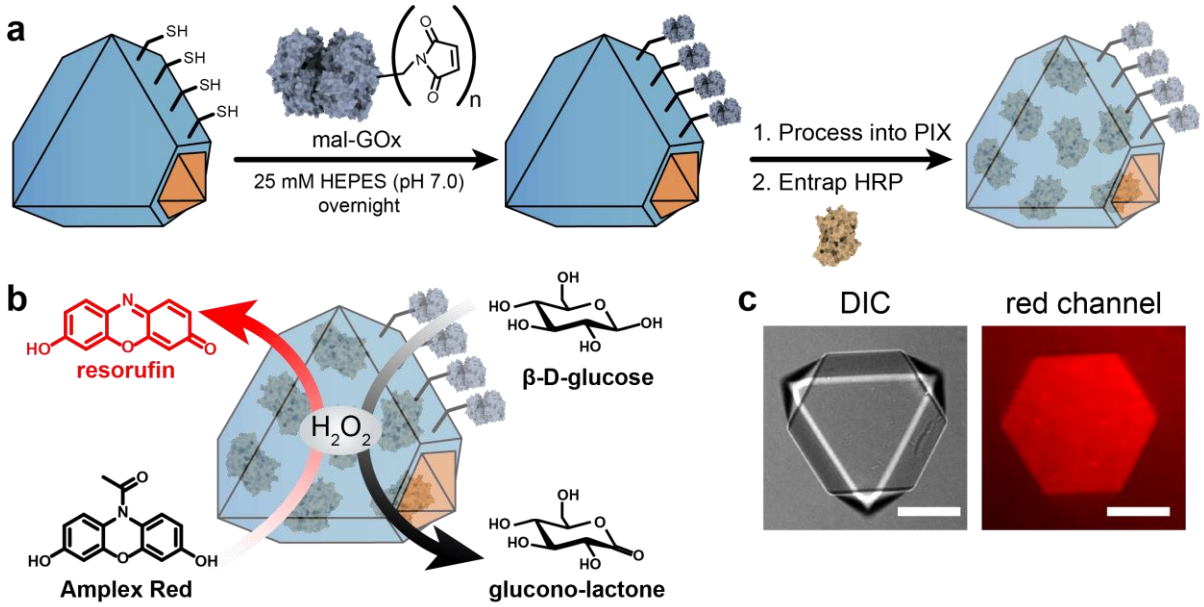

Figure 4.19. Preparation and characterization of multi-enzyme patterned HuHF crystals with GOx and HRP. **(a)** Cartoon illustration for the preparation of GOx- and HRP-functionalized crystals. The crystal surface is first labeled with mal-GOx and subsequently processed into PIX for the entrapment of HRP in the crystal void space. **(b)** Cartoon illustration representing the cascade reaction between GOx and HRP. **(c)** Confocal microscopy images of a single HuHF crystal, functionalized with GOx and HRP, displaying cooperative catalytic reactions to form resorufin. Red channel: 575-650 nm. Scale bar: 50 μm

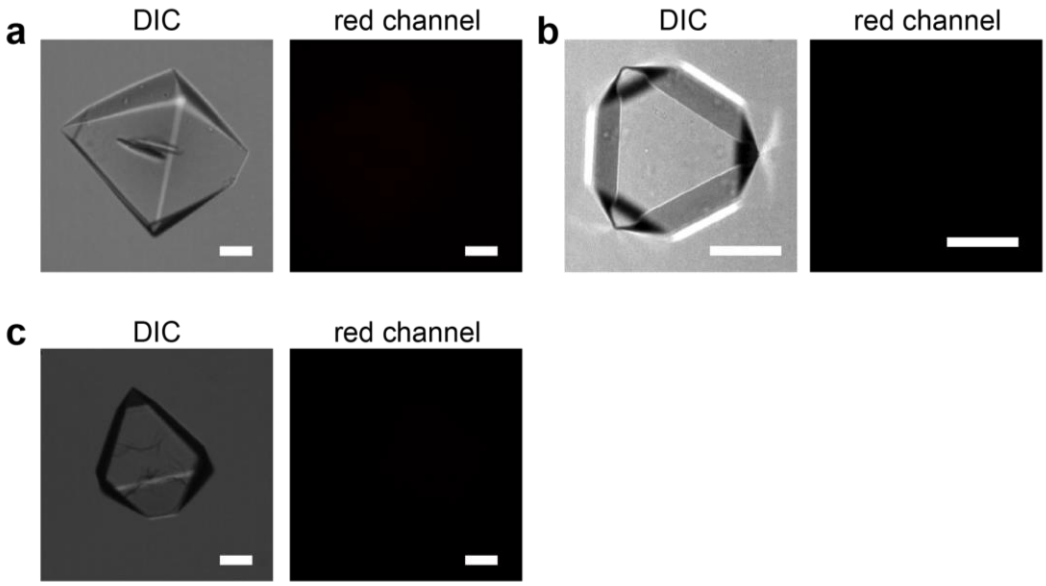

Figure 4.20. Confocal microscopy images of control $^{\Delta C}$HuHF@^{C157}HuHF PIX samples: **(a)** crystal functionalized with both GOx and HRP without any glucose present, **(b)** crystal functionalized with only HRP and not GOx, **(c)** PIX sample without GOx nor HRP. The three control samples did not display peroxidase activity, confirming both enzymes and glucose are necessary for cascade reactions to occur. Red channel: 575-650 nm. Scale bar: 50 μm.

Next, we explored a reaction scheme in which the shell of the $^{\Delta C}$HuHF@^{C157}HuHF PIX could be tailored as a chemical barrier to the interior, enabled by high catalytic efficiency of a peripherally placed enzyme. In this regard, we were inspired by certain nitrogen-fixing bacteria (*e.g.*, *Azotobacter vinelandii*), which are also obligate aerobes. These organisms display a very high O_2 consumption rate owing to their membrane-bound respiratory enzymes, which allows them to maintain a low-O_2 environment in the cytosol required for the activity of the highly O_2-sensitive nitrogenase complex.[88.] To realize an analogous–albeit simpler–scenario with the $^{\Delta C}$HuHF@^{C157}HuHF core-shell PIX platform, we replaced the GOx in the cooperative HRP(core)/GOx(shell) system with catalase (Cat; dimensions: 10.0 × 9.3 × 5.4 nm^3), an exceptionally efficient enzyme that catalyzes the disproportionation of H_2O_2 into H_2O and O_2.[89-90.] In this scenario, the outer layer in $^{\Delta C}$HuHF@^{C157}HuHF PIX modified with Cat would reduce the amount H_2O_2 that permeates into the lattice interior by Cat-catalyzed decomposition, which would be reflected in a diminished catalytic activity by HRP that uses H_2O_2 as a substrate (**Figure 4.21**).

The preparation of maleimide-functionalized Cat (mal-Cat) required a different approach than that used for mal-GFP and mal-GOx, as Cat natively contains 16 Cys residues. Therefore, we first treated Cat with fluorescein-5-maleimide which served the dual purpose of (a) passivating the native Cys residues on the catalase surface and (b) attaching a fluorophore for imaging (**Figure 4.22a**). The Lys residues on this fluorescein-labeled variant were then reacted with sulfo-SMCC to generate mal-Cat (**Figure 4.22a**); mal-Cat retained the native catalytic activity for H_2O_2 decomposition (**Figure 4.23**). Upon labeling $^{\Delta C}$HuHF@^{C157}HuHF core-shell crystals with mal-Cat, we observed a green-fluorescent outer shell (**Figure 4.24**), confirming covalent attachment of Cat to the surface. Next, we processed these crystals into a PIX to enable the uptake of rhodamine-labeled HRP (r-HRP) (**Figures 4.22b, c**). Confocal fluorescence imaging of the resulting crystals

revealed that Cat was immobilized on the periphery, whereas r-HRP was entrapped throughout the entire crystal volume. Comparison of the intensities of r-HRP fluorescence in the Cat-functionalized versus non-Cat-functionalized crystals indicated that the labeling of the shell with Cat reduced the HRP uptake into the lattice by ≤30% (**Figure 4.25**).

To assess the efficiency of the Cat-functionalized shell in reducing H_2O_2 permeation, HRP (unlabeled)- and Cat-functionalized $^{\Delta C}$HuHF@^{C157}HuHF PIX were placed in a solution containing 1-10 mM H_2O_2 and 100 μM Amplex Red, and were monitored by confocal fluorescence microscopy (**Figure 4.26**). Control samples were prepared using PIX loaded with unlabeled HRP but lacking the Cat modification. At 1 mM H_2O_2, the control samples displayed a 69±4% higher red-fluorescence intensity compared to the Cat/HRP-labeled PIX (**Figure 4.22d**), indicating a lower amount of H_2O_2 penetrating into the crystal core. Increase in added H_2O_2 concentrations (5 mM and 10 mM), led to a reduction in the observed blockage of H_2O_2 (50% and 13%, respectively; **Figure 4.26**), consistent with a saturation effect. Nonetheless, our observations demonstrate that the Cat-functionalized shell can provide an effective catalytic barrier to H_2O_2 diffusion to the lattice interior at moderate H_2O_2 concentrations, even after accounting for the lower HRP uptake in this system and despite the fact that Cat-modification is likely only limited to the outermost ^{C157}HuHF molecules in the shell.

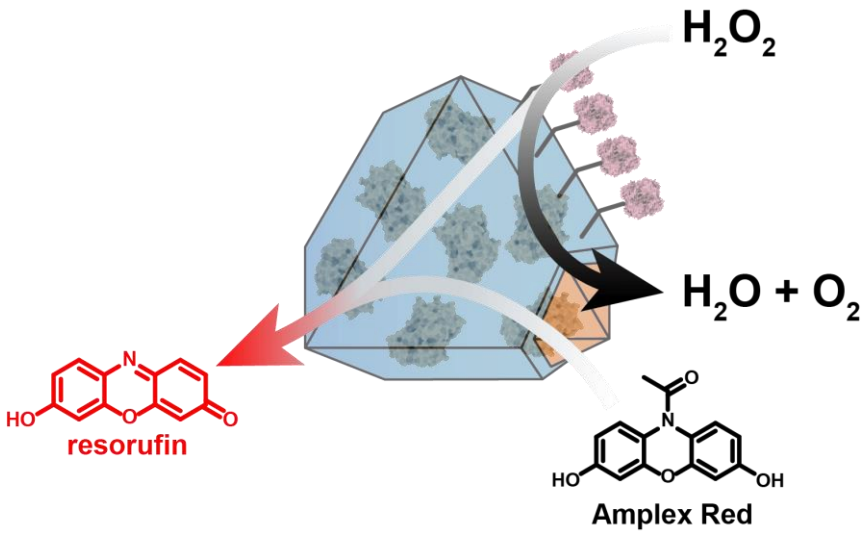

Figure 4.21. Cartoon illustration representing the competing reactions between HRP and Cat. The surface layer of Cat serves as a molecular barrier that limits the diffusion of H_2O_2, thereby reducing the production of resorufin.

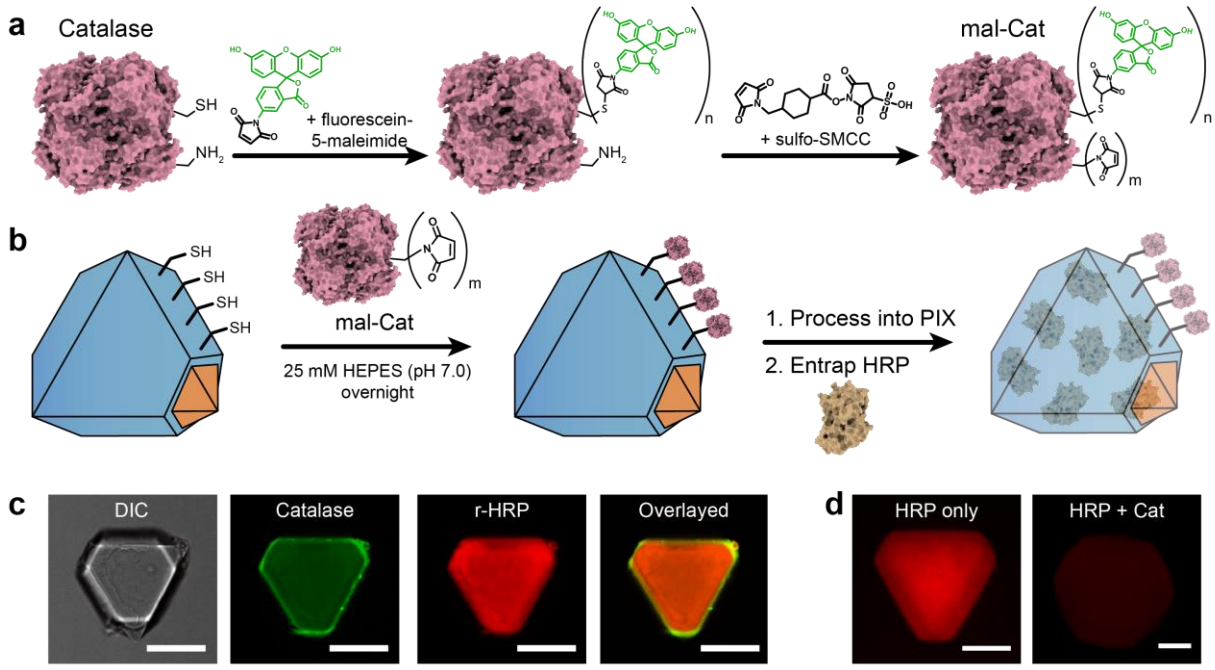

Figure 4.22. Preparation and characterization of multi-enzyme patterned HuHF crystals with Cat and HRP. **(a)** Cartoon illustration for the synthesis of mal-Cat. Catalase is first treated with fluorescein-5-maleimide to quench the reactive thiols, and subsequently labeled with sulfo-SMCC to form mal-Cat. **(b)** Cartoon illustration for the preparation of Cat- and HRP-functionalized crystals. **(c)** Confocal microscopy images of a single crystal functionalized with Cat and r-HRP. Merging the green (Cat) and red channels (r-HRP) reveal that the HRP is entrapped inside the crystal, while Cat is on the crystal surface. **(d)** Fluorescence micrographs of a crystal displaying peroxidase activity. The crystal without a layer of Cat (left) on the surface displays a higher fluorescence intensity than a crystal with Cat (right), confirming the Cat is serving as a H_2O_2 barrier. Red channel: 575-650 nm. Scale bar: 50 μm.

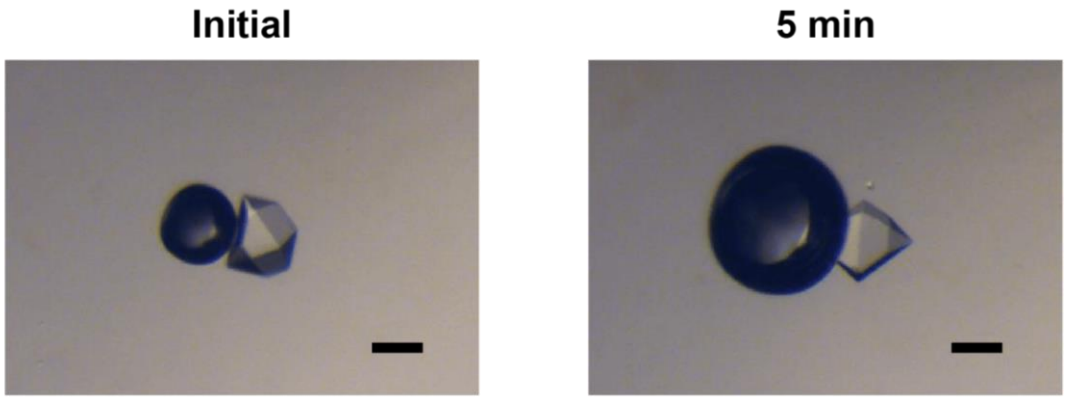

Figure 4.23. Light micrographs of a $^{\Delta C}$HuHF@^{C157}HuHF crystal, functionalized with Cat on the surface, in a solution containing H_2O_2 (500 mM). The crystal forms a bubble due to Cat continuously producing O_2, confirming the mal-Cat retains its native enzymatic activity. Scale bar: 100 μm.

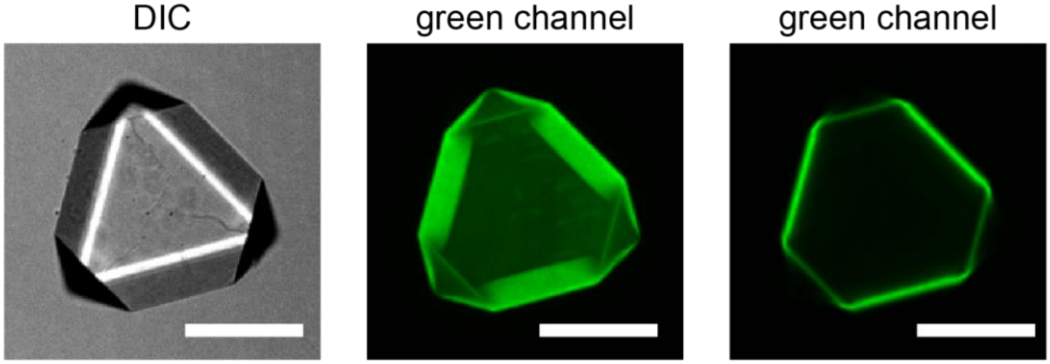

Figure 4.24. Confocal microscopy of a Cat-modified $^{\Delta C}$HuHF@^{C157}HuHF crystal. The center cross-section (right) of the crystal reveals a green perimeter on the crystal surface, confirming Cat is attached to the crystal. Green channel: 500-550 nm. Scale bar: 50 μm.

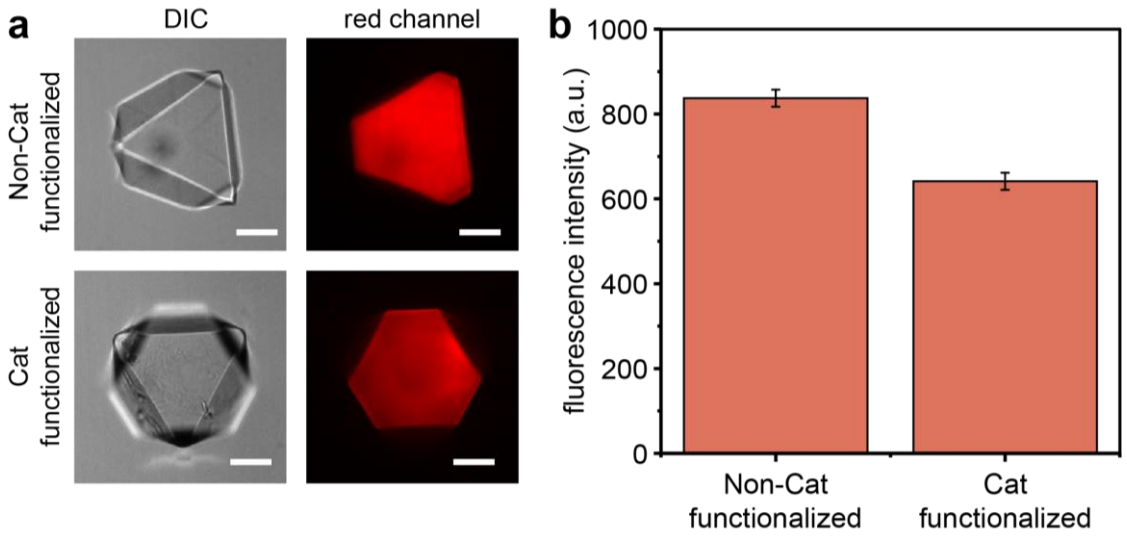

Figure 4.25. Analysis of r-HRP loading in HuHF crystals. **(a)** Confocal microscopy images of r-HRP loaded crystals. **(b)** Measuring the fluorescence intensity of the crystals reveals Cat functionalization hinders HRP loading by ≤30%. Red channel: 575-650 nm. Scale bar: 50 μm.

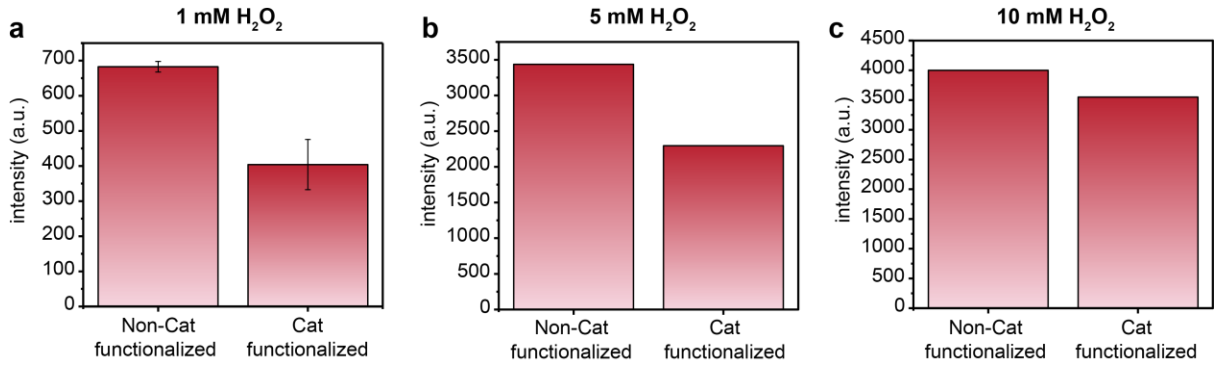

Figure 4.26. Fluorescence intensities of Non-Cat and Cat-functionalized samples. At **(a)** 1 mM, **(b)** 5 mM and **(c)** 10 mM H_2O_2, the non-Cat functionalized samples exhibited 69%, 50%, and 13% higher fluorescence, respectively.

4.3.4 Janus-like Patterning of HuHF Crystals

During the course of our studies on core-shell systems, we noticed that HuHF was capable of forming crystals with several distinct morphologies. Interestingly, instead of the expected octahedral morphology that typically represents the most stable crystal form for an fcc lattice (as discussed below), we observed alternative crystal habits that could correspond to higher-energy forms (**Figure 4.27a**). This prompted us to think more deeply about the nucleation/growth process for HuHF crystals and explore whether it can be exploited to obtain crystals with alternative spatial patterns.

The equilibrium shapes of atomic crystals or nanoparticles grown in solution (in an unsupported fashion) are generally governed by the minimization of their surface energies, as predicted by Wulff construction.[91-92.] For fcc systems such as the Ca^{2+}-directed HuHF crystals, the {111} faces usually represent the lowest energy surfaces according to the broken-bond model.[93.] On these faces, the individual atoms/molecules make contacts with nine neighbors, thus losing only three contacts from a total of twelve in the 3D lattice, whereas on the {100} plane (which is typically the next lowest in energy), there are contacts with eight neighbors, corresponding to a loss of four bonds (**Figure 4.27b**). Thus, solution-grown fcc crystals ideally have an octahedral morphology (hereafter referred to as Type 1) bounded by eight {111} faces (**Figure 4.28**), although there can be system-specific deviations and HuHF may exhibit a more complex crystallization behavior compared to atoms or colloidal particles due to its heterogenous chemical composition. Interestingly we rarely observed HuHF crystals that exhibited the Type 1 habit. Most frequently, we observed an atypical morphology (referred to as Type 2) as shown, for example, in Figures 4.4b and 4.11b, which corresponds to a halved octahedron sectioned in the <111> direction (**Figure 4.27a and 4.28**). Type 2 crystals are also all bounded by {111} planes and thus also

represent a low-energy morphology. Less frequently, we observed square-pyramidal crystals (Type 3), which again correspond to half octahedra, but this time sectioned along the <100> direction (**Figure 4.27c, 4.28, and 4.29**). Again, while the chemical heterogeneity of HuHF molecules may lead to complex self-assembly behavior, the Type 2 and Type 3 morphologies are almost certainly due to substrate-supported nucleation/growth routes. These morphologies can be respectively modeled by double- or single-Winterbottom construction,[94-95.] an extension of the Wulff model that incorporates crystal interactions with solid substrates (**Figure 4.30**). Indeed, we found that the HuHF crystals with Type 2 and Type 3 habits grew attached to the bottom of the plastic crystallization wells, consistent with substrate-templated growth.

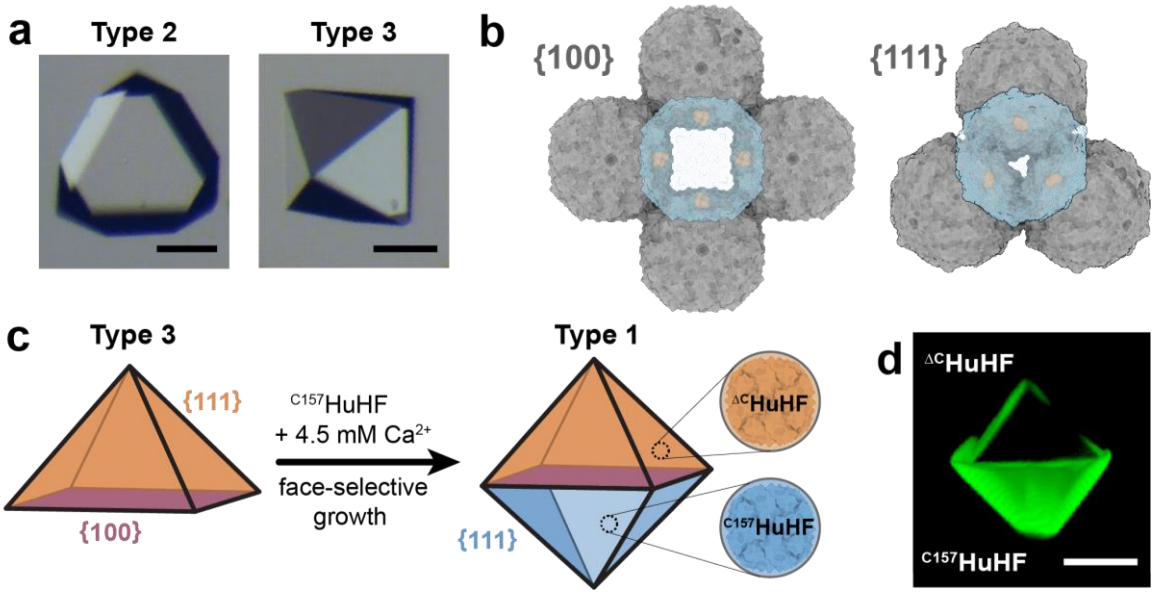

Figure 4.27. Leveraging face-selective HuHF assembly to form Janus protein crystals. **(a)** Light micrographs of two HuHF crystals with different macroscopic morphologies. Scale bar: 100 µm. **(b)** Binding modes of a new HuHF molecule (blue) on a {100} face involves 4 contacts (tan), while {111} involves 3 contacts (tan). **(c)** Cartoon illustrating the formation of a Type 1 crystal from a Type 3 seed crystal. Different HuHF variants can be used during the selective growth process to form a Janus-type protein crystal. **(d)** 3D confocal fluorescence microscopy image of a protein crystal where the top and bottom half are composed of $^{\Delta C}$HuHF and ^{C157}HuHF, respectively. Labeling with fluorescein reveals a Janus-type morphology, where only the ^{C157}HuHF molecules are labeled. Note that there is also a small amount of labeling on the {111}faces (top half of the crystals), consistent with the lower rate of shell growth off of these faces compared to {100}. Scale bar: 50 µm.

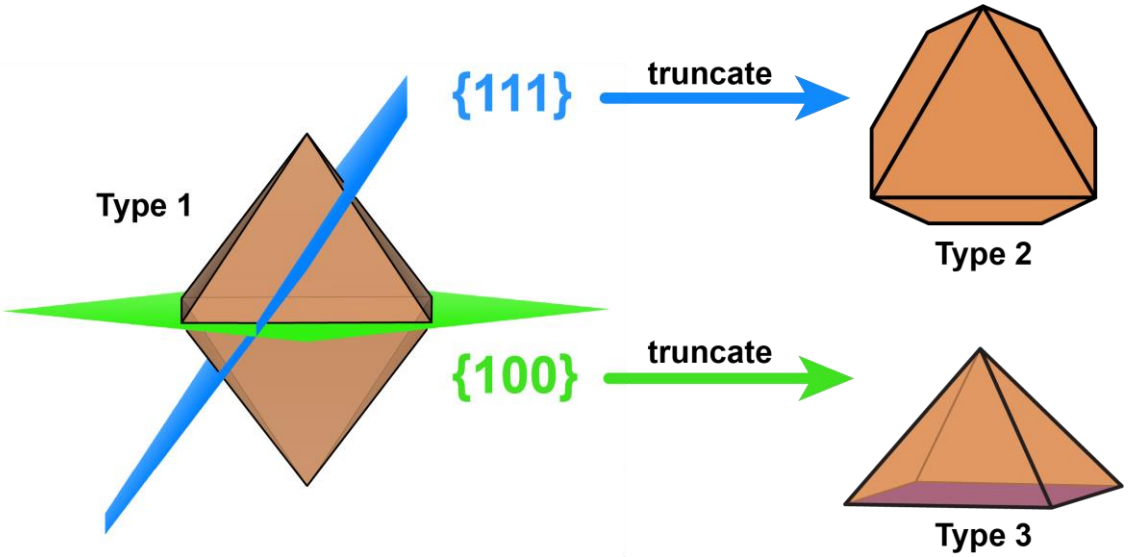

Figure 4.28. Cartoon illustration representing how Type 2 and Type 3 crystals morphologies are related to Type 1 crystals. Type 1 crystals exhibit a complete octahedron with {111} faces. Truncating Type 1 crystals along the {111} plane (blue) yields a Type 2 crystal, with all the {111} faces. Truncating along the {100} plane (green) yields a Type 3 crystal, with an exposed {100} crystal face.

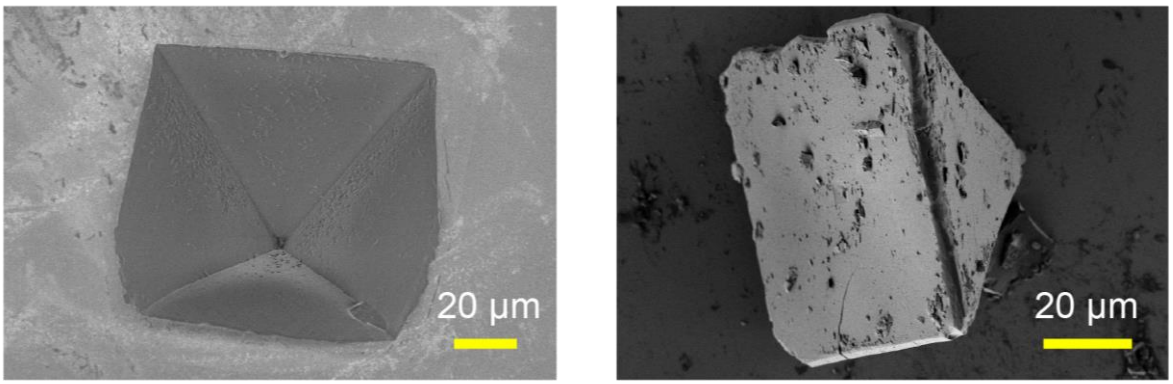

Figure 4.29. SEM images of two separate Type 3 $^{\Delta C}$HuHF crystals displays the side crystal faces (left) and the rectangular base of the crystal (right).

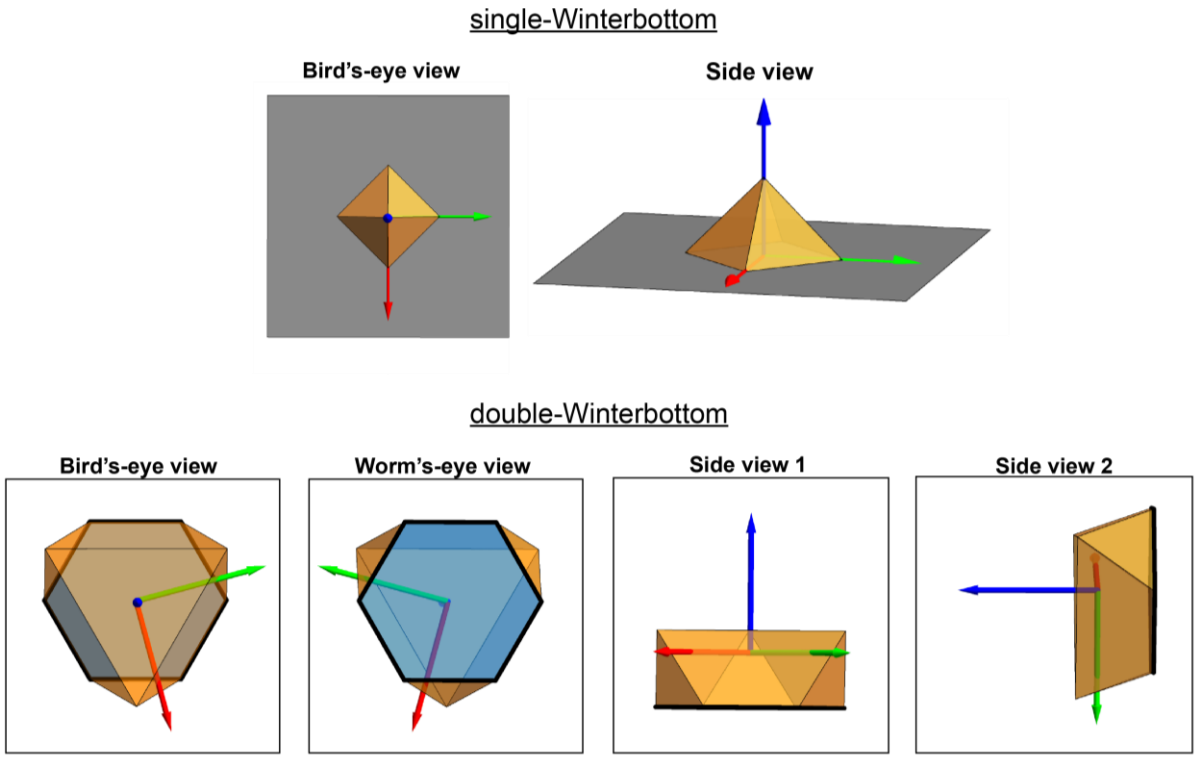

Figure 4.30. Winterbottom constructions of fcc crystals with different morphologies. Single-Winterbottom constructs afford Type 3 crystals, where the crystal is bound to the substrate (*i.e.*, plastic crystallization well), gray plane, along the {100} face. Double-Winterbottom constructs between two fcc (F432 lattice symmetry) yield Type 2 crystals. The interface is indicated by the blue plane and bold lines.

In line with their all-{111}-bounded surfaces, Type 2 crystals grew isotropically when incubated in a fresh solution of HuHF molecules as previously described (**Figures 4.2b and 4.3**). By contrast, when we placed the square-pyramidal, Type 3 crystals in a fresh solution of $^{\Delta C}$HuHF molecules in the presence of Ca^{2+}, we observed that the growth was predominantly restricted to the {100} face that formed the base of the pyramid. As expected from the lower stability/higher reactivity of the {100} plane, the growth rate off of the {100} face (≥2 nm/s) was ≥4-fold greater than that observed for the {111} faces (**Figure 4.31**), eventually leading to the formation of the ideal octahedral (Type 1) morphology (**Figure 4.32**). When we repeated the same experiment by placing Type 3 $^{\Delta C}$HuHF seed crystals in a solution of ^{C157}HuHF and Ca^{2+}, followed by treatment with fluorescein-5-maleimide, we obtained octahedral crystals with two distinct square-pyramidal halves: one non-fluorescent domain composed of $^{\Delta C}$HuHF and one fluorescent domain composed of ^{C157}HuHF (**Figure 4.27d**), yielding Janus-patterned protein crystals. The differential surface energies of metallic materials and nanocrystals are central to their reactivities/catalytic properties and have been frequently exploited to modulate their growth kinetics and morphologies.[62, 69, 96-98.] Our results thus illustrate that the same principles can also be applied to control the morphologies of protein crystals and obtain anisotropic spatial patterns within.

While not explored in the current study, we envision that the anisotropic patterning in the Janus HuHF crystals can be leveraged for compartmentalization of incompatible enzymes/catalytic reactions and for engineering optically and magnetically active materials, especially when combined with the ability of HuHF to encapsulate plasmonic or magnetic nanoparticles. At a more fundamental level, Janus HuHF crystals represent unique, anisotropic nano/micro-scale particles that may display unusual self-assembly behavior in solution and at interfaces to generate spatial patterning at even longer length scales.

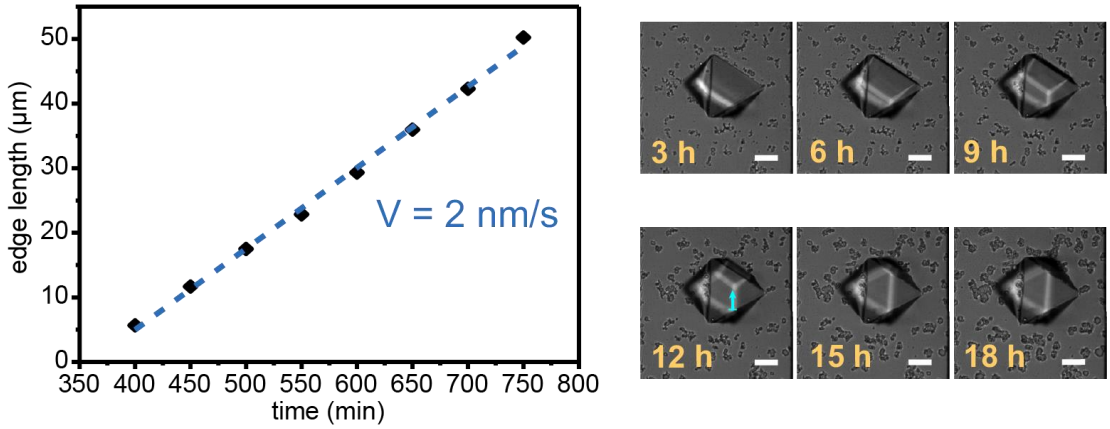

Figure 4.31. Plot displaying (right) the measured edge length (cyan) of a crystal over time. The epitaxial growth rate of ^{C157}HuHF was determined to be 2 nm/s. Left: Confocal microscopy images displaying a single $^{\Delta C}$HuHF crystal transforming into a $^{\Delta C}$HuHF-^{C157}HuHF Janus-type crystal. Scale bars: 50 µm

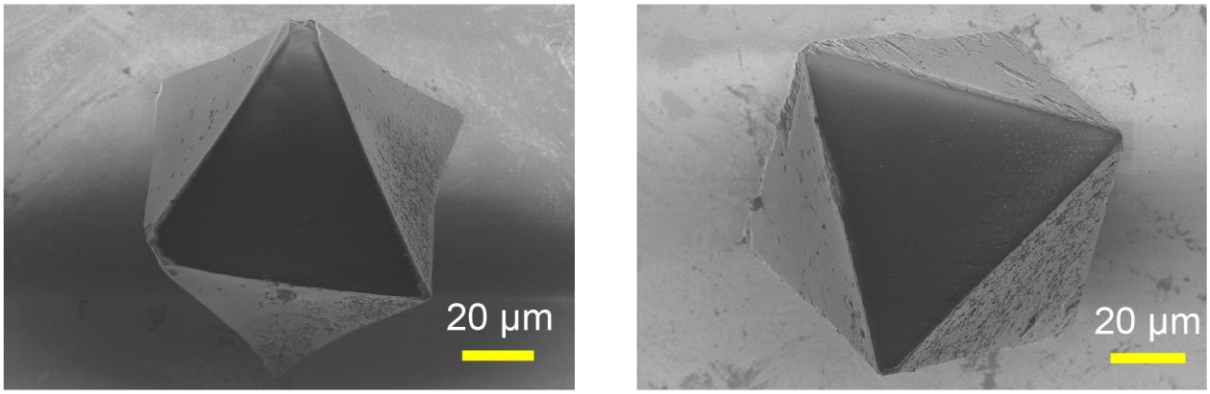

Figure 4.32. SEM images of two separate Type 1 $^{\Delta C}$HuHF-^{C157}HuHF Janus-type crystals.

4.4 Conclusions

Porous protein crystals are emerging as promising functional materials owing to their structural and functional diversity, their ability to be modified genetically and chemically with atomic precision, and their inherent biocompatibility. We have reported here that the utility of protein crystals as functional materials can be further augmented through their tunable spatial organization. By taking advantage of the chemically/kinetically controllable nature of HuHF crystallization, we assembled core-shell platforms with chemically distinct domains, tunable structures and structural patterns. The structural tunability of HuHF crystals was further combined with their mesoporosity and their processability into adaptive PIX systems to engineer multi-enzyme frameworks with cooperative catalytic functions. Of note, we constructed a cell-like system in which the catalytic activity by an enzyme in the framework periphery controls molecular access to the framework interior, affecting the activity of another enzyme located therein. Further, we showed that the interactions of HuHF crystals with solid substrates can give rise to alternative crystal habits with different surface energies, which in turn can be exploited to assemble anisotropically patterned, Janus-type crystals. These examples illustrate that crystal engineering approaches that are commonly used to fabricate functional solid-state materials (*e.g.*, layer-by-layer growth, template-directed crystallization, crystal-facet-selective chemistry) can also be applied in the case of crystalline protein frameworks. On the one hand, the inherently high symmetry and spherical shape of HuHF molecules, which are not present in a majority of proteins, greatly facilitated the formation of porous crystals and therefore the realization of the proof-of-principle examples reported here. On the other hand, the most important attribute of HuHF molecules in generating spatially patterned crystals was their self-assembly through reversible, metal coordination interactions, which enabled the externally controllable initiation and stoppage

of the crystallization process as well as the nucleation/growth kinetics. Given the rapid advances in the chemical and computational design of protein assemblies, it should soon be possible to render the 3D crystallization of arbitrary proteins similarly chemically inducible, thus expanding the library of designer protein crystals with tunable morphologies and spatial patterns.

4.5 Methods

4.5.1 General Methods.

All reagents were purchased from commercial sources and used without further purification unless noted otherwise. Fluorescein-5-maleimide (Fisher, Cat. No. F081025MG). Sulfosuccinimidyl 4-(N-maleimidomethyl)cyclohexane-1-carboxylate (Sulfo-SMCC, Chem-Impex, Cat. No. 23033). Horseradish peroxidase (Fisher, Cat. No. AAJ60026MC). Catalase (Sigma, Cat. No. C9322), Glucose oxidase (Sigma, Cat. No. G7141-50KU). NHS-Rhodamine (Thermo Scientific, Cat. No. 46406). Amplex Red (Invitrogen, Cat. No. 12222). A 10 mM stock solution of Amplex Red was prepared in 50% DMSO and used for subsequent studies. All light micrograph images and videos were obtained on an SZX7 (Olympus) microscope equipped with an Infinity1 CCD (Lumenera).

4.5.2 Expression, purification, and characterization of HuHF.

The plasmid for the ΔC variant of human heavy-chain ferritin (HuHF), devoid of all native cysteine residues (C90E, C102A, and C130A), was obtained via site-directed mutagenesis as previously described.[99.] ^{C157}HuHF was prepared using QuikChange mutagenesis with primers obtained from Integrated DNA Technologies shown in Table S1. Mutant plasmids were transformed into XL-1 blue E. coli cells and purified with QIAprep Spin Miniprep kit (Qiagen). The variant was sequenced (Retrogen) to verify mutagenesis. Expression and purification of

$^{\Delta C}$HuHF and ^{C157}HuHF were performed according to previously published protocol.[50.] When handling ^{C157}HuHF, 2 mM dithiothreitol (DTT) was added at each step during purification to prevent disulfide-mediated protein aggregation.

4.5.3 Expression, isolation, and purification of GFP.

The gene for monomeric superfolder GFP (GFP) was provided by Dr. Suckjoon Jun's group (UC San Diego) and incorporated into the plasmid vector pJexpress through restriction enzyme ligation. Restriction enzyme sites *NdeI* (5') and *XhoI* (3') were first added to the gene through PCR amplification. Then, the restriction enzymes *NdeI* and *XhoI* were used to digest the gene following the protocol of New England Biolabs (NEB, https://nebcloner.neb.com). The resulting gene fragments were separated using a spin column with a 30 kDa MWCO. T4 ligase was used for the ligation of the GFP gene into the plasmid following the protocol of NEB. The final vector was transformed into XL-1 Blue cells by heat-shock. Expression and purification of GFP were performed according to previously published protocol.[85.]

4.5.4 Preparation of ^{Pt}HuHF.

The inner cavity of HuHF was loaded with Pt nanoparticles following a previously described protocol with minor modifications.[74.] To a buffered solution (20 mM HEPES pH 8.5) containing $^{\Delta C}$HuHF (250 μL, 2 μM final concentration), K_2PtCl_4 (62.3 mg, 50 mM final concentration) was added. The 3 mL mixture was stirred in a 5 mL conical tube at room temperature using a triangular stir bar (Spinvane). After 2 h, $NaBH_4$ (56.7 mg, 500 mM final concentration) was added to the tube and left to stir for an additional 3 h. Then, the solution was passed through a PD-10 desalting column (GE Healthcare) equilibrated with a solution containing 15 mM Tris (pH 7.4) and 150 mM NaCl. The filtrate was concentrated down to ~200 μL using a 100 kDa MWCO spin concentrator (Amicon Ultra-0.5) and transferred into a 1.5 mL tube. The

tube was centrifuged for 6 min at 13,800xg to pellet the excess Pt nanoparticles. The supernatant was carefully decanted using a pipette and the protein concentration was measured via Bradford analysis. The solution was further concentrated to a final concentration of 25 μM ^{Pt}HuHF.

4.5.5 Preparation of core-shell and Janus-type crystals.

Protein crystals were formed by sitting drop vapor diffusion. The conditions that gave macroscopic $^{\Delta C}$HuHF crystals are detailed in Table S2. After ferritin crystal formation (which takes 1-2 days), they were washed with a solution containing 25 mM HEPES (pH 7.0) and placed in 20 μL of HuHF crystal forming conditions (Table S2). It is important to note that the sitting drop solution was homogenized using a pipette before the addition of a crystal.

4.5.6 Preparation of multi-layered HuHF crystals.

Freshly formed core-shell crystals were washed with a mixture containing 25 mM HEPES (pH 7.0) and 30 mM $CaCl_2$. Then, they were washed again with 25 mM HEPES (pH 7.0) before being placed in $^{\Delta C}$HuHF or ^{C157}HuHF crystal forming conditions to create another layer. These steps were repeated to create multiple layers. Upon formation, HuHF crystals can be stored in a mixture containing 25 mM HEPES (pH 7.0) and 30 mM $CaCl_2$.

4.5.7 Labeling of HuHF crystals with fluorescein.

Washed HuHF crystals were placed in a well with a 20 μL mixture containing 25 mM HEPES (pH 7.0), 30 mM $CaCl_2$, and 200 μM fluorescein-5-maleimide. The crystallization tray was subsequently wrapped in Al foil to prevent photobleaching of the dye. After 1 h, the crystals were washed and stored in 25 mM HEPES (pH 7.0) and 30 mM $CaCl_2$.

4.5.8 SEM imaging of HuHF crystals.

Washed protein crystals were individually transferred with a mounted CryoLoop onto silicon chips with 5×5 mm dimensions on top of conductive carbon tape. SEM images were

obtained using a Zeiss Sigma 500 scanning electron microscope (Zeiss) at an accelerating voltage of 1 kV to 1.5 kV using a 10-30 μm aperture with an ETD detector.

4.5.9 X-ray crystallographic measurements of core-shell single crystals.

Core-shell crystal samples were freshly prepared in sitting drop trays as previously described. $^{\Delta C}$HuHF@^{C157}HuHF crystallographic data were collected using a Bruker Apex II homesource at the UCSD crystallography facility and analyzed using Bruker Apex4 crystallography software suite. Additional X-ray diffraction and fluorescence measurements of HuHF crystals were collected at 100 K at ALS beamline 8.3.1 and were indexed, integrated, and scaled using XDS.[100-101.]

4.5.10 Confocal microscopy measurements of crystals.

Crystal samples were suspended in a 10-20 μL solution containing 25 mM HEPES (pH 7.0) and 30 mM $CaCl_2$, transferred onto a glass slide, and monitored with a 10x or 20x air objective installed on a spinning-disk confocal Axio Observer. Fluorescein and GFP fluorescence data were measured using a filter to collect light at 500-550 nm (green channel). Rhodamine and resorufin/Amplex Red data were measured using a filter to collect light at 575-650 nm (red channel). Differential interference contrast (DIC) and fluorescence images were captured with 100 ms exposure. Images were collected in Slidebook 6 (Intelligent Imaging Innovations) and analyzed using Fiji (http://fiji.sc/Fiji).

4.5.11 Preparation of maleimide-functionalized proteins.

A 1 mL solution containing 100 μM protein, 1 mM sulfo-SMCC, and 20 mM HEPES (pH 8.0) was prepared in an Eppendorf tube equipped with a triangular stir bar (Spinvane). After stirring at room temperature for 30 min, the mixture was passed through a PD-10 desalting column (GE Healthcare) equilibrated with 25 mM HEPES (pH 7.0) and 30 mM $CaCl_2$ to remove the excess

sulfo-SMCC molecules and buffer exchange the maleimide-functionalized protein. The protein solution was then concentrated to 200 μM protein using a 10 kDa MWCO spin concentrator (Amicon Ultra-0.5).

4.5.12 Preparation of fluorescein-labeled catalase.

Before functionalizing catalase with sulfo-SMCC groups, the protein was treated with fluorescein-5-maleimide. To a solution buffered by 50 mM potassium phosphate (pH 7.0), catalase (3.5 mg), fluorescein (1 mM final concentration), and TCEP (500 μM, final concentration) were added. The 3.5 mL solution was stirred in a 5 mL conical tube at room temperature using a triangular stir bar (Spinvane). After 2 h, the solution was buffer exchanged into H_2O (Milli-Q) using a 30 kDa MWCO spin concentrator (6 mL, Vivaspin). The fluorescein-labeled catalase was subsequently used to prepare maleimide-functionalized catalase as described above.

4.5.13 Preparation of rhodamine-labeled horseradish peroxidase (r-HRP).

HRP stock solution: 200 μM in 20 mM HEPES (pH 8.0). *NHS-Rhodamine stock solution*: 1 mg/10 μL (189 mM) in DMF. In a 5 mL conical tube with a triangular stir bar, a 2 mL solution was prepared by adding 989.4 μL of 20 mM HEPES (pH 8.0), 1 mL of the HRP stock solution, and 10.6 μL of the NHS-Rhodamine stock solution. The solution was wrapped in foil and left to stir at room temperature. After 1 h, the solution was buffer exchanged and washed excessively with 20 mM MES (pH 6.0) using a 10 kDa MWCO. The resulting rhodamine-labeled HRP (r-HRP) was concentrated to 200 μM.

4.5.14 Labeling of $^{\Delta C}$HuHF@^{C157}HuHF core-shell crystals with proteins.

Washed $^{\Delta C}$HuHF@^{C157}HuHF core-shell crystals were placed in a well containing a 20 μL mixture of 25 mM HEPES (pH 7.0), 30 mM $CaCl_2$, and 500 μM TCEP. After >30 min, the solution was replaced with a buffered solution containing 25 mM HEPES (pH 7.0), 30 mM $CaCl_2$, and 200

μM maleimide-functionalized protein. The tray was subsequently wrapped in foil and placed on the benchtop at room temperature. After >12 h, the protein-functionalized core-shell crystals were washed and stored in a mixture containing 25 mM HEPES (pH 7.0) and 30 mM $CaCl_2$.

4.5.15 Preparation of PIX samples.

Polymer precursor solution: 25 mM HEPES (pH 7.0), 30 mM $CaCl_2$, 917 mM (8.625% w/v) sodium acrylate, 352 mM (2.5% w/v) acrylamide and 13 mM (0.2% w/v) *N,N′*-methylenebis(acrylamide). *Polymerization solution*: 4 M NaCl, 1% (w/v) APS and 1% (v/v) TEMED. HuHF crystals were formed using sitting drop crystallization trays (Hampton), as described above and in Table S2. After crystal formation, the well solution was replaced with the polymer precursor solution (20 μL) and left to incubate for >12 h to ensure full infusion of the monomers. The crystals were then placed in the polymerization solution (20 μL) for ≥20 min to effectively form PIX. Crystal expansion was initiated by placing a single $^{\Delta C}$HuHF@^{C157}HuHF PIX sample in H_2O and monitored via light microscopy.

4.5.16 Activity studies using glucose oxidase and HRP-functionalized crystals.

HRP stock solution: 200 μM in 20 mM MES (pH 6.0). *Amplex Red reaction solution*: 20 mM MES (pH 6.0), 30 mM $CaCl_2$, 2 mM glucose, and 200 μM Amplex Red. Maleimide-functionalized glucose oxidase (mal-GOx) was prepared and used to decorate the surface of $^{\Delta C}$HuHF@^{C157}HuHF crystals as described above. The GOx-functionalized $^{\Delta C}$HuHF@^{C157}HuHF crystals were then washed with a solution containing 25 mM HEPES (pH 7.0) and 30 mM $CaCl_2$ and processed into PIX in sitting drop wells. The polymerization solution was then replaced with a 20 μL wash solution containing 20 mM MES (pH 6.0). The solution was decanted and 20 μL of the HRP stock solution was added to the well. After 1 min, the PIX samples expanded, and 10 μL of 1 M $CaCl_2$ was added to initiate contraction, entrapping the HRP molecules in the crystal

interstitial space. The HRP-loaded crystals were washed and stored in a solution containing 20 mM MES (pH 6.0) and 30 mM $CaCl_2$. Individual crystals were suspended with a 10 μL solution of the same MES wash buffer and transferred onto a glass slide. Before monitoring the crystal via confocal microscopy, as described above, 10 μL of the Amplex Red reaction solution was added to the droplet to initiate cascade reactivity. Control samples were prepared and monitored in parallel.

4.5.17 Activity studies using catalase and HRP functionalized crystals.

HRP stock solution: 200 μM in 20 mM MES (pH 6.0). *Amplex Red reaction solution*: 20 mM MES (pH 6.0), 30 mM $CaCl_2$, 2 mM H_2O_2, and 200 μM Amplex Red. Maleimide-functionalized catalase (mal-Cat) was prepared and used to decorate the surface of $^{\Delta C}$HuHF@^{C157}HuHF crystals as described above. The Cat-functionalized $^{\Delta C}$HuHF@^{C157}HuHF crystals were then washed with a solution containing 25 mM HEPES (pH 7.0) and 30 mM $CaCl_2$ and processed into PIX in sitting drop wells. Upon formation, the polymerization solution was replaced with a 20 μL wash solution containing 20 mM MES (pH 6.0). The solution was decanted and 20 μL of the HRP stock solution was added to the well. After 1 min, the PIX samples expanded, and 10 μL of 1 M $CaCl_2$ was added to initiate contraction, entrapping the HRP molecules in the crystal interstitial space. The HRP-loaded crystals were washed and stored in a solution containing 20 mM MES (pH 6.0) and 30 mM $CaCl_2$. Individual crystals were suspended with a 10 μL solution of the same MES wash buffer and transferred onto a glass slide. Before monitoring the crystals via confocal microscopy, as described above, 10 μL of the Amplex Red reaction solution was added to the droplet to initiate the reaction. *Amplex Red reaction solutions* containing 10 mM or 20 mM H_2O_2 were prepared for additional studies. Control samples without Cat were prepared and monitored in parallel.

4.5.18 Monitoring H_2O_2 decomposition by HuHF crystals.

HuHF crystals were prepared as described above and washed with a buffered solution containing 25 mM HEPES (pH 7.0) and 30 mM $CaCl_2$. Individual crystals were transferred into a 20 μL mixture containing 25 mM HEPES (pH 7.0), 30 mM $CaCl_2$, 400 mM H_2O_2, using a mounted CryoLoop, and monitored via light microscopy.

4.5.19 Peroxidase activity of ^{Pt}HuHF crystals.

Amplex Red reaction solution: 20 mM MES (pH 6.0), 30 mM $CaCl_2$, 2 mM H_2O_2, and 200 μM Amplex Red. $^{\Delta C}$HuHF@^{Pt}HuHF crystals were prepared as described above and were washed with a buffered solution containing 20 mM MES (pH 6.0) and 30 mM $CaCl_2$. Individual crystals were suspended with a 10 μL solution of the same MES wash buffer and transferred onto a glass slide. Before monitoring the samples via confocal microscopy, as described above, 10 μL of the Amplex Red reaction solution was added to the droplet to initiate the reaction.

4.5.20 TEM and EDX analysis of ^{Pt}HuHF.

A 3 μL suspension of ^{Pt}HuHF was pipetted onto Formvar/carbon-coated Cu grids (Ted Pella, Inc.) that had been negatively glow discharged for 45−60 s. Samples were incubated for 5 min, washed with 50 μL filtered milli-Q H_2O, and blotted with filter paper. For negatively-stained samples, a 3.5 μL drop of 2% uranyl acetate in water was pipetted onto the grid, incubated for 3 min, and blotted dry with filter paper. Grids were imaged using a JEOL 1400 plus transmission electron microscope operating at 80 kV, equipped with a bottom-mount Gatan OneView (4k x 4k) camera. Scanning TEM and EDX images were collected using a Thermo Fisher Talos F200X Scanning/Transmission Electron Microscope (STEM) operating at 200 kV. Scanning TEM and EDX images were acquired using Velox software, and the images were processed with Thermo Scientific software.

4.5.21 Modeling Winterbottom structures.

Crystal morphologies were constructed using the WulffMaker: (Double)Winterbottom shapes v3.0 software.[95.] Type 3 crystal shapes are single-Winterbottom constructs modeled by using *F*432 lattice symmetry and keeping the ratio of γ_{111}:γ_{100} to 1:1.732.[102.] Type 2 crystal shapes are double-Winterbottom constructs modeled by using two *F*432 lattice symmetries, keeping the ratio of γ_{111}:γ_{111} to 1:0.6 with Euler angle $\Phi_1 = 0$ and (111) hkl values for the normal interface.

Table 4.1. Primers for site-directed mutagenesis.

Variant	Mutation	Primer Sequence
157C ΔC	K157C	5'-CCAACCTGCGTTGCATGGGTGCACC-3' 5'-GGTGCACCCATGCAACGCAGGTTGG-3'

Table 4.2. Crystallization conditions for $^{\Delta C}$HuHF, ^{C157}HuHF, and ^{Pt}HuHF.

$^{\Delta C}$HuHF	Stock protein solution	25 µM in 15 mM Tris (pH 7.4), 150 mM NaCl
	Reservoir	500 µL total volume: 50 mM HEPES (pH 7.0), 11 mM $CaCl_2$
	Sitting drop	7.5 µL of 25 µM $^{\Delta C}$HuHF, 7.5 µL reservoir
^{C157}HuHF	Stock protein solution	25 µM in 15 mM Tris (pH 7.4), 150 mM NaCl, 2 mM DTT
	Reservoir	500 µL total volume: 50 mM HEPES (pH 7.0), 9 mM $CaCl_2$
	Sitting drop	10 µL of 25 µM ^{C157}HuHF, 10 µL reservoir
^{Pt}HuHF	Stock protein solution	25 µM in 15 mM Tris (pH 7.4), 150 mM NaCl
	Reservoir	500 µL total volume: 50 mM HEPES (pH 7.0), 10 mM $CaCl_2$
	Sitting drop	10 µL of 25 µM ^{Pt}HuHF, 10 µL reservoir

4.6 Acknowledgements

We thank the members of the Tezcan group and Prof. Robert Macfarlane for helpful discussions, Prof. W. J. Rappel for access to confocal microscopy instrumentation, and Prof. Suck-joon Jun for providing the GFP gene. This work was supported by US Department of Energy (BES, Division of Materials Sciences, Biomolecular Materials Program, DE-SC0003844; for the development of the PIX concept, protein encapsulation, activity measurements), US Army Research Office (W911NF-19-1-0228; for the development of spatially patterned crystals). Z.Z. was supported by DOE-BES as part of the Energy Frontier Research Centers program: CSSAS–The Center for the Science of Synthesis Across Scales–under Award Number DE-SC0019288 (SEM and TEM measurements). X-ray crystallographic measurements were done at Beamline 8.3.1 at the Ad-vanced Light Source, which is operated by the University of California at San Francisco with generous grants from the National Institutes of Health (R01 GM124149 for technology development and P30 GM124169 for beam-line operations), and the Integrated Diffraction Analysis Technologies program of the US DOE-BER. F.A.T. acknowledges the John Simon Guggenheim Memorial Foundation for a fellowship.

Chapter 4 is reproduced, in part, with permission, from: Han, K., Zhang, Z., Tezcan, F. A. "Spatially Patterned, Porous Protein Crystals as Multifunctional Materials" *Journal of the American Chemical Society* **2023** (Accepted). The dissertation author was the primary author on all reprinted materials.

4.7 References

1. Furukawa, H.; Cordova, K. E.; O'Keeffe, M.; Yaghi, O. M., The chemistry and applications of metal-organic frameworks. *Science* **2013,** *341*, 1230444.

2. Corma, A.; Garcia, H.; Llabres i Xamena, F. X., Engineering metal organic frameworks for heterogeneous catalysis. *Chem. Rev.* **2010,** *110*, 4606-55.

3. Das, S.; Heasman, P.; Ben, T.; Qiu, S., Porous Organic Materials: Strategic Design and Structure-Function Correlation. *Chem. Rev.* **2017,** *117*, 1515-1563.

4. Horike, S.; Shimomura, S.; Kitagawa, S., Soft porous crystals. *Nat. Chem.* **2009,** *1*, 695-704.

5. Kowalski, A. E.; Johnson, L. B.; Dierl, H. K.; Park, S.; Huber, T. R.; Snow, C. D., Porous protein crystals as scaffolds for enzyme immobilization. *Biomater. Sci.* **2019,** *7*, 1898-1904.

6. Kojima, M.; Abe, S.; Ueno, T., Engineering of protein crystals for use as solid biomaterials. *Biomater. Sci.* **2022,** *10*, 354-367.

7. Ueno, T., Porous protein crystals as reaction vessels. *Chem.* **2013,** *19*, 9096-102.

8. Margolin, A. L.; Navia, M. A., Protein Crystals as Novel Catalytic Materials. *Angew. Chem. Int. Ed.* **2001,** *40*, 2204-2222.

9. Khanh Nguyen, T.; Toan Pham, T.; Ueno, T., Engineering of protein crystals for development of bionanomaterials. *Jpn. J. Appl. Phys.* **2019,** *58*.

10. Nguyen, T. K.; Abe, S.; Kasamatsu, M.; Maity, B.; Yamashita, K.; Hirata, K.; Kojima, M.; Ueno, T., In-Cell Engineering of Protein Crystals with Nanoporous Structures for Promoting Cascade Reactions. *ACS Appl. Nano Mater.* **2021,** *4*, 1672-1681.

11. Abe, S.; Maity, B.; Ueno, T., Design of a confined environment using protein cages and crystals for the development of biohybrid materials. *Chem. Commun.* **2016,** *52*, 6496-512.

12. Abe, S.; Ijiri, H.; Negishi, H.; Yamanaka, H.; Sasaki, K.; Hirata, K.; Mori, H.; Ueno, T., Design of Enzyme-Encapsulated Protein Containers by In Vivo Crystal Engineering. *Adv. Mater.* **2015,** *27*, 7951-6.

13. Heater, B. S.; Lee, M. M.; Chan, M. K., Direct production of a genetically-encoded immobilized biodiesel catalyst. *Sci. Rep.* **2018,** *8*, 12783.

14. Heater, B. S.; Yang, Z.; Lee, M. M.; Chan, M. K., In Vivo Enzyme Entrapment in a Protein Crystal. *J. Am. Chem. Soc.* **2020,** *142*, 9879-9883.

15. Maita, N., Crystal Structure Determination of Ubiquitin by Fusion to a Protein That Forms a Highly Porous Crystal Lattice. *J. Am. Chem. Soc.* **2018,** *140*, 13546-13549.

16. Basu, S. K.; Govardhan, C. P.; Jung, C. W.; Margolin, A. L., Protein crystals for the delivery of biopharmaceuticals. *Expert. Opin. Biol. Ther.* **2004,** *4*, 301-17.

17. Guli, M.; Lambert, E. M.; Li, M.; Mann, S., Template-Directed Synthesis of Nanoplasmonic Arrays by Intracrystalline Metalization of Cross-Linked Lysozyme Crystals. *Angewandte Chemie* **2010,** *122*, 530-533.

18. Cavazza, C.; Bochot, C.; Rousselot-Pailley, P.; Carpentier, P.; Cherrier, M. V.; Martin, L.; Marchi-Delapierre, C.; Fontecilla-Camps, J. C.; Menage, S., Crystallographic snapshots of the reaction of aromatic C-H with O(2) catalysed by a protein-bound iron complex. *Nat. Chem.* **2010,** *2*, 1069-76.

19. Kowalski, A. E.; Huber, T. R.; Ni, T. W.; Hartje, L. F.; Appel, K. L.; Yost, J. W.; Ackerson, C. J.; Snow, C. D., Gold nanoparticle capture within protein crystal scaffolds. *Nanoscale* **2016,** *8*, 12693-6.

20. Ward, A. R.; Snow, C. D., Porous crystals as scaffolds for structural biology. *Current Opinion in Structural Biology* **2020,** *60*, 85-92.

21. Shenoy, B.; Wang, Y.; Shan, W.; Margolin, A. L., Stability of crystalline proteins. *Biotechnol. Bioeng.* **2001,** *73*, 358-69.

22. Zelinski, T.; Waldmann, H., Cross-Linked Enzyme Crystals(CLECs): Efficient and Stable Biocatalysts for Preparative Organic Chemistry. *Angew. Chem. Int. Ed.* **1997,** *36*, 722-724.

23. Lopez, S.; Rondot, L.; Lepretre, C.; Marchi-Delapierre, C.; Menage, S.; Cavazza, C., Cross-Linked Artificial Enzyme Crystals as Heterogeneous Catalysts for Oxidation Reactions. *J. Am. Chem. Soc.* **2017,** *139*, 17994-18002.

24. Jegan Roy, J.; Emilia Abraham, T., Strategies in making cross-linked enzyme crystals. *Chem. Rev.* **2004,** *104*, 3705-22.

25. Hartje, L. F.; Snow, C. D., Protein crystal based materials for nanoscale applications in medicine and biotechnology. *Wiley Interdiscip. Rev. Nanomed. Nanobiotechnol.* **2019,** *11*, e1547.

26. Tabe, H.; Abe, S.; Hikage, T.; Kitagawa, S.; Ueno, T., Porous protein crystals as catalytic vessels for organometallic complexes. *Chem. Asian. J.* **2014,** *9*, 1373-8.

27. Nepal, M.; Sheedlo, M. J.; Das, C.; Chmielewski, J., Accessing Three-Dimensional Crystals with Incorporated Guests through Metal-Directed Coiled-Coil Peptide Assembly. *J. Am. Chem. Soc.* **2016,** *138*, 11051-11057.

28. Curtis, R. W.; Scrudders, K. L.; Ulcickas, J. R. W.; Simpson, G. J.; Low-Nam, S. T.; Chmielewski, J., Supramolecular Assembly of His-Tagged Fluorescent Protein Guests within Coiled-Coil Peptide Crystal Hosts: Three-Dimensional Ordering and Protein Thermal Stability. *ACS Biomater. Sci. Eng.* **2022,** *8*, 1860-1866.

29. Kunzle, M.; Eckert, T.; Beck, T., Binary Protein Crystals for the Assembly of Inorganic Nanoparticle Superlattices. *J. Am. Chem. Soc.* **2016,** *138*, 12731-12734.

30. Kostiainen, M. A.; Hiekkataipale, P.; Laiho, A.; Lemieux, V.; Seitsonen, J.; Ruokolainen, J.; Ceci, P., Electrostatic assembly of binary nanoparticle superlattices using protein cages. *Nature Nanotech* **2013,** *8*, 52-56.

31. Liu, Q.; Zhou, Y.; Shaukat, A.; Meng, Z.; Kyllonen, D.; Seitz, I.; Langerreiter, D.; Kuntze, K.; Priimagi, A.; Zheng, L.; Kostiainen, M. A., Optically Controlled Construction of Three-Dimensional Protein Arrays. *Angew. Chem. Int. Ed.* **2023**, e202303880.

32. Brodin, J. D.; Auyeung, E.; Mirkin, C. A., DNA-mediated engineering of multicomponent enzyme crystals. *Proc. Natl. Acad. Sci.* **2015,** *112*, 4564-9.

33. Yang, Z.; Lee, M. M. M.; Chan, M. K., Efficient intracellular delivery of p53 protein by engineered protein crystals restores tumor suppressing function in vivo. *Biomater.* **2021,** *271*, 120759.

34. Yang, Z.; Zheng, J.; Chan, C. F.; Wong, I. L. K.; Heater, B. S.; Chow, L. M. C.; Lee, M. M. M.; Chan, M. K., Targeted delivery of antimicrobial peptide by Cry protein crystal to treat intramacrophage infection. *Biomater.* **2019,** *217*, 119286.

35. Zhu, J.; Avakyan, N.; Kakkis, A.; Hoffnagle, A. M.; Han, K.; Li, Y.; Zhang, Z.; Choi, T. S.; Na, Y.; Yu, C. J.; Tezcan, F. A., Protein Assembly by Design. *Chem. Rev.* **2021,** *121*, 13701-13796.

36. Luo, Q.; Hou, C.; Bai, Y.; Wang, R.; Liu, J., Protein Assembly: Versatile Approaches to Construct Highly Ordered Nanostructures. *Chem. Rev.* **2016,** *116*, 13571-13632.

37. Wicky, B. I. M.; Milles, L. F.; Courbet, A.; Ragotte, R. J.; Dauparas, J.; Kinfu, E.; Tipps, S.; Kibler, R. D.; Baek, M.; DiMaio, F.; Li, X.; Carter, L.; Kang, A.; Nguyen, H.; Bera, A. K.; Baker, D., Hallucinating symmetric protein assemblies. *Science* **2022,** *378*, 56-61.

38. King, N. P.; Sheffler, W.; Sawaya, M. R.; Vollmar, B. S.; Sumida, J. P.; Andre, I.; Gonen, T.; Yeates, T. O.; Baker, D., Computational design of self-assembling protein nanomaterials with atomic level accuracy. *Science* **2012,** *336*, 1171-4.

39. Huang, P. S.; Boyken, S. E.; Baker, D., The coming of age of de novo protein design. *Nature* **2016,** *537*, 320-7.

40. Shen, H.; Fallas, J. A.; Lynch, E.; Sheffler, W.; Parry, B.; Jannetty, N.; Decarreau, J.; Wagenbach, M.; Vicente, J. J.; Chen, J.; Wang, L.; Dowling, Q.; Oberdorfer, G.; Stewart, L.; Wordeman, L.; De Yoreo, J.; Jacobs-Wagner, C.; Kollman, J.; Baker, D., De novo design of self-assembling helical protein filaments. *Science* **2018,** *362*, 705-709.

41. Humphreys, I. R.; Pei, J.; Baek, M.; Krishnakumar, A.; Anishchenko, I.; Ovchinnikov, S.; Zhang, J.; Ness, T. J.; Banjade, S.; Bagde, S. R.; Stancheva, V. G.; Li, X. H.; Liu, K.; Zheng, Z.; Barrero, D. J.; Roy, U.; Kuper, J.; Fernandez, I. S.; Szakal, B.; Branzei, D.; Rizo, J.; Kisker, C.; Greene, E. C.; Biggins, S.; Keeney, S.; Miller, E. A.; Fromme, J. C.; Hendrickson, T. L.; Cong, Q.; Baker, D., Computed structures of core eukaryotic protein complexes. *Science* **2021,** *374*, eabm4805.

42. Golub, E.; Subramanian, R. H.; Esselborn, J.; Alberstein, R. G.; Bailey, J. B.; Chiong, J. A.; Yan, X.; Booth, T.; Baker, T. S.; Tezcan, F. A., Constructing protein polyhedra via orthogonal chemical interactions. *Nature* **2020,** *578*, 172-176.

43. McMillan, J. R.; Hayes, O. G.; Winegar, P. H.; Mirkin, C. A., Protein Materials Engineering with DNA. *Acc. Chem. Res.* **2019,** *52*, 1939-1948.

44. Hayes, O. G.; Partridge, B. E.; Mirkin, C. A., Encoding hierarchical assembly pathways of proteins with DNA. *Proc. Natl. Acad. Sci.* **2021,** *118*.

45. Partridge, B. E.; Winegar, P. H.; Han, Z.; Mirkin, C. A., Redefining Protein Interfaces within Protein Single Crystals with DNA. *J. Am. Chem. Soc.* **2021,** *143*, 8925-8934.

46. Huber, T. R.; Hartje, L. F.; McPherson, E. C.; Kowalski, A. E.; Snow, C. D., Programmed Assembly of Host-Guest Protein Crystals. *Small* **2017,** *13*.

47. Radford, R. J.; Tezcan, F. A., A superprotein triangle driven by nickel(II) coordination: exploiting non-natural metal ligands in protein self-assembly. *J. Am. Chem. Soc.* **2009,** *131*, 9136-7.

48. Brodin, J. D.; Ambroggio, X. I.; Tang, C.; Parent, K. N.; Baker, T. S.; Tezcan, F. A., Metal-directed, chemically tunable assembly of one-, two- and three-dimensional crystalline protein arrays. *Nat. Chem.* **2012,** *4*, 375-82.

49. Brodin, J. D.; Carr, J. R.; Sontz, P. A.; Tezcan, F. A., Exceptionally stable, redox-active supramolecular protein assemblies with emergent properties. *Proc. Natl. Acad. Sci.* **2014,** *111*, 2897-902.

50. Sontz, P. A.; Bailey, J. B.; Ahn, S.; Tezcan, F. A., A Metal Organic Framework with Spherical Protein Nodes: Rational Chemical Design of 3D Protein Crystals. *J. Am. Chem. Soc.* **2015,** *137*, 11598-601.

51. Suzuki, Y.; Cardone, G.; Restrepo, D.; Zavattieri, P. D.; Baker, T. S.; Tezcan, F. A., Self-assembly of coherently dynamic, auxetic, two-dimensional protein crystals. *Nature* **2016,** *533*, 369-73.

52. Alberstein, R.; Suzuki, Y.; Paesani, F.; Tezcan, F. A., Engineering the entropy-driven free-energy landscape of a dynamic nanoporous protein assembly. *Nat. Chem.* **2018,** *10*, 732-739.

53. Subramanian, R. H.; Smith, S. J.; Alberstein, R. G.; Bailey, J. B.; Zhang, L.; Cardone, G.; Suominen, L.; Chami, M.; Stahlberg, H.; Baker, T. S.; Tezcan, F. A., Self-Assembly of a Designed Nucleoprotein Architecture through Multimodal Interactions. *ACS Cent. Sci.* **2018,** *4*, 1578-1586.

54. Subramanian, R. H.; Zhu, J.; Bailey, J. B.; Chiong, J. A.; Li, Y.; Golub, E.; Tezcan, F. A., Design of metal-mediated protein assemblies via hydroxamic acid functionalities. *Nat Protoc* **2021,** *16*, 3264-3297.

55. Liljestrom, V.; Mikkila, J.; Kostiainen, M. A., Self-assembly and modular functionalization of three-dimensional crystals from oppositely charged proteins. *Nat. Commun.* **2014,** *5*, 4445.

56. Hayes, O. G.; McMillan, J. R.; Lee, B.; Mirkin, C. A., DNA-Encoded Protein Janus Nanoparticles. *J. Am. Chem. Soc.* **2018,** *140*, 9269-9274.

57. Ramberg, K. O.; Engilberge, S.; Skorek, T.; Crowley, P. B., Facile Fabrication of Protein-Macrocycle Frameworks. *J. Am. Chem. Soc.* **2021,** *143*, 1896-1907.

58. Guagnini, F.; Engilberge, S.; Flood, R. J.; Ramberg, K. O.; Crowley, P. B., Metal-Mediated Protein–Cucurbituril Crystalline Architectures. *Cryst. Growth Des.* **2020,** *20*, 6983-6989.

59. Dotan, N.; Arad, D.; Frolow, F.; Freeman, A., Self-Assembly of a Tetrahedral Lectin into Predesigned Diamondlike Protein Crystals. *Angew. Chem., Int. Ed.* **1999,** *38*, 2363-2366.

60. Sakai, F.; Yang, G.; Weiss, M. S.; Liu, Y.; Chen, G.; Jiang, M., Protein crystalline frameworks with controllable interpenetration directed by dual supramolecular interactions. *Nat. Commun.* **2014,** *5*, 4634.

61. Yang, G.; Ding, H. M.; Kochovski, Z.; Hu, R.; Lu, Y.; Ma, Y. Q.; Chen, G.; Jiang, M., Highly Ordered Self-Assembly of Native Proteins into 1D, 2D, and 3D Structures Modulated by the Tether Length of Assembly-Inducing Ligands. *Angew. Chem. Int. Ed.* **2017,** *56*, 10691-10695.

62. Boles, M. A.; Engel, M.; Talapin, D. V., Self-Assembly of Colloidal Nanocrystals: From Intricate Structures to Functional Materials. *Chem. Rev.* **2016,** *116*, 11220-89.

63. Kim, Y.; Macfarlane, R. J.; Jones, M. R.; Mirkin, C. A., Transmutable nanoparticles with reconfigurable surface ligands. *Science* **2016,** *351*, 579-82.

64. Landy, K. M.; Gibson, K. J.; Chan, R. R.; Pietryga, J.; Weigand, S.; Mirkin, C. A., Programming Nucleation and Growth in Colloidal Crystals Using DNA. *ACS Nano* **2023**, acsnano.2c11674.

65. Dong, A.; Ye, X.; Chen, J.; Kang, Y.; Gordon, T.; Kikkawa, J. M.; Murray, C. B., A Generalized Ligand-Exchange Strategy Enabling Sequential Surface Functionalization of Colloidal Nanocrystals. *J. Am. Chem. Soc.* **2011,** *133*, 998-1006.

66. Ghosh Chaudhuri, R.; Paria, S., Core/Shell Nanoparticles: Classes, Properties, Synthesis Mechanisms, Characterization, and Applications. *Chem. Rev.* **2012,** *112*, 2373-2433.

67. Holtz, J. H.; Asher, S. A., Polymerized colloidal crystal hydrogel films as intelligent chemical sensing materials. *Nature* **1997,** *389*, 829-32.

68. Zhang, Z.; Glotzer, S. C., Self-Assembly of Patchy Particles. *Nano Lett.* **2004,** *4*, 1407-1413.

69. Ha, M.; Kim, J. H.; You, M.; Li, Q.; Fan, C.; Nam, J. M., Multicomponent Plasmonic Nanoparticles: From Heterostructured Nanoparticles to Colloidal Composite Nanostructures. *Chem. Rev.* **2019,** *119*, 12208-12278.

70. Lewis, D. J.; Zornberg, L. Z.; Carter, D. J. D.; Macfarlane, R. J., Single-crystal Winterbottom constructions of nanoparticle superlattices. *Nat. Mater.* **2020,** *19*, 719-724.

71. Jutz, G.; van Rijn, P.; Santos Miranda, B.; Böker, A., Ferritin: A Versatile Building Block for Bionanotechnology. *Chem. Rev.* **2015,** *115*, 1653-1701.

72. Maity, B.; Fujita, K.; Ueno, T., Use of the confined spaces of apo-ferritin and virus capsids as nanoreactors for catalytic reactions. *Curr. Opin. Chem. Biol.* **2015,** *25*, 88-97.

73. Uchida, M.; Klem, M. T.; Allen, M.; Suci, P.; Flenniken, M.; Gillitzer, E.; Varpness, Z.; Liepold, L. O.; Young, M.; Douglas, T., Biological Containers: Protein Cages as Multifunctional Nanoplatforms. *Adv. Mater.* **2007,** *19*, 1025-1042.

74. Fan, J.; Yin, J.-J.; Ning, B.; Wu, X.; Hu, Y.; Ferrari, M.; Anderson, G. J.; Wei, J.; Zhao, Y.; Nie, G., Direct evidence for catalase and peroxidase activities of ferritin–platinum nanoparticles. *Biomater.* **2011,** *32*, 1611-1618.

75. Fan, K.; Cao, C.; Pan, Y.; Lu, D.; Yang, D.; Feng, J.; Song, L.; Liang, M.; Yan, X., Magnetoferritin nanoparticles for targeting and visualizing tumour tissues. *Nat. Nanotechnol.* **2012,** *7*, 459-64.

76. Abe, S.; Niemeyer, J.; Abe, M.; Takezawa, Y.; Ueno, T.; Hikage, T.; Erker, G.; Watanabe, Y., Control of the coordination structure of organometallic palladium complexes in an apo-ferritin cage. *J. Am. Chem. Soc.* **2008,** *130*, 10512-4.

77. Uchida, M.; Flenniken, M. L.; Allen, M.; Willits, D. A.; Crowley, B. E.; Brumfield, S.; Willis, A. F.; Jackiw, L.; Jutila, M.; Young, M. J.; Douglas, T., Targeting of cancer cells with ferrimagnetic ferritin cage nanoparticles. *J. Am. Chem. Soc.* **2006,** *128*, 16626-33.

78. Pulsipher, K. W.; Villegas, J. A.; Roose, B. W.; Hicks, T. L.; Yoon, J.; Saven, J. G.; Dmochowski, I. J., Thermophilic Ferritin 24mer Assembly and Nanoparticle Encapsulation Modulated by Interdimer Electrostatic Repulsion. *Biochemistry* **2017,** *56*, 3596-3606.

79. Joyce, M. G.; King, H. A. D.; Elakhal-Naouar, I.; Ahmed, A.; Peachman, K. K.; Macedo Cincotta, C.; Subra, C.; Chen, R. E.; Thomas, P. V.; Chen, W. H.; Sankhala, R. S.; Hajduczki, A.; Martinez, E. J.; Peterson, C. E.; Chang, W. C.; Choe, M.; Smith, C.; Lee, P. J.; Headley, J. A.; Taddese, M. G.; Elyard, H. A.; Cook, A.; Anderson, A.; McGuckin Wuertz, K.; Dong, M.; Swafford, I.; Case, J. B.; Currier, J. R.; Lal, K. G.; Molnar, S.; Nair, M. S.; Dussupt, V.; Daye, S. P.; Zeng, X.; Barkei, E. K.; Staples, H. M.; Alfson, K.; Carrion, R.; Krebs, S. J.; Paquin-Proulx, D.; Karasavva, N.; Polonis, V. R.; Jagodzinski, L. L.; Amare, M. F.; Vasan, S.; Scott, P. T.; Huang, Y.; Ho, D. D.; de Val, N.; Diamond, M. S.; Lewis, M. G.; Rao, M.; Matyas, G. R.; Gromowski, G. D.; Peel, S. A.; Michael, N. L.; Bolton, D. L.; Modjarrad, K., A SARS-CoV-2 ferritin nanoparticle vaccine elicits protective immune responses in nonhuman primates. *Sci. Transl. Med.* **2022,** *14*, eabi5735.

80. Cai, J.; Sweeney, A. M., The Proof Is in the Pidan: Generalizing Proteins as Patchy Particles. *ACS Cent. Sci.* **2018,** *4*, 840-853.

81. Lawson, D. M.; Artymiuk, P. J.; Yewdall, S. J.; Smith, J. M.; Livingstone, J. C.; Treffry, A.; Luzzago, A.; Levi, S.; Arosio, P.; Cesareni, G.; et al., Solving the structure of human H ferritin by genetically engineering intermolecular crystal contacts. *Nature* **1991,** *349*, 541-4.

82. Bailey, J. B.; Zhang, L.; Chiong, J. A.; Ahn, S.; Tezcan, F. A., Synthetic Modularity of Protein-Metal-Organic Frameworks. *J. Am. Chem. Soc.* **2017,** *139*, 8160-8166.

83. Zhang, L.; Bailey, J. B.; Subramanian, R. H.; Groisman, A.; Tezcan, F. A., Hyperexpandable, self-healing macromolecular crystals with integrated polymer networks. *Nature* **2018,** *557*, 86-91.

84. Han, K.; Bailey, J. B.; Zhang, L.; Tezcan, F. A., Anisotropic Dynamics and Mechanics of Macromolecular Crystals Containing Lattice-Patterned Polymer Networks. *J. Am. Chem. Soc.* **2020,** *142*, 19402-19410.

85. Han, K.; Na, Y.; Zhang, L.; Tezcan, F. A., Dynamic, Polymer-Integrated Crystals for Efficient, Reversible Protein Encapsulation. *J. Am. Chem. Soc.* **2022,** *144*, 10139-10144.

86. Wu, G.; Li, M.; Luo, Z.; Qi, L.; Yu, L.; Zhang, S.; Liu, H., Designed Synthesis of Compartmented Bienzyme Biocatalysts Based on Core–Shell Zeolitic Imidazole Framework Nanostructures. *Small* **2023,** *19*, 2206606.

87. Chen, W.-H.; Vázquez-González, M.; Zoabi, A.; Abu-Reziq, R.; Willner, I., Biocatalytic cascades driven by enzymes encapsulated in metal–organic framework nanoparticles. *Nat. Catal.* **2018,** *1*, 689-695.

88. Poole, R. K.; Hill, S., Respiratory protection of nitrogenase activity in Azotobacter vinelandii--roles of the terminal oxidases. *Biosci. Rep.* **1997,** *17*, 303-17.

89. Sanchez, S.; Solovev, A. A.; Mei, Y.; Schmidt, O. G., Dynamics of biocatalytic microengines mediated by variable friction control. *J. Am. Chem. Soc.* **2010,** *132*, 13144-5.

90. Yang, Y.; Arqué, X.; Patiño, T.; Guillerm, V.; Blersch, P.-R.; Pérez-Carvajal, J.; Imaz, I.; Maspoch, D.; Sánchez, S., Enzyme-Powered Porous Micromotors Built from a Hierarchical Micro- and Mesoporous UiO-Type Metal–Organic Framework. *J. Am. Chem. Soc.* **2020,** *142*, 20962-20967.

91. Wulff, G., XXV. Zur Frage der Geschwindigkeit des Wachsthums und der Auflösung der Krystallflächen. *Z. Kristallogr. - Cryst. Mater.* **1901,** *34*, 449-530.

92. Lovette, M. A.; Browning, A. R.; Griffin, D. W.; Sizemore, J. P.; Snyder, R. C.; Doherty, M. F., Crystal Shape Engineering. *Ind. Eng. Chem.* **2008,** *47*, 9812-9833.

93. Wang, S. G.; Tian, E. K.; Lung, C. W., Surface energy of arbitrary crystal plane of bcc and fcc metals. *J. Phys. Chem. Solids.* **2000,** *61*, 1295-1300.

94. Winterbottom, W. L., Equilibrium shape of a small particle in contact with a foreign substrate. *Acta Metall.* **1967,** *15*, 303-310.

95. Zucker, R. V.; Chatain, D.; Dahmen, U.; Hagège, S.; Carter, W. C., New software tools for the calculation and display of isolated and attached interfacial-energy minimizing particle shapes. *J. Mater. Sci.* **2012,** *47*, 8290-8302.

96. Wang, S.; Liu, G.; Wang, L., Crystal Facet Engineering of Photoelectrodes for Photoelectrochemical Water Splitting. *Chem. Rev.* **2019,** *119*, 5192-5247.

97. Read, C. G.; Steinmiller, E. M.; Choi, K. S., Atomic plane-selective deposition of gold nanoparticles on metal oxide crystals exploiting preferential adsorption of additives. *J. Am. Chem. Soc.* **2009,** *131*, 12040-1.

98. Li, R.; Zhang, F.; Wang, D.; Yang, J.; Li, M.; Zhu, J.; Zhou, X.; Han, H.; Li, C., Spatial separation of photogenerated electrons and holes among 010 and 110 crystal facets of BiVO4. *Nat. Commun.* **2013,** *4*, 1432.

99. Huard, D. J.; Kane, K. M.; Tezcan, F. A., Re-engineering protein interfaces yields copper-inducible ferritin cage assembly. *Nat. Chem. Biol.* **2013,** *9*, 169-76.

100. Kabsch, W., Integration, scaling, space-group assignment and post-refinement. *Acta. Crystallogr. D Biol. Crystallogr.* **2010,** *66*, 133-44.

101. Kabsch, W., Xds. *Acta. Crystallogr. D Biol. Crystallogr.* **2010,** *66*, 125-32.

102. Zhou, D.; Jin, S.; Li, Y.; Qiu, F.; Deng, F.; Wang, J.; Jiang, Q., Effect of stoichiometry on the surface energies of {100} and {111} and the crystal shape of TiCx and TiNx. *CrystEngComm* **2013,** *15*, 643-649.